

FOUR-DIMENSIONAL (4D) PRINTING

EDITED BY: Yusheng Shi, Shoufeng Yang, Kun Zhou and Chunze Yan
PUBLISHED IN: *Frontiers in Materials*



frontiers

Frontiers eBook Copyright Statement

The copyright in the text of individual articles in this eBook is the property of their respective authors or their respective institutions or funders. The copyright in graphics and images within each article may be subject to copyright of other parties. In both cases this is subject to a license granted to Frontiers.

The compilation of articles constituting this eBook is the property of Frontiers.

Each article within this eBook, and the eBook itself, are published under the most recent version of the Creative Commons CC-BY licence.

The version current at the date of publication of this eBook is CC-BY 4.0. If the CC-BY licence is updated, the licence granted by Frontiers is automatically updated to the new version.

When exercising any right under the CC-BY licence, Frontiers must be attributed as the original publisher of the article or eBook, as applicable.

Authors have the responsibility of ensuring that any graphics or other materials which are the property of others may be included in the CC-BY licence, but this should be checked before relying on the CC-BY licence to reproduce those materials. Any copyright notices relating to those materials must be complied with.

Copyright and source acknowledgement notices may not be removed and must be displayed in any copy, derivative work or partial copy which includes the elements in question.

All copyright, and all rights therein, are protected by national and international copyright laws. The above represents a summary only. For further information please read Frontiers' Conditions for Website Use and Copyright Statement, and the applicable CC-BY licence.

ISSN 1664-8714

ISBN 978-2-88971-597-8

DOI 10.3389/978-2-88971-597-8

About Frontiers

Frontiers is more than just an open-access publisher of scholarly articles: it is a pioneering approach to the world of academia, radically improving the way scholarly research is managed. The grand vision of Frontiers is a world where all people have an equal opportunity to seek, share and generate knowledge. Frontiers provides immediate and permanent online open access to all its publications, but this alone is not enough to realize our grand goals.

Frontiers Journal Series

The Frontiers Journal Series is a multi-tier and interdisciplinary set of open-access, online journals, promising a paradigm shift from the current review, selection and dissemination processes in academic publishing. All Frontiers journals are driven by researchers for researchers; therefore, they constitute a service to the scholarly community. At the same time, the Frontiers Journal Series operates on a revolutionary invention, the tiered publishing system, initially addressing specific communities of scholars, and gradually climbing up to broader public understanding, thus serving the interests of the lay society, too.

Dedication to Quality

Each Frontiers article is a landmark of the highest quality, thanks to genuinely collaborative interactions between authors and review editors, who include some of the world's best academicians. Research must be certified by peers before entering a stream of knowledge that may eventually reach the public - and shape society; therefore, Frontiers only applies the most rigorous and unbiased reviews.

Frontiers revolutionizes research publishing by freely delivering the most outstanding research, evaluated with no bias from both the academic and social point of view. By applying the most advanced information technologies, Frontiers is catapulting scholarly publishing into a new generation.

What are Frontiers Research Topics?

Frontiers Research Topics are very popular trademarks of the Frontiers Journals Series: they are collections of at least ten articles, all centered on a particular subject. With their unique mix of varied contributions from Original Research to Review Articles, Frontiers Research Topics unify the most influential researchers, the latest key findings and historical advances in a hot research area! Find out more on how to host your own Frontiers Research Topic or contribute to one as an author by contacting the Frontiers Editorial Office: frontiersin.org/about/contact

FOUR-DIMENSIONAL (4D) PRINTING

Topic Editors:

Yusheng Shi, Huazhong University of Science and Technology, China

Shoufeng Yang, University of Southampton, United Kingdom

Kun Zhou, Nanyang Technological University, Singapore

Chunze Yan, Huazhong University of Science and Technology, China

Citation: Shi, Y., Yang, S., Zhou, K., Yan, C., eds. (2021). Four-dimensional (4D) Printing. Lausanne: Frontiers Media SA. doi: 10.3389/978-2-88971-597-8

Table of Contents

04	<i>Editorial: "Four-Dimensional (4D) Printing"</i>	Yusheng Shi, Shoufeng Yang, Kun Zhou and Chunze Yan
06	<i>Hexagon-Twist Frequency Reconfigurable Antennas via Multi-Material Printed Thermo-Responsive Origami Structures</i>	Ya-Jing Zhang, Li-Chen Wang, Wei-Li Song, Mingji Chen and Daining Fang
17	<i>Intelligent Hydrogel Actuators With Controllable Deformations and Movements</i>	Qian Zhao, Zhenglei Yu, Yunhong Liang, Lei Ren and Luquan Ren
28	<i>Recent Advances of 4D Printing Technologies Toward Soft Tactile Sensors</i>	Yuneng Tang, Baiqian Dai, Bin Su and Yusheng Shi
38	<i>Graphene Oxide-Modified Microcapsule Self-Healing System for 4D Printing</i>	Bowen Ma, Yuping Zhang, Yongjie Wei, Mingrui Li and Dongdong Li
48	<i>4D Printing Pre-Strained Structures for Fast Thermal Actuation</i>	Yu Zou, Zhongyi Huang, Xiyang Li and Pengyu Lv
57	<i>Plant-Morphing Strategies and Plant-Inspired Soft Actuators Fabricated by Biomimetic Four-Dimensional Printing: A Review</i>	Luquan Ren, Bingqian Li, Kunyang Wang, Xueli Zhou, Zhengyi Song, Lei Ren and Qingping Liu
73	<i>4D Printing Dual Stimuli-Responsive Bilayer Structure Toward Multiple Shape-Shifting</i>	Luquan Ren, Bingqian Li, Qingping Liu, Lei Ren, Zhengyi Song, Xueli Zhou and Peng Gao
84	<i>Four-Dimensional Printing of Alternate-Actuated Composite Structures for Reversible Deformation under Continuous Reciprocation Loading</i>	Guanghao Chu, Bin Zhou, Guangbin Shao, Dianjin Zhang and Longqiu Li
94	<i>4D Printing of Lead Zirconate Titanate Piezoelectric Composites Transducer Based on Direct Ink Writing</i>	Kai Liu, Qingqing Zhang, Chenyang Zhou, Yusheng Shi, Ce Sun, Huajun Sun, Changxia Yin, Jiaming Hu, Shuyu Zhou, Yuzhen Zhang and Yu Fu
105	<i>Design of Shape Reconfigurable, Highly Stretchable Honeycomb Lattice With Tunable Poisson's Ratio</i>	Le Dong, Chengru Jiang, Jinqiang Wang and Dong Wang



Editorial: “Four-Dimensional (4D) Printing”

Yusheng Shi^{1*}, Shoufeng Yang², Kun Zhou³ and Chunze Yan¹

¹State Key Laboratory of Material Processing and Die and Mould Technology, School of Materials Science and Engineering, Huazhong University of Science and Technology, Wuhan, China, ²Materials Research Group, Faculty of Engineering and the Environment, University of Southampton, Southampton, United Kingdom, ³Singapore Centre for 3D Printing, School of Mechanical and Aerospace Engineering, Nanyang Technological University, Singapore

Keywords: four-dimensional (4D) printing, three-dimensional (3D) printing, additive manufacturing, intelligent component, controllable change

Editorial on the Research Topic

Four-Dimensional (4D) Printing

Four-dimensional (4D) printing has received widespread attention since its conceptualization in 2013. It is a revolutionary manufacturing technology based on the high degree of cross-integration of the disciplines including materials, mechanical engineering, dynamics, and informatics, etc. 4D printing, a cutting-edge branch of additive manufacturing (AM) technology, shows the capability of fabricating intelligent components through the active design of smart materials and structures, as well as the shapes, properties, or functionalities that can controllably vary with time and space dimensions. In recent years, a growing body of research has investigated the change in shapes of the 4D printed components. The main challenges that need to be addressed are the implementation of the change in properties and functionalities, as well as research on simulation technology for 4D printing. The 4D printed products have vast potential for various applications in the field of aerospace, automotive, biomedical, and soft robots, etc. Therefore, 4D printing is a very promising and valuable research field. It is encouraging that this Special Issue on 4D printing has collected ten articles, covering research on the materials, structures, functionalities, and applications in 4D printing.

The most popular way to develop 4D printing is to adopt intelligent materials in the AM process. Therefore, many researchers are interested in developing new intelligent materials. Zhao et al. fabricated a near-infrared laser driven intelligent hydrogel actuator system via extrusion-typed 3D printing and hydrothermal synthesis. The intelligent hydrogel actuator reached an effective displacement of 20 mm within 10 s through the forward movement, providing a material candidate for practical applications of 4D printing in the soft robot, information sensing, and health engineering. Ma et al. prepared a kind of self-healing material that is a promising intelligent material. The material was prepared by melamine-formaldehyde resin microcapsules using *in-situ* polymerization, and then it was fabricated through a 3D printer. The printed component showed excellent repair effect with a tensile strength of 50.93 MPa and a recovery rate of up to 87.22%.

Besides the intelligent materials, another representative way to realize 4D printing is through non-intelligent materials combined with specific structure design. As a result, the structure design is of particular importance. Dong et al. developed a shape reconfigurable, highly stretchable lattice structure with tunable Poisson's ratio. The lattice was built based on a hexagonal honeycomb structure, demonstrating tunable shape reconfigurability as the ambient temperature changes, which was investigated by experiment and simulation. Chu et al. presented a structure design using alternate actuation to attain competent loading capacity in different deformed states. The two components were programmed to have the deformation behavior and stimulated by thermal expansion mismatch between polylactic acid (PLA) and carbon-fiber-reinforced PLA. Zou et al.

OPEN ACCESS

Edited and reviewed by:

Wei Hua Li,
University of Wollongong, Australia

*Correspondence:

Yusheng Shi
shiyusheng@hust.edu.cn

Specialty section:

This article was submitted to
Smart Materials,
a section of the journal
Frontiers in Materials

Received: 12 August 2021

Accepted: 31 August 2021

Published: 20 September 2021

Citation:

Shi Y, Yang S, Zhou K and Yan C
(2021) Editorial: “Four-Dimensional
(4D) Printing”.
Front. Mater. 8:757479.
doi: 10.3389/fmats.2021.757479

proposed a pre-strained strategy to accelerate the actuation of thermal responsive structures. A bilayer structure with one pre-strained layer and the other non-pre-strained layer was integrally printed. Through experiments and finite element analysis, it was demonstrated that the pre-strain plays a key role in the deformation and also greatly accelerates the actuation of the bilayer structure.

Multi-material printing processes that can respond to diverse stimuli have become a research hotspot in 4D printing. Zhang et al. fabricated a typical hexagon-twist origami structure via multi-material printing technology. The printed structure has multi-stable features and the stiffness of the deformable structure is dramatically reduced under thermal triggering. The existing 4D printing technology is mostly subjected to only responsiveness to a single stimulus. To overcome this limit, Ren et al. proposed a 4D printing strategy with a dual stimuli-responsive shape-shifting structure that responds to both temperature and water. The structure was printed by direct ink writing (DIW) method to deposit a polyurethane elastomer material with water-swelling characteristics on a heat-shrinkage shape memory polymer material to form a bilayer structure. The multiple stimuli-responsive 4D printing method can effectively improve the intelligent responsiveness of 4D printed structures by combining multiple smart materials.

One of the research emphases of 4D printing rests with the achievement of the controllable changes in properties and functionalities of 4D printed components. To reflect this trend, this Special Issue has a collection of papers related to the changes in properties and functionalities based on sensing and energy conversion. Tang et al. summarized the recent advances of 4D printing towards soft tactile sensors, which combine the flexibility and the converting ability between mechanical forces and electrical signals. The review paper also discussed future perspectives for this emerging field. Liu et al. fabricated an underwater acoustic transducer by DIW using lead zirconate titanate (PZT) piezoelectric composites combined with furnace firing and resin impregnation. The electrical signal generated by the underwater acoustic transducer changed autonomously with the acoustic stimulation, which indicated the application mode of 4D printing in functional devices in the future.

In addition to artificial and active material and structural design of intelligent components, biomimetic design, which seeks inspiration from nature, is an extraordinary interesting method and worthy of in-depth exploration. Ren et al. published a review paper related to biomimetic 4D printing. By this novel method, they proposed morphing strategies and fabricated plant-inspired soft actuators. Plants can arouse inspiration because they exhibit ingenious adaptive motions that respond autonomously to environmental stimuli by varying cellular organization, the anisotropic orientation of cellulose fibers, and mechanical instabilities design, etc. This review summarized the morphing and actuation mechanisms of plants and concluded the recent development of 4D printed smart materials inspired by the locomotion and structures of plant systems.

4D printing is a rapidly growing research area. The collection of the papers in this Special Issue offers a snapshot of the attractive emerging field and future development trends. We hope this Special Issue can attract the attention of researchers from diverse disciplines. Finally, on behalf of the Editorial Board, we sincerely thank the contributors and staff at Frontiers, without whom this Special Issue would not have been possible.

AUTHOR CONTRIBUTIONS

KZ and CY write the first draft; YS and SY revise and finalize the manuscript.

Conflict of Interest: The authors declare that the research was conducted in the absence of any commercial or financial relationships that could be construed as a potential conflict of interest.

Publisher's Note: All claims expressed in this article are solely those of the authors and do not necessarily represent those of their affiliated organizations, or those of the publisher, the editors and the reviewers. Any product that may be evaluated in this article, or claim that may be made by its manufacturer, is not guaranteed or endorsed by the publisher.

Copyright © 2021 Shi, Yang, Zhou and Yan. This is an open-access article distributed under the terms of the Creative Commons Attribution License (CC BY). The use, distribution or reproduction in other forums is permitted, provided the original author(s) and the copyright owner(s) are credited and that the original publication in this journal is cited, in accordance with accepted academic practice. No use, distribution or reproduction is permitted which does not comply with these terms.



Hexagon-Twist Frequency Reconfigurable Antennas via Multi-Material Printed Thermo-Responsive Origami Structures

Ya-Jing Zhang^{1,2†}, Li-Chen Wang^{1,2†}, Wei-Li Song^{1,2*}, Mingji Chen^{1,2} and Daining Fang^{1,2}

¹Institute of Advanced Structure Technology, Beijing Institute of Technology, Beijing, China, ²Beijing Key Laboratory of Lightweight Multi-functional Composite Materials and Structures, Beijing Institute of Technology, Beijing, China

OPEN ACCESS

Edited by:

Yusheng Shi,
Huazhong University of Science and
Technology, China

Reviewed by:

Yu Wang,
University of Science and Technology
of China, China
Haibao Lu,
Harbin Institute of Technology, China

*Correspondence:

Wei-Li Song
weilis@bit.edu.cn

[†]These authors have contributed
equally to this work

Specialty section:

This article was submitted to Smart
Materials,
a section of the journal
Frontiers in Materials

Received: 31 August 2020

Accepted: 03 November 2020

Published: 23 November 2020

Citation:

Zhang Y-J, Wang L-C, Song W-L,
Chen M and Fang D (2020) Hexagon-
Twist Frequency Reconfigurable
Antennas via Multi-Material Printed
Thermo-Responsive
Origami Structures.
Front. Mater. 7:600863.
doi: 10.3389/fmats.2020.600863

The origami structure has caused a great interest in the field of engineering, and it has fantastic applications in the deployable and reconfigurable structures. Owing to the unique multi-stable states, here a typical hexagon-twist origami structure is fabricated via multi-material printing technology. The printed structure has multi-stable features and the stiffness of the deformable structure is dramatically reduced under thermal triggering. Such behavior causes an increase in the structural degree of freedom, allowing for self-deployment via releasing the prestored energy in the elastic crease. The response time and reaction time of the self-deployment process are also studied and illustrate the higher energy barrier of the folded state, the longer self-deployment time. Utilizing such unique features and design principles, a prototype of frequency reconfigurable origami antenna of nine diverse operating modes is subsequently designed and assembled with the hexagon-twist origami structure as the dielectric substrate. The antenna implements the cross-band from two different frequency bands, enabling to realize frequency reconfigurable under thermal condition.

Keywords: multi-material 4D printed, origami structures, reconfigurable antennas, hexagon-twist, self-deployment

INTRODUCTION

Origami is an ancient oriental art and an emerging frontier science. It is in the intersecting fields of mathematics, mechanics, materials, control, biology, medicine and other basic disciplines, resulting in many scientific applications, such as solar panels design, airbag structure, and even the spatial folding of biological macro-molecules such as DNA and proteins (Xie, 2010; Leng et al., 2011; Fernandes and Gracias, 2012; Hu et al., 2012; Felton et al., 2014; Ge et al., 2014; Gladman et al., 2015; Zhao et al., 2015; Li et al., 2017; Zhao et al., 2017). Origami technology has always been regarded as a means of developing deployable and reconfigurable engineering systems because of its characteristics of easy bending and twisting (Anfinson et al., 1973; Bromberg and Ron, 1998; Li and Lewis, 2003; Ahn et al., 2010; Lu et al., 2010b; Leng et al., 2011; Erb et al., 2012; Ge et al., 2012; Ge et al., 2013; Therien-Aubin et al., 2013; Tibbits, 2014; Breger et al., 2015; Gladman et al., 2015; Luo et al., 2015; Mu et al., 2015; Su et al., 2018). This technology can be used in designing large-scale planar structures such as building structures (Overvelde et al., 2016; Faber et al., 2018), and

space antenna reflection surfaces, as well as the design of micro surgical instrument (Wong et al., 1994; Fernandes and Gracias, 2012; Breger et al., 2015).

As electromagnetic communication systems are more widely used in life, the demand for the number of antennas is also growing. In order to reduce electromagnetic coupling and system weight, the frequency reconfigurable antenna that can replace the function of multiple antennas with one antenna has become a research hotspot for engineers and scientists (Li et al., 2014; Song et al., 2017).

In this paper, a multi-material printed hexagon-twist origami structure was designed. When folded according to different crease pattern, the origami structure unit had three different folding stable states (Silverberg et al., 2015). Due to the property of the structural material, the folded stable state configuration could self-deploy under the influence of temperature, and the self-deployment temperature could be controlled by the geometric parameters of the structure. The dipole antenna is a hotspot in antenna research because of its simple principle, low cost, and ease of manufacturing. In our research, a hexagonal twist origami structure was used as the antenna substrate to design a dipole frequency reconfigurable antenna with simulation and experiment.

MATERIALS AND METHODS

Fabrication of the Hexagon-Twist Origami Structure

All of the hexagon-twist origami structures in this work were fabricated using the multimaterial polyjet 3D printing technique after the structure designed with specific geometry parameter by the CAD software SOLIDWORKS. In the 3D printing process, two different mechanical properties materials VeroWhitePlusPlus (VW) and TangoBlackPlus (TG) used in the fabrication were all available from the multimaterial 3D printer (Object 350, Stratasys). For hexagon-twist origami structure, the crease and paper face material were adopted with TG and VW, respectively, which was determined by their material property (Figure 1). Of the two materials, TG is a soft

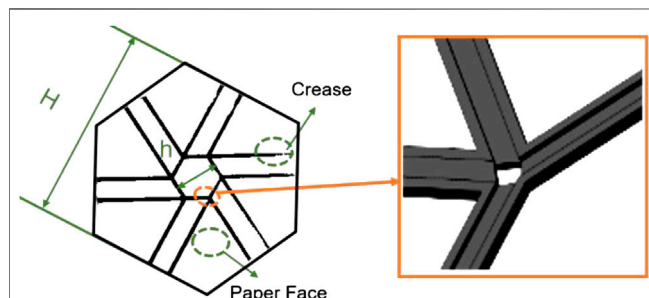


FIGURE 1 | Fabrication of the hexagon-twist origami structure. The multimaterial 3D printed hexagon-twist origami structure with the specific design parameter. H denotes the height of outer hexagon. h denotes the height of inter hexagon. The design details about the vertex is shown in the illustration.

elastomer that mainly consists of exo-1,7,7-trimethyl-bicyclo [2.2.1]hept-2-yl acrylate and photoinitiators, and VW is a rigid polymer mainly consisting of exo-1,7,7-trimethylbicyclo [2.2.1] hept-2-ylacrylate, tricyclodecane dimethanol diacrylate, titanium dioxide, and photoinitiators. Both TangoBlackPlus and VeroWhitePlus can be cured by ultraviolet light at room temperature. The corresponding uniaxial stretching mechanical testing results were shown in Figure 2A (adopted with INSTRON electronic universal testing machine LEGEND 2367). According to the stress-strain curve, the material TG in the crease area undergone large deformation when stretched under a small stress

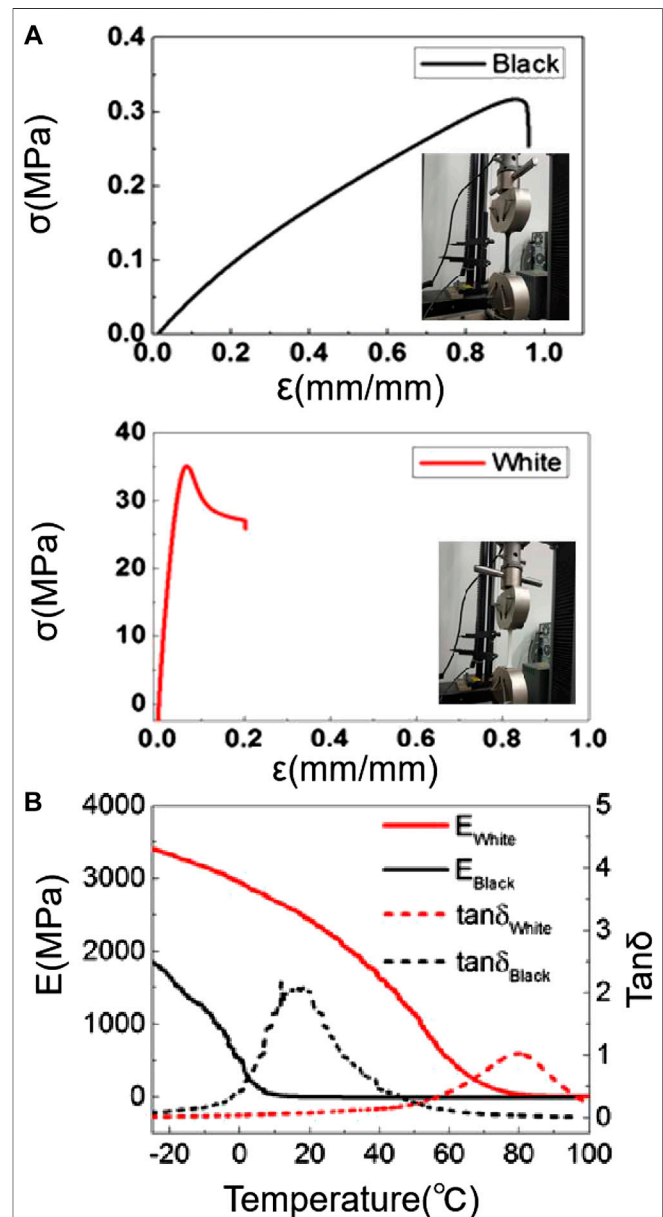


FIGURE 2 | Basic mechanical test results of 3D printed materials VeroWhitePlus and TangoBlackPlus. (A) The uniaxial stretching mechanical and (B) the dynamic mechanical analysis testing results of the two materials.

and the material VW in the paper face area is a high elastic modulus material (~ 527 MPa) compared with the material TG (~ 0.5 MPa). When the structure was folded, the crease area could withstand relatively large elastic deformation and the paper face area shown small strain. The folding stable state of the hexagon-twist origami structure could achieve self-deployment at high temperature. In order to explore the mechanical principle of self-deployment behavior, it was necessary to analyze the thermodynamic behavior of the TG and VW material via dynamic mechanical analysis (DMA). In the typical measurement, a preload of 1 mN was applied to the sample (dimensions of $12 \times 5.0 \times 0.5$ mm) and the strain was oscillated at a frequency of 1 Hz with a peak-to-peak amplitude of 0.1%. In the process, the samples were firstly heated up to 150°C and stabilized for 10 min to reach thermal equilibrium. The temperature was then decreased from 150°C to -50°C at a rate of $2^\circ\text{C}/\text{min}$. The temperature dependence of the storage modulus and $\tan\delta$ are shown in **Figure 2B**. The glass transition temperature (T_g) is identified as the temperature corresponding to the peak of the $\tan\delta$ curve. The T_g values of the VeroWhitePlus and the TangoBlackPlus are ~ 80 and $\sim 20^\circ\text{C}$, respectively. DMA tests were performed on a dynamic mechanical analyzer (Model Q800, TA Instruments, New Castle, DE, USA) in the uniaxial tension mode. When the folding stable state of the hexagon-twist origami structure is at a high temperature range (20 – 80°C), the storage modulus of the material VW decreased rapidly and the material TG remains essentially constant.

Measurements of Hexagon-Twist Origami Structure Self-Deployment Temperature

The self-deployment temperatures were measured in a water bath. The heat source was from the magnetic heating stirrer that could set the final heated temperature. The thermocouple temperature sensor was used as a feedback for the real time water temperature. The square-twist origami structures with the transformation modes I and II stable state were put in a round beaker with a certain amount of water that was heated at a required temperature, according to the various experimental requirements. The heat rate was kept in a constant value while heating these structures. The self-deployment temperature was defined as the temperature when the structure was obviously converted to the flat state. When the stable state of the structure was altered, the temperature was recorded as one measurement. In this paper, two different methods were used to generate thermal stimulus for driving square-twist origami structures: water bath and infrared light. The first type was mainly based on heat conduction, while the second type was heat radiation. Considering the heat effects on the twist structures, the method of using uniform heat conduction was selected in the water bath. For practical application, a noncontact infrared radiation heating method was applied. The multi-material 3D printed square-twist origami structures were manipulated by temperature, triggering for self-deployment under heating.

Design and Fabrication of Frequency Reconfigurable Dipole Antenna

In this work, three design principles were obeyed for designing frequency reconfigurable dipole antennas. Primarily, the dipole antenna required center symmetry of the radiation pattern. Additionally, for pursuing large degree of short circuit, the radiation pattern should be designed across creases as much as possible. Finally, to maintain the foldability of hexagon-twist structure media board, the radiation pattern should avoid the vertices of the hexagon-twist structure as far as possible. Based on the above rules, a basic configuration design of dipole antenna is shown in **Figure 3**, and then the 3D electromagnetic simulation software HFSS was used to simulate the specific geometry size of the hexagon-twist frequency reconfigurable dipole antenna. The pattern of the antenna radiation patch were arranged along the distribution and arrangement of the folds for the antenna substrate. The material of the antenna arm was set ideal conductor. Since the dipole antenna had a symmetrical structure, the lumped port excitation method was used to feed the antenna, and the simulation frequency band was set to 1–6 GHz. According to the initial simulation results, the design parameters could be optimized by running loop variables for obtaining the optimal performance with the condition of impedance matching. For fabricating aspects of the frequency reconfigurable antenna, the origami dielectric substrate and the radiation patch were fabricated with multi-material 3D printing technology and copper tape, respectively. For the antenna arm of the dipole antenna, that is, the radiation patch, the sputtered copper foil was initially selected to be directly glued to the surface of the dielectric substrate. However, due to its small toughness during the folding and unfolding with the structure, it was easy to break and result antenna failure, so the double-sided conductive copper tape was selected as the radiation patch. Because of its good toughness, the reliability of the antenna was effectively improved during the folding and unfolding process. Coaxial feeder feeding method was adopted

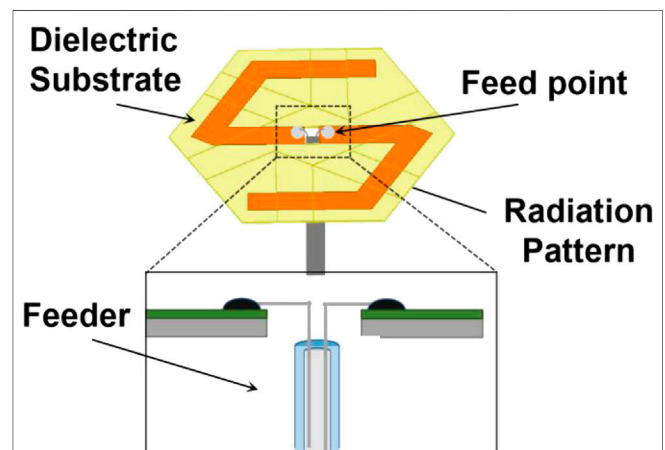


FIGURE 3 | The components of a hexagon-twist origami antenna.

for the hexagon-twist frequency reconfigurable origami antenna (Figure 3).

RESULTS AND DISCUSSION

Based on our previous work experience research on polygon-twist origami structure (Wang et al., 2019), the length and proportion of the inner and outer sides have an important role in the origami folding stability. In this work, the height of the inner and outer hexagons structure was selected as a key parameter for studying the stability of hexagon-twist origami. The varies size structure were described with h - H where h and H denotes the height of the inner and outer hexagon, respectively. According to the results in Figure 4A, the hexagon-twist structure with sizes 15–50, 15–60, 17–70 existed no stable state which meant “unfoldable” and were unsuitable for reconfigurable dielectric substrate. As for the size of 30–100, 30–120, 30–140, the hexagon-twist structure showed multi-stable state which meant “foldable”, and the specific folded stable state with size 30–100 were shown in Figure 4B. When all the outer panels were folded up counterclockwise around the center hexagon, this self-locking stable state was regarded as state A; When four outer panels and the other two outer panel were symmetrically folded up and down counterclockwise around the center hexagon, respectively, this stable state was named state B; When five outer panels and one outer panel were folded up and down counterclockwise around the center hexagon, this stable state was regarded as state C

(Figure 4B). According to our previous work (Wang et al., 2020), because the elastic modulus of material VW decreased drastically as the temperature increased (Figure 2B), the stiffness ratio of the paper facet to the crease was varied (Tawk et al., 2010), thereby decreasing the energy barrier of the structure. The self-deployment of the multi-material 3D printed polygon-twist origami structure was driven by the energy stored in the crease material TG. The hexagon-twist 3D printed origami structure could also self-deploy under the higher temperature condition as shown in Figure 5 for state A, state B and state C. In order to further research the influence of the key geometric parameters of the origami structure on its self-deployment behavior, the self-deployment behavior of stable state A, state B, and state C with varies geometry size under the 65°C water bath condition was studied. To quantify the self-deployment process, the response time and reaction time required to be defined. Response time referred to the time from the beginning of excitation to the moment of observing apparent motion. The reaction time was defined as the subsequent time from the moment of observing apparent motion to the completion of deployment. As the outer contour of the hexagonal increased ($H = 100, 120, 140$ mm) with the same central hexagon ($h = 30$ mm), the response time and reaction time of the stable state during self-deployment gradually increased (Figure 6). This was because the larger geometric size of the outer hexagon, the greater energy barrier of the structure, and the more energy that needed to be absorbed during self-deployment, so the time required increased. By comparing the self-deployment behavior

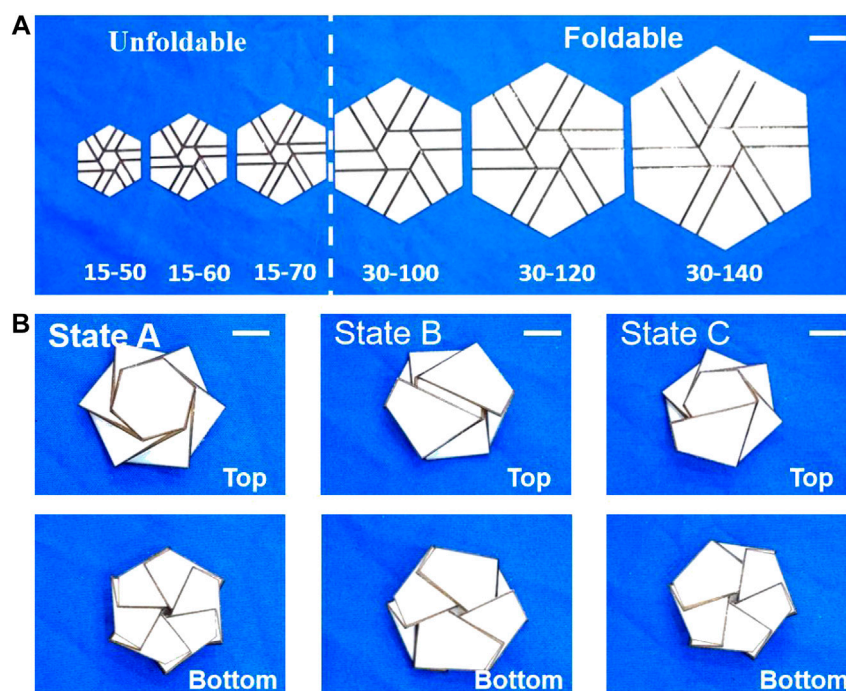


FIGURE 4 | The multi-material 3D printed hexagon-twist origami structure. **(A)** Multi-stable research about hexagon-twist origami structure with different size (h - H : h and H denotes the height of the inner and outer hexagon, respectively). Scale bar, 30 mm. **(B)** The multi-stable states of 3D printed hexagon-twist origami structure with size 30–100. Scale bar, 10 mm.

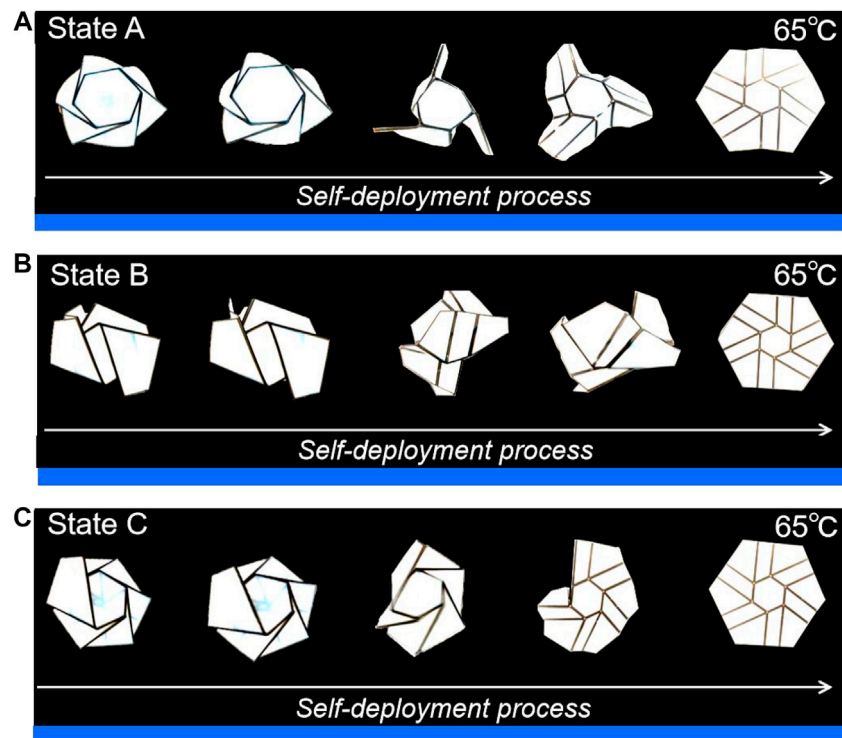


FIGURE 5 | The self-deployment process of multi-material 3D printed hexagon-twist origami structure with (A) state A, (B) state B and (C) state C under 65°C water bath condition. Each image of the structure during the self-deployment process is scaled to ensure the overall picture effect.

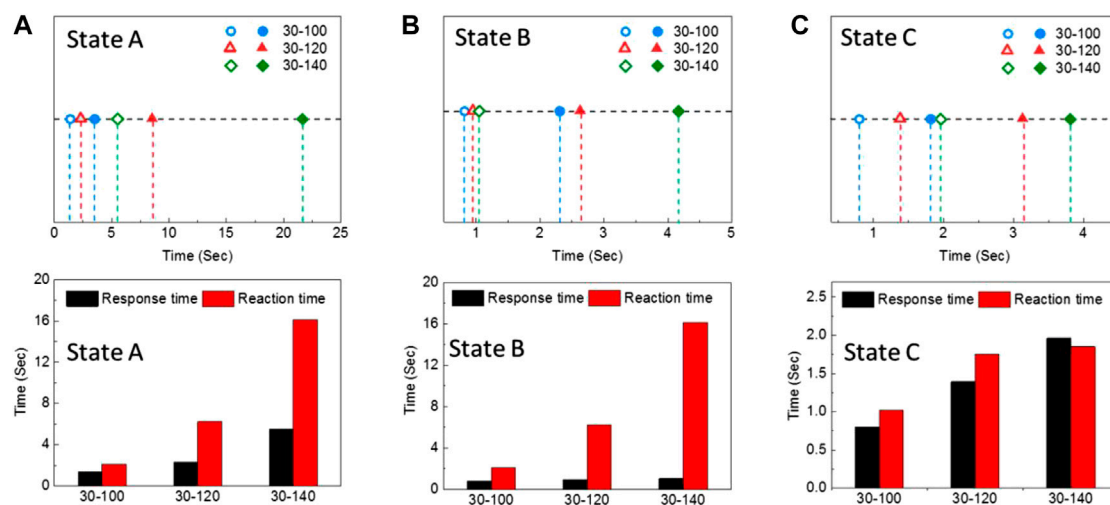


FIGURE 6 | The self-deployment response and reaction time results of (A) state A, (B) state B and (C) state C with various size. In the top row of graphs, the response time is from zero to the hollow point, and the reaction time is from the hollow point to the solid point.

time between different stable states, state C and state A required the shortest and the longest reaction time with the same geometric parameter ratio of the origami structure, respectively. According to the author's previous work (Wang et al., 2020), the order of energy barriers of different states can be

obtained based on their reaction time as state A > state B > state C. (Although the crease pattern of square-twist and hexagon-twist structure are different, they have the same self-deployment mechanism, and both them belong to the twist origami category).

In the following content, a frequency reconfigurable dipole antenna was manufactured with the 3D multi-material printed hexagon-twist origami structure as the dielectric substrate. The thickness, the height of central hexagon and the outer hexagon of the hexagon-twist origami dielectric substrate were 0.5, 30, and 100 mm, respectively (**Figure 3**). The relative dielectric constant ϵ and the loss tangent angle $\tan\delta$ for the structure were 2.8 and 0.0001, respectively. Keeping the dielectric substrate in a flat state, the dipole arms were not in contact with each other, which was the initial frequency state. When the dielectric substrate maintained various folded stable state, the antenna dipole arms were in contact with each other to produce a short circuit, which in turn reduced the electrical length of the dipole antenna, thereby ultimately leading to an increase in the antenna frequency. It was worth noting that even if the dipole arms were not in contact with each other, the relative position of the antenna arm changes would also produce spatial resonance, which could make the antenna reconfigurable frequency. In order to shorten the design cycle and save costs, the simulation for antenna performance was carried out (*Materials and Methods*). The simulation results about the current distribution of the hexagon-twist frequency reconfigurable antenna clearly illustrated different state with various operating frequency

(**Figure 7**). It should be noted here that pasting a radiation patch on one side of the dielectric substrate to form an antenna resulted in various electrical lengths of the dipole antenna with folded forward and backward in a stable state. Because of the position of the radiation patch fixed relative to the structure, even if various folding methods formed the same state, different electrical lengths would be generated, thereby forming different operating frequencies for frequency reconfigurable antenna. Through the above illustration, the frequency reconfigurable antenna had nine antenna configurations (Flat state, State A, state B, and state C generated one, two, three and three antenna configurations, respectively.) with hexagon-twist origami substrate. In order to better design and manufacture frequency reconfigurable antenna, the influence of geometric parameters on the antenna frequency was discussed via finite element simulation (**Figure 8**). The frequency of the antenna was related to the geometric parameters of the substrate and the antenna arm. In this paper, the parameters l , w , d , and H which denoted the length, the width of the antenna arm, the thickness of the dielectric plate and the size of the outer contour, respectively, were selected as specific research factors. In order to study the influence of these parameters on the antenna resonance frequency, a standard model was chosen with $l = 50$ mm, $w =$

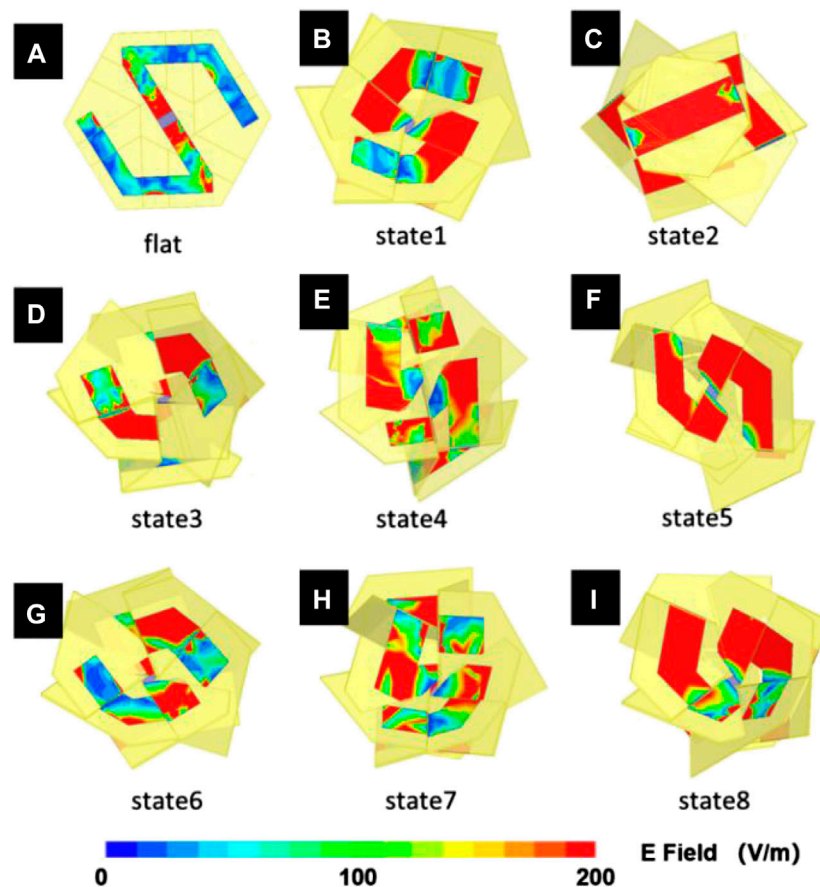


FIGURE 7 | The current distribution finite element simulation results of the hexagon-twist origami structure stable (A) flat state and (B–I) state 1–8.

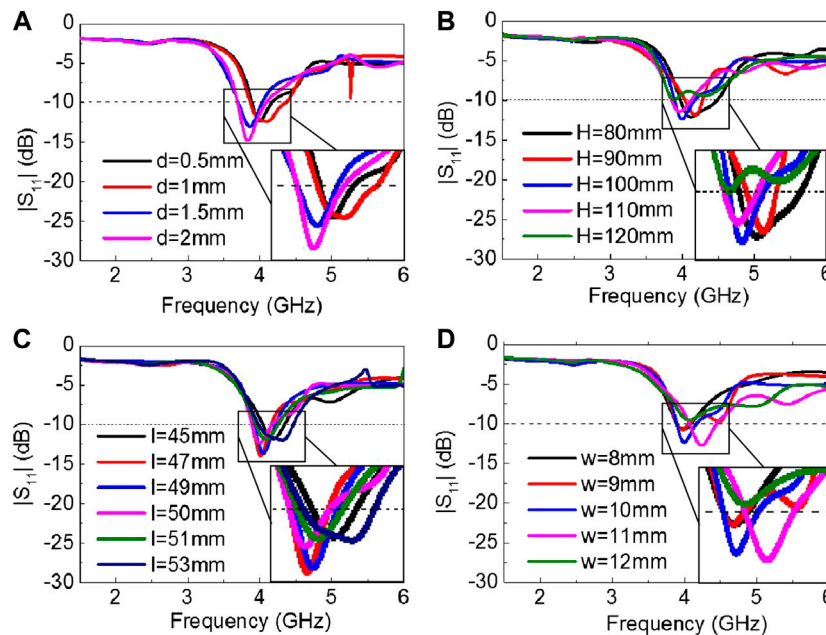


FIGURE 8 | Geometric parameters (A) the thickness of the dielectric substrate- d , (B) the height of outer hexagon for the dielectric substrate- H , (C) the length of antenna arm- l , and (D) the width of antenna arm- w effect on antenna frequency.

10 mm, $d = 0.5$ mm and $H = 100$ mm, maintaining 30 mm for the height of central hexagon. Considering the thickness d of the dielectric substrate with 0.5–2 mm, the antenna frequency decreased as the thickness of the dielectric substrate increased. The change of the overall hexagon-twist origami size H had little effect on the frequency. In the design of a general dipole antenna, the equivalent electrical length of the antenna is inversely proportional to the center resonance frequency. In **Figure 8C**, as the antenna arm l grows, the center resonance frequency did not show an obvious inverse law. Perhaps due to the error of the finite element model itself, the antenna arm growth did not increase the equivalent electrical length. The influence of the width of the antenna arm on the resonance frequency had no obvious linear law. According to the above study, the hexagon-twist origami structure exhibited self-deployment behavior due to the rapidly decrease in the storage modulus of the paper surface material under heating conditions. This kind of behavior was introduced into the antenna design, so that the antenna could realize deployment and frequency reconfigurable under the temperature field conditions. **Figure 9** showed the self-deployment deformation of the dipole antenna in the initial folded state under infrared heating and the experiment conditions of light intensity and temperature were 3.96 mW/cm^2 and approximately 75°C , respectively. The unfolding time principle of the antennas in different folded states is consistent with the unfolding law of the dielectric substrate studied in the high temperature field. The actual operating frequency of the antenna could be obtained by measuring the return loss S_{11} parameter. In this work, the S_{11} parameter was measured by the E5071C vector network analyzer that was produced by Keysight, whose test frequency range was from 0.5 to 6 GHz.

The dual port of the vector network analyzer was calibrated with an electronic calibration component prior to testing, and then connected the coaxial line of the antenna to the test interface of the vector network analyzer port1. Finally, related parameters about the analyzer was adjusted to test the various states of their parameter S_{11} via changing the configuration of the hexagon-twist dielectric substrate. In **Figure 10**, the actual test results of the antenna were in agreement with the simulation results, although there existed a certain error. It could be seen from the test results that the return loss of each antenna's operating frequency was below -10 dB, which met the basic requirements for antenna operation. Maintaining the antenna in flat state, the center resonance frequency was 3.97 GHz. According to the actual measurement results, when the antenna was folded to the state 1, the center resonance frequency was 3.39 GHz. The antenna center resonance frequencies of folded state 2~state 9 were 2.39, 2.41, 4.13, 3.67, 3.07, 2.77, and 2.66 GHz, respectively. The antenna realized nine kinds of center operating frequency changes with nine various stable states, and implemented multi-mode frequency reconfiguration.

The traditional frequency reconfigurable antenna mainly used a switch to change the electrical length of the antenna to achieve antenna frequency reconfiguration. The on and off of the switch determined the antenna reconfigurable mode. Not only were there fewer reconfigurable modes, but also the external bias circuit affected the performance of the antenna and reduced the antenna efficiency. Compared with the work of other frequency reconfigurable antennas (**Table 1**), the dipole frequency reconfigurable antenna implemented in this paper used an origami structure to self-deploy at high temperature to achieve reconfigurable frequency without additional bias

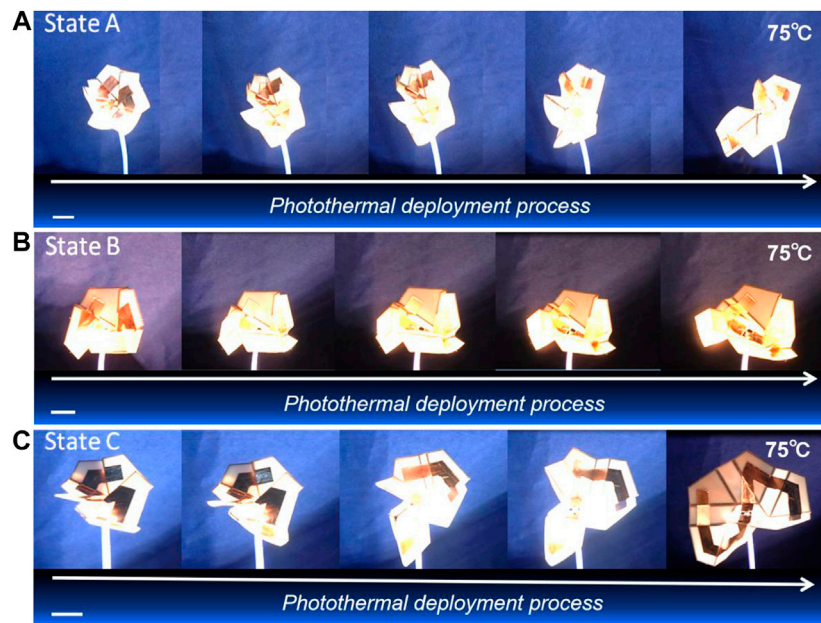


FIGURE 9 | The self-deployment process of hexagon-twist frequency reconfigurable antenna with (A) state A, (B) state B and (C) state C under photothermal condition. Scale bar, 30 mm.

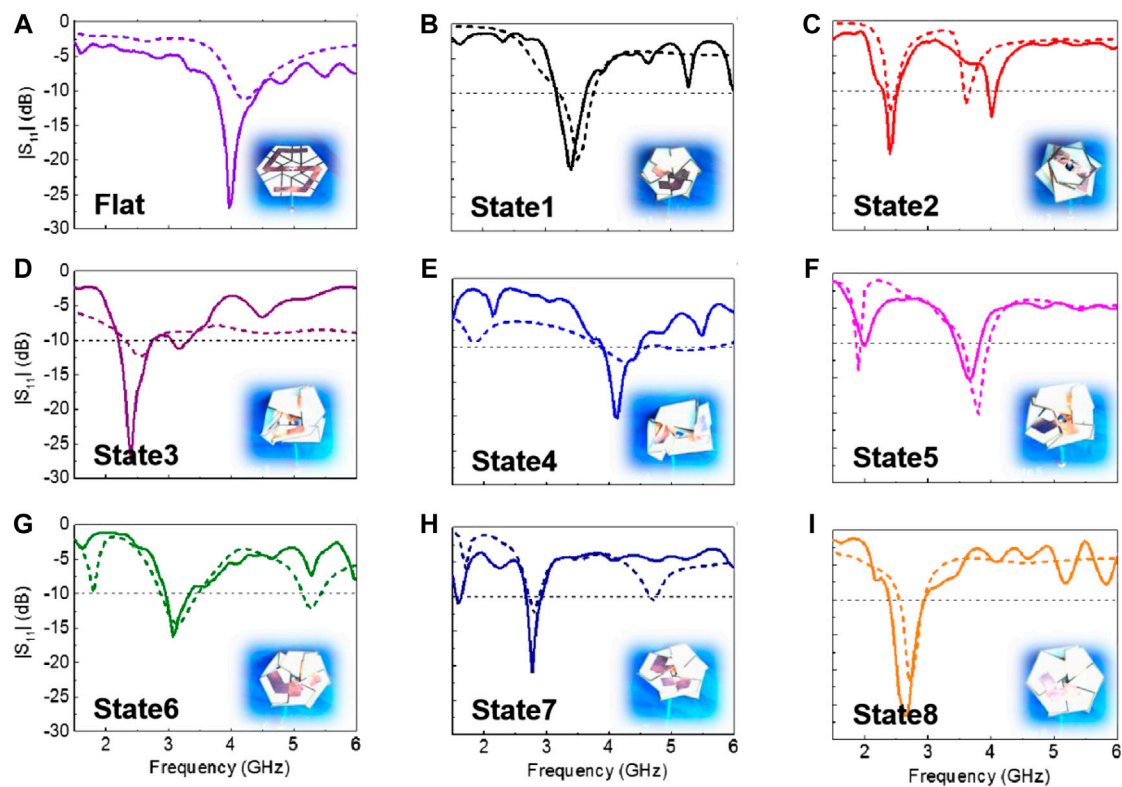
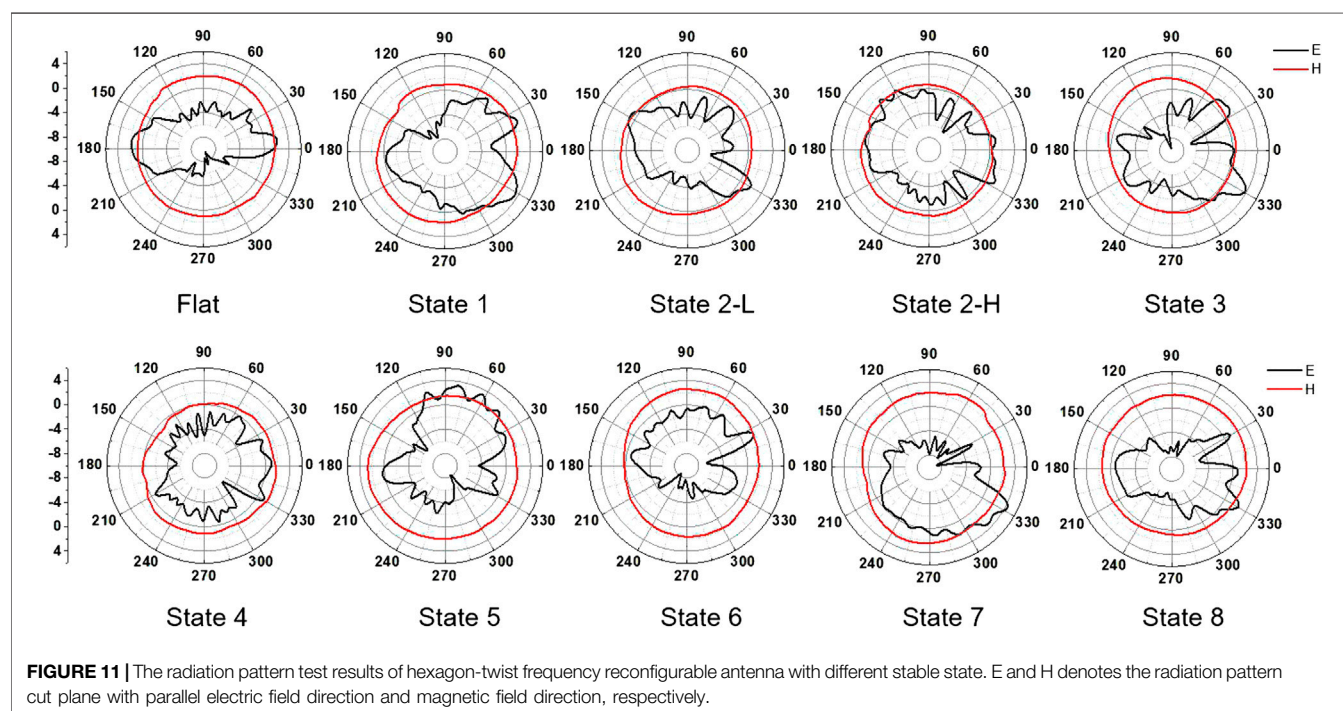


FIGURE 10 | The results of hexagon-twist origami antenna return loss. (A–I) Comparison of measured and simulated results of antenna return loss in nine different stable state for hexagon-twist origami structure. The corresponding stable state configurations are shown in the illustration.

TABLE 1 | Comparison of the frequency reconfigurable antenna works

Antenna type	Reconfigurable frequency mechanism	Number of modes	Reconfigurable frequency
Printed antenna Overvelde et al. (2016)	PIN diode switch control	2	No
Monopole antenna Wong et al. (1994)	SPST single pole single throw switch control	2	No
Microstrip patch antenna Tawk et al. (2010)	Silicon light guide switch control	2	No
Yagi dipole antenna Ahyat et al. (2013)	PIN diode switch control	4	No
Beam steering radial array antenna Jamlos et al. (2010)	PIN diode switch control	4	No
MIMO antenna Lee and Cho (2015)	Single pole SP4T switch control	4	No
Patch reconfigurable antenna Tawk et al. (2011)	Mechanical control	5	No
Microstrip slot antenna Majid et al. (2012)	PIN diode switch control	6	No
Planar parasitic array antenna Guo et al. (2014)	PIN diode switch control	7	No
Origami structure dipole antenna (This work)	Temperature control	9	Yes

**FIGURE 11** | The radiation pattern test results of hexagon-twist frequency reconfigurable antenna with different stable state. E and H denotes the radiation pattern cut plane with parallel electric field direction and magnetic field direction, respectively.

circuit affects. The antenna made in this paper was a dipole antenna, that was, an omnidirectional antenna. The radiation pattern was also tested using the microwave far-field darkroom (Figure 11). From the results of the radiation pattern, the H-plane graphic showed an omnidirectional antenna, but the E-plane graphic illustrated a non-omnidirectional antenna. This was because the electric field in the vertical plane tilted down due to the feeder, which affected the radiation characteristics in the horizontal direction. One thing to note was that state 2 had two operation frequency points, so the radiation pattern at the two frequency points were measured in state 2.

In this paper, a self-deployment origami antenna was realized based on a multi-material 3D printed hexagon twist structure dielectric substrate, and the multi-material hexagon twist structure played an important part to realize the function. In the future, the following aspects will be further studied. In terms of the self-deployment mechanism of the structure, more attention will be

paid to the influence of polymer swelling and relaxation time on the self-deployment behavior and deployment time of the structure (Lu et al., 2010a; Lu et al., 2010b; Lu and Du, 2014). In terms of driving methods, the photothermal driving method in this article will have shortcomings in practical applications, and more reliable electronic control methods may be used in subsequent work (Lu et al., 2011). In addition, the multi-stability of the hexagonal twist structure can also be applied in many aspects, such as a smart substrate with buckling-induced kirigami structure (Pang et al., 2020), making multi-stable mechanical metamaterials (Ma et al., 2016; Yan et al., 2020), or making flexible electronic devices (Ma and Zhang, 2016).

CONCLUSIONS

In this paper, a dipole cross-band frequency reconfigurable antenna based on a multi-material hexagon-twist origami

structure was designed. The specific conclusion contents were as follows:

- (1) The multi-stable state of the hexagon-twist origami structure was studied. The hexagon-twist origami structure was prepared via 3D multi-material printing, in which the paper face and the crease area were printed with resin-based materials VW and rubber-like materials TG, respectively. It was found that the folded stable state was related to the ratio and size of the inner and outer hexagons of the structure. The structure had three kinds of stable state called state A, state B and state C.
- (2) The mechanism and law of self-deployment behavior with hexagonal twist origami structure at high temperature were studied. The self-deployment behavior in the folded state was because that the storage modulus of the material VW decreased rapidly at high temperature, causing a sharp reduction in stiffness, and thereby reducing the energy barrier of the structure to less than the elastic driving energy stored in the crease material TG. The various folded states had different self-deployment behavior. The higher the energy barrier of the structure, the longer the self-deployment time was required. In this paper, the self-deployment time was state A greater than state B and state B greater than state C.
- (3) A dipole frequency reconfigurable antenna based on hexagon-twist origami structure was designed. The operating frequency and radiation pattern of the dipole antenna had been tested. The frequency reconfigurable antenna had nine operating modes according to different

crease pattern, which implemented cross-band reconfigurable frequency from S to C band. The dielectric substrate could self-deploy from the folded state at high temperature. Therefore, the antenna could realize the function of deformation and frequency reconfiguration.

DATA AVAILABILITY STATEMENT

The raw data supporting the conclusions of this article will be made available by the authors, without undue reservation.

AUTHOR CONTRIBUTIONS

W-LS, MC, and DF conceived the idea and experimental work; Y-JZ and L-CW led the experiments and simulation with assistance from W-LS and MC; W-LS and Y-JZ contributed to data analysis and interpretation and wrote the paper. All authors provided feedback.

FUNDING

Financial support from Beijing Natural Science Foundation (Grant No. 2182065) and National Natural Science Foundation of China (Grant No. 11872113) is gratefully acknowledged.

REFERENCES

- Ahn, B. Y., Shoji, D., Hansen, C. J., Hong, E., Dunand, D. C., and Lewis, J. A. (2010). Printed origami structures. *Adv. Mater.* 22, 2251–2254. doi:10.1002/adma.200904232
- Ahyat, E. N., Kamarudin, M. R., Rahman, T. A., Jamlos, M. F., Hamid, M. R., Jamaluddin, M. H., et al. (2013). Frequency and pattern reconfigurable dipole-yagi antenna. *Microw. Opt. Techn. Lett.* 55, 447–450. doi:10.1002/mop.27323
- Anfinsen, C. B. (1973). Principles that govern the folding of protein chains. *Science* 181, 223–230. doi:10.1126/science.181.4096.223
- Breger, J. C., Yoon, C., Xiao, R., Kwag, H. R., Wang, M. O., Fisher, J. P., et al. (2015). Self-folding thermomagnetically responsive soft microgrippers. *ACS Appl. Mater. Interfaces* 7, 3398–3405. doi:10.1021/am508621s
- Bromberg, L., and Ron, E. S. (1998). Temperature-responsive gels and thermogelling polymer matrices for protein and peptide delivery. *Adv. Drug Delivery Rev.* 31, 197–221. doi:10.1016/S0169-409X(97)00121-X
- Erb, R. M., Sander, J. S., Grisch, R., and Studart, A. R. (2012). Self-shaping composites with programmable bioinspired microstructures. *Nat. Commun.* 4, 1712. doi:10.1038/ncomms2666
- Faber, J. A., Arrieta, A. F., and Studart, A. R. (2018). Bioinspired spring origami. *Science* 359, 1386–1391. doi:10.1126/science.aap7753
- Felton, S., Tolley, M., Demaine, E., Rus, D., and Wood, R. (2014). A method for building self-folding machines. *Science* 345, 644–646. doi:10.1126/science.1252610
- Fernandes, R., and Gracias, D. H. (2012). Self-folding polymeric containers for encapsulation and delivery of drugs. *Adv. Drug Delivery Rev.* 64, 1579–1589. doi:10.1016/j.addr.2012.02.012
- Ge, Q., Dunn, C. K., Qi, H. J., and Dunn, M. L. (2014). Active origami by 4D printing. *Smart Mater. Struct.* 23, 094007. doi:10.1088/0964-1726/23/9/094007
- Ge, Q., Luo, X., Rodriguez, E. D., Zhang, X., Mather, P. T., Dunn, M. L., et al. (2012). Thermomechanical behavior of shape memory elastomeric composites. *J. Mech. Phys. Solids* 60, 67–83. doi:10.1016/j.jmps.2011.09.011
- Ge, Q., Qi, H. J., and Dunn, M. L. (2013). Active materials by four-dimension printing. *Appl. Phys. Lett.* 103, 131901. doi:10.1063/1.4819837
- Gladman, A. S., Matsumoto, E. A., Nuzzo, R. G., Mahadevan, L., and Lewis, J. A. (2015). Biomimetic 4D printing. *Nat. Mater.* 15, 413–418. doi:10.1038/NMAT4544
- Guo, T. F., Leng, W., Wang, A. G., Li, J. J., and Zhang, Q. F. (2014). A novel planar parasitic array antenna with frequency and pattern-reconfigurable characteristics. *IEEE Antenn. Wirel. Pr.* 13, 1569–1572. doi:10.1109/LAWP.2012.2221073
- Hu, J., Meng, H., Li, G., and Lbekwe, S. I. (2012). A review of stimuli-responsive polymers for smart textile applications. *Smart Mater. Struct.* 21, 053001. doi:10.1088/0964-1726/21/5/053001
- Jamlos, M. F., Aziz, O. A., Rahman, T. A., Kamarudin, M. R., Saad, P., Ali, M. T., and Md Tan, M. N. (2010). A beam steering radial line slot array (RLSA) antenna with reconfigurable operating frequency. *J. Electromagnet. Wave* 24, 1079–1088. doi:10.1163/156939310791586034
- Lee, W. W., and Cho, Y. S. (2015). A frequency reconfigurable MIMO antennas using RF tuning element for mobile handset. *Microw. Opt. Techn. Lett.* 57, 1092–1096. doi:10.1002/mop.29023
- Leng, J., Lan, X., Liu, Y., and Du, S. (2011). Shape-Memory polymers and their composites: stimulus methods and applications. *Prog. Mater. Sci.* 56, 1077–1135. doi:10.1016/j.msec.2018.12.054
- Li, Q., and Lewis, J. A. (2003). Nanoparticle inks for directed assembly of three-dimensional periodic structures. *Adv. Mater.* 15, 1639–1643. doi:10.1002/adma.200305413
- Li, T., Zhai, H. Q., Long, Li., and Liang, C. H. (2014). Frequency-reconfigurable bow-tie antenna with a wide tuning range frequency. *IEEE Antenn. Wirel. Pr.* 13, 1549–1552. doi:10.1109/LAWP.2014.2344676

- Li, Y. C., Zhang, Y. S., Akpek, A., Shin, S. R., and Khademhosseini, A. (2017). 4D bioprinting: the next-generation technology for biofabrication enabled by stimuli-responsive materials. *Biofabrication* 9, 012001. doi:10.1088/1758-5090/9/1/012001
- Lu, H. B., and Du, S. Y. (2014). A phenomenological thermodynamic model for the chemo-responsive shape memory effect in polymers based on Flory–Huggins solution theory. *Polym. Chem.* 5, 1155–1162. doi:10.1039/c3py01256e
- Lu, H. B., Liang, F., and Gou, J. H. (2011). Nanopaper enabled shape-memory nanocomposite with vertically aligned nickel nanostrand: controlled synthesis and electrical actuation. *Soft Matter* 7, 7416. doi:10.1039/c1sm05765k
- Lu, H. B., Liu, Y. J., Leng, J. S., and Du, S. Y. (2010a). Qualitative separation of the physical swelling effect on the recovery behavior of shape memory polymer. *Eur. Polym. J.* 46, 1908–1914. doi:10.1016/j.eurpolymj.2010.06.013
- Lu, H., Liu, Y., Gou, J., Leng, J., and Du, S. (2010b). Electrical properties and shape-memory behavior of self-assembled carbon nanofiber nanopaper incorporated with shape-memory polymer. *Smart Mater. Struct.* 19, 075021. doi:10.1088/0964-1726/19/7/075021
- Luo, R., Wu, J., Dinh, N. D., and Chen, C. H. (2015). Gradient porous elastic hydrogels with shape-memory property and anisotropic responses for programmable locomotion. *Adv. Funct. Mater.* 25, 7272–7279. doi:10.1002/adfm.201507029
- Ma, Q., Cheng, H., Jang, K. I., Luan, H., Hwang, K. C., Rogers, J. A., et al. (2016). A nonlinear mechanics model of bio-inspired hierarchical lattice materials consisting of horseshoe microstructures. *J. Mech. Phys. Solids* 90, 179–202. doi:10.1016/j.jmps.2016.02.012
- Ma, Q., and Zhang, Y. H. (2016). Mechanics of fractal-inspired horseshoe microstructures for applications in stretchable electronics. *Int. J. Appl. Mech.* 83, 111008. doi:10.1115/1.4034458
- Majid, H. A., Kamal, M., Rahim, A., Hamid, M. R., and Ismail, M. F. (2012). A compact frequency-reconfigurable narrowband microstrip slot antenna. *IEEE Antenn. Wirel. Pr.* 11, 616–619. doi:10.1109/LAWP.2012.2202869
- Mu, J., Hou, C., Wang, H., Li, Y., Zhang, Q., and Zhu, M. (2015). Origami inspired active graphene-based paper for programmable instant selffolding walking devices. *Sci. Adv.* 1, e1500533. doi:10.1126/sciadv.1500533
- Overvelde, J. T. B., Jong, T. A., Shevchenko, Y., Becerra, S. A., Whitesides, G. M., Weaver, J. C., et al. (2016). A three-dimensional actuated origami-inspired transformable metamaterial with multiple degrees of freedom. *Nat. Commun.* 7, 10929. doi:10.1038/ncomms10929
- Pang, W., Cheng, X., Zhao, H., Guo, X., Ji, Z., Li, G., et al. (2020). Electro-mechanically controlled assembly of reconfigurable 3D mesostructures and electronic devices based on dielectric elastomer platforms. *Natl. Sci. Rev.* 7, 342–354. doi:10.1093/nsr/nwz164
- Silverberg, J. L., Na, J. H., Evans, A. A., Liu, B., Hull, T. C., Santangelo, C. D., et al. (2015). Origami structures with a critical transition to bistability arising from hidden degrees of freedom. *Nat. Mater.* 14, 389–393. doi:10.1038/nmat4275
- Song, Y. X., Xu, Q. H., Tian, Y., Yang, J., Wu, Y. Q., Tang, X. H., et al. (2017). An on-chip frequency-reconfigurable antenna for q-band broadband applications. *IEEE Antenn. Wirel. Pr.* 16, 2232–2235. doi:10.1109/LAWP.2017.2709911
- Su, J. W., Xie, T., Deng, H., Zhang, C., Jiang, S., Lin, Y., et al. (2018). 4D printing of a self-morphing polymer driven by a swellable guest medium. *Soft Matter* 14, 765–772. doi:10.1039/c7sm01796k
- Tawk, Y., Albrecht, A. R., Hemmady, S., Balakrishnan, G., and Christodoulou, C. G. (2010). Optically pumped frequency reconfigurable antenna design. *IEEE Antenn. Wirel. Pr.* 9, 280–283. doi:10.1109/LAWP.2010.2047373
- Tawk, Y., Costantine, J., Avery, K., and Christodoulou, C. G. (2011). Implementation of a cognitive radio front-end using rotatable controlled reconfigurable antennas. *IEEE T. Antenn. Propag.* 59, 1773–1778. doi:10.1109/TAP.2011.2122239
- Therien-Aubin, H., Wu, Z. L., Nie, Z., and Kumacheva, E. (2013). Multiple shape transformations of composite hydrogel sheets. *J. Am. Chem. Soc.* 135, 4834–4839. doi:10.1021/ja400518c
- Tibbitts, S. (2014). 4D printing: multi-material shape change. *Archit. Des.* 84, 116–121. doi:10.1002/ad.1710
- Wang, L. C., Song, W. L., and Fang, D. N. (2019). Twistable origami and kirigami: from structure-guided smartness to mechanical energy storage. *ACS Appl. Mater. Interfaces* 11, 3450–3458. doi:10.1021/acsami.8b17776
- Wang, L. C., Song, W. L., Zhang, Y. J., Qu, M. J., Zhao, Z. A., Chen, M. J., et al. (2020). Active reconfigurable tristable square-twist origami. *Adv. Funct. Mater.* 30, 1909087. doi:10.1002/adfm.201909087
- Wong, J. Y., Langer, R., and Ingber, D. E. (1994). Electrically conducting polymers can noninvasively control the shape and growth of mammalian cells. *Proc. Natl. Acad. Sci.* 91, 3201–3204. doi:10.1073/pnas.91.8.3201
- Xie, T. (2010). Tunable polymer multi-shape memory effect. *Nature* 464, 267–270.
- Yan, D., Chang, J., Zhang, H., Liu, J., Song, H., Xue, Z., et al. (2020). Soft Three-dimensional network materials with rational bio-mimetic designs. *Nat. Commun.* 11, 1180. doi:10.1038/s41467-020-14996-5
- Zhao, Q., Qi, H. J., and Xie, T. (2015). Recent progress in shape memory polymer: new behavior, enabling materials, and mechanistic understanding. *Prog. Polym. Sci.* 49–50, 79–120. doi:10.1016/j.progpolymsci.2015.04.001
- Zhao, Z., Wu, J., Mu, X., Chen, H., Qi, H. J., and Fang, D. N. (2017). Origami by frontal photopolymerization. *Sci. Adv.* 3, e1602326. doi:10.1126/sciadv.1602326

Conflict of Interest: The authors declare that the research was conducted in the absence of any commercial or financial relationships that could be construed as a potential conflict of interest.

Copyright © 2020 Zhang, Wang, Song, Chen and Fang. This is an open-access article distributed under the terms of the Creative Commons Attribution License (CC BY). The use, distribution or reproduction in other forums is permitted, provided the original author(s) and the copyright owner(s) are credited and that the original publication in this journal is cited, in accordance with accepted academic practice. No use, distribution or reproduction is permitted which does not comply with these terms.



Intelligent Hydrogel Actuators With Controllable Deformations and Movements

Qian Zhao, Zhenglei Yu, Yunhong Liang*, Lei Ren and Luquan Ren

The Key Laboratory of Bionic Engineering, Ministry of Education, Jilin University, Changchun, China

OPEN ACCESS

Edited by:

Yusheng Shi,
Huazhong University of Science and
Technology, China

Reviewed by:

Tongqing Lu,
Xi'an Jiaotong University, China
Shaoxing Qu,
Zhejiang University, China
Yan Zhou,
China University of Geosciences
Wuhan, China

*Correspondence:

Yunhong Liang
liangyunhong@jlu.edu.cn

Specialty section:

This article was submitted to
Smart Materials,
a section of the journal
Frontiers in Materials

Received: 30 January 2021

Accepted: 08 March 2021

Published: 13 April 2021

Citation:

Zhao Q, Yu Z, Liang Y, Ren L and
Ren L (2021) Intelligent Hydrogel
Actuators With Controllable
Deformations and Movements.
Front. Mater. 8:661104.
doi: 10.3389/fmats.2021.661104

Near infrared laser- (NIR-) driven intelligent hydrogel actuator systems including printable N-isopropylacrylamide- (NIPAm-) nanosized synthetic hectorite clay-nanofibrillated cellulose (NFC) hydrogels and NIPAm-4-hydroxybutyl acrylate- (4HBA-) NFC hydrogels with a high response rate were prepared via three-dimensional (3D) printing and hydrothermal synthesis, respectively. The addition of NFC was beneficial to the improvement in rheology. The 3D printed intelligent hydrogel actuators with a structure pattern of Model I and Model II exhibited the saddle and inverted saddle deformations, respectively, to prove the validity of 3D printing. In order to improve the response rate and enrich movement patterns, the hydrothermal synthesized intelligent hydrogel actuators were prepared on the base of the 3D printed intelligent hydrogel compositions. The addition of NFC maintained the controllable NIR response. Based on a wedge-shaped design, the hydrothermal synthesized intelligent hydrogel pushed the resin ball with weight of 130 mg forward 8 mm in 39 s. By changing the torque values of a hydrogel in a different direction, the actuator realized controllable continuous rollover movement. Attributed to the longilineal shape, the intelligent hydrogel actuator reached an effective displacement of 20 mm in 10 s via a forward movement. The characteristics and structure design of a hydrogel material significantly realized multiple controllable functional four-dimensional (4D) printed deformations and movements. The combination of advantages of the 3D printed and hydrothermal synthesized intelligent hydrogels provided a new direction of development and abundant material candidates for the practical applications of 4D printing in soft robot, information sensing, and health engineering.

Keywords: 4D printing, intelligent hydrogel, nanofibrillated cellulose, near infrared laser response, controllable movement

INTRODUCTION

With the development of materials and equipment manufacturing technology, intelligent materials and corresponding advanced preparation methods promote the integrative development of materials, mechanics, and information (Zhang et al., 2014; Hakan et al., 2016; Wang et al., 2018). By stimulation of temperature (Gladman et al., 2016), light (Wang et al., 2013), electricity (Must et al., 2015), and humidity (Xue et al., 2015), intelligent materials own the basic shape variation property. The soft intelligent materials in combination with a specific structure design can realize controllable deformation and movements, which enrich the material candidates of (four-dimensional) 4D printing in the field of application of soft actuator, artificial muscle, etc.

As a kind of typical soft intelligent materials, intelligent hydrogels possess the swelling and deswelling properties initiated by stimulating on the base of a three-dimensional (3D) net structure. Attributed to the outstanding biocompatibility, intelligent hydrogels have been used in the practical applications of soft actuator, electron device, and medical appliance (Liu et al., 2017). Attributed to the characteristics of non-invasive safety (Jiang et al., 2014) and non-contact control (Weissleder, 2001), a near infrared laser (NIR) of 808 nm is one type of convenient common stimulation methods. The addition of a photothermal conversion agent, including graphene oxide (GO) (Fujigaya et al., 2008), carbon nanotube (Lu and Panchapakesan, 2007), gold nanoparticle (Lo et al., 2011), etc., into a hydrogel matrix is a key point for a laser-driven property of hydrogels. Based on the volume shrinkage response, NIR-driven intelligent hydrogels own bending/unbending deformation property. Intelligent hydrogels in combination with a structure design own the swimming, capturing, and crawling (Wang et al., 2015; Yao et al., 2015; Hu et al., 2017) movement properties. Considering a significance of the application of the deformation and movement, the response rate is a basis for the functional requirement of continuous movement of intelligent hydrogels. Attributed to the crosslinking patterns and a relatively low swelling/deswelling rate, the existing NIR-driven intelligent hydrogels including 3D printed hydrogels exhibit a relatively low response rate, which restricts functional movement abilities. Therefore, the question of how to improve the response rate and balance mechanical strength is a key point for the functional application of the 4D printed intelligent hydrogels.

Many researches focused on the enhancement of functional movement properties of intelligent hydrogels including the manipulation of material components and a structure design. Luo et al. (2015) prepared a kind of gradient temperature-responsive hydrogel via the heterobifunctional crosslinker of 4-hydroxybutyl acrylate (4HBA), which realized a relatively high swelling/deswelling rate. By using polypyrrole nanoparticles as photothermal transducers, the prepared hydrogel exhibited a high NIR response rate. However, the relatively low mechanical strength and single Young's modulus value further restricted the functional applications. In our previous studies (Zhao et al., 2018b,c), the nanofibrillated cellulose (NFC) exhibited an excellent role of the mechanical strength reinforcement in poly-N-isopropylacrylamide- (NIPAm-) nanosized synthetic hectorite clay hydrogels prepared via molding and 3D printing. Moreover, in addition to relatively high mechanical strength, the prepared NFC-reinforced gradient intelligent hydrogels own a relatively high response rate, multiple response patterns, and diversified self-driven functions under the stimulation of NIR (Zhao et al., 2018b, 2020), which realizes a perfect balance between the strength and response rate. The infiltration of GO in a hydrogel matrix realized an efficient NIR response. Even though the NFC-reinforced intelligent hydrogels realized the 3D printing and function properties, the effect of NFC content on the rheology characteristics of the 3D printed hydrogel reaction mixture and on movement patterns especially the controllable functional movement properties of the hydrothermal synthesized hydrogels should be further investigated.

Facing the requirements of a 4D printing developing application, two kinds of hydrogel system including 3D printed intelligent hydrogel actuator and hydrothermal synthesized intelligent hydrogel actuator were prepared. As the reinforcement, the effect of NFC content on rheology and printable ability of the 3D printed hydrogel reaction mixtures was investigated. The NFC-reinforced hydrothermal synthesized intelligent hydrogels, in combination with entirety infiltration of GO, were prepared to further extend the corresponding functional movement patterns. Moreover, the mechanisms of movement were also explained via an analysis of mathematics and mechanics.

EXPERIMENTAL SECTION

Materials

Intelligent hydrogels were synthesized via the monomer of NIPAm (Aladdin, Shanghai, China, 2% stabilizer), a crosslinking agent of the nanosized synthetic hectorite clay [Laponite XLG, $\text{Mg}_{5.34}\text{Li}_{0.66}\text{Si}_8\text{O}_{20}(\text{OH})_4$, Rockwood, Ltd., Geesthacht, Germany], and 4HBA (J&K Scientific, Ltd., Beijing, China), a reinforcement of NFC without carboxyl (Guilin Qihong Technology Co., Ltd., Guilin, China), an initiator of ammonium persulfate [APS, $(\text{NH}_4)_2\text{S}_2\text{O}_8$, Sinopharm Chemical Reagent Co., Ltd., Shanghai, China] and potassium peroxydisulfate [KPS, $\text{K}_2\text{S}_2\text{O}_8$, Shanghai Aibi Chemical Reagent Co., Ltd., Shanghai, China, analytical reagent (AR)], and a catalyst of N,N,N',N'-tetramethylethylenediamine (TEMED, Tianjin Weiyi Chemical Technology Co., Ltd., Tianjin, China, 98%). GO (Suzhou Hengqiu Graphene Technology Co., Ltd., Suzhou, China) was treated as a photothermal conversion agent and used as normal. Pure water (resistivity $\geq 18.2 \text{ M}\Omega\cdot\text{cm}$) was obtained by deionization and filtration.

Preparation of 3D Printed Intelligent Hydrogel Actuator

In order to prepare a hydrogel reaction mixture with GO, GO dispersed in pure water by ultrasonic radiation for 30 min and stirred for 1 h via a magnetic stirrer (Model MS-H380-Pro, DLAB Scientific Co., Ltd., China). Then, XLG clay was added and stirred for 1 h. Then, NFC with different weights was added and stirred for 1 h in an ice-water bath. Then, NIPAm was added into miscible liquids of GO, XLG, and NFC and stirred for another 2 h. Finally, KPS solution and TEMED were added under stirring. The hydrogel composition for 3D printing is listed in **Table 1**. Based on our previous study (Zhao et al., 2018a), GO content of 2 mg/ml exhibited maximum photothermal conversion efficiency, which was adopted in this experiment. Attributed to the NFC content, the hydrogel reaction mixtures were named as GO2-NFC0, GO2-NFC8, GO2-NFC9, GO2-NFC10, GO2-NFC11, and GO2-NFC12, respectively. After the preparation of a hydrogel reaction mixture for 3D printing, the STL files were generated from Solidworks and sliced by Slic3r software³⁹. After 3D printing via a laboratory-made 3D printer with a needle of 20 G, the printed samples were placed in a vacuum dryer immediately at room temperature for *in situ* free radical polymerization under vacuum. A preparation process of the 3D printed intelligent

TABLE 1 | Compositions of intelligent hydrogel reaction mixture for three dimensional (3D) printing.

Reaction mixture	NIPAm (g)	GO (mg)	NFC (mg)	XLG (g)	KPS (mg)	TEMED (μ L)	H ₂ O (mL)
GO2-NFC0	1.13	20	0	0.349	10	5	10
GO2-NFC8	1.13	20	80	0.349	10	5	10
GO2-NFC9	1.13	20	90	0.349	10	5	10
GO2-NFC10	1.13	20	100	0.349	10	5	10
GO2-NFC11	1.13	20	110	0.349	10	5	10
GO2-NFC12	1.13	20	120	0.349	10	5	10

TABLE 2 | Compositions of hydrothermal synthesized intelligent hydrogels.

Sample	NFC (mg)	NIPAm (g)	APS (mg)	4HBA (μ L)	H ₂ O (mL)
NFC0	0	1	10	210	10
NFC2	20	1	10	210	10

hydrogel actuators is shown in **Figure 1A**. The compositions are listed in **Table 1**.

Preparation of Hydrothermal Synthesized Intelligent Hydrogel Actuator

Nanofibrillated cellulose was added into 10 ml of pure water, which was degassed in a continuous nitrogen-saturated atmosphere and stirred for 0.5 h via a magnetic stirrer (Model MS-H380-Pro, DLAB Scientific Co., Ltd., Beijing, China) under the circumstances of ice-water bath. Then, NIPAm and APS were added into NFC aqueous solution and stirred for 1 h. Finally, 4HBA was added into the aqueous solution and stirred for 5 min. After the hydrothermal synthesis in a 200-ml reaction kettle under the circumstances of 190°C for 5 h, an intelligent hydrogel was successfully prepared. In order to realize different deformation and movement patterns, the hydrothermal synthesized intelligent hydrogel without NFC and with 2 mg/ml of NFC was prepared, and was named as NFC0 and NFC2, respectively. The compositions are listed in **Table 2**.

The GO aqueous solution with the concentration of 4 mg/ml was prepared for the GO infiltration of hydrothermal synthesized intelligent hydrogels. Based on the porous microstructure, the GO aqueous solution can be efficiently infiltrated into the hydrogels. Before the infiltration, a filter paper was repeatedly used to absorb the water in hydrogels. Then, the hydrogel entirety or the hydrogel block with specific dimensions was immersed into the GO aqueous solution and maintained for 5 min to finish entirety infiltration. The preparation and GO infiltration process of the hydrothermal synthesized intelligent hydrogel actuator can be observed in **Figure 1B**.

Characteristics of Intelligent Hydrogels Microstructure

After freeze-drying (LGJ-10C, Beijing Four Ring Scientific Instrument Factory Co., Ltd., Beijing, China), the cross sections

of the hydrothermal synthesized intelligent hydrogels were observed via field emission scanning electron microscopy (FESEM; Model XL-30, FEI Company, OR, USA) to disclose the characteristics of microstructure.

Infrared Spectroscopy and Differential Scanning Calorimetry

IRAffinity-1 Fourier transform infrared (FTIR) spectrometer (Shimadzu Corporation, Kyoto, Japan) was used to analyze the FTIR spectra characteristics of hydrothermal synthesized intelligent hydrogels. The wavenumber range was set as 500–4,000 cm^{-1} . The volume phase transition temperatures were tested via differential scanning calorimetry (DSC; Model DSC25-RCS90, TA Company, New Castle, DE, USA). The samples were heated from 10 to 60°C at a rate of 20°C/min under nitrogen atmosphere.

Young's Modulus

The ultrasound image diagnostic apparatus (Alxplorer, Supersonic Imagine, Aix-en-Provence, France) was used to test the values of Young's modulus of hydrothermal synthesized intelligent hydrogels. A SL15-4 probe was adopted to measure the full swollen hydrogels in water. Young's modulus can be directly obtained in the image.

Rheological Analysis

The rotational rheometer (DHR, TA Instruments, New Castle, DE, USA) with a parallel plate geometry of 40 mm in diameter and a gap of 0.55 mm was used to test the rheological properties of the 3D printed hydrogel reaction mixture. Strain sweeps in the range of 0.1–100% with frequencies of 0.1–2 Hz were used to determine the linear viscoelastic range.

Deformations and Movements of Intelligent Hydrogel Actuators

NIR Response Measurement of 3D Printed Intelligent Hydrogel Actuator

In order to analyze the effect of a structure design on deformation characteristics of the 3D printed hydrogel actuators, two kinds of structure pattern, which were named as Model I and Model II, were constructed. Model I was a cylindrical bilayer structure with 90°/0° configuration, owning a dimension of 30 mm in diameter, a thickness of 0.96 mm, and a filling rate of 100%. Model II was also a bilayer structure with the same dimensions of Model I. But the filamentary of Model II was arc. The bilayer constructed with

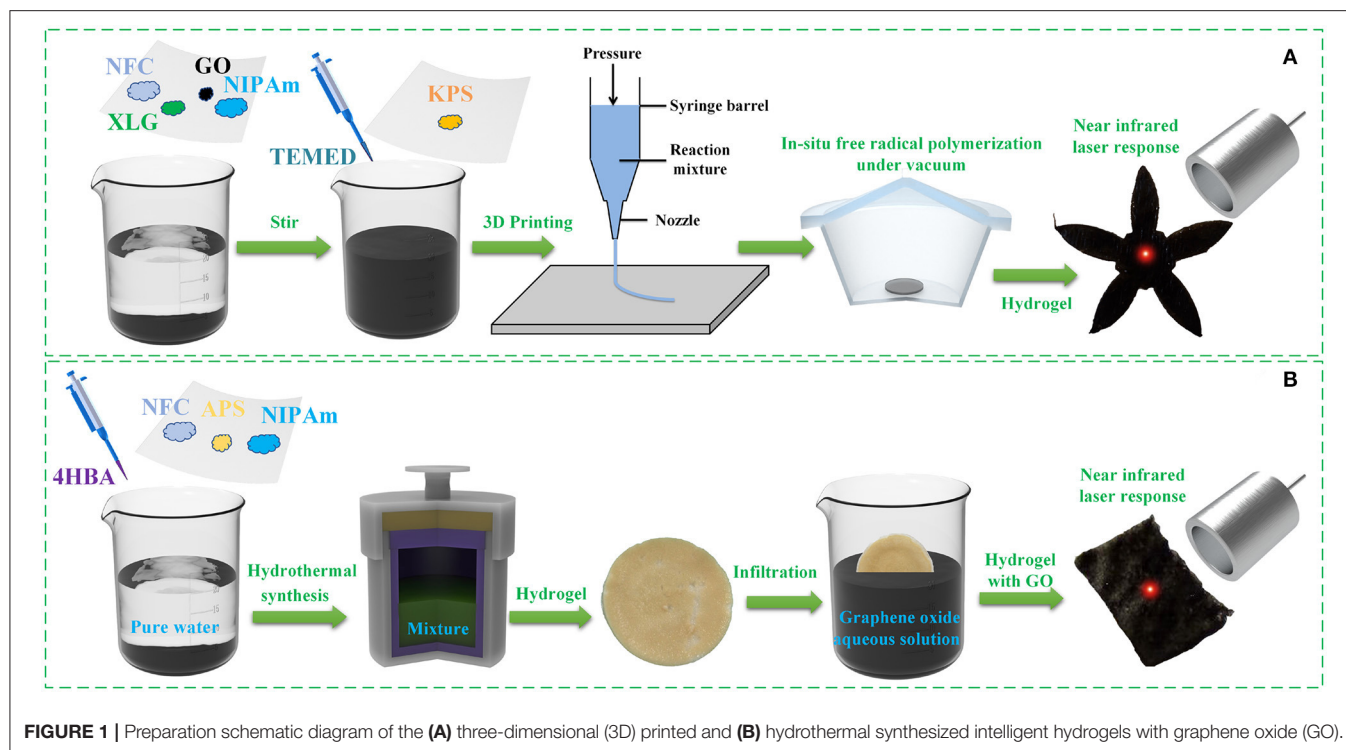


FIGURE 1 | Preparation schematic diagram of the (A) three-dimensional (3D) printed and (B) hydrothermal synthesized intelligent hydrogels with graphene oxide (GO).

arcs was also $90^\circ/0^\circ$ configuration. The 3D printed intelligent actuators with full swelling state were placed in water of room temperature. NIR with wavelength of 808 nm (Model FC-W-808-30W, Changchun New Industries Optoelectronics Technology Co., Ltd., Changchun, China) was treated as a source of stimulation. The deformation and movement processes were recorded by digital camera.

NIR Response Measurement of Hydrothermal Synthesized Intelligent Hydrogel Actuator

After the infiltration of GO, the wedge-shaped NFC2 intelligent hydrogel with dimensions of $12\text{ mm} \times 3\text{ mm} \times 4\text{ mm}$ (length \times width \times maximal thickness) was used to push the resin ball ($\Phi 6\text{ mm}$) with weight of 130 mg on a glass surface. The NIR power was 7.1 W.

After transitory infiltration of GO, the middle part of the NFC0 hydrogel block was adopted to realize the rollover movement. Attributed to the infiltration depth, GO particles existed in the outer surface of a sample. After cutting off two opposite outer surfaces, there were no GO particles in the middle part of the remaining strip sample with dimensions of $10\text{ mm} \times 3\text{ mm} \times 4\text{ mm}$ (length \times width \times thickness). The NIR with power of 7.1 W was irradiated on the middle part of a strip sample to realize the rollover movement.

After infiltration of GO, the bottom part of the NFC0 hydrogel with dimensions of $23\text{ mm} \times 2\text{ mm} \times 2\text{ mm}$ (length \times width \times thickness) was cutting off to exhibit the forward movement under the stimulation of NIR with power of 7.1 W.

RESULTS AND DISCUSSION

NIR Responses of 3D Printed Hydrogel Actuator

In order to prove the effect of NFC addition on printability of intelligent hydrogel reaction mixtures and disclose the optimal NFC content for 3D printing of intelligent hydrogel actuators, the rheology characteristics including apparent viscosity, storage modulus, and loss modulus are analyzed in **Figure 2**. The apparent viscosity in **Figure 2A** indicated that the hydrogel reaction mixtures owned shear thinning characteristic. The addition and variation of NFC content increased the apparent viscosity and changed variation tendency of a hydrogel reaction mixture. As shown in **Figure 2B**, the storage modulus and loss modulus of the hydrogel reaction mixtures with NFC were higher than those without NFC, which exhibited the gel-sol transition point in the strain range of 10^1 - $10^2\%$. The hydrogel reaction mixtures with NFC owned higher property of energy storage by elastic deformation and energy loss by viscous deformation, exhibiting perfect printability. The hydrogel with a relatively low NFC content owned a relatively high swelling kinetics characteristic (Zhao et al., 2018a,c). Considering the swelling and rheology, the GO2-NFC10 hydrogel reaction mixture was used for the 3D printed hydrogel actuators.

In situ free radical polymerization under vacuum realized the solidification of the 3D printed hydrogel actuators successfully with GO (Zhao et al., 2018a). Based on high printable property (**Supplementary Movie 1**), the 3D printed GO2-NFC10 hydrogel actuators with the structure of Model I and Model II after the polymerization exhibited controllable NIR deformations in

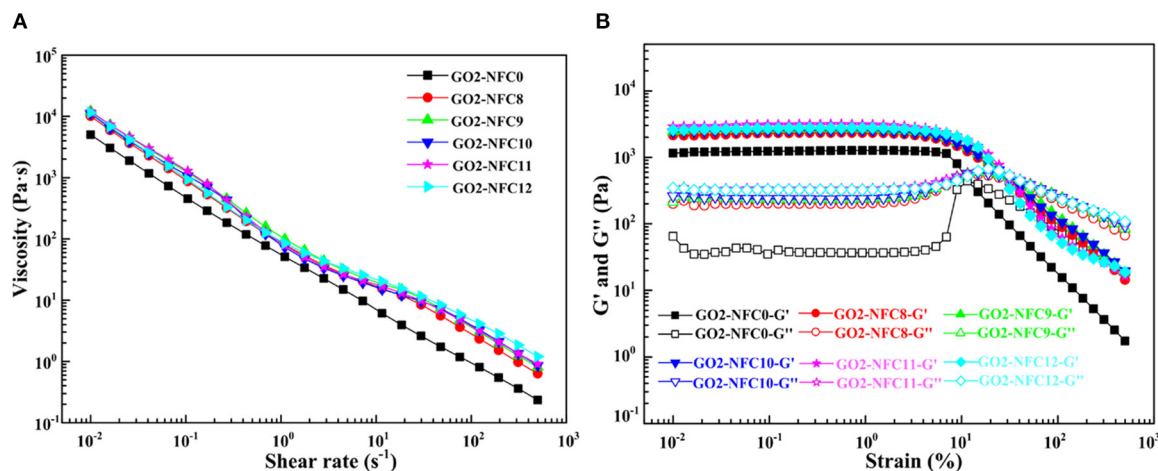


FIGURE 2 | (A) Apparent viscosity, **(B)** storage modulus G' and loss modulus G'' of intelligent hydrogel reaction mixtures with GO.

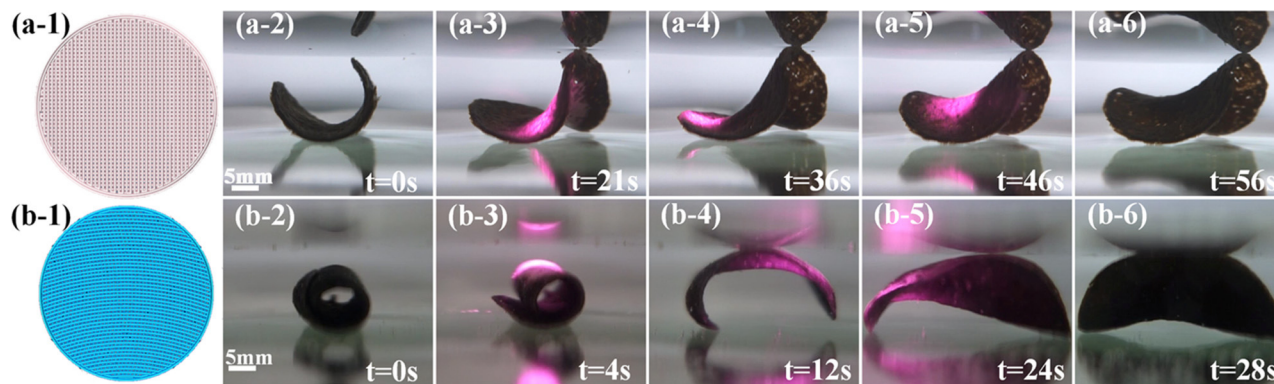


FIGURE 3 | Near infrared laser (NIR) responses of the 3D printed hydrogel actuators with **(a-1)–(a-6)** Model I and **(b-1)–(b-6)** Model II structures.

Figure 3. Figure 3a-1 shows the structure pattern of Model I. In the initial state of Figure 3a-2, Model I exhibited a cincinal shape. When the NIR laser irradiated the right part, left part, and middle part in a sequence, the corresponding parts unfolded and rose, as shown in Figures 3a-3–a-5. After irradiation, Model I exhibited the final state of saddle in Figure 3a-6. The deformation process of Model I was exhibited in **Supplementary Movie 2**. Figure 3b-1 shows the structure pattern of Model II. The initial state of Model II exhibited a hollow cylindrical shape in Figure 3b-2. Under the NIR irradiation, the right and left parts unfolded in a sequence, as shown in Figures 3b-3–b-5. The final state of Model II was an inverted saddle in Figure 3b-6. The deformation process of Model II was exhibited in **Supplementary Movie 3**. Based on a different printing structure, Model I and Model II owned a different deformation process and pattern.

The polymerization and structure were the key points for intelligent deformation of 3D printing of hydrogel actuators. The anisotropic swelling/deswelling behavior of a printed structure built a base of the deformation mechanism of the 3D printed

hydrogel actuators. Even though the 3D printed hydrogel actuator realized precise structure patterns and controllable intelligent deformation, the deformation patterns were restricted by the response rate of hydrogel materials. Therefore, in order to improve the response rate of a hydrogel actuator and realized multiple deformation and movement patterns, a crosslinking agent was changed from XLG to 4HBA on the base of the 3D printed hydrogel compositions. The regulatory material composition provided a new method for the improvement and application of the 4D printed hydrogel actuators.

NIR Responses of Hydrothermal Synthesized Hydrogel Actuator Material Characteristics

Figure 4 shows the microstructure characteristics of NFC0 and NFC2. Based on the micropore size variation scale, NFC0 can be divided into four layers (including Layer 1, Layer 2, Layer 3, and Layer 4) qualitatively, which exhibited a gradient structure. From Layer 1 to Layer 4, micropore size decreased gradually along with the thickness direction, as shown in

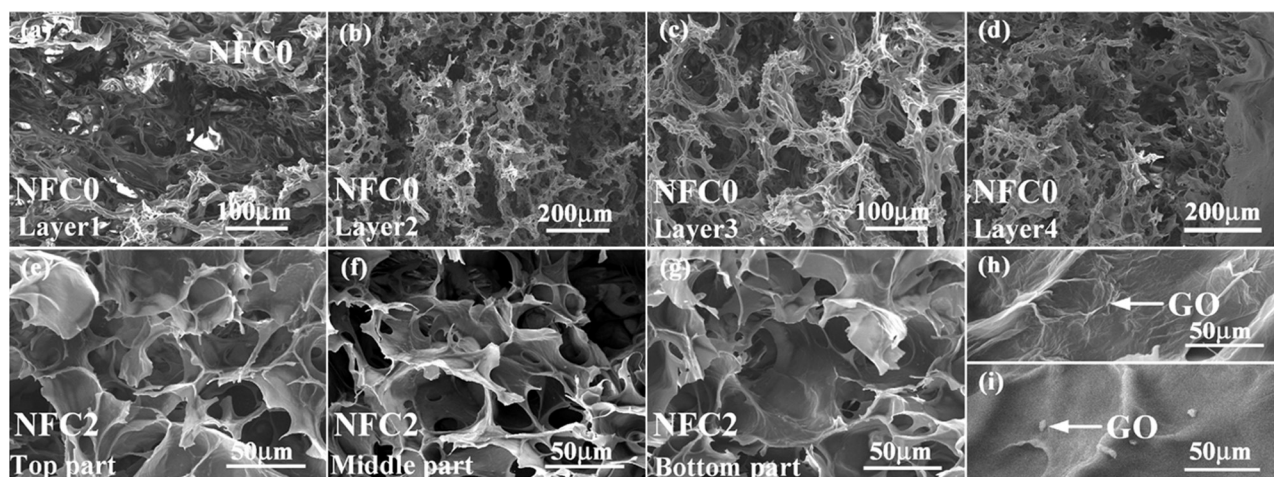


FIGURE 4 | Microstructure characteristics of different parts in (a–d) nanofibrillated cellulose 0 (NFC0), (e–g) NFC2 and GO distribution patterns in (h) the top and (i) middle parts of NFC2.

Figures 4a–d. The addition of NFC significantly affected the microstructure characteristics of the NFC2 intelligent hydrogel, which weakened the original gradient structure. The NFC2 hydrogel was divided into bottom part, middle part, and top part, as shown in **Figures 4e–g**. Because of the existence of NFC and corresponding amount, convex structure existed on micropore surfaces of the NFC2 hydrogel. The addition of reinforcement maintained the infiltration property of the NFC2 hydrogel. Attributed to the infiltration method, the infiltrated GO amount was different between the top part and middle part of the NFC2 hydrogel. The synthesized mechanisms of the NFC0 and NFC2 intelligent hydrogels can be explained (Zhao et al., 2020). As the monomer and crosslinking agent, the addition reaction of double bond occurred between NIPAm and 4HBA, leading to the polymer with a hydroxide radical (PNIPAm-4HBA-OH). In the sediment process of synthesized polymers, the dehydration synthesis existed in hydroxide radical, forming a gradient network structure of NFC0. NFC owned another role of crosslinking agent in the material system. Because of the existence of hydroxide radical in NFC, the dehydration synthesis of hydroxide radical of NFC, and polymer with hydroxide radical (PNIPAm-4HBA-OH) via the addition reaction led to the existence of a relatively homogeneous network structure in NFC2. The typical network structure of NFC0 and NFC2 built the functional material base of hydrogel actuators. Moreover, the difference in the microstructure characteristics of NFC0 and NFC2 provided selective materials for hydrogel actuators with different functional applications.

Attributed to the Young's modulus range (1.2–2.7 KPa) in **Figure 5a**, NFC0 hydrogel can be divided into four layers, which was similar to the microstructure partition pattern in **Figures 4a–d**. As shown in **Figure 5b**, the maximum Young's modulus of the NFC2 hydrogel was 11.3 KPa, indicating that the addition of NFC increased the corresponding Young's modulus. In addition to the higher Young's modulus, the thickness of the NFC2 hydrogel was lower than that of the NFC0 hydrogel.

Based on the variation in Young's modulus, NFC realized the reinforcement role in a hydrogel material system, which provided a selective base for the driving force of hydrogel actuators.

Fourier transform infrared analysis of the NFC0 and NFC2 hydrogels are shown in **Figure 6**. The band between 3,200 and 3,600 cm^{-1} represented N-H stretching vibration peaks. The band at 1,655 cm^{-1} was the C=O stretching vibration peak. The band at 1,548 cm^{-1} was assigned to the N-H bending vibration peak. The bands at 1,381 and 1,456 cm^{-1} represented the absorption peaks of $-\text{CH}(\text{CH}_3)_2$, respectively. The hydrophilic acylamino and the hydrophobic isopropyl existed in the intelligent hydrogels. The functional chemical bonds of NIPAm were maintained in the NFC2 hydrogel, which built a functional base of NIR responses for controllable hydrogel actuators.

Fourier transform infrared disclosed the temperature response functional base of the NFC0 and NFC2 hydrogels. **Figure 6** shows the corresponding volume phase transition temperature (VPTT) of NFC0 (37.8°C) and NFC2 (35.3°C), respectively. The results of DSC were similar to the results of FTIR. The addition of NFC maintained the temperature response behavior of hydrogels. The NFC0 and NFC2 intelligent hydrogels, in combination with an analysis of microstructure, Young's modulus, FTIR, and DSC, owned the intelligent temperature response property base. Based on the infiltration of GO, the prepared intelligent hydrogels can realize NIR responses. In combination with a structure design, the controllable functional movements of hydrogels can also be obtained.

Controllable Movement Characteristics

Pushball Movement

Figures 4–6 indicated that the NFC0 and NFC2 hydrogels owned the intelligent deformation properties from a material point of view. In combination with a structure design, the NFC0 and NFC2 hydrogel actuators with the GO infiltration possessed

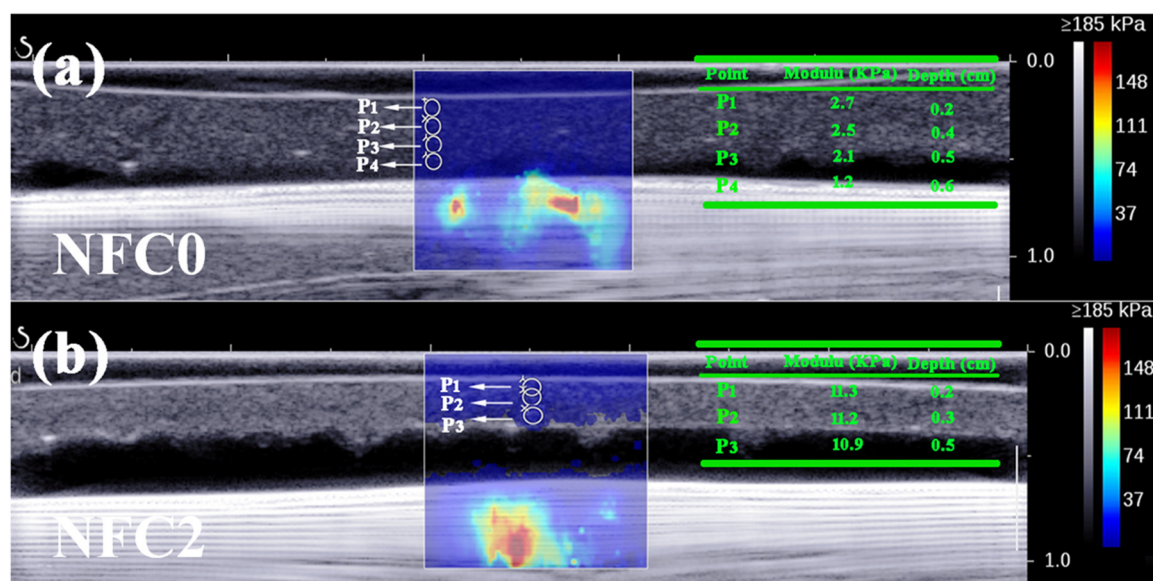


FIGURE 5 | Distribution characteristics of Young's modulus of the (a) NFC0 and (b) NFC2 intelligent hydrogels.

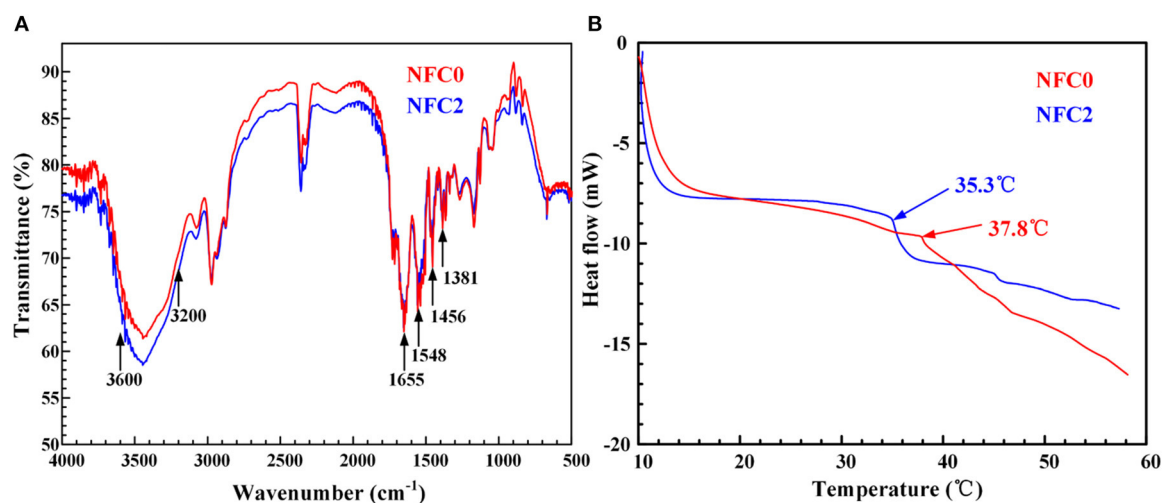


FIGURE 6 | (A) Typical Fourier transform infrared (FTIR) spectra and (B) differential scanning calorimetry (DSC) curves of the NFC0 and NFC2 intelligent hydrogels.

controllable movement properties under the stimulation of NIR from a point view of function application.

The NFC2 hydrogel actuator with a wedge-shaped structure having GO was designed to conduct the pushball movement, as shown in **Figure 7**. The hydrogel actuator used for the pushball movement was cut into a wedge shape first, and then infiltrated GO. **Figure 7a** exhibits the original position of the hydrogel actuator and resin ball. After infiltration, a part of the hydrogel actuator exhibited black. Based on Young's modulus distribution characteristics of the NFC2 hydrogel and perviousness of NIR, the bottom part of the NFC2 hydrogel was treated as the top part of the actuator to ensure the NIR

contact of the middle part of the NFC2 hydrogel and bending deformation of the NFC2 hydrogel actuator. NIR irradiated on the middle part of the NFC2 hydrogel actuator, which led to the contraction deformation in **Figure 7b**. After removing NIR irradiation, the NFC2 hydrogel actuator conducted extension deformation and reached the original straight state. Attributed to the weight distribution of wedge shape, the right part of the NFC2 hydrogel actuator acted as a fulcrum role, driving the actuator forward in **Figure 7c**. In the first distance, the resin ball was pushed forward about 2 mm. The pushball movement of the NFC2 hydrogel actuator was repeatable. By repeating NIR irradiation, the actuator moved another

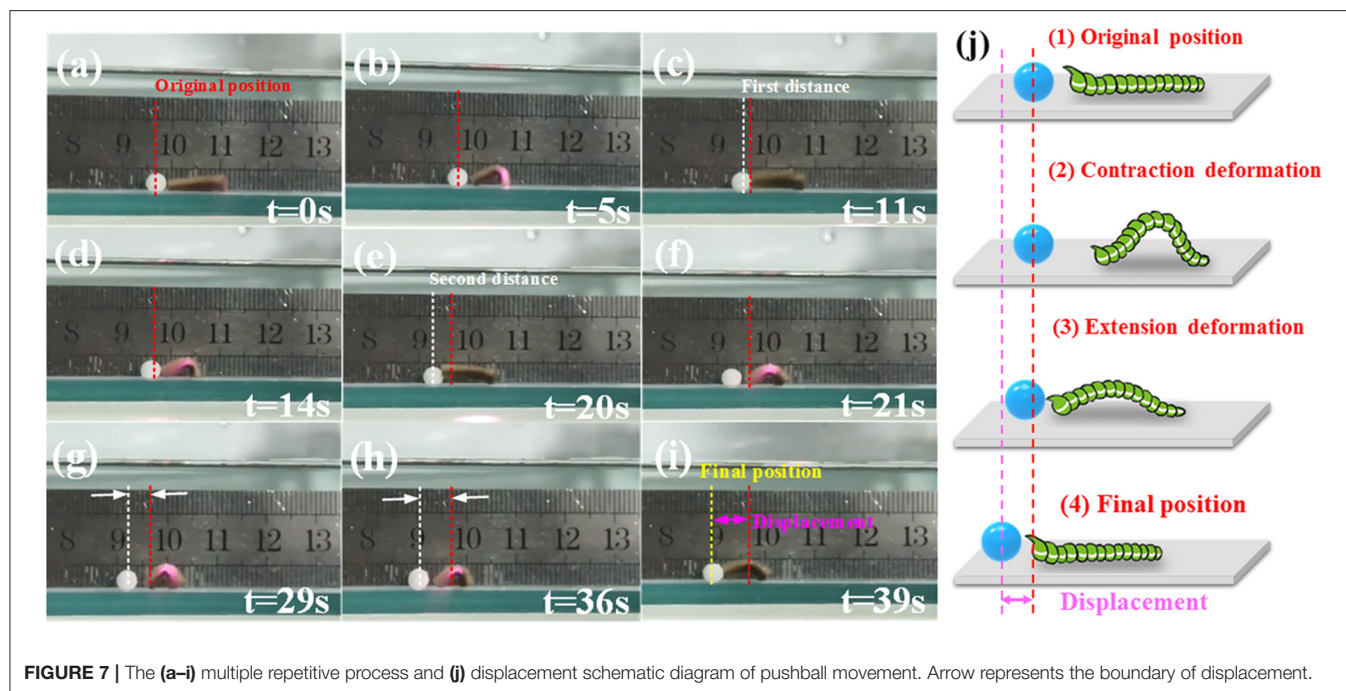


FIGURE 7 | The (a–i) multiple repetitive process and (j) displacement schematic diagram of pushball movement. Arrow represents the boundary of displacement.

four steps in 15 s. The resin ball was pushed four distances correspondingly, as shown in **Figures 7d–i**. The vivid movement can be observed in **Figure 7j** and **Supplementary Movie 4**. Compared with the original position and final position, the effective displacement of pushball movement was 8 mm in 39 s, which exhibited a controllable movement characteristic of NFC2 hydrogel actuators.

The swelling/deswelling property and artful structure designs were the key points for NIR-driven pushball movements, on the base of GO infiltration. Relatively high Young's modulus restricted the movement rate and improved the driving force to some extent. In the pushball movement process, the movement of resin ball was independent of the hydrogel actuator deformation. The hydrogel actuator contacted with a resin ball via the driving force in extension deformation, leading to the corresponding forward displacement along with the movement direction of the NFC2 hydrogel actuator.

Rollover Movement

Figure 8 exhibits the rollover movement process of the NFC0 intelligent hydrogel actuator. **Figure 8a** shows the initial state of a hydrogel actuator. After the infiltration and ordered cutting, GO particles existed in the specific four sides. NIR irradiated the middle part of the hydrogel actuator, which induced the volume shrinkage of the middle part. Under continuous NIR irradiation, the irradiated long side of the hydrogel actuator switched to another long side direction. When the NIR irradiated another long side, the irradiated long side continued the rollover movement, which formed a continuous rollover movement, as shown in **Figures 8b–e**. After removing the NIR irradiation, the NFC0 hydrogel actuator returned to the initial state, as shown in **Figure 8f**. A reversible and repeatable rollover movement process

can be observed in **Supplementary Movie 5**. In our previous study (Zhao et al., 2020), the curvature variation was selected to build relationships of bending degree, deformation displacement, material properties, and incentive intensity on the base of mechanical analysis to disclose the self-driven mechanisms of hydrogel actuators. Moreover, based on the Foppl–von Karman elastic theory, the relationship between the curvature of the hydrogel actuator on x-axis and y-axis and the NIR power was constructed. By using the Rayleigh–Ritz method, the NIR power intensity value directly affected the longitudinal and transverse curvatures. With an increase in the NIR power, the relationship between the longitudinal and transverse curvatures changed from equality to inverse. Different NIR power densities affected the torque values of intelligent hydrogel actuators on x-axis and y-axis, respectively. Therefore, when the NIR power reached a specific value, the variation between the longitudinal and transverse curvatures affected the torque values (M_{xx} and M_{yy}) of the NFC0 hydrogel actuator on the stated x-axis and y-axis and realized a rollover movement, as shown in **Figure 8g**.

Forward Movement

Figure 9 shows the forward movement characteristics of the NFC0 intelligent hydrogel actuator. The initial state of the hydrogel actuator was straight strip in **Figure 9a**. As shown in **Figure 9b**, under the NIR irradiation, the middle part of the NFC0 hydrogel actuator exhibited a bending deformation. When the actuator reached the minimum bending degree, the NIR was removed. The middle part of the actuator moved forward about 13 mm in **Figure 9c**. Even though the actuator moved back in the extension process, the whole actuator moved forward about 9 mm in **Figure 9d**. The forward movement was repeatable. Compared with the original position, after

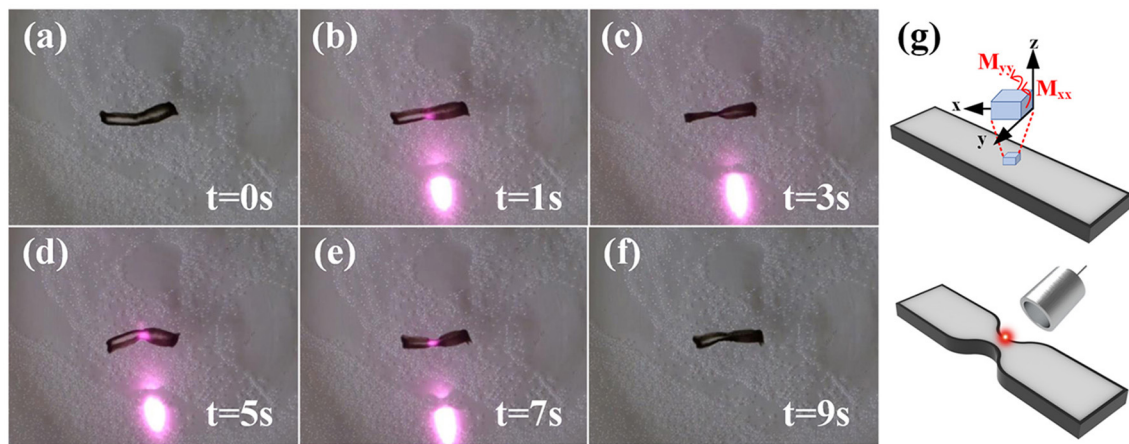


FIGURE 8 | The (a–f) multiple repetitive process and (g) a schematic diagram of rollover movement.

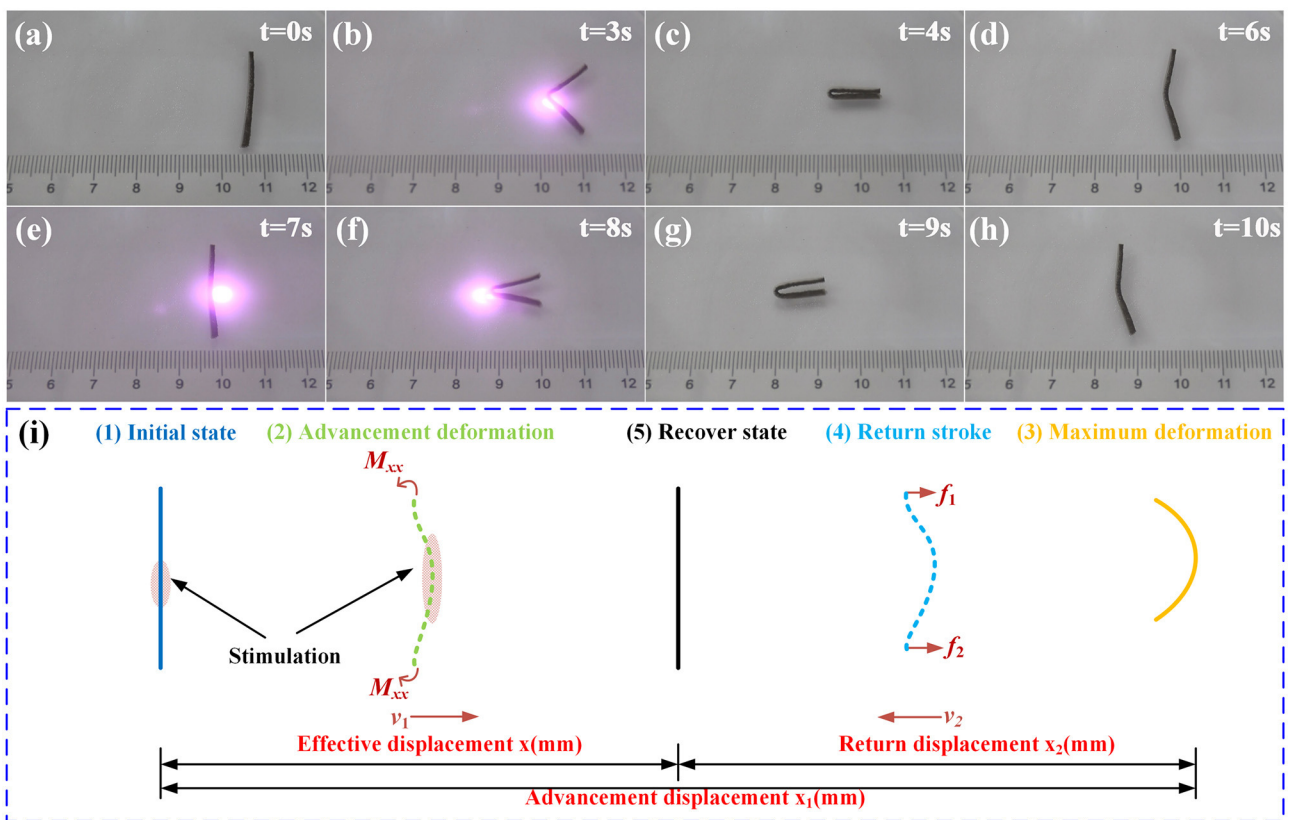


FIGURE 9 | The (a–h) multiple repetitive process and (i) a schematic diagram of forward movement.

another NIR irradiation cycle in **Figures 9e–g**, the NFC0 hydrogel actuator reached an effective displacement of 20 mm in **Figure 9h**. The forward movement process can be observed in **Supplementary Movie 6**. **Figure 9i** explains the forward movement mechanism on the base of the Foppl–von Karman elastic theory. Under NIR irradiation, the sample exhibited

longitudinal and transverse deformation, which realized the advanced displacement of x_1 via the torque of M_{xx} . After removing irradiation, both ends of a sample acted as paddles leading to the backward motion. The hydrogel actuator exhibited a return displacement of x_2 via the forces of f_1 and f_2 . The distance between the initial and recover states was an effective

displacement of forward movement. In addition to **Figures 7–9**, the prepared NFC0 and NFC2 hydrogel actuators realized controllable functional NIR-driven movements. Based on the hydrogels with different microstructures and Young's modulus, the hydrogel actuators exhibited different functional abilities.

Three-dimensional printing technology realized the precise, complicated 4D printed deformation structures of PNIPAm-XLG-NFC intelligent hydrogel actuators. The hydrothermal synthesized PNIPAm-4HBA-NFC intelligent hydrogel actuators owned the advantages of high response rate movement properties. Two kinds of intelligent hydrogel actuator owned distinct characteristics. The combination of advantages of different hydrogels can enrich the application fields of 4D printed hydrogel actuators in the field of soft intelligent actuator, artificial muscle, etc.

CONCLUSION

As a novel kind of reinforcement, NFC increased the crosslinking degree of intelligent hydrogels, which realized 3D printing of hydrogel reaction mixtures via the free radical polymerization under vacuum based on the improvement in the rheology property and increased Young's modulus of the hydrothermal synthesized hydrogels via a hydroxide radical on the dehydration synthesis between a monomer and crosslinking agent. The designed structure patterns affected NIR-driven deformation characteristics, which realized controllable deformations of saddle and inverted saddle based on the Model I and Model II, respectively. Attributed to a relatively high response rate and multiple deformation patterns, the hydrothermal synthesized intelligent hydrogel actuators were prepared. Based on the functional chemical bonds of NIPAm, the NFC0 and NFC2 intelligent hydrogels owned the specific volume phase transition temperatures, which built the material base for intelligent deformations combined with a typical network structure and the enhanced mechanical strength. Attributed to a unique structure design, the NFC0 and NFC2 intelligent hydrogels realized controllable functional movements. The wedge-shaped NFC2 intelligent hydrogel actuator pushed the resin ball with weight of 130 mg forward 8 mm in 39 s. Under the continuous NIR irradiation, the NFC0 hydrogel actuator realized controllable continuous rollover movement via the change of the torque values of the NFC0 hydrogel actuator on x-axis and y-axis. Based on the designed longilineal shape, the NFC0 hydrogel actuator realized forward movement, which reached an effective displacement of 20 mm in 10 s via two

movement steps. The composition variation and structure design of a material were the key points of 4D printing. The hydrothermal synthesized intelligent hydrogel actuators owned abundant movement patterns and lacked a precise structure and mechanical strength. The combination of advantages of the 3D printed and hydrothermal synthesized intelligent hydrogel actuators provided a new development direction of 4D printing. The controllable NIR-driven deformations and functional pushball movement, rollover movement, and forward movement built abundant function bases for the practical applications of 4D printing in soft robot, drug delivery, and artificial muscle.

DATA AVAILABILITY STATEMENT

The original contributions presented in the study are included in the article/**Supplementary Material**, further inquiries can be directed to the corresponding author/s.

AUTHOR CONTRIBUTIONS

QZ performed investigation, experiments, processing data, and writing original draft. ZY performed mechanical analysis. YL performed methodology, resources, and review. LeR performed methodology and review. LuR performed methodology and supervision. All authors contributed to the article and approved the submitted version.

FUNDING

This work was supported by the Project of National Key Research and Development Program of China (2018YFB1105100, 2018YFC0703300, and 2018YFA2001300), the National Natural Science Foundation of China (Nos. 5167050531, 51822504, and 91848204), Key Scientific and Technological Project of Jilin Province (20180201051GX), Program for JLU Science and Technology Innovative Research Team (2017TD-04), Joint Fund of Ministry of Education for Equipment Pre-research (2018G944J00084), and China Postdoctoral Science Foundation (2020M670845).

SUPPLEMENTARY MATERIAL

The Supplementary Material for this article can be found online at: <https://www.frontiersin.org/articles/10.3389/fmats.2021.661104/full#supplementary-material>

REFERENCES

- Fujigaya, T., Morimoto, T., Niidome, Y., and Nakashima, N. (2008). NIR laser-driven reversible volume phase transition of single-walled carbon nanotube/Poly(N-isopropylacrylamide) composite gels. *Adv. Mater.* 20, 3610–3614. doi: 10.1002/adma.200800494
- Gladman, A. S., Matsumoto, E. A., Nuzzo, R. G., Mahadevan, L., and Lewis, J. A. (2016). Biomimetic 4D printing. *Nat. Mater.* 15, 413–439. doi: 10.1038/nmat4544
- Hakan, A. N., Lee, A. K., and Yum, K. (2016). Bioinspired 3D structures with programmable morphologies and motions. *Nat. Commun.* 9, 3705–3716. doi: 10.1038/s41467-018-05569-8
- Hu, Y., Liu, J. Q., Chang, L. F., Yang, L. L., Xu, A. F., Qi, K., et al. (2017). Electrically and sunlight-driven actuator with versatile biomimetic motions based on rolled carbon nanotube bilayer composite. *Adv. Funct. Mater.* 27, 1704388–1704397. doi: 10.1002/adfm.201704388

- Jiang, W. T., Niu, D., Liu, H. Z., Wang, C. H., Zhao, T. T., Yin, L., et al. (2014). Photoresponsive soft-robotic platform: biomimetic fabrication and remote actuation. *Adv. Funct. Mater.* 24, 7598–7604. doi: 10.1002/adfm.201402070
- Liu, X., Yuk, H., Lin, S., Parada, G. A., Tang, T. C., Tham, E., et al. (2017). 3D printing of living responsive materials and devices. *Adv. Mater.* 30, 1704821–1704829. doi: 10.1002/adma.201704821
- Lo, C., Zhu, D., and Jiang, H. (2011). An infrared-light responsive graphene-oxide incorporated poly(N-isopropylacrylamide) hydrogel nanocomposite. *Soft Matter* 7, 5604–5609. doi: 10.1039/c1sm00011j
- Lu, S., and Panchapakesan, B. (2007). Photomechanical responses of carbon nanotube/polymer actuators. *Nanotechnology* 18, 305502–305510. doi: 10.1088/0957-4484/18/30/305502
- Luo, R. C., Wu, J., Dinh, N. D., and Chen, C. H. (2015). Gradient porous elastic hydrogels with shape-memory property and anisotropic responses for programmable locomotion. *Adv. Funct. Mater.* 25, 7272–7279. doi: 10.1002/adfm.201503434
- Must, B. I., Kaasik, F., Pöldsalu, I., Mikkels, L., Johanson, U., Punning, A., et al. (2015). Ionic and capacitive artificial muscle for biomimetic soft robotics. *Adv. Eng. Mater.* 17, 84–94. doi: 10.1002/adem.201400246
- Wang, E., Desai, M. S., and Lee, S. W. (2013). Light-controlled graphene-elastin composite hydrogel actuators. *Nano Lett.* 13, 2826–2830. doi: 10.1021/nl401088b
- Wang, L., Liu, Y., Cheng, Y., Cui, X. G., Lian, H. Q., Liang, Y. R., et al. (2015). A bioinspired swimming and walking hydrogel driven by light-controlled local density. *Adv. Sci.* 2, 1500084–1500089. doi: 10.1002/advs.201500084
- Wang, Y., Zhang, J. Y., Qiu, C. B., Li, J. B., Cao, Z. X., Ma, C. S., et al. (2018). Self-recovery magnetic hydrogel with high strength and toughness using nanofibrillated cellulose as a dispersing agent and filler. *Carbohydr. Polym.* 196, 82–91. doi: 10.1016/j.carbpol.2018.05.023
- Weissleder, R. (2001). A clearer vision for *in vivo* imaging. *Nat. Biotechnol.* 19, 316–317. doi: 10.1038/86684
- Xue, L. J., Kovalev, A., Volf, A. E., Steinhart, M., and Gorb, S. N. (2015). Humidity-enhanced wet adhesion on insect-inspired fibrillar adhesive pads. *Nat. Commun.* 6, 6621–6629. doi: 10.1038/ncomms7621
- Yao, C., Liu, Z., Yang, C., Wang, W., Ju, X. J., Xie, R., et al. (2015). Poly (N-isopropylacrylamide)-clay nanocomposite hydrogels with responsive bending property as temperature-controlled manipulators. *Adv. Funct. Mater.* 25, 2980–2991. doi: 10.1002/adfm.201500420
- Zhang, E. Z., Wang, T., Hong, W., Sun, W. X., Liu, X. X., and Tong, Z. (2014). Infrared-driving actuation based on bilayer graphene oxide-poly(N-isopropylacrylamide) nanocomposite hydrogels. *J. Mater. Chem. A* 2, 15633–15639. doi: 10.1039/c4ta02866j
- Zhao, Q., Chang, Y. J., Yu, Z. L., Liang, Y. H., Ren, L., and Ren, L. Q. (2020). Bionic intelligent soft actuators: high-strength gradient intelligent hydrogels with diversified controllable deformations and movements. *J. Mater. Chem. B* 8, 9362–9373. doi: 10.1039/D0TB01927E
- Zhao, Q., Liang, Y. H., Ren, L., Qiu, F., Zhang, Z. H., and Ren, L. Q. (2018a). Study on temperature and near-infrared driving characteristics of hydrogel actuator fabricated via molding and 3D printing. *J. Mech. Behav. Biomed.* 78, 395–403. doi: 10.1016/j.jmbbm.2017.11.043
- Zhao, Q., Liang, Y. H., Ren, L., Yu, Z. L., Zhang, Z. H., Qiu, F., et al. (2018c). Design and fabrication of nanofibrillated cellulose-containing bilayer hydrogel actuators with temperature and near infrared laser responses. *J. Mater. Chem. B* 6, 1260–1272. doi: 10.1039/c7tb02853a
- Zhao, Q., Liang, Y. H., Ren, L., Yu, Z. L., Zhang, Z. H., and Ren, L. Q. (2018b). Bionic intelligent hydrogel actuators with multimodal deformation and locomotion. *Nano Energy* 51, 621–631. doi: 10.1016/j.nanoen.2018.07.025

Conflict of Interest: The authors declare that the research was conducted in the absence of any commercial or financial relationships that could be construed as a potential conflict of interest.

Copyright © 2021 Zhao, Yu, Liang, Ren and Ren. This is an open-access article distributed under the terms of the Creative Commons Attribution License (CC BY). The use, distribution or reproduction in other forums is permitted, provided the original author(s) and the copyright owner(s) are credited and that the original publication in this journal is cited, in accordance with accepted academic practice. No use, distribution or reproduction is permitted which does not comply with these terms.



Recent Advances of 4D Printing Technologies Toward Soft Tactile Sensors

Yuneng Tang¹, Baiqian Dai^{1*}, Bin Su^{2*} and Yusheng Shi²

¹ Department of Chemical Engineering, Monash University, Clayton, VIC, Australia, ² State Key Laboratory of Material Processing and Die and Mould Technology, School of Materials Science and Engineering, Huazhong University of Science and Technology, Wuhan, China

OPEN ACCESS

Edited by:

Ilkwon Oh,

Korea Advanced Institute of Science and Technology, South Korea

Reviewed by:

Rouhollah Dermanaki Farahani,

École de Technologie Supérieure

(ÉTS), Canada

Yu Wang,

University of Science and Technology of China, China

*Correspondence:

Baiqian Dai

Bai-Qian.Dai@monash.edu

Bin Su

subin@hust.edu.cn

Specialty section:

This article was submitted to

Smart Materials,

a section of the journal

Frontiers in Materials

Received: 25 January 2021

Accepted: 23 March 2021

Published: 15 April 2021

Citation:

Tang Y, Dai B, Su B and Shi Y (2021) Recent Advances of 4D Printing Technologies Toward Soft Tactile Sensors.

Front. Mater. 8:658046.

doi: 10.3389/fmats.2021.658046

Soft tactile sensors (STs) combine the flexibility and the converting ability between mechanical forces and electrical signals. 4D printing was first introduced in 2013, and attracted great interest because of its versatile functionalities in actuators, artificial muscles, STs, soft energy harvesting, pneumatic nets, electroactive polymers, and soft electronics. Using the 4D printing concept to fabricate STs is promising, yet it is at its infant stage. At present, researchers have utilized two types of strategies: one is directly using smart materials through 3D printing manufacturing, and the other is programming codes of components and structures to create controllable changes. This review summarizes the recent research on 4D printing toward STs and discusses the future perspectives of this emerging field.

Keywords: 4D printing, multi-material, flexible, soft, tactile sensors

INTRODUCTION

Additive manufacturing (AM) has attracted lots of attention as a versatile technology to fabricate complicated structures from various materials, such as polymers, metals, ceramics, and other smart materials or stimulus-responsive materials (Oropallo and Piegler, 2015; Balogun et al., 2018). Unlike those traditional subtractive manufacturing methods, AM usually piles up materials to form objects layer by layer according to the data of the computer models. As a result, AM can manufacture items with very sophisticated and complex geometries with no need for post-processing or other assistive tools like molds, dies, or lithographic masks. As an exciting branch of AM, 4D printing was proposed in 2013 by Tibbitts (2013), which soon gained considerable interest in public media and research communities (Momeni et al., 2017). In the beginning, 4D printing was primarily known as “3D printing + time” (Spiegel et al., 2019), but the definition evolved in recent years. Shi et al. extended the definition of 4D printing as “the change of shape, property, and functionality from a 3D printed structure response to time or external stimulus” (Yintang et al., 2020), namely, heat (Phuhongsung et al., 2020), water (Melocchi et al., 2019), light (Nishiguchi et al., 2020), and pH (Lin et al., 2018). Owing to manufacturing simplicity and attainable complication of printed material species, 4D printing, as a new branch of AM, has been applied in the fabrication of various functional devices, such as actuators (Akdogan et al., 2005), soft electronics (Zheng et al., 2013; Wang et al., 2015), and soft tactile sensors (STs) (Xu et al., 2017), as well as in the industry of different disciplines.

Soft tactile sensors (STs) are a new type of wearable electronic devices, which provide the possibility of mechanical signal interaction between the human/machine and the surrounding

environments (Truby and Lewis, 2016). The research of STSs is an emerging field following the rapid development of flexible electronics in the recent two decades (Zarek et al., 2016). Based on diverse working mechanisms, STSs can be divided into five categories: piezoelectric, piezoresistive, capacitive, triboelectric, and magnetic types (Wan et al., 2017). The fabrication of STSs relies on traditional manufacturing methods, namely, film patterning, metallic deposition, molding, and assembly techniques, indicating the complex and high-cost features. Alternatively, multi-material-type AM processing can simultaneously integrate diverse material species to their on-demand positions, allowing for the rapid and cost-effective fabrication of electronic devices. The functionality of as-prepared structures was endowed, which can be recognized as a branch of 4D printing. Thus, it is urgently required to develop novel 4D printing techniques in the further advance of STSs.

In the past few years, there has been a significant trend toward applying 4D printing technology to manufacture various STSs. In other words, a growing number of researchers from different research backgrounds have begun to recognize the importance of this effective technique. By controlling the spatial positions of diverse material species to endow the final products with a new mechano-electric transducing functionality, this concept, no doubt, falls in the definition of 4D printing. More intuitively, as shown in **Figure 1**, the number of publications and citations in this topic has rapidly boosted. The citations increase more sharply than the publications. Thus, it is deduced that the future of 4D printing research combined with the STSs will be positively promoted, which will generate promising interest in the years to come.

This article reviews the recent research outcomes concerning 4D printed STSs. At the first stage, it is crucial to understand the AM manufacturing features to adapt to the working mechanisms of STSs. Therefore, this article is organized as follows. Section “Diverse AM Techniques Toward the Fabrication of STSs” gives a detailed and comprehensive description of the fundamental techniques of AM process, including the specially used materials. Section “4D Printing for STSs” describes the five types of 4D-printed STSs. Finally, section “Conclusions and Outlook” provides some important conclusions, which share the viewpoints on the future development of 4D-printed STSs.

DIVERSE AM TECHNIQUES TOWARD STSs

Additive manufacturing enables the realization of 3D objects directly from computer-aided design (CAD) models (Frazier, 2014; Herzog et al., 2016; Schmidt et al., 2017). CAD models are transformed into special formats that can be read by computers. The formats are then sliced into control codes to force 3D printers to manufacture objects in a layer-by-layer fashion (Rengier et al., 2010; Oropallo and Piegler, 2015). Up to now, many different types of AM technologies have been developed for generating STSs, namely, selective laser sintering (SLS), stereolithography (SLA), fused filament fabrication (FFF), direct ink writing (DIW), and inkjet printing. For different printing methods and device

requirements, materials should be carefully considered for the final products. The subsequent sections will briefly introduce those five types of AM techniques about the printing procedures and related materials.

Selective Laser Sintering

Selective laser sintering, also known as selective laser melting (SLM), is an AM process that uses an electron beam or a laser as a power source to sinter powder materials. The materials used as the SLM deposition material to form 3D objects include metals, polymers, ceramics, and composites. The building procedure (**Figure 2A**) of this AM can be separated into three steps: (1) The feed powders with diameters from 10 to 100 μm are rolled over the construction platform. (2) The laser beam is directed into the powders to melt, and the melted powder content is solidified. (3) Then, the powders are rolled over the top of the deposition layer again with the platform declining. The process is repeated until the desired 3D object is completely produced. Unused powder that does not form a part of the as-prepared 3D object has been retained on the construction platform to support the object, thus achieving nearly 100% material utilization. This technique is suitable for metal-based sensor fabrication.

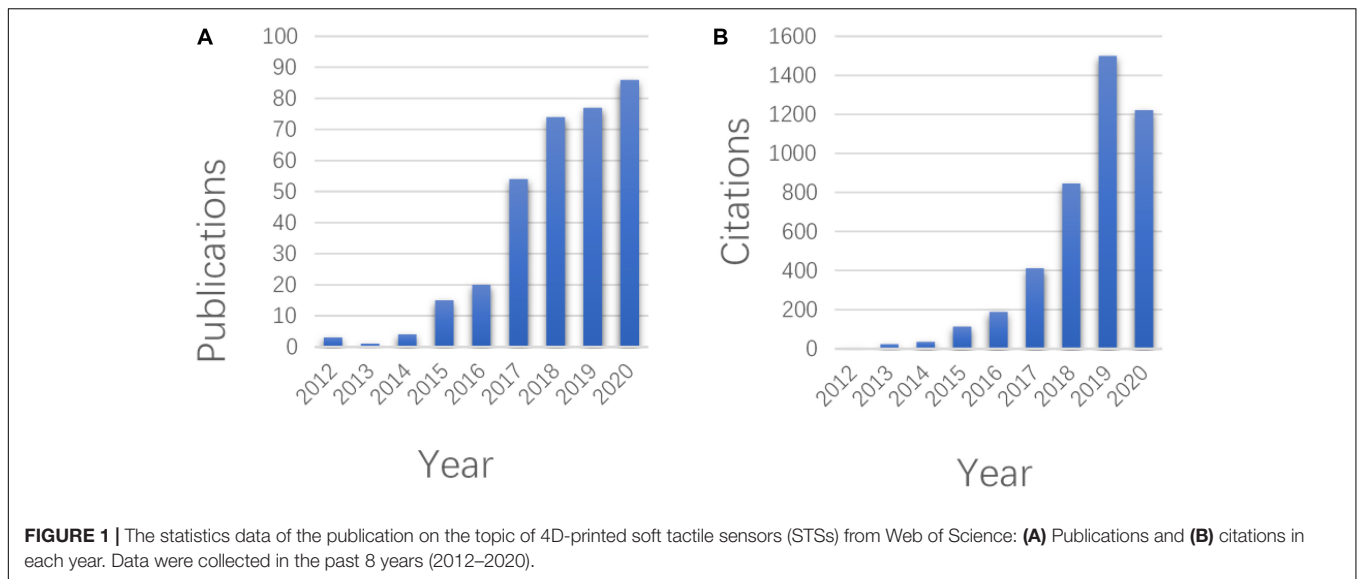
Stereolithography

Stereolithography is the first vat photopolymerization method developed in the early 1980s, which uses specific light to solidify liquid materials in the vat layer by layer to fabricate 3D printing objects. Some other innovative AM techniques like digital projection lithography (DLP) have the same print concept of SLA printing, yielding similar fundamental printing. **Figure 2B** depicts the printing procedure using the SLA technique. The light source of the laser emits light to cure the liquid polymer. Following the movement of the laser, a thin patterned layer is formed. After the first printing layer, the build platform moves by one-layer height, and a new layer of liquid photopolymer is introduced and cured by the local illumination.

Compared with the SLA technique, the most important improvement of DLP is the printing speed. DLP uses micro-mirror array devices or dynamic liquid-crystal masks to cure an entire pattern of one layer, instead of using a point light source to solidify only one voxel at a time. Thus, the fabrication speed of the SLA is much slower than that of the DLP technique. These two techniques are suitable for polymer-based sensor fabrication.

Fused Filament Fabrication

Fused deposition modeling is a type of material extrusion or extrusion printing. During its working process, a melted thermoplastic-based filament is extruded through a nozzle as a form of continuous filament because of mechanical force. The filament is selectively deposited to fabricate the target entity. As shown in **Figure 2C**, the typical printer for FFF is comprised of an X-Y-Z axis motion platform, and the extrusion nozzle is filled with diverse material species. The X-Y axis movements are controlled by the computer software, allowing the nozzle to extrude the filament at the designed position in one layer. When one layer is accomplished, either the build platform moves down or the extrusion head moves up, leading to the beginning



of the next layer. This process repeats for numerous cycles till the designed entity is completed. The printed materials of this technique are widely selected. They include polycarbonate, polylactic acid (PLA), acrylonitrile butadiene styrene (ABS), and other thermoplastic elastomers and their composites with functional particles or liquids. All of the extruded materials should have thermoplasticity and rheological balance. Since the FFF resolution is lower than SLA, this technique is fit for generating tactile sensors with low-resolution-structural polymer structures.

Direct Ink Writing

Direct ink writing is a powerful alternative printing technique to FFF, especially for viscoelastic materials. As shown in **Figure 2D**, different from FFF, DIW uses air pressure or a piston to extrude the printing material. Some curing procedures, like thermal curing or photopolymerization, are required to solidify the materials after deposition. The primary working mechanism for the DIW process is that, when the inks leave the nozzles, their viscosity will considerably increase, allowing them to take a gel state to keep their shape. DIW technique tolerates a wide variety of materials, namely, electrical, biological, and structural materials (Truby and Lewis, 2016). Thermoset polymers, fugitive inks, colloidal suspension, and hydrogels can be used as different ink materials. DIW can realize multi-material fabrication using microfluidic print heads that can switch flexibility or use multiple printheads with disparate ink compositions. The advantages of DIW are numerous, such as free of dying, no need for lithographic masks, or expensive tooling. Since this technique is of low cost and fits a wide variety of materials, it will be a successful candidate to fabricate arbitrary 3D structural tactile sensors with multi-material design.

Inkjet Printing

Inkjet printing, also known as material jetting, is an AM process similar to SLA in many aspects, yet a movable nozzle is utilized

in this technique. **Figure 2E** illustrates that the nozzle and accessory curing devices like UV light sources are formed on an X-Y-Z three-axis motion platform. The liquid photopolymer is ejected from the nozzles and deposited on the print platform and then it is cured as a solid. It is widely accepted that the SLA technique relies on photopolymerizable resins. Comparatively, inkjet printing has the advantage of fabricating patterns utilizing numerous soft materials in the form of formulated inks using various molecular or polymeric species. This technique is suitable for fabricating multi-material STSs.

4D PRINTING FOR STSs

Usually, an STS consists of several parts, namely, a flexible substrate, sensing parts, flexible electrodes, and other support materials. The fabrication of STSs involves multi-material selections and their precise positioning, which is quite suitable for the design of 4D printing. By controlling the spatial positions of diverse material species to endow the final products with a new mechano-electric transducing functionality, this concept, no doubt, falls in the definition of 4D printing. Many researchers have utilized AM techniques to fabricate a part of or even the entire tactile sensors to date. This section has listed representative studies of 4D printed tactile sensors categorized into five subsections according to the working mechanisms.

Piezoresistive-Type STSs

The principle of piezoresistive-type STSs is the resistance changes of the interface material with the external stimuli, through which the external stimuli were converted into electrical signals. Due to the advantages, such as simple structure, low energy consumption, and wide testing range, piezoresistive-type STSs have been widely studied. In the beginning, piezoresistive sensors are fabricated by thin-film processing, molding, or nanomaterial assembly, indicating causal manufacturing features without standard manufacturing. With the continuous development of

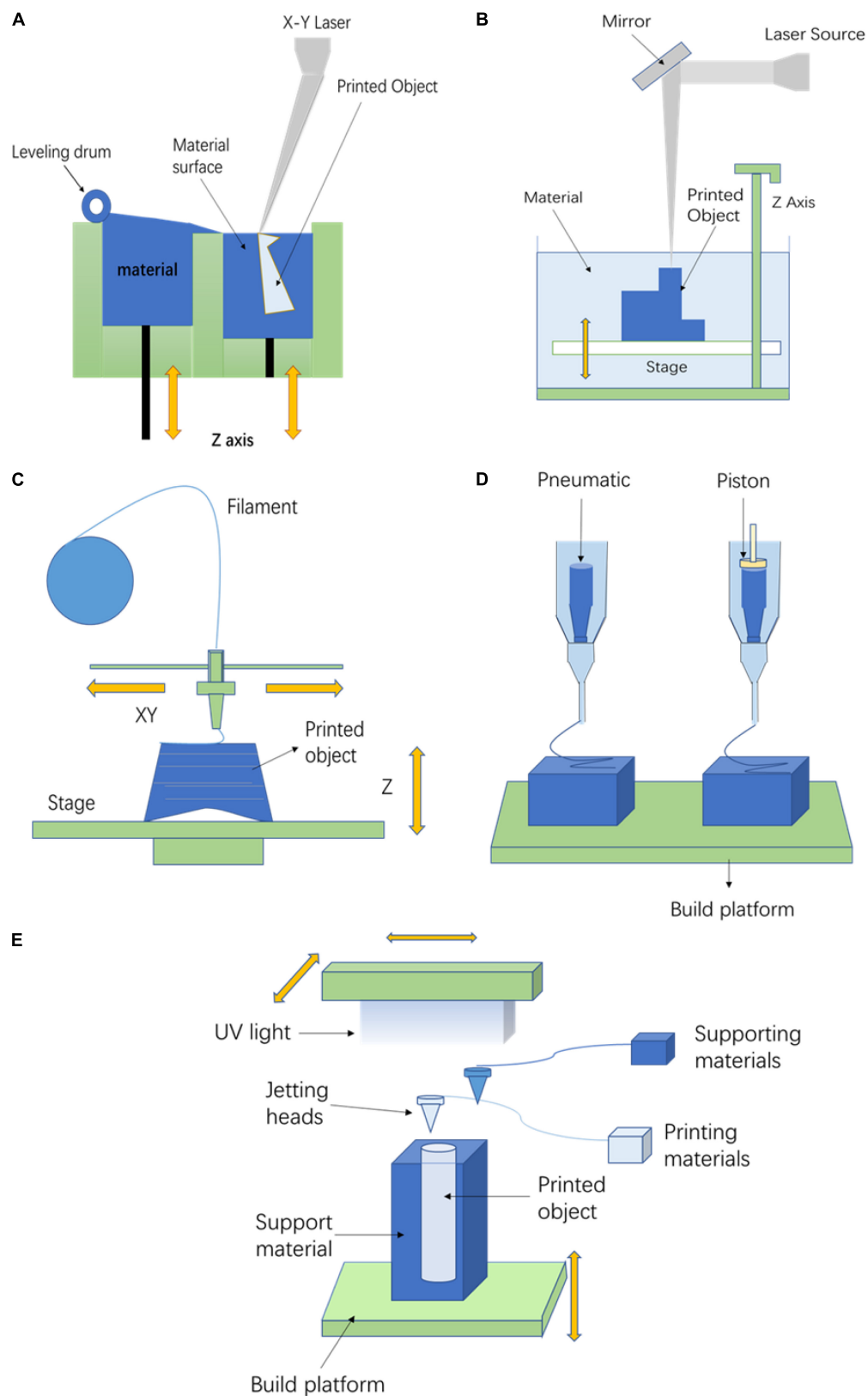


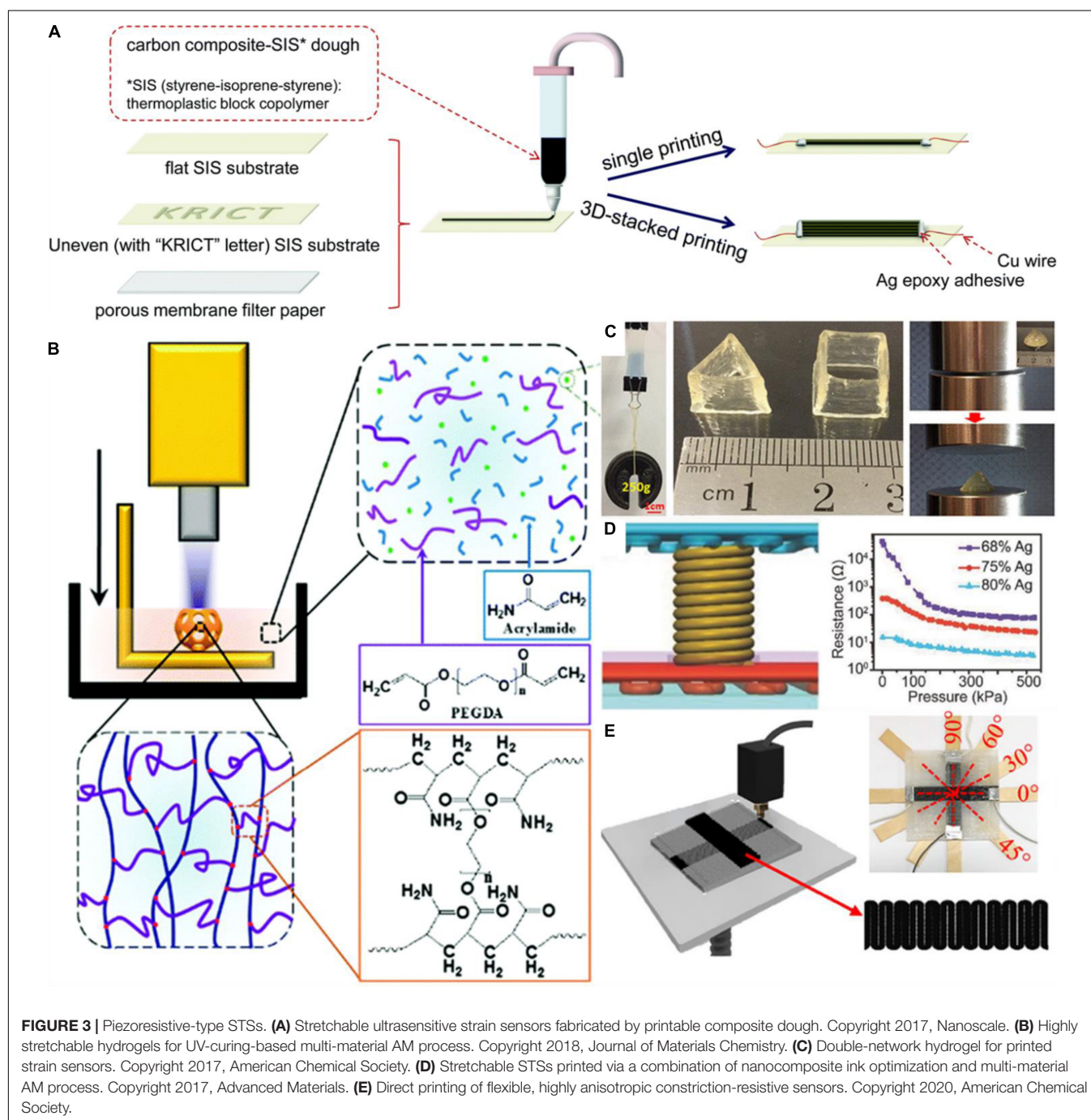
FIGURE 2 | Schematic illustrations of different AM technologies toward the fabrication of STSs. **(A)** Selective laser sintering. **(B)** Stereolithography. **(C)** Fused deposition modeling. **(D)** Direct ink writing. **(E)** Inkjet printing.

AM techniques, numerous researchers have recognized AM as a powerful tool to generate STSs.

Kim et al. (2017b) demonstrated a piezoresistive STS formed by a specially designed composite dough. The sophisticated dough is comprised of a carbon composite and a thermoplastic triblock-copolymer elastomer, namely polystyrene-polyisoprene-polystyrene (SIS). The carbon composite was made by mixing multi-walled carbon nanotubes (MWNTS) with graphene oxides (GOs). As shown in **Figure 3A**, the 3D printable dough materials were printed on 400 μm thick SIS substrates using

three-axis-programmable nozzle-based dispensing equipment. After drying at 80°C, both ends of the printed sensor layers were electrically connected with Cu wires and conductive Ag adhesive paste. It had been demonstrated that the printed strain sensor devices exhibited an extremely high gauge factor of 72 with linearity (R^2) of 0.94 when the GOs were added to the carbon composite at a ratio of 9.

A strain sensor based on microchannel had been designed by Agarwala et al. (2017). The dimensions of the sensor were 2.5×2.5 cm. The diameter and the length of each microchannel



were 500 μm and 24 cm, respectively. The microchannels were filled with a kind of silver conducting ink. **Figure 3B** exhibits the complete fabrication process of a printed strain sensor. A photopolymer composite material was used to build the substrate; then, wax was injected into the channels as support materials. After that, the channels were flushed with warm oil to remove the wax, allowing a syringe to fill the microchannel with Novacentrix® JS-B25HV silver conducting ink. Finally, the channels were sealed with a connecting wire. When the sensor suffered a strain in the axial direction of microchannels, the cross-sectional area and the length changed. Thus, the overall resistance of the channels would change accordingly. In the study of Agarwala et al., the change in the resistance of the sensor has been examined when strains were applied in two directions, parallel and orthogonal. It can be noticed that the strain sensor has good repeatability, fast recovery, and negligible hysteresis when the applied strain is below 6%.

Zhang et al. (2018) developed highly stretchable and UV curable hydrogels for the DLP technique. **Figure 3B** depicts the hydrogel preparation method. An acrylamide-PEGDA (AP)-based hydrogel precursor was made by mixing acrylamide as the monomer and poly(ethylene glycol) diacrylate (PEDGA) as the crosslinker. 2,4,6-trimethylbenzoyl-diphenylphosphine oxide (TPO) nanoparticles were chosen as the photo-initiator in water (water content: 50–80 wt%). This AP hydrogel system has several considerable advantages, such as high stretchability and compatibility with the DLP AM technology. More importantly, the AP hydrogels can form strong interfacial bonding with commercial printable elastomers, leading to printed hydrogel-elastomer hybrid structures. The study shows a highly stretchable electronic board by printing an ionic hydrogel circuit on an elastomeric substrate, yielding AP hydrogels as promising materials for tactile strain sensors.

Liu et al. created a novel, 3D printable hydrogel with admirable recoverability and significant self-healing capability. This hydrogel can print sensitive strain sensors because of its good strain sensitivity (Liu and Li, 2017). κ -carrageenan and acrylamide (AAM) were used to fabricate the hybrid double-network (DN) hydrogels through a photopolymerization process. The self-healing capability comes from the thermo-responsive nature of κ -carrageenan. A sheet sample of DN hydrogel could hold a weight of 250 g (**Figure 3C**). The printability and flexibility of the DN hydrogel are shown in **Figure 3C**. The DN hydrogel can be printed into various types (hollow triangular prism or hollow cube) but it regains its original height after being pressed.

Many other researchers contribute to wearable electronics systems by combining piezoresistive stretchable materials and AM techniques. Guo et al. (2017) created a type of sinter-free ink with electrical conductivities and adjustable viscosities to fabricate STSs. The sensors were formed by several layers: a base layer, a sensor layer, two electrode layers, an isolating layer, and a sacrificial supporting layer. The final model of the sensor is shown in **Figure 3D**. The electrical properties of the sensor were attributed to the cured inks by mixing submicrometer-sized silver particles within a highly stretchable silicone elastomer. It was found that the ink with 68 wt% had the best piezoresistive performance, as indicated in **Figure 3D**.

Mousavi et al. (2020) used a carbon-nanotube-reinforced polylactic acid (PLA-CNT) to fabricate a piezoresistive STS. In this research, they employed a novel approach by engineering appropriate anisotropic structures as multidirectional tactile sensors. The group selected a sandwich design to characterize the printed anisotropic tactile sensing under large deformation. The PLA-CNT sensor was encapsulated between two thermoplastic polyurethane (TPU) layers (**Figure 3E**). Direct stretching and bending tests characterized the sensor performance. Wooden strips were used in tensile tests in different directions. **Figure 3E** shows the tensile sensitivity testing results at 0°, 30°, 45°, 60°, and 90°, in which a 1% tensile strain was applied for three cycles in each direction. The printed sensors have high sensitivity with strain gauge factors ($k \sim 1,342$).

Christ et al. (2017) used TPU to develop a 3D-printable, flexible, conductive material, which was demonstrated as an excellent piezoresistive STS. They compounded TPU with multi-walled carbon nanotube (TPU/MWCNT) to print TPU/MWCNT samples. Then, the as-prepared STSs investigated their mechanical, electrical, and piezoresistive properties. The TPU/MWCNT nanocomposites provided various flexibility and sensitivity features, tunable for diverse applications. The cyclic response indicates a strong and consistent behavior over strain loadings and outstanding electric conductivity and piezoresistivity.

Capacitive-Type STSs

Capacitance is the capability of a capacitor to store/release charge. A capacitor consists of two parallel plates and a dielectric layer sandwiched between them. Capacitive-type STSs have shown high sensitivity, compatibility with static force measurement, and low power consumption. However, capacitive devices are susceptible to interference from surrounding objects because these objects might change the fringe field of the capacitor (Cheng et al., 2010), causing it to produce uncertain signals during the measurement. There have been plenty of studies about AM-processed capacitive-type STSs in recent decades.

Nag et al. (2018) used graphite powder and polydimethylsiloxane (PDMS) to develop a kind of capacitive sensor patches. They combined casting and AM technology. The production process, has been divided into several consecutive steps. First, a mold was fabricated through the AM technique using PDMS. Then, graphite powders were cast onto the trenches of the mold. Finally, the patches were cured, yielding the generation of capacitive sensors. Nag's group investigated the characteristics of the sensor patches. The change in the capacitance values to the forces is nearly linear, with a force sensitivity of $0.2542 \text{ pF mN}^{-1}$ during a range from 3.5 to 17.5 mN. These capacitive properties of sensor patches are due to the high electrical conductivity and corrosion resistance of graphite.

Huang et al. (2016) fabricated a new flexible three-axial force sensor using PDMS. This flexible sensor had four-unit capacitors providing it with high sensitivity to 3-axial forces. The four capacitors were formed by four sensing electrodes and the public electrode upon the flexible printed circuit board (FPCB) layer. The dielectric layer and the bump layer were fabricated by the

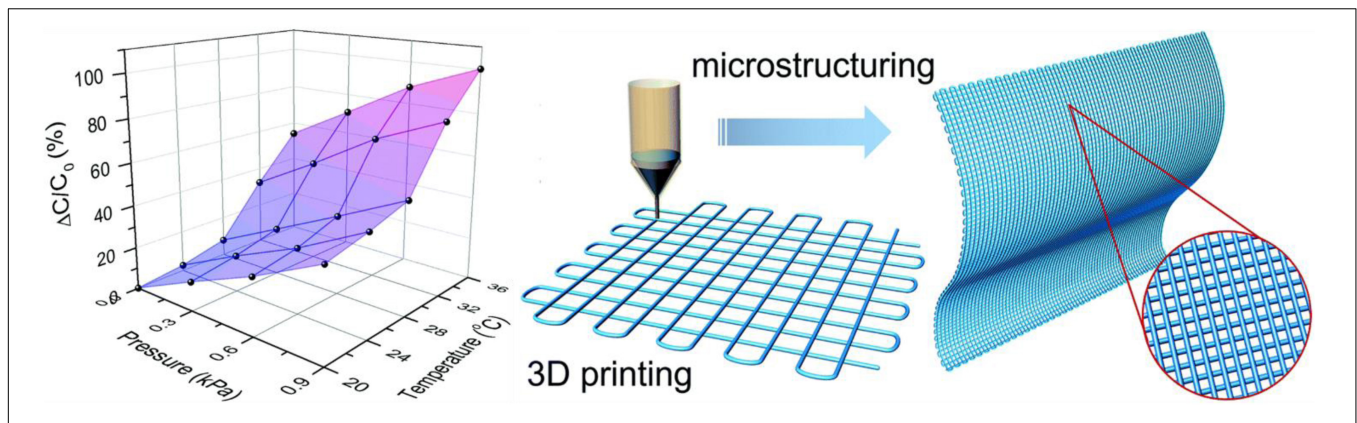


FIGURE 4 | Multifunctional skin-like STSs based on a printed thermo-responsive hydrogel. Copyright 2017, Materials Horizons.

3D printing process using PDMS. These two layers were bonded together after the oxygen plasma treatment. The response of the four capacitors in the sensor unit was observed when applied to external forces. Three charts represent three forces: z-axis normal force, x-axis shear force, and y-axis shear force. It is indicated that the capacitances changed linearly concerning the forces.

Hydrogels have been used to fabricate capacitive sensors as well. Lei et al. (2017) came up with an effective strategy to prepare a multifunctional skin-like sensor using thermo-responsive hydrogel in the AM technique. This microstructured double-network hydrogel was synthesized by hydrophobic n-octadecyl acrylate (C18) and sodium dodecyl sulfate (SDS) through a micellar-copolymerization method. The prepared hydrogels could be printed using an FFF-type printing system, as shown in **Figure 4**. A polyethylene film was sandwiched between two bulk/grid-structured hydrogels connected to two metallic electrodes to fabricate the final sensor. The capacitive STS can respond to manifold pressure (P) and temperature (T). It indicated that the resulting skin-like hydrogel sensor exhibited high sensitivity to those stimuli.

Piezoelectric-Type STSs

Piezoelectricity is a phenomenon in which voltage is generated by applied mechanical stress, which is commonly used for tactile sensors (Choong et al., 2014). The piezoelectricity comes from the oriented permanent dipole in materials. The deformation of the oriented non-centrosymmetric crystal structure causes the electric dipole moment to separate and generate a piezoelectric voltage on both sides, thus the appearance of the electric dipole moment (Wegener et al., 2005). Due to the high sensitivity and fast response time of piezoelectric sensors, they are widely used in the detection of dynamic pressure, such as sound and sliding vibration (Hammock et al., 2013). Besides, because of the unique energy harvesting characteristics of piezoelectric materials, they are considered as a potential candidate for low-power or self-powered tactile sensors.

Lee et al. (2017) fabricated a 3D customized STS. This piezoelectric-type mechanoelectrical sensor is mainly composed of sandwich-shaped substrates and a core piezoelectric layer.

Three parts formed the sandwich-shaped substrate, the upper mold, the lower mold, and their connecting hinge, fabricated by 3D printing using PDMS. The piezoelectric core was a nanofibrous material prepared by electrospinning poly (vinylidene fluoride trifluoroethylene) (PVDF-TrFE). Lee et al. investigated the sensitivity of the sensor. They tested three types of sensors: flat, wrist-form, and fingertip-form sensors. Hence, this customizable sensor can be widely used in wearable electronic devices because of its combined flexibility and sensitivity.

Using the same polymer material (PVDF), Kim et al. (2017a) came up with a unique process to fabricate piezoelectric films through an integrated FFF printing and other corona poling process. The fabrication of as-prepared sensors was as follows: First, the PVDF polymer was heated and extruded from the nozzle, allowing it to harden immediately and deposit with a predominantly α -phase crystalline structure. Then, the PVDF molecules were transformed from α - to β -phase crystalline structure under a high electric field, yielding the rising piezoelectric response.

Fuh et al. (2017) utilized piezoelectric PVDF to fabricate a flexible sensor through an FFF printing process, resulting in the wavy surface of thermoplastic elastomer (TPE) substrate. The integration process of the sensor is shown in **Figure 5**. Initially, the Cu foil was deposited to the wavy surface of the TPE substrate. Then, PVDF fibers were attached to the surface *via* near-field electrospinning (NEFS). Finally, the PDMS was used to encapsulate the device entirely. The devices with three different surfaces, namely, planar, square, and sinusoidal surfaces, were fabricated to measure the output voltage and current versus cyclic stretching–releasing deformation. This proposed piezoelectric sensor has great potential in promising applications for wearable electronics.

Triboelectric-Type STSs

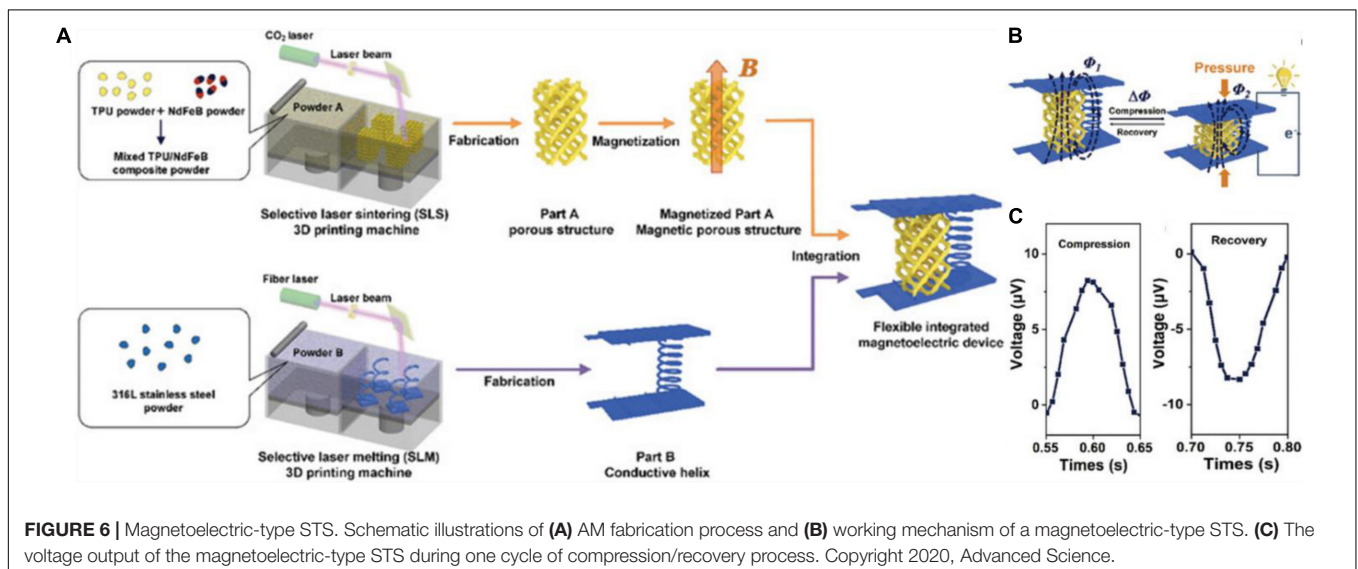
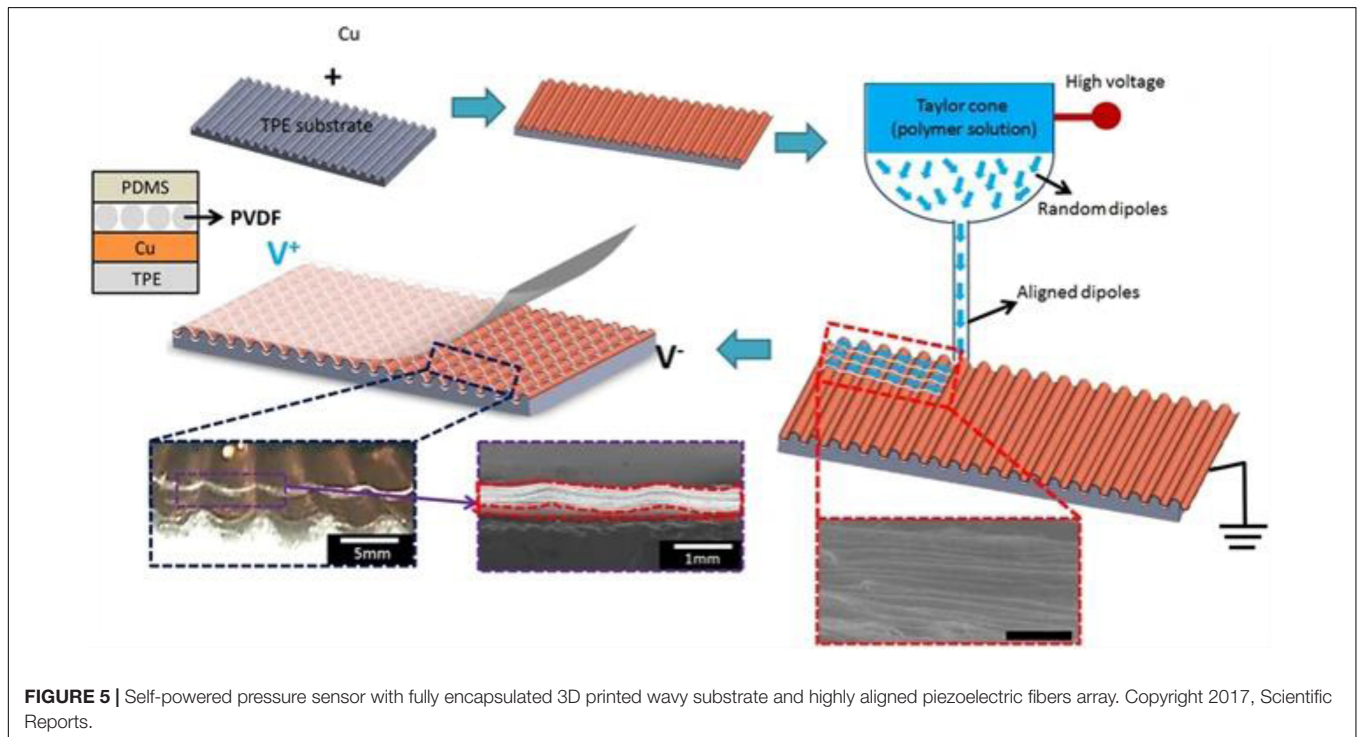
The triboelectric effect is a common phenomenon in our daily lives. It occurs when the contacting materials are subjected to friction caused by touching, shearing, or torsions. However, the mechanism behind the triboelectric effect is still under study.

It is generally believed that charges will be induced on the surface when two different materials move against each other. The amount of charge generated depends on the difference in triboelectricity polarities between the two contacted materials (Sun et al., 2018).

Haque et al. (2018) used several printable soft materials as functional triboelectric sensor components. They found that PDMS, combined with commercial TangoBlack (TB), showed the highest triboelectric responses. Polyamide (PA) was utilized to fabricate the 3D-printed spring structure. The fabrication process of the triboelectric

touch sensor, indicates that the sensor is composed of three printed layers: PDMS layer with electrodes, PA spring structure layer, and TB layer with electrodes. The output power can reach up to $60 \mu\text{W}$ when the operating frequency is 5 Hz.

Chen et al. (2018) fabricated an ultra-flexible 3D triboelectric nanogenerator (TENG) using printed composite resin parts and ionic hydrogels. These two materials were utilized as the electrification layer and the electrode. The fabrication process of the 3D-TENG is that the liquid photopolymer resins and support materials were directly printed using a single process within an



integrated platform through inkjet printing. The voltage output of the 3D-TENG was as high as 70 V.

Magnetoelectric-Type STSs

The magnetoelectric tactile sensor is a newly emerging technology that enables the mechanical pressure to be converted into electrical signals with the help of the magnetic field. This mechanism of a tactile sensor is known as electromagnetic induction, and the relative movement between magnets and conductive wires can generate electricity. These tactile sensors are self-powered without an external power supply due to their magnetoelectric working systems.

Wu et al. (2020) designed a flexible integrated magnetoelectric sensor, and the fabrication of this sensor fulfills the brand-new concept of 4D printing. The 4D-printed tactile sensor exhibited a piezoelectric ability to convert the external pressure into electric energy without any piezoelectric parts, conforming to the 4D printing concept. The magnetoelectric tactile sensor is comprised of two parts, as shown in **Figure 6A**. One part is a porous structure fabricated by SLS using TPU/NdFeB composite powders, while the other part is a helix structure with two flat plates fabricated by SLM using 316 stainless steel powders. **Figure 6B** shows the working mechanism: After the magnetic part was magnetized to acquire permanent magnetism, the magnetic field lines would pass through the coil. When the structure was compressed due to external forces, the magnetic flux would change and generate electricity according to the electromagnetic induction principle. **Figure 6C** is one typical cycle of output voltages by a compression/recovery process.

REFERENCES

- Agarwala, S., Goh, G. L., Yap, Y. L., Goh, G. D., Yu, H., Yeong, W. Y., et al. (2017). Development of bendable strain sensor with embedded microchannels using 3D printing. *Sensors Actuators A: Phys.* 263, 593–599. doi: 10.1016/j.sna.2017.07.025
- Akdogan, E. K., Allahverdi, M., and Safari, A. (2005). Piezoelectric composites for sensor and actuator applications. *IEEE Trans. Ultrason. Ferroelectr. Freq. Control* 52, 746–775. doi: 10.1109/tuffc.2005.1503962
- Balogun, V. A., Otanocha, O. B., and Ibadode, A. O. (2018). The impact of 3D printing technology to the nigerian manufacturing GDP. *Modern Mechan. Eng.* 08, 140–157. doi: 10.4236/mme.2018.82010
- Chen, B., Tang, W., Jiang, T., Zhu, L., Chen, X., He, C., et al. (2018). Three-dimensional ultraflexible triboelectric nanogenerator made by 3D printing. *Nano Energy* 45, 380–389. doi: 10.1016/j.nanoen.2017.12.049
- Cheng, M. Y., Lin, C. L., Lai, Y. T., and Yang, Y. J. (2010). A polymer-based capacitive sensing array for normal and shear force measurement. *Sensors (Basel)* 10, 10211–10225. doi: 10.3390/s101110211
- Choong, C. L., Shim, M. B., Lee, B. S., Jeon, S., Ko, D. S., Kang, T. H., et al. (2014). Highly stretchable resistive pressure sensors using a conductive elastomeric composite on a micropillar array. *Adv. Mater.* 26, 3451–3458. doi: 10.1002/adma.201305182
- Christ, J. F., Aliheidari, N., Ameli, A., and Pötschke, P. (2017). 3D printed highly elastic strain sensors of multiwalled carbon nanotube/thermoplastic polyurethane nanocomposites. *Mater. Des.* 131, 394–401. doi: 10.1016/j.matdes.2017.06.011
- Frazier, W. E. (2014). Metal additive manufacturing: a review. *J. Mater. Eng. Perform.* 23, 1917–1928. doi: 10.1007/s11665-014-0958-z
- Fuh, Y. K., Wang, B. S., and Tsai, C. Y. (2017). Self-Powered pressure sensor with fully encapsulated 3D printed wavy substrate and highly-aligned piezoelectric fibers array. *Sci. Rep.* 7:6759. doi: 10.1038/s41598-017-07360-z

CONCLUSION AND OUTLOOK

In summary, this review summarizes the latest advances in the application of 4D-printed STSs. Compared with the traditional manufacturing methods that have limitations such as tedious fabrication steps, low material utilization, and low manufacturing freedom, AM provides unique advantages to fabricate STSs, namely, the substrate, the sensing element, electrodes, and dielectric layers with complex 3D structures, in a highly efficient and low-cost manner. Furthermore, the structural optimization of the AM technique can make sensors achieve faster response speed, higher sensitivity, and better flexibility. Although AM-processed sensors have already achieved many advantages, some challenging points need to be focused. First, materials that can be used to fabricate soft sensors are minimal, and novel printable materials with improved properties need further evolution. Second, it will be a great breakthrough if a whole STS can be fabricated in a continuous multi-material AM process, instead of printing parts of a sensor. The advancement of AM technology has the potential to conceive more compelling sensors for future research and applications. We expect that all these efforts will make AM-processed STSs to own a glorious future.

AUTHOR CONTRIBUTIONS

YT and BS collected the references. YT, BD, BS, and YS discussed and wrote the manuscript. All authors contributed to the article and approved the submitted version.

- Guo, S. Z., Qiu, K., Meng, F., Park, S. H., and McAlpine, M. C. (2017). 3D printed stretchable tactile sensors. *Adv. Mater.* 29:1701218. doi: 10.1002/adma.201701218
- Hammock, M. L., Chortos, A., Tee, B. C., Tok, J. B., and Bao, Z. (2013). 25th anniversary article: the evolution of electronic skin (e-skin): a brief history, design considerations, and recent progress. *Adv. Mater.* 25, 5997–6038. doi: 10.1002/adma.201302240
- Haque, R. I., Chandran, O., Lani, S., and Briand, D. (2018). Self-powered triboelectric touch sensor made of 3D printed materials. *Nano Energy* 52, 54–62. doi: 10.1016/j.nanoen.2018.07.038
- Herzog, D., Seyda, V., Wycisk, E., and Emmelmann, C. (2016). Additive manufacturing of metals. *Acta Materialia* 117, 371–392. doi: 10.1016/j.actamat.2016.07.019
- Huang, Y., Yuan, H., Kan, W., Guo, X., Liu, C., and Liu, P. (2016). A flexible three-axial capacitive tactile sensor with multilayered dielectric for artificial skin applications. *Microsystem Technol.* 23, 1847–1852. doi: 10.1007/s00542-016-2936-x
- Kim, H., Torres, F., Wu, Y., Villagran, D., Lin, Y., and Tseng, T.-L. (2017a). Integrated 3D printing and corona poling process of PVDF piezoelectric films for pressure sensor application. *Smart Mater. Structures* 26:085027. doi: 10.1088/1361-665X/aa738e
- Kim, H., Ji, S., Jung, S., Ryu, B. H., Kim, H. S., Lee, S. S., et al. (2017b). 3D printable composite dough for stretchable, ultrasensitive and body-patchable strain sensors. *Nanoscale* 9, 11035–11046. doi: 10.1039/c7nr01865g
- Lee, H. B., Kim, Y. W., Yoon, J., Lee, N. K., and Park, S.-H. (2017). 3D customized and flexible tactile sensor using a piezoelectric nanofiber mat and sandwich-molded elastomer sheets. *Smart Mater. Structures* 26:045032. doi: 10.1088/1361-665X/aa64ca
- Lei, Z., Wang, Q., and Wu, P. (2017). A multifunctional skin-like sensor based on a 3D printed thermo-responsive hydrogel. *Mater. Horizons* 4, 694–700. doi: 10.1039/c7mh00262a

- Lin, Q., Li, L., Tang, M., Hou, X., and Ke, C. (2018). Rapid macroscale shape morphing of 3D-printed polyrotaxane monoliths amplified from pH-controlled nanoscale ring motions. *J. Mater. Chem. C* 6, 11956–11960. doi: 10.1039/c8tc02834f
- Liu, S., and Li, L. (2017). Ultrastretchable and self-healing double-network hydrogel for 3D printing and strain sensor. *ACS Appl. Mater. Interfaces* 9, 26429–26437. doi: 10.1021/acsami.7b07445
- Melocchi, A., Inverardi, N., Uboldi, M., Baldi, F., Maroni, A., Pandini, S., et al. (2019). Retentive device for intravesical drug delivery based on water-induced shape memory response of poly(vinyl alcohol): design concept and 4D printing feasibility. *Int. J. Pharm.* 559, 299–311. doi: 10.1016/j.ijpharm.2019.01.045
- Momeni, F., Mehdi Hassani, S. M. N., Liu, X., and Ni, J. (2017). A review of 4D printing. *Mater. Des.* 122, 42–79. doi: 10.1016/j.matdes.2017.02.068
- Mousavi, S., Howard, D., Zhang, F., Leng, J., and Wang, C. H. (2020). Direct 3D printing of highly anisotropic, flexible, constriction-resistive sensors for multidirectional proprioception in soft robots. *ACS Appl. Mater. Interfaces* 12, 15631–15643. doi: 10.1021/acsami.9b21816
- Nag, A., Feng, S., Mukhopadhyay, S. C., Kosel, J., and Inglis, D. (2018). 3D printed mould-based graphite/PDMS sensor for low-force applications. *Sensors Actuators A: Phys.* 280, 525–534. doi: 10.1016/j.sna.2018.08.028
- Nishiguchi, A., Zhang, H., Schweizerhof, S., Schulte, M. F., Mourran, A., and Moller, M. (2020). 4D printing of a light-driven soft actuator with programmed printing density. *ACS Appl. Mater. Interfaces* 12, 12176–12185. doi: 10.1021/acsami.0c02781
- Oropallo, W., and Piegler, L. A. (2015). Ten challenges in 3D printing. *Eng. Comp.* 32, 135–148. doi: 10.1007/s00366-015-0407-400
- Phuhongsung, P., Zhang, M., and Bhandari, B. (2020). 4D printing of products based on soy protein isolate via microwave heating for flavor development. *Food Res. Int.* 137:109605. doi: 10.1016/j.foodres.2020.109605
- Rengier, F., Mehndiratta, A., von Tengg-Koblog, H., Zechmann, C. M., Unterhinninghofen, R., Kauczor, H. U., et al. (2010). 3D printing based on imaging data: review of medical applications. *Int. J. Comput. Assist. Radiol. Surg.* 5, 335–341. doi: 10.1007/s11548-010-0476-x
- Schmidt, M., Merklein, M., Bourell, D., Dimitrov, D., Hausotte, T., Wegener, K., et al. (2017). Laser based additive manufacturing in industry and academia. *CIRP Annals* 66, 561–583. doi: 10.1016/j.cirp.2017.05.011
- Spiegel, C. A., Hippler, M., Münchinger, A., Bastmeyer, M., Barner-Kowollik, C., Wegener, M., et al. (2019). 4D Printing at the Microscale. *Adv. Funct. Mater.* 30:1907615. doi: 10.1002/adfm.201907615
- Sun, J., Pu, X., Liu, M., Yu, A., Du, C., Zhai, J., et al. (2018). Self-Healable, stretchable, transparent triboelectric nanogenerators as soft power sources. *ACS Nano* 12, 6147–6155. doi: 10.1021/acsnano.8b02479
- Tibbits (2013). *The Emergence of 4D Printing*. Available online at: https://www.ted.com/talks/skylar_tibbits_the_emergence_of_4d_printing/up-next (accessed April 4, 2013).
- Truby, R. L., and Lewis, J. A. (2016). Printing soft matter in three dimensions. *Nature* 540, 371–378. doi: 10.1038/nature21003
- Wan, Y., Wang, Y., and Guo, C. F. (2017). Recent progresses on flexible tactile sensors. *Mater. Today Phys.* 1, 61–73. doi: 10.1016/j.mtphys.2017.06.002
- Wang, Q., Yu, Y., Yang, J., and Liu, J. (2015). Fast fabrication of flexible functional circuits based on liquid metal dual-trans printing. *Adv. Mater.* 27, 7109–7116. doi: 10.1002/adma.201502200
- Wegener, M., Wirges, W., and Gerhard-Multhaupt, R. (2005). Piezoelectric Polyethylene Terephthalate (PETP) foams – specifically designed and prepared ferroelectric films. *Adv. Eng. Mater.* 7, 1128–1131. doi: 10.1002/adem.200500177
- Wu, H., Zhang, X., Ma, Z., Zhang, C., Ai, J., Chen, P., et al. (2020). A material combination concept to realize 4D printed products with newly emerging property/functionality. *Adv. Sci. (Weinh)* 7:1903208. doi: 10.1002/advs.201903208
- Xu, Y., Wu, X., Guo, X., Kong, B., Zhang, M., Qian, X., et al. (2017). The boom in 3D-Printed sensor technology. *Sensors (Basel)* 17:1166. doi: 10.3390/s17051166
- Yintang, W. E. N., Shuquan, Z., Jiankang, H. E., Qingliang, Z., Bo, L., Shifeng, W. E. N., et al. (2020). Four-dimensional printing — the additive manufacturing technology of intelligent components. *J. Mechan. Eng.* 56, 1–25. doi: 10.3901/jme.2020.15.001
- Zarek, M., Layani, M., Cooperstein, I., Satchani, E., Cohn, D., and Magdassi, S. (2016). 3D printing of shape memory polymers for flexible electronic devices. *Adv. Mater.* 28, 4449–4454. doi: 10.1002/adma.201503132
- Zhang, B., Li, S., Hingorani, H., Serjouei, A., Larush, L., Pawar, A. A., et al. (2018). Highly stretchable hydrogels for UV curing based high-resolution multimaterial 3D printing. *J. Mater. Chem. B* 6, 3246–3253. doi: 10.1039/c8tb00673c
- Zheng, Y., He, Z., Gao, Y., and Liu, J. (2013). Direct desktop printed-circuits-on-paper flexible electronics. *Sci. Rep.* 3:1786. doi: 10.1038/srep01786

Conflict of Interest: The authors declare that the research was conducted in the absence of any commercial or financial relationships that could be construed as a potential conflict of interest.

Copyright © 2021 Tang, Dai, Su and Shi. This is an open-access article distributed under the terms of the Creative Commons Attribution License (CC BY). The use, distribution or reproduction in other forums is permitted, provided the original author(s) and the copyright owner(s) are credited and that the original publication in this journal is cited, in accordance with accepted academic practice. No use, distribution or reproduction is permitted which does not comply with these terms.



Graphene Oxide-Modified Microcapsule Self-Healing System for 4D Printing

Bowen Ma¹, Yuping Zhang², Yongjie Wei¹, Mingrui Li¹ and Dongdong Li^{3*}

¹ Key Laboratory of Automobile Materials of Minister of Education, Department of Materials Science and Engineering, Jilin University, Changchun, China, ² School of Chemistry and Chemical Engineering, Huazhong University of Science and Technology, Wuhan, China, ³ State Key Laboratory for Materials Processing and Die and Mould Technology, School of Materials Science and Engineering, Huazhong University of Science and Technology, Wuhan, China

OPEN ACCESS

Edited by:

Kun Zhou,

Nanyang Technological University,
Singapore

Reviewed by:

Jiayao Chen,

Nanyang Technological University,
Singapore

Huijun Li,

Nanyang Technological University,
Singapore

*Correspondence:

Dongdong Li

lidongdong0@hust.edu.cn

Specialty section:

This article was submitted to
Smart Materials,
a section of the journal
Frontiers in Materials

Received: 24 January 2021

Accepted: 18 March 2021

Published: 16 April 2021

Citation:

Ma B, Zhang Y, Wei Y, Li M and
Li D (2021) Graphene Oxide-Modified
Microcapsule Self-Healing System
for 4D Printing.
Front. Mater. 8:657777.
doi: 10.3389/fmats.2021.657777

Self-healing materials as a type of promising smart materials are gradually applied to electronics, biology, and engineering. In this study, we used *in situ* polymerization to make melamine-formaldehyde (MF) resin microcapsules to wrap the epoxy oxide as a repairing agent and Cu(MI)₄Br₂ as a latent-curing agent to protect epoxy oxide E-51 from broken melamine-formaldehyde resin microcapsules. In addition, graphene oxide was used as a reinforcing phase through its two-dimensional-layered structure to increase the tensile strength to 41.91 MPa, which is higher than the initial materials. The melamine-formaldehyde capsules and latent-curing agents were uniformly distributed in the materials according to the digital photos and scanning electron microscope (SEM) pictures. It is worth noting that the mechanical strength of the broken materials can be restored to 35.65 MPa after heating to 130°C for 2 h to repair the damage, and the self-healing efficiency reached up to 85.06%. Furthermore, we also fabricated the 4D printed material with a tensile strength of 50.93 MPa through a 3D printer. The obtained materials showed excellent repair effect, with a recovery rate of up to 87.22%. This study confirms that the designed self-healing system has potential applications in many areas due to its excellent self-healing performance, which provides valuable guidance for designing the 4D system.

Keywords: 4D printing, self-healing, microcapsules, polymermatrix composites, smart materials

INTRODUCTION

Smart materials have attracted widespread attention due to their shape and properties which can be altered with external environment changes, such as light, electricity, and magnetism (Wu et al., 2019). 3D printing smart materials, which are also referred to as “4D printing,” change configurations over time. So far, 4D printing has been used to develop many types of smart materials, such as shape-memory materials (Cheng et al., 2020), smart gel materials (Jang et al., 2020), and self-healing materials (Chen et al., 2016), which demonstrated great applications in the fields of biology (Aronsson et al., 2020; Kim et al., 2020), medicine (Javaid and Haleem, 2020; Lin et al., 2021), and bionics (Correa et al., 2020). Among them, the self-healing materials used for 3D printing mainly comprise soft active materials (SAMs), as a type of polymer, which can be mainly divided into five parts: engineering plastics (such as polyethersulfone, poly-ether-ether-ketone,

and polyphenylene sulfide), bioplastics (such as polylactic acid and polycaprolactone), thermoset materials, photosensitive resin, and polymer gels (Tan et al., 2020). The polymer should be selected and designed to achieve the properties required in accordance with the different environments and chemical properties. Wei et al. (2017) proposed 3D direct-write printing of ultraviolet (UV) cross-linking poly(lactic acid)-based inks, and its tensile strength reached 1.7 MPa. Shiblee et al. (2019) developed a shape memory hydrogel, which contains poly (N,N-dimethyl acrylamide-co-stearyl acrylate) [P(DMAAm-co-SA)], with the tensile strength of only 4.57 MPa. Although SAMs are characterized by high-tensile deformation and simple molding, their low-tensile strength limits their wide application (Enriquez-Cabrera et al., 2020). Therefore, some researchers are targeting hard materials.

Hard materials, which are aptly named, have generally high-tensile strengths. However, most hard materials cannot heal the physical damage autonomously, which is self-healing. The microcapsule strategy is one of the most prevalent self-healing strategies for hard materials, encapsulating substances that can produce healing effects without being affected by the curing of hard materials. When the microcapsules are broken, the coated core material flows out, and the corresponding chemical reaction occurs to achieve a self-healing effect. Zhao et al. (2020) prepared a microcapsule-type latent-curing agent with imidazole (IZ) as the core material, which is prepared by interfacial polymerization of triethanolamine (TEOA) and diphenylmethane diisocyanate (MDI). The tensile strength of IZ/E-51 reached 13.2 MPa. Nevertheless, the combination of microcapsules and graphene oxide (GO) has a wide range of applications in many areas in recent years, such as self-lubrication (Li H. et al., 2020; Li X. et al., 2020), thermal conductivity (Zhou Y. et al., 2020), and functionalization (Zhou Y. et al., 2020). Without doubts, GO itself has excellent properties, such as high specific surface areas, superb tensile strength, and electrical conductivity (Khan et al., 2020). On the one hand, recent studies on the combination of GO and microcapsules are mainly focused on the modification of GO to the microcapsules themselves. Ma et al. (2020) conceived a graphene-modified self-healing microcapsule, 1,6-diaminohexane as the inner core, and GO-isophorone diisocyanate (IPDI)-based prepolymer as the outer core. The results showed that the GO-modified microcapsules obtained a spherical shape with a mean diameter of 0.50 μm , and self-healing efficiency reaches 80.43%. A self-healing microcapsule material encapsulating linseed oil, using polyether ammonia molecules sutured with GO as the shell layer, was prepared by Li et al. (2019); the impedance modulus of the composite coating after healing was four orders of magnitude higher than that of pure polyurethane. On the other hand, some researchers have also incorporated GO into polymer substrates to prepare microcapsules self-healing systems with high-tensile strength. Akhan et al. (2020) developed UV-cured polyurethane GO nanocomposite microcapsules with a self-healing coating; the tensile strength of the self-healing coating came up to 36.10 MPa, which is the highest. As one of the hard materials, epoxy oxide has excellent mechanical properties and low shrinkage (less than 2%) (Farooq et al., 2020), so epoxy oxide remains virtually invariable

in volume after 4D printing and curing, with a slight increase in its original mechanical properties. For thermosetting hard resin, epoxy oxide requires the addition of curing agents to repair the damage (Gholipour-Mahmoudalilou et al., 2018; Gao et al., 2020; Seidi et al., 2020). The mechanical properties exhibit differently depending on the types of curing agents (Haddadi et al., 2019; Xie et al., 2020). The combination of epoxy oxide, microcapsules, graphene oxide, and 4D printing can be formed as a sort of self-healing material with high tensile strength and stable properties, showing a great potential for application in biology, medicine, and bionics.

In this study, we present a method to prepare the epoxy oxide-based self-healing system for 4D printing (**Scheme 1**). Microcapsules and $\text{Cu}(\text{MI})_4\text{Br}_2$ served as the healing units and latent-curing agents, respectively. Meanwhile, GO was also incorporated into the epoxy oxide self-healing system as the toughening phase to provide higher tensile strength. It is worth noting that the tensile strength of 4D printing GO that modified microcapsules of the epoxy oxide self-healing system can reach 50.93 MPa (the tensile strength of pouring samples with the same components is only 41.91 MPa), much higher than SAMs. When the scratches were healed, the tensile strength could still be restored to 44.42 MPa, with a high healing efficiency of up to 89.98%. The development of 4D printing epoxy oxide self-healing system will extend the usage of the new self-healing system and will be beneficial to a variety of practical 4D-printing-related applications, including material surface protection and aerospace structures.

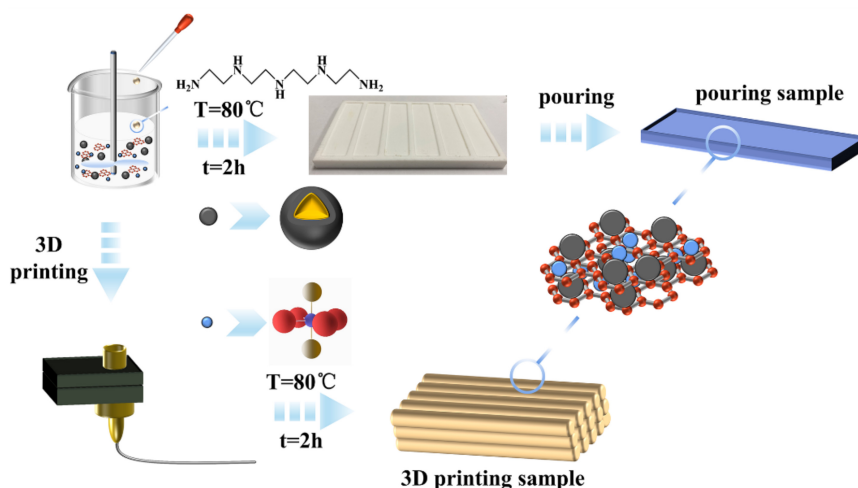
MATERIALS AND METHODS

Materials

Epoxy oxide (E-51), n-octanol, 2-methylimidazole (2-MI), and cupric bromide were supplied by Shanghai Macklin Biochemical Co., Ltd., China. Urea, melamine, tetraethylenepentamine (TEPA), and sodium dodecylbenzenesulfonate (SDBS) were obtained from Tianjin Guangfu Fine Chemical Research Institute, China. Formaldehyde was made by Liaoning Quan Rui Reagent Co., Ltd., China.

Preparation of Epoxy Oxide Microcapsules

The microcapsules, with phenolic resin as the wall and epoxy oxide as the core, were prepared *via* an *in situ* polymerization microencapsulation process. The fabrication method consisted of three steps, which can be described as the following: First, melamine (3.2 g), urea (0.8 g), and formaldehyde solution (2.7 g) were mixed in a 100 mL beaker equipped with a magnetic stirrer. The pH value of the solution was adjusted to 8–9 by slowly adding TEOA solution and continuing reaction for 1 h under 70°C. Second, a certain amount of epoxy oxide E-51 was added to 100 mL of 1 wt% aqueous solution of SDBS with the above phenolic resin at 25°C. The mixture was stirred at 700 rpm for 10 min to form an emulsion. Third, the pH of the reaction mixture was slowly tuned to 3–4 by adding 0.1 mol/L hydrochloric acid. The resultant microcapsules were filtrated and



SCHEME 1 | Preparation of the epoxy oxide-based self-healing system for 4D printing.

washed with acetone, ethanol, and deionized water several times to remove impurities. The synthesis reaction equation is shown in **Supplementary Schemes 1–3**.

Preparation of the Latent-Curing Agent

CuBr_2 (11.17 g, 0.05 mol) and 2-MI (16.42 g, 0.2 mol) were dissolved in the beaker with methanol solution (50 mL) by ultrasonication. Then, the two solutions were mixed and stirred at 25°C for 24 h. The sediment was obtained by centrifugation and dried at 50°C in a vacuum oven for 6 h.

Preparation of the 3D Printing Sample

About 0.3 wt% (based on the E-51 epoxy oxide) GO was added to 10 g epoxy oxide and stirred magnetically for 30 min at 800 rpm, and sonicated for 30 min, and then, 1 g of microcapsules and 0.2 g of the latent-curing agent were added sequentially and stirred magnetically at 400 rpm for 5 min; at the same time, 0.15 g of TEPA was added through the whole process and additionally stirred magnetically for 2 min. All of the above steps were carried out at 25°C. The mixture was degassed by vacuum to remove the air mixed into the mixture during the mixing process. The degassed mixture was then added to the resin bath of the 3D printer (Nordson ASYMTEK CN DS Quantum Q-6800, American). A STL file of the structure, which we designed, was loaded into Fluidmove software in order to generate a series of G.codes. The thickness of the single print layer was set to 500 μm . The 3D printer then read the G.code and printed layer by layer at the printing speed of 1 mm/s by using the syringe print head in a predetermined path. The whole process was carried out at 60°C. The finished product was removed from the substrate and cured at 80°C for 2 h.

Preparation of Pouring Sample

About 0.3 wt% (based on the E-51 epoxy oxide) GO was added to 10 g epoxy oxide and stirred magnetically for 30 min at 800 rpm, and sonicated for 30 min, and then, 1 g of microcapsules and 0.2 g

of the latent-curing agent were added sequentially and stirred magnetically at 400 rpm for 5 min; at the same time, 0.15 g TEPA was added through the whole process and additionally stirred magnetically for 2 min. All of the above steps were carried out at 25°C. The mixture was poured in a preheated Teflon mold, which was preheated at 100°C, vacuumed to remove air bubbles, and heated at 80°C for 2 h. The samples were allowed to cool at 25°C and were then removed.

Preparation of Self-Healing Samples

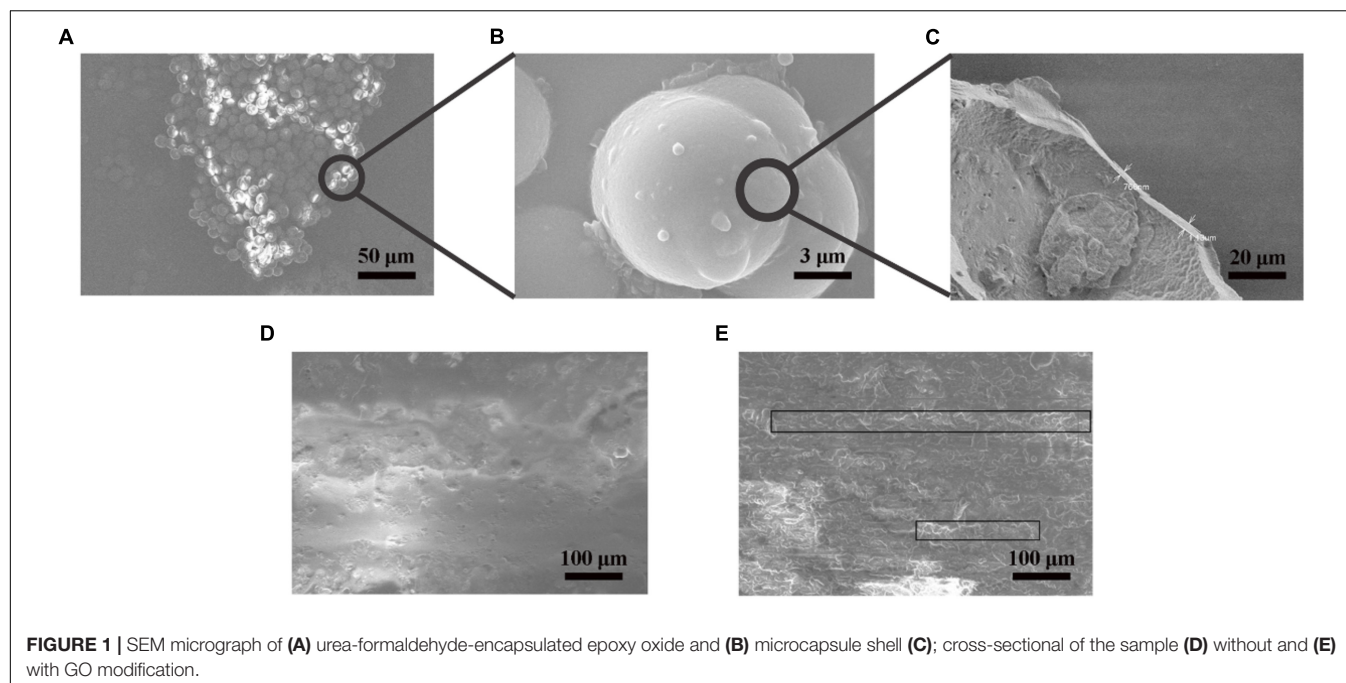
The surface of samples was cut a scratch with a depth of 1 mm, with an scalpel. Then, the scratch samples were immediately heated at 130°C for 2 h. The self-healing process of the sample was recorded by taking photographs. Healing performance was confirmed by comparing the tensile strength of original, scratch, and scratch repair samples.

Characterization

Micrographs of the microcapsules were taken with Field Emission Scanning Electron Microscope (FE-SEM) (Hitachi, Regulus 8220, Japan) at 5 kV and a current of 10 μA . FTIR studies were conducted on a Bruker spectrophotometer (ALPHA, German). The powdered samples of 2-MI and $\text{Cu}(\text{MI})_4\text{Br}_2$ were mixed with KBr at a ratio of 1:100 to produce tablets for FTIR measurement. The thermogravimetric analysis of 2-MI, $\text{Cu}(\text{MI})_4\text{Br}_2$, and microcapsules were conducted by Mettler Toledo TGA 2 (Switzerland) at air atmosphere with the heating interval ranging from 25 to 800°C and at the speed of 5°C/min. The tensile strength of pouring samples and 3D printing samples were tested by Instron 3400 (United States), and the tensile state was 2 mm/min under 5 kN load.

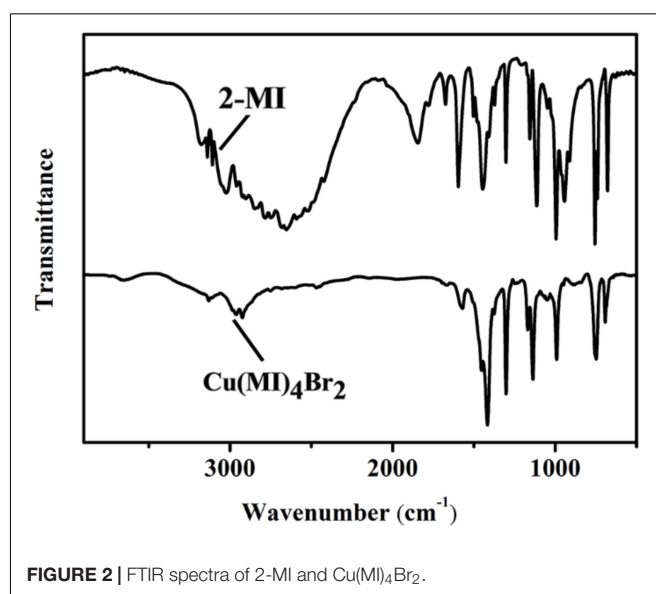
RESULTS AND DISCUSSION

The capsules present a regular spherical configuration, and their size was uniform, which prove the correctness of the



colloid theory (Figures 1A,B). The diameters of microcapsule are about 10–12 μm , and their surface is smooth, which is caused by precipitation, aggregation, and deposition of polyuria; microcapsules with rough shell morphology have also been reported (Keller et al., 2007). Due to the brittle nature of microencapsulated shells, after the microcapsules were ruptured by compression force, a clear image of a core-shell structure of microcapsule can be observed under SEM (Figure 1C). It can be clearly seen to have a width of 0.7–1.5 μm , proving that the microcapsules are the core-shell structure rather than a mixture state. The cross-section of the self-healing system without GO is smooth and appears to have no obvious structure (Figure 1D). When the self-healing system was modified with graphene oxide, its cross-section shows clearly that GO sheets were formed with a tightly layered structure, comprising waves that look like fine alternating layers (Figure 1E). The reason is that the reactive groups achieve robust interaction with epoxy oxide through covalent or hydrogen bonding, which greatly improves the interfacial compatibility of the GO with the epoxy oxide matrix (Yu et al., 2019). The structure of the self-healing system changes from disorder to layer, with the addition of graphene oxide, which will improve its toughness to a great extent (Ye et al., 2014).

2-methylimidazole can react with copper ions to form stable metal complexes with square pyramidal geometry, namely, $\text{Cu}(\text{MI})_4\text{Br}_2$ (Zhu et al., 2015). Br^- occupies two vertices, and MI groups are distributed at the four vertices in the middle of the diamond. Improving the temperature will lead to the dissociation of $\text{Cu}(\text{MI})_4\text{Br}_2$ and the release of MI groups, which will react with epoxy oxide to change the repair effect (Supplementary Scheme 4; Pilawka and Maka, 2011; Tripathi et al., 2015). The FTIR spectra of 2-MI and $\text{Cu}(\text{MI})_4\text{Br}_2$ are illustrated in Figure 2. All of the characteristic bands of the MI group can be clearly

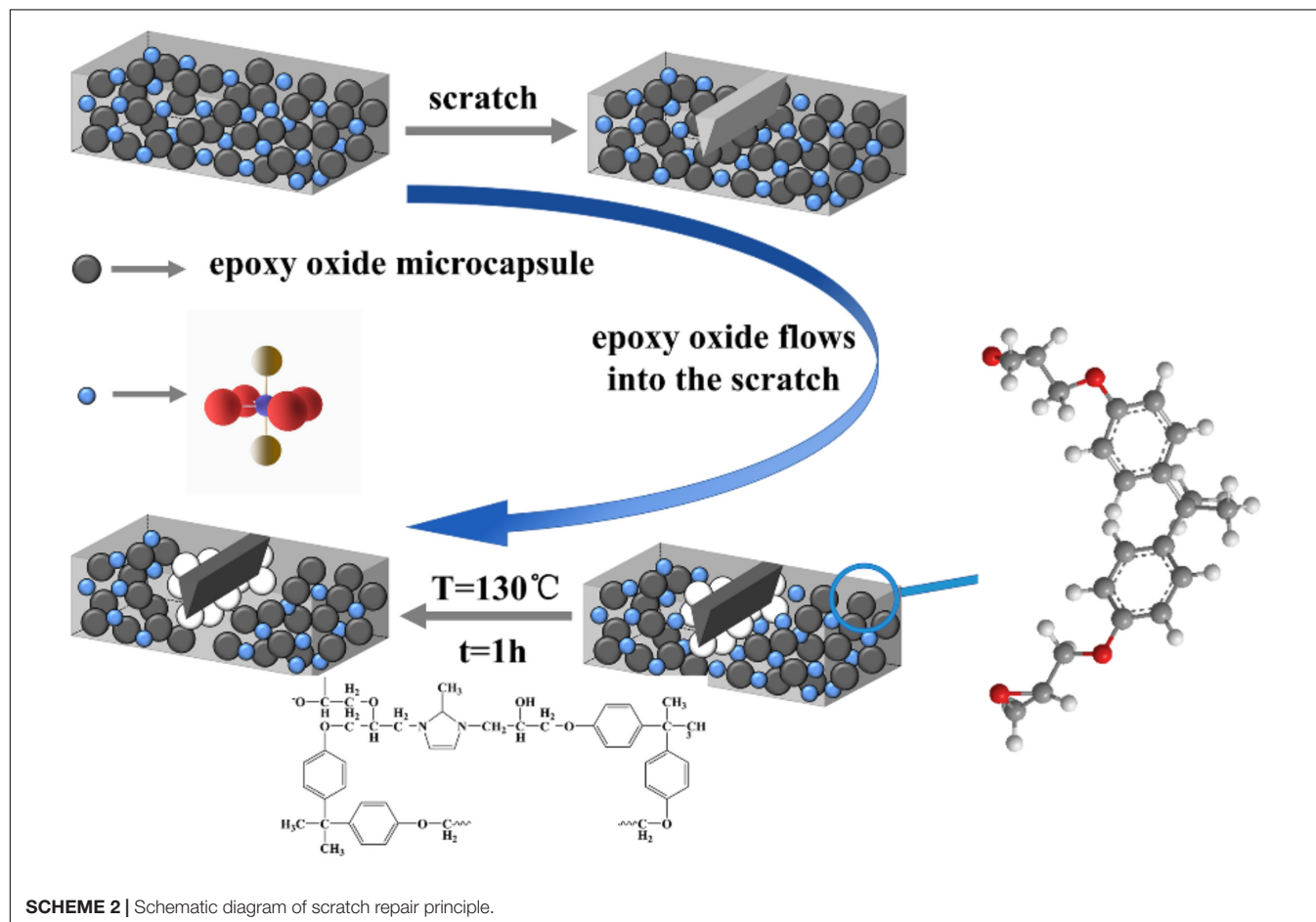
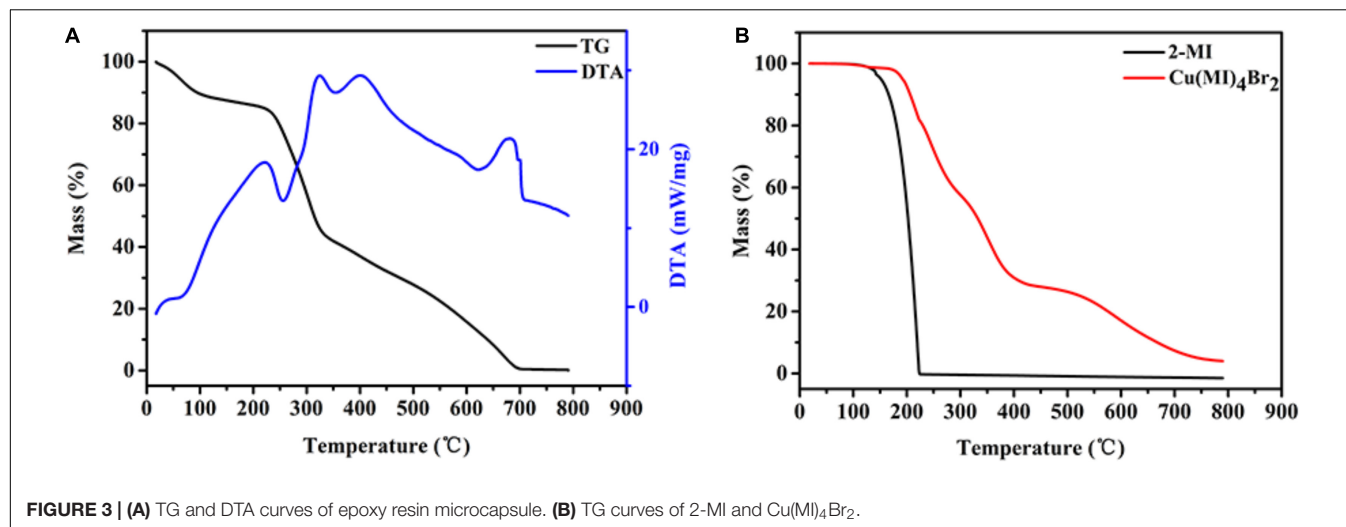


observed, including N–H stretching at $3,400\text{ cm}^{-1}$, N–H wagging vibration at 650 cm^{-1} , C–N stretching at $1,600\text{ cm}^{-1}$, C = N stretching at $1,700\text{ cm}^{-1}$, =CH rocking vibration at $1,460\text{ cm}^{-1}$. But, in the FTIR of $\text{Cu}(\text{MI})_4\text{Br}_2$, the N–H stretching cannot be observed. That is because the H on the nitrogen atom of 2-MI secondary amine reacts with Cu ions. The appearance of these peaks shows that $\text{Cu}(\text{MI})_4\text{Br}_2$ was successfully prepared.

Figure 3A illustrates the TG and DTA curves of epoxy oxide microcapsule. The evaporation of water is mainly below 113°C . When the temperature reached 316°C , the wall of microcapsule decomposed. The core material began to evaporate in large

quantities due to the loss of protection of the wall under high temperature. **Figure 3B** shows the TG curves of 2-MI and $\text{Cu}(\text{MI})_4\text{Br}_2$. 2-MI begins to decompose at 152°C , while the decomposition temperature of $\text{Cu}(\text{MI})_4\text{Br}_2$ is 216°C , suggesting the improved thermal stability of MI groups after forming a complex. The schematic diagram of the self-healing system

is shown in **Scheme 2**. The microcapsules and the latent-curing agent $\text{Cu}(\text{MI})_4\text{Br}_2$ are evenly embedded in the epoxy oxide substrate. Under the action of external destruction, the microcapsules will break, leading to the flow out of epoxy oxide. In addition, the $\text{Cu}(\text{MI})_4\text{Br}_2$ will be decomposed at high temperature in the MI group, which will solidify the epoxy



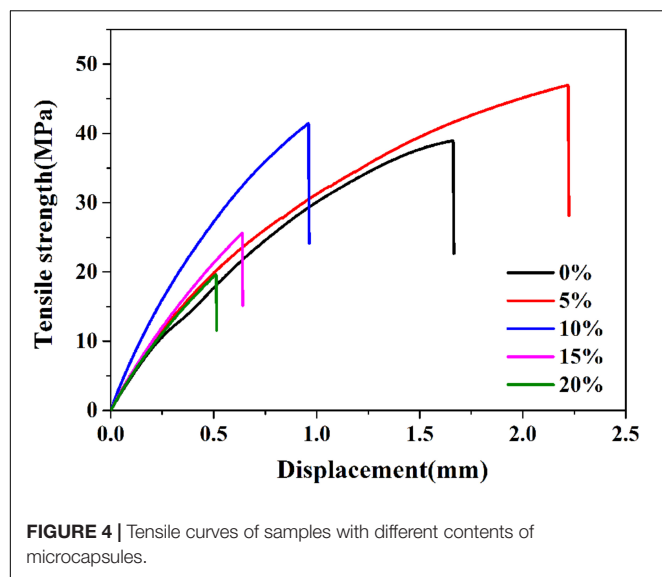


FIGURE 4 | Tensile curves of samples with different contents of microcapsules.

oxide at the damaged area to achieve the purpose of repair. Therefore, the core-shell structure also ensures the integrity of the epoxy oxide inwardly under high temperature, which will not be thermally decomposed and react with the MI groups cured by the high-temperature decomposition of the latent-curing agent $\text{Cu}(\text{MI})_4\text{Br}_2$. Meanwhile, the stabilized complex structure of $\text{Cu}(\text{MI})_4\text{Br}_2$ ensures that the MI groups will not react with the epoxy oxide matrix when heating at 100°C but will decompose out of the complexed structure when it reaches 130°C and then react with the epoxy oxide overflow from microcapsules for curing.

Figure 4 shows the effect of different contents of microcapsules on the mechanical properties of the system. With the increasing number of microcapsules embedded, the tensile strength of the sample first shows an increasing trend and then a decreasing trend. Microcapsules in epoxy oxide can be seen as “enlarged” vacancy defects, and epoxy oxide substrate surface area can be enlarged. When the fracture crack extends to the location where the microcapsules are in contact with the epoxy oxide, there is an interface problem between shell materials of microcapsules and epoxy oxide matrix because both materials are different (Yuan et al., 2019). The walls of the microcapsules allow the stress to be dispersed rather than following a straight line. The distance between microcapsules reached the optimum distance when 10% content of microcapsules was added to the epoxy oxide matrix. While the sample is stretched, the distance of atoms, molecules, and other components at the fracture increases, the repulsive force decreases, and tension occurs macroscopically; a greater tensile stress is needed to make the sample fracture because the microcapsules disperse the stress and reduce the strain, which makes the final manifestation of large stress and a small strain, resulting in a large Young’s modulus. When the content of microcapsules is 5%, the distance between microcapsules increases so that few parts of the tensile stress will extend between the walls of microcapsules and epoxy oxide, augmenting its tensile strength. When the content of

TABLE 1 | Four kinds of samples with different compositions.

	$\text{Cu}(\text{MI})_4\text{Br}_2$	Microcapsule	Graphene oxide
Sample 1	×	×	×
Sample 2	✓	×	×
Sample 3	✓	✓	×
Sample 4	✓	✓	✓

microcapsules increased to 15 and 20%, the distance between microcapsules decreased, but the existence of microcapsules greatly reduces the continuity of epoxy oxide substrate, the macroscopic tensile strength decreases sharply, and the microscopic displacement of atoms and molecules is greatly restricted, so that the elastic deformation decreases sharply and fracture occurs at small displacement, which results in the decrease of its tensile strength. In order to make the sample possess optimum tensile strength and repair efficiency, we chose the blending amount of microcapsule to be 10 wt%.

The effect of GO on the tensile strength of the sample, which contains microcapsules and $\text{Cu}(\text{MI})_4\text{Br}_2$, is carefully investigated as shown in **Figure 5**. Test results showed that the tensile strength of the samples increases significantly with increasing GO content. The enhancement of GO to the tensile strength of the sample is mainly due to the chemical bonding between GO and $\text{Cu}(\text{MI})_4\text{Br}_2$ /microcapsule/epoxy oxide segments in the GO-modified microcapsule self-healing system. The strong interfacial covalent bonding is favorable to the loading transfer from the polymer matrix to GO, with superior tensile strength (Xia et al., 2015). Furthermore, because of the immense modulus difference between GO and epoxy oxide, GO functions as a stress-concentration point and induces microcracks around it, which consumes additional fracture energy to improve the tensile strength (Chen et al., 2017).

Several experiments have been conducted to analyze the effect of each component on the overall performance. **Table 1**

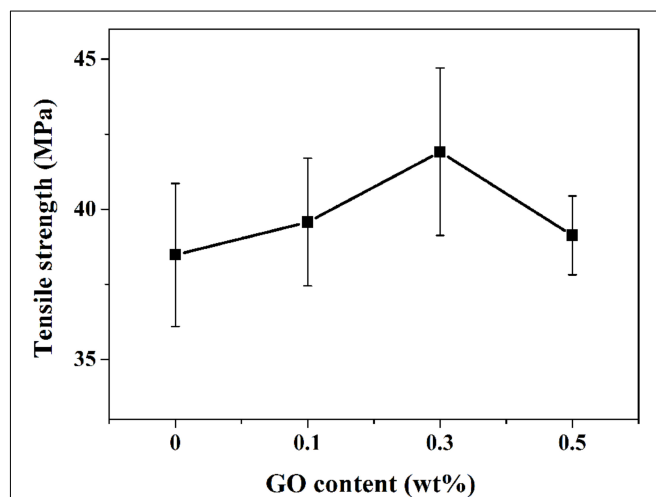
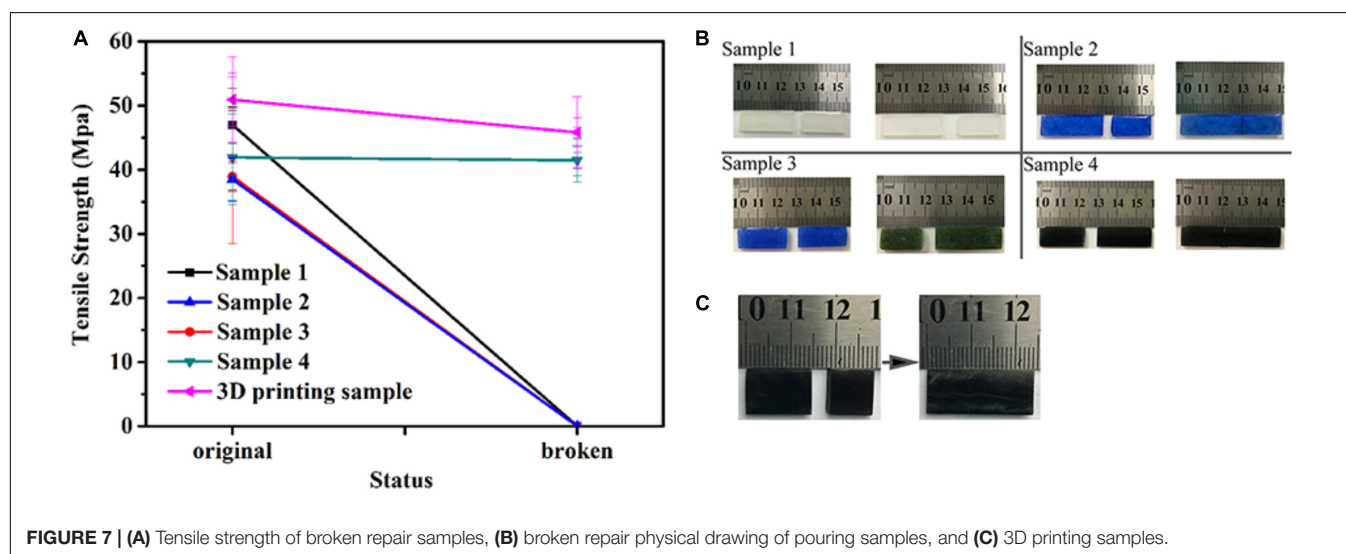
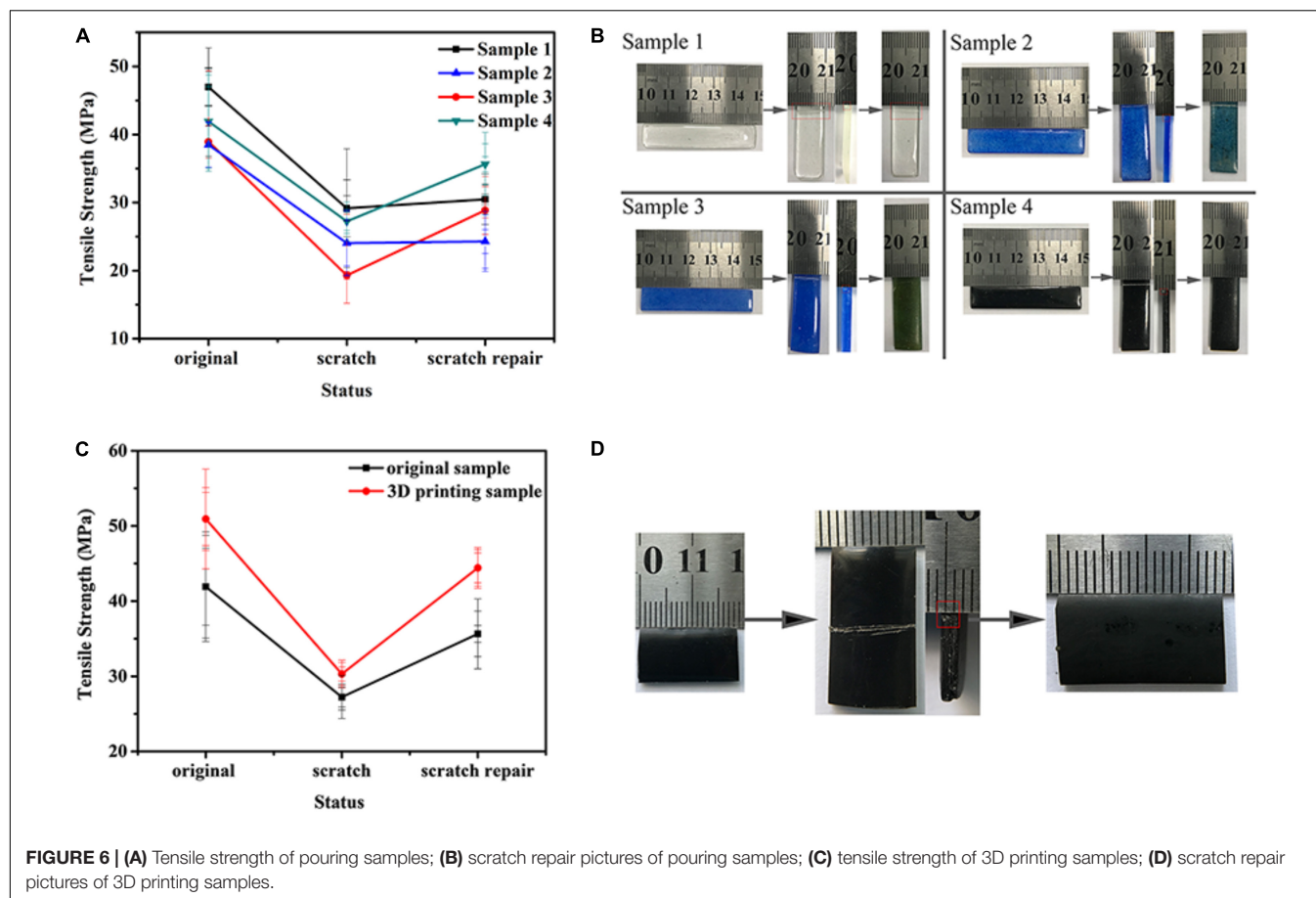


FIGURE 5 | Tensile curves of different GO content.



shows four kinds of samples with different compositions. Their corresponding repair experiment and tensile strength are shown in **Figure 6**. According to **Figure 6A**, samples without added microcapsules cannot achieve a self-healing effect. It indicates that microcapsules are the necessary healing units in the self-healing system. While the microcapsules were incorporated

into the epoxy oxide matrix (sample 3), the tensile strength increased to 0.45 MPa compared with that of sample 2, demonstrating that a small portion of the stress was dispersed, along with the shells of the microcapsules and the epoxy oxide matrix, resulting in an increase in the tensile strength. The tensile strength of GO-modified samples (sample 4) can restore

to 85.04%, while the sample 3 without GO-modified samples only restores to 63.07%. This demonstrates that GO as a toughening phase can improve to some extent the reduction of the tensile strength of the samples due to the lower continuity of the epoxy oxide matrix, which is caused by the incorporation of microcapsules and latent-curing agents $\text{Cu}(\text{MI})_4\text{Br}_2$. The stress diffused in the network structure, which was composed of GO and epoxy oxide matrix, which required higher stress to fracture the sample, and the tensile stress increased. The tensile strength curves and the scratch repair pictures of 3D printing samples are shown in **Figures 6C,D**. After 3D printing, the tensile strength of the sample is 21.51% higher than the pouring sample 4. After repair, the tensile strength of 3D printing sample can be restored to 87.23%, which is higher than that of the pouring sample at 85.04%. Because the potential difference inside the epoxy oxide is smaller than the gravitational force between the microcapsules, the little number of microcapsules coalesces and sinks. Nevertheless, the 3D printed samples were printed directly layer by layer, with a thickness of 500 μm , and cured by heating while printing. This minimized the settling of the microcapsules, and the dispersion of each component in the epoxy oxide was higher in the 3D printed samples compared with the pouring samples, which showed the macroscopic improvement of tensile strength.

At the same time, we also text the extreme situation of the sample. The tensile strength of the broken and repair of samples are given in **Figure 7**. The pouring samples 1, 2, and 3 cannot repair the broken, but sample 4 and 3D printing sample can repair the broken. After repair, the tensile strength of sample 4 can be recovered to 98.90%, and the tensile strength of 3D printing sample can be recovered to 89.97%. Unlike scratch repair, the broken repair efficiency of Sample 4 was higher than 3D-printed samples. It can be explained that, because the internal potential difference of epoxy oxide is less than the gravitational force between microcapsules, a small number of microcapsules coalesce and sink, which makes the dispersion of microcapsules uneven and epoxy oxide flow from the broken microcapsules to gather in these sinking parts. The repair efficiency of the pouring sample was increased to 98.90% because the two sections of the fracture overlapped together at both ends under the external force, while the epoxy oxide overflowing from the aggregated microcapsules deposited at the bottom of the sample was squeezed and spread in all directions, causing the non-uniformity of the repair (the repair efficiency of the upper part of the sample was lower than that of the lower part). The 3D-printed sample had the maximum repair efficiency of 89.97% because the repair area was only around the broken microcapsules due to a less settling phenomenon.

CONCLUSION

In summary, we report an approach to develop a GO-modified microcapsule self-healing system for 4D printing.

The measurement of SEM showed that the epoxy oxide microcapsules, as the healing unit, have a smooth surface, uniform particle size at 10–12 μm , and 0.70–1.5 μm microcapsule shell thickness. The thermodynamic measurement indicated that the thermal decomposition temperature of the prepared microcapsule is 316°C, which can largely protect the epoxy oxide inside the microcapsules from decomposition under high temperature. The tensile measurement has shown that the tensile strength of the 3D printing sample modified by GO was 21.51% more than the pouring sample, reaching to 50.93 MPa. Physical restoration experiments have proved that scratch repair efficiency comes up to 87.23% and broken repair efficiency carries to 89.97%. The incorporation of 10 wt% microcapsules can improve the tensile strength of the samples, which is attributed to the dispersion of stress between the microcapsule shell and the epoxy oxide matrix. The incorporation of a 0.3 wt% (based on epoxy oxide) GO further increased the mechanical strength of the sample, which is facilitated by chemical bonding between GO and $\text{Cu}(\text{MI})_4\text{Br}_2$ /microcapsule/epoxy oxide segments and the immense modulus difference between GO and epoxy oxide. This GO-modified microcapsule self-healing system holds great potential in the field of engineering, surface protection, and electronic packaging.

DATA AVAILABILITY STATEMENT

The original contributions presented in the study are included in the article/**Supplementary Material**, further inquiries can be directed to the corresponding author/s.

AUTHOR CONTRIBUTIONS

BM performed the main experimental work and characterization. YZ helped with tensile strength testing. YW and ML assisted with relevant experiments and characterization. DL conducted instructional work for this experiment. All authors contributed to the article and approved the submitted version.

FUNDING

This work was supported by the National Natural Science Foundation of China (Nos. 51627805 and U19A2085), the Optical Valley Science Research Project, WEHDZ (No. 2019001).

SUPPLEMENTARY MATERIAL

The Supplementary Material for this article can be found online at: <https://www.frontiersin.org/articles/10.3389/fmats.2021.657777/full#supplementary-material>

REFERENCES

- Akhan, S., Oktay, B., Özdemir, O. K., Madakbaş, S., and Kayaman Apohan, N. (2020). Polyurethane graphene nanocomposites with self-healing properties by azide-alkyne click reaction. *Mater. Chem. Phys.* 254:123315. doi: 10.1016/j.matchemphys.2020.123315
- Aronsson, C., Jury, M., Naeimipour, S., Boroojeni, F. R., Christofferson, J., Lifwergren, P., et al. (2020). Dynamic peptide-folding mediated biofunctionalization and modulation of hydrogels for 4D bioprinting. *Biofabrication* 12:035031. doi: 10.1088/1758-5090/ab9490
- Chen, B., Tang, J., Zhang, G., Chen, S., and Zhang, J. (2017). Properties and morphologies of epoxy resin based composites reinforced by polyurethane and graphene Oxide. *Mater. Trans.* 58, 842–844. doi: 10.2320/matertrans.M2016464
- Chen, L., Li, W., Liu, Y., and Leng, J. (2016). Nanocomposites of epoxy-based shape memory polymer and thermally reduced graphite oxide: mechanical, thermal and shape memory characterizations. *Compos. Part B Eng.* 91, 75–82. doi: 10.1016/j.compositesb.2016.01.019
- Cheng, C.-Y., Xie, H., Xu, Z.-Y., Li, L., Jiang, M.-N., Tang, L., et al. (2020). 4D printing of shape memory aliphatic copolyester via UV-assisted FDM strategy for medical protective devices. *Chem. Eng. J.* 396:125242. doi: 10.1016/j.cej.2020.125242
- Correa, D., Poppinga, S., Mylo, M. D., Westermeier, A. S., Bruchmann, B., Menges, A., et al. (2020). 4D pine scale: biomimetic 4D printed autonomous scale and flap structures capable of multi-phase movement. *Philos. Trans. A Math. Phys. Eng. Sci.* 378:20190445. doi: 10.1098/rsta.2019.0445
- Enriquez-Cabrera, A., Rapakousiou, A., Piedrahita Bello, M., Molnár, G., Salmon, L., and Bousseksou, A. (2020). Spin crossover polymer composites, polymers and related soft materials. *Coord. Chem. Rev.* 419:213396. doi: 10.1016/j.ccr.2020.213396
- Farooq, U., Teuwen, J., and Dransfeld, C. (2020). Toughening of epoxy systems with interpenetrating polymer network (IPN): a review. *Polymers* 12:1908. doi: 10.3390/polym12091908
- Gao, X., Yan, R., Lv, Y., Ma, H., and Ma, H. (2020). In situ pretreatment and self-healing smart anti-corrosion coating prepared through eco-friendly water-base epoxy resin combined with non-toxic chelating agents decorated biomass porous carbon. *J. Clean. Prod.* 266:121920. doi: 10.1016/j.jclepro.2020.121920
- Gholipour-Mahmoudalilou, M., Roghani-Mamaqani, H., Azimi, R., and Abdollahi, A. (2018). Preparation of hyperbranched poly (amidoamine)-grafted graphene nanolayers as a composite and curing agent for epoxy resin. *Appl. Surface Sci.* 428, 1061–1069. doi: 10.1016/j.apsusc.2017.09.237
- Haddadi, S. A., Ramazani, S. A. A., Mahdavian, M., Taheri, P., Mol, J. M. C., and Gonzalez-Garcia, Y. (2019). Self-healing epoxy nanocomposite coatings based on dual-encapsulation of nano-carbon hollow spheres with film-forming resin and curing agent. *Compos. Part B Eng.* 175:107087. doi: 10.1016/j.compositesb.2019.107087
- Jang, J. W., Park, J. H., Kim, I. J., Sim, J. H., Yu, S. G., Lee, D. J., et al. (2020). Preparation and characterization of thermoresponsive poly(N-isopropylacrylamide-co-N-isopropylmethacrylamide) hydrogel materials for smart windows. *J. Appl. Polym. Sci.* 138:49788. doi: 10.1002/app.49788
- Javadi, M., and Haleem, A. (2020). Significant advancements of 4D printing in the field of orthopaedics. *J. Clin. Orthop. Trauma* 11(Suppl. 4), S485–S490. doi: 10.1016/j.jcot.2020.04.021
- Keller, M. W., White, S. R., and Sottos, N. R. (2007). A self-healing poly(Dimethyl Siloxane) elastomer. *Adv. Funct. Mater.* 17, 2399–2404. doi: 10.1002/adfm.200700086
- Khan, F., Khan, M. S., Kamal, S., Arshad, M., Ahmad, S. I., and Nami, S. A. A. (2020). Recent advances in graphene oxide and reduced graphene oxide based nanocomposites for the photodegradation of dyes. *J. Mater. Chem. C* 8, 15940–15955. doi: 10.1039/d0tc03684f
- Kim, S. H., Seo, Y. B., Yeon, Y. K., Lee, Y. J., Park, H. S., Sultan, M. T., et al. (2020). 4D-bioprinted silk hydrogels for tissue engineering. *Biomaterials* 260:120281. doi: 10.1016/j.biomaterials.2020.120281
- Li, H., Chen, S., Li, Z., Feng, Y., and Zhang, M. (2020). Preparation of PU/GO hybrid wall microcapsules and their self-lubricating properties for epoxy composites. *Colloids Surf. A Physicochem. Eng. Asp.* 596:124729. doi: 10.1016/j.colsurfa.2020.124729
- Li, J., Li, Z., Feng, Q., Qiu, H., Yang, G., Zheng, S., et al. (2019). Encapsulation of linseed oil in graphene oxide shells for preparation of self-healing composite coatings. *Prog. Org. Coat.* 129, 285–291. doi: 10.1016/j.porgcoat.2019.01.024
- Li, X., Yu, R., He, Y., Zhang, Y., Yang, X., Zhao, X., et al. (2020). Four-dimensional printing of shape memory polyurethanes with high strength and recyclability based on Diels-Alder chemistry. *Polymer* 200:122532. doi: 10.1016/j.polymer.2020.122532
- Lin, C., Liu, L., Liu, Y., and Leng, J. (2021). 4D printing of bioinspired absorbable left atrial appendage occluders: a proof-of-concept study. *ACS Appl. Mater. Interfaces* 13, 12668–12678. doi: 10.1021/acsami.0c17192
- Ma, Y., Zhang, Y., Liu, J., Ge, Y., Yan, X., Sun, Y., et al. (2020). GO-modified double-walled polyurea microcapsules/epoxy composites for marine anticorrosive self-healing coating. *Mater. Des.* 189:108547. doi: 10.1016/j.matdes.2020.108547
- Pilawka, R., and Maka, H. (2011). Epoxy adhesive formulations using latent imidazole metal cation complexes. *Pol. J. Chem. Technol.* 13, 63–66.
- Seidi, F., Jouyandeh, M., Taghizadeh, M., Taghizadeh, A., Vahabi, H., Habibzadeh, S., et al. (2020). Metal-organic framework (MOF)/Epoxy coatings: a review. *Materials* 13:2881. doi: 10.3390/ma13122881
- Shiblee, M. D. N. I., Ahmed, K., Kawakami, M., and Furukawa, H. (2019). 4D printing of shape-memory hydrogels for soft-robotic functions. *Adv. Mater. Technol.* 4:1900071. doi: 10.1002/admt.201900071
- Tan, L. J., Zhu, W., and Zhou, K. (2020). Recent progress on polymer materials for additive manufacturing. *Adv. Funct. Mater.* 30:2003062. doi: 10.1002/adfm.202003062
- Tripathi, M., Dwivedi, R., Kumar, D., and Roy, P. K. (2015). Thermal activation of mendable epoxy through inclusion of microcapsules and imidazole complexes. *Polym. Plast. Technol. Eng.* 55, 129–137. doi: 10.1080/03602559.2015.1070866
- Wei, H., Zhang, Q., Yao, Y., Liu, L., Liu, Y., and Leng, J. (2017). Direct-write fabrication of 4D active shape-changing structures based on a shape memory polymer and its nanocomposite. *ACS Appl. Mater. Interfaces* 9, 876–883. doi: 10.1021/acsami.6b12824
- Wu, H., Chen, P., Yan, C., Cai, C., and Shi, Y. (2019). Four-dimensional printing of a novel acrylate-based shape memory polymer using digital light processing. *Mater. Des.* 171:107704. doi: 10.1016/j.matdes.2019.107704
- Xia, S., Liu, Y., Pei, F., Zhang, L., Gao, Q., Zou, W., et al. (2015). Identical steady tribological performance of graphene-oxide-strengthened polyurethane/epoxy interpenetrating polymer networks derived from graphene nanosheet. *Polymer* 64, 62–68. doi: 10.1016/j.polymer.2015.03.036
- Xie, W., Huang, S., Tang, D., Liu, S., and Zhao, J. (2020). Synthesis of a furfural-based DOPD-containing co-curing agent for fire-safe epoxy resins. *RSC Adv.* 10, 1956–1965. doi: 10.1039/c9ra06425g
- Ye, X. J., Song, Y. X., Zhu, Y., Yang, G. C., Rong, M. Z., and Zhang, M. Q. (2014). Self-healing epoxy with ultrafast and heat-resistant healing system processable at elevated temperature. *Compos. Sci. Technol.* 104, 40–46. doi: 10.1016/j.compscitech.2014.08.028
- Yu, Z., Wang, Z., Li, H., Teng, J., and Xu, L. (2019). Shape memory epoxy polymer (SMEP) composite mechanical properties enhanced by introducing graphene oxide (GO) into the matrix. *Materials* 12:1107. doi: 10.3390/ma12071107
- Yuan, L., Sun, T., Hu, H., Yuan, S., Yang, Y., Wang, R., et al. (2019). Preparation and characterization of microencapsulated ethylenediamine with epoxy resin for self-healing composites. *Sci. Rep.* 9:18834. doi: 10.1038/s41598-019-55268-7
- Zhao, L., Yang, X., Ma, L., and Li, Q. (2020). Preparation of imidazole embedded polyurea microcapsule for latent curing agent. *J. Appl. Polym. Sci.* 137:49340. doi: 10.1002/app.49340
- Zhou, J., Zhao, J., Li, H., Cui, Y., and Li, X. (2020). Enhanced thermal properties for nanoencapsulated phase change materials with functionalized graphene oxide

- (FGO) modified PMMA. *Nanotechnology* 31:295704. doi: 10.1088/1361-6528/ab898b
- Zhou, Y., Li, C., Wu, H., and Guo, S. (2020). Construction of hybrid graphene oxide/graphene nanoplates shell in paraffin microencapsulated phase change materials to improve thermal conductivity for thermal energy storage. *Colloids Surfaces A Physicochem. Eng. Asp.* 597:124780. doi: 10.1016/j.colsurfa.2020.124780
- Zhu, D. Y., Rong, M. Z., and Zhang, M. Q. (2015). Self-healing polymeric materials based on microencapsulated healing agents: from design to preparation. *Prog. Polym. Sci.* 4, 175–220. doi: 10.1016/j.progpolymsci.2015.07.002

Conflict of Interest: The authors declare that the research was conducted in the absence of any commercial or financial relationships that could be construed as a potential conflict of interest.

Copyright © 2021 Ma, Zhang, Wei, Li and Li. This is an open-access article distributed under the terms of the Creative Commons Attribution License (CC BY). The use, distribution or reproduction in other forums is permitted, provided the original author(s) and the copyright owner(s) are credited and that the original publication in this journal is cited, in accordance with accepted academic practice. No use, distribution or reproduction is permitted which does not comply with these terms.



4D Printing Pre-Strained Structures for Fast Thermal Actuation

Yu Zou, Zhongyi Huang, Xiyang Li and Pengyu Lv*

State Key Laboratory for Turbulence and Complex Systems, Department of Mechanics and Engineering Science, BIC-ESAT, College of Engineering, Peking University, Beijing, China

OPEN ACCESS

Edited by:

Yusheng Shi,
Huazhong University of Science
and Technology, China

Reviewed by:

Feng Chen,
Zhejiang University of Technology,
China
Xingzhe Wang,
Lanzhou University, China

*Correspondence:

Pengyu Lv
lvpy@pku.edu.cn

Specialty section:

This article was submitted to
Smart Materials,
a section of the journal
Frontiers in Materials

Received: 31 January 2021

Accepted: 31 March 2021

Published: 20 April 2021

Citation:

Zou Y, Huang Z, Li X and Lv P
(2021) 4D Printing Pre-Strained
Structures for Fast Thermal Actuation.
Front. Mater. 8:661999.
doi: 10.3389/fmats.2021.661999

Four-dimensional (4D) printing is an emerging technology by adding the dimension of time-dependent reconfiguration into 3D printing. It enables the 3D printed structure to change the shape, property, or functionality under external stimuli such as temperature, magnetic field, and light, etc. Among the existing 4D printed structures, thermal responsive structures are widely used for their easy operation. However, the slow actuation of the thermal responsive structures impedes the applications like soft robotics. In the current work, a pre-strained strategy is proposed to accelerate the actuation of thermal responsive structures. A 4D printing platform that can apply strain during the printing process is constructed to fabricate the pre-strained structures under the aid of in-situ tensile of the printing base. A bilayer structure with one pre-strained layer and the other non-pre-strained layer is integrally printed. Through experiments and the finite element analysis, it is demonstrated that the aspect ratio has little effect on the deformation of the bilayer structure, whereas the pre-strain plays a key role in the deformation and also greatly accelerates the actuation of the bilayer structure. Based on the 4D printed pre-strained bilayer structure, an energy-free gripper is fabricated and a fully soft crawler is printed to achieve a high running speed.

Keywords: 4D printing, pre-strain, bilayer structure, thermal response, fast actuation

INTRODUCTION

3D printing is a widely used additive manufacturing technology that can embody objects from digital 3D models rapidly and inexpensively in contrast to traditional manufacturing techniques. By combining with smart materials, 3D printing is further extended to 4D printing with the addition of time-dependent response to external stimuli. 4D printing enables the printed structure to change its shape, property, and functionality under the external stimuli such as temperature (Ambulo et al., 2017; Ding et al., 2017; Kotikian et al., 2018), magnetic field (Kim et al., 2018, 2019; Zhu et al., 2018), light (Kuksenok and Balazs, 2016; Leist and Zhou, 2016; Yang et al., 2017), and pH (Nadgorny et al., 2016), etc. In view of the characteristics of shape morphing, applications of the 4D printed structure can be extended to diverse areas such as soft robotics (Kim et al., 2018, 2019; Kotikian et al., 2018; Yang et al., 2018; Zhu et al., 2018), origami (Ge et al., 2014; Liu et al., 2018; Teoh et al., 2018), biomedical device (Morrison et al., 2015; Gao et al., 2016; Zarek et al., 2017; Lin et al., 2020), tissue engineering (Villar et al., 2013; Li et al., 2016; Gill et al., 2018), and metamaterials (Xin et al., 2020), etc.

In consideration of the simplicity of operation and the applicability, the thermal responsive structure is one of the most widely used 4D printed structures. For example, the thermal responsive

hydrogel is used to realize programmable deformation of the soft sheet by patterning chemically distinct, fiber-like regions that exhibit different shrinkage and modulus under the external stimulus (Wu et al., 2013). Similarly, Naficy et al. (2017) print composite hydrogel structures which is capable of reversible deformation under the stimulus of hydration and temperature. Ge et al. (2013) fabricate thermal responsive 4D printed structure by printing shape memory polymer fibers in an elastomeric matrix. Although widely used in 4D printing, thermal responsive structures (Le Duigou et al., 2019; Nishiguchi et al., 2020) have a major problem in slow actuation resulting from the low heat conduction rate of the structures, especially the cooling rate.

In order to enhance the actuation rate of the thermal responsive structure, methods have been proposed. For example, Bartlett et al. (2017) increase the thermal conductivity by incorporating liquid metal microdroplets into the elastomer. Ze et al. (2020) report a novel magnetic shape memory polymer composite (M-SMP) that is softened by heating and actuated by a magnetic field. Based on this M-SMP, the structures can achieve faster actuation than conventional SMP-base structures (Ze et al., 2020). In spite of the current strategies for fast actuation of thermal responsive structure, there is still a long way to develop a simple and effective method to increase actuation speed of the thermal responsive structure.

Because the transmission rate of force is faster than the thermal conduction rate, it is an effective method to increase the actuation speed of the structure by combining mechanical response and thermal response. In this work, we construct a pre-strained 4D printing platform and propose a pre-strained strategy for fast actuation of 4D printed bilayer structures. Through experiments and finite element analysis (FEA), it is demonstrated that the aspect ratio has little effect on the deformation of the bilayer structure, whereas the pre-strain greatly affects the deformation and greatly increase the actuation speed of the thermal responsive structure. Based on this simple and effective strategy, we have designed a soft energy-free gripper with high responsive capacity and a soft crawler with a larger locomotion step and high speed. The current work provides a new solution based on pre-strain to increase the thermal actuation speed of 4D printed structures, which has a wide range of applications such as soft robotics with high locomotion speed, grippers with high responsive capacity and so on.

EXPERIMENTAL SETUP

Materials and Fabrication

A bilayer structure with one pre-strained layer (i.e., the thermal responsive layer) and the other non-pre-strained layer is integrally printed. For the fabrication of the thermal responsive layer, the precursors of Ecoflex™ 00-35, Part A and Part B (Smooth-On, Inc.) were first mixed with ethanol (98%) in a volume ratio of 4:1, respectively. The well-mixed precursors of Ecoflex™ 00-35, Part A and Part B were blended in a volume ratio of 1:1 for 4 min. Then, the mixture was poured into a mold and cured at room temperature for 5 min to obtain the ethanol-silicon composite. For the fabrication of the non-pre-strained

layer, the base and curing agent of PDMS (polydimethylsiloxane, Dow Corning 184) were mingled in a mass ratio of 10:1. Then, the mixture was poured into a syringe and degassed for printing.

4D Printing Platform With Pre-Strain Stage

As shown in **Figure 1A**, the pre-strained 4D printing platform includes a 3D movement platform for spatial printing, and a clamping device fixed on a precision displacement table (**Figure 1B**) for applying the pre-strain. To show the printing capability of this pre-strained 4D printing platform, a bilayer structure consisting of a pre-strained bottom layer and a non-pre-strained top layer was printed. On the one hand, the bottom layer was made from the ethanol-silicon composite that is relatively soft (Young's modulus is 52 kPa) and can perform isotropic deformation under the thermal stimulation (Li et al., 2020). On the other hand, the top layer was fabricated with PDMS that is relatively stiff (Young's modulus is 2 MPa) and exhibits almost no expansion compared with the bottom layer fabricated of ethanol-silicon composite under the thermal stimulation (Schneider et al., 2009; Müller et al., 2019). Between the layers, resistance wire was embedded to provide the thermal stimulation. During printing as shown in **Figure 1C**, the bottom layer was stretched by the clamping device and served as the substrate for the printing of the top PDMS layer. Then, the resistance wire with a diameter of 0.15 mm was fixed by surface adhesion on the pre-stretched substrate and patterned into a zigzag line in order to increase the heating efficiency and reduce the impact on the deformation of the bilayer structure. Finally, the well-mixed PDMS precursor was squeezed out of the nozzle and heated at the nozzle by the resistance wire closely twisting around the nozzle (Hardin et al., 2015; Ober et al., 2015). 3 W was applied to the resistance wire of the nozzle to heat the PDMS precursor. After printing, the heated PDMS was cured at room temperature for 4 h.

Actuation Method

The printed bilayer structure is actuated by heating and cooling of the resistance wire embedded in the bilayer structure through a DC power. The DC power supply is connected to the resistance wire through the copper wires. The heating speed is regulated by the power. Increasing the current power will enhance the heating speed. The power is directly set to and remains 7 W for all the following experiments. The heated bilayer structure is cooled due to the natural heat dissipation after cutting off the power supply. The cooling rate depends on the thermal conductivity of the printed materials and the temperature difference, which is constant in our experiments.

DEFORMATION OF THE PRE-STRAINED BILAYERS

After 3D printing and releasing the pre-stretched substrate, the bilayer structure bends towards to bottom pre-stained layer. We denote the initial curvature as positive and the inverse bending curvature as negative. When the thermal stimulus is applied, the bottom layer begins to expand. As the temperature increase, the

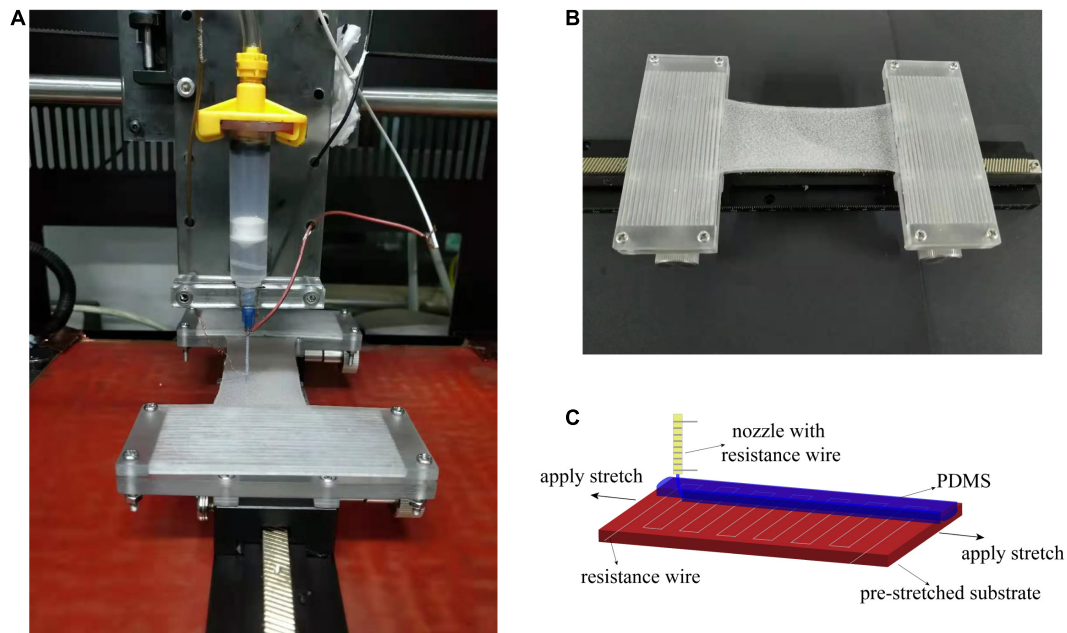


FIGURE 1 | Pre-strained 4D printing platform. **(A)** 3D movement platform for spatial printing. **(B)** The clamping device. **(C)** Schematic of the 4D printing with a pre-strain stage.

expansion of the bottom layer reaches the maximum swelling rate at the boiling point of ethanol, i.e., 78°C and finally reaches the maximum deformation at 95°C (Li et al., 2020). As shown in **Figure 2**, the slender and wide bilayer structure both bend towards to bottom layer for the pre-strain at the beginning. With the thermal stimulus applied, the bottom pre-strained layer made from the ethanol-silicon composite begins to expand while the top layer made from PDMS exhibits almost no expansion. For the expansion of the bottom layer, the mismatch strain between two layers as well as the curvature gradually decreases to zero. With further expansion of the bottom layer, the opposite mismatch strain between two layers appears, the bilayer structure bends upwards and the curvature becomes negative. Besides, the slender pre-strained bilayer structure whose width is much smaller than its length can be regarded as a beam and thus we can neglect the deformation in the width direction. For the wide pre-strained bilayer structure whose deformation in the width direction cannot be neglected, as the temperature increases, the curvature in the short-axis direction decreases, and the curvature in the long-axis direction increases. This phenomenon attributes to the isotropic expansion of the ethanol-silicon composite during the thermal stimulation. Combined with the powerful manufacturing capabilities of 3D printing, more pre-stretched structures have been fabricated (see details in **Supplementary Figure 1**).

To explore the deformation of a slender pre-strained bilayer structure, the effect of aspect ratio (length/width) and pre-strain on the deformation is experimentally investigated. **Figure 3** show the variation in the average curvature of the slender pre-strained bilayer structure as a function of the heating power of resistance wire. All the data in **Figure 3** represent the deformation of

pre-strained bilayer structures with the width of 1 cm, and the thicknesses of the top and the bottom layers of 2 mm and 3 mm, respectively. **Figure 3A** shows the effect of the aspect ratio by changing the length of the bilayer structure from 3 cm to 4 cm and 5 cm under a constant pre-strain of 60%. **Figure 3B** shows the effect of the pre-strain by changing the pre-strain of the bottom layer from 40% to 60% and 80% under a constant structure length of 3 cm. The experimental data in **Figure 3** reflect that the average curvature decreases monotonically and nonlinearly as the heating power increases. Besides, the aspect ratio has less effect on the average curvature, while the pre-strain has much influence on the deformation of slender pre-strained bilayer structure.

Given the pre-strain ε_0 , the curvature of the pre-strained bilayer structure κ can be predicted by the classical bi-strip model with the mismatch strain given by Timoshenko S.P (Timoshenko, 1925),

$$\kappa_{\text{Initial}} = \frac{6\varepsilon_0(1+m)^2}{h(1+\varepsilon_0)[3(1+m)^2 + (1+mn)(m^2 + \frac{1}{mn})]}, \quad (1)$$

where m and n are the thickness ratio and Young's modulus ratio between the non-pre-strained layer and the pre-strained layer, respectively (see details in **Supplementary Text**). The solid lines and filled dots in **Figure 4** show the initial average curvatures of the pre-strained bilayer structure as a function of the pre-strain obtained by theory and experiments. All the structures in **Figure 4** have the same size, i.e., the length of 3 cm, the width of 1 cm, the thickness of the top layer of 2 mm, and the thickness of the bottom layer

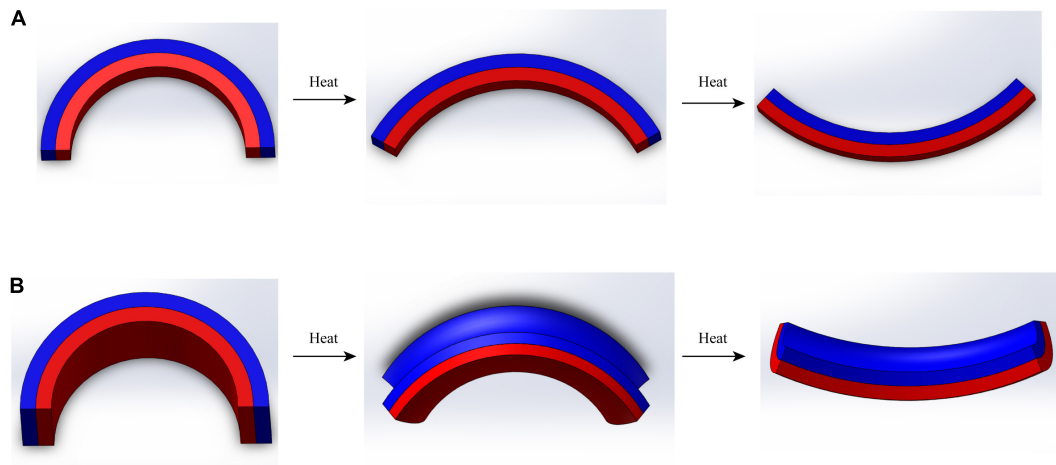


FIGURE 2 | Bi-directional deformation of pre-strained bilayer structure. Schematic of deformation of slender pre-strained bilayer structure **(A)** and of wide pre-strained bilayer structure **(B)**.

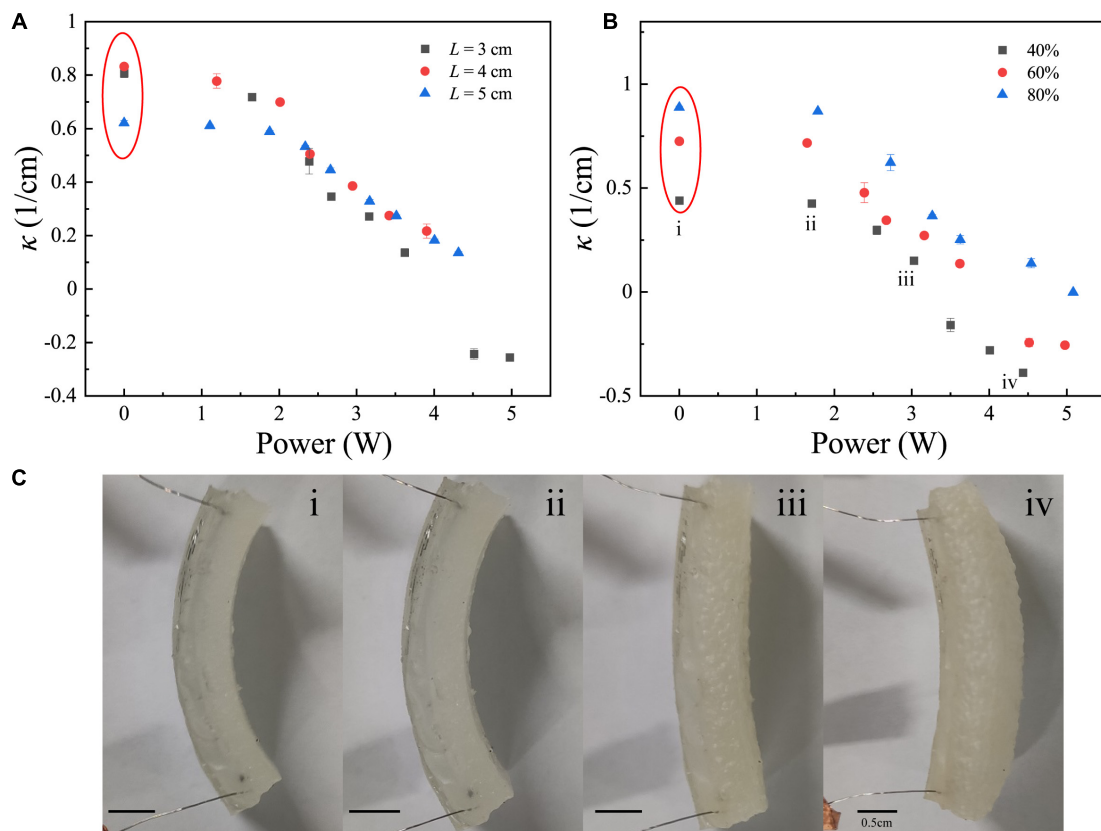


FIGURE 3 | Variation in the average curvature of the slender pre-strained bilayer structure. **(A)** Effect of the aspect ratio on the deformation under a constant pre-strain of 60%. **(B)** Effect of the pre-strain on the deformation under a constant structure length of 3 cm. **(C)** Deformation sequence as the thermal stimulus is applied to the bilayer structure with 40% pre-strain and 3-cm length.

of 3 mm. It is found that the data are in good agreement with the theoretical prediction when the pre-strain is smaller than 40%. When the pre-strain is greater than 40%, the experimentally measured values are slightly greater than the

theoretical prediction. This deviation originates from the hypothesis of the theory that the constitutive relation of the model is linear elastic, whereas the materials in the experiments are hyperelastic.

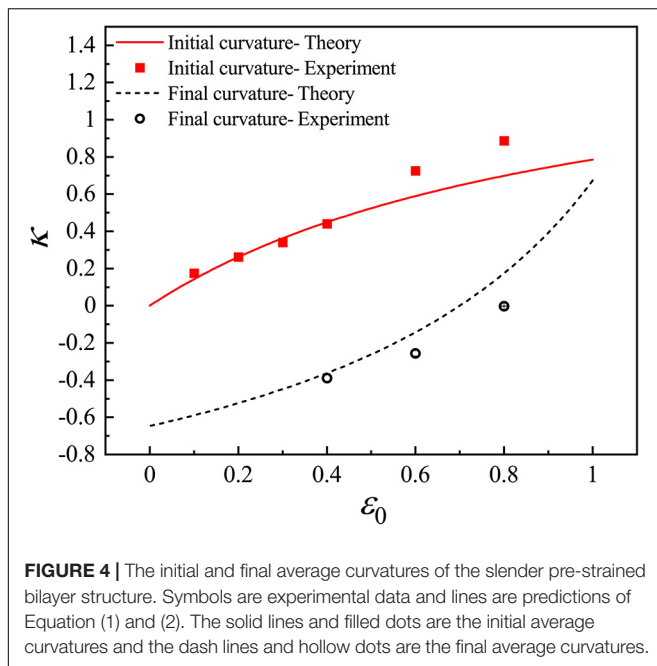


FIGURE 4 | The initial and final average curvatures of the slender pre-strained bilayer structure. Symbols are experimental data and lines are predictions of Equation (1) and (2). The solid lines and filled dots are the initial average curvatures and the dash lines and hollow dots are the final average curvatures.

The final curvatures of the pre-strained bilayer structures can be also predicted by the theory through introducing the maximum thermal expansion strain ε_{\max} of the pre-strained layer. The final curvature is

$$\kappa_{\text{Final}} = \frac{6(\varepsilon_0 - \varepsilon_{\max})(1 + m)^2}{h(1 + \varepsilon_0 - \varepsilon_{\max}) \left[3(1 + m)^2 (1 + mn) \left(m^2 + \frac{1}{mn} \right) \right]}, \quad (2)$$

The maximum thermal expansion strain of our structures is nearly 70% obtained by experiment. Dash lines and hollow dots in **Figure 4** show the final curvatures as a function of the pre-strain, which presents a good agreement between the experimental data and the theoretical prediction.

For the wide pre-strained bilayer structure, Finite Element Analysis (FEA) is conducted by COMSOL Multiphysics to explore the effect of size and pre-strain on the deformation. The moduli of the top and the bottom layers in the FEA model are set to 2 MPa and 52 kPa, respectively. The coefficients of thermal expansion of the top and the bottom layers are 0 and 0.0025, respectively. As the temperature increases from 20°C to 100°C, curvatures in two directions are analyzed for the wide pre-strained bilayer structure with the width of 2 cm as shown in **Figure 5**. For the cases of FEA simulation, three lengths of the bilayer structure (5 cm and 7 cm) are considered under a constant pre-strain of 20% and two pre-strains (10% and 20%) are considered under a constant length of 7 cm. As shown in **Figures 5A,B**, the curvature κ_1 decreases monotonically and the curvature κ_2 increases monotonically as the temperature increases. The curvature κ_1 and κ_2 increase notably as the pre-strain increases and are insensitive to the aspect ratio.

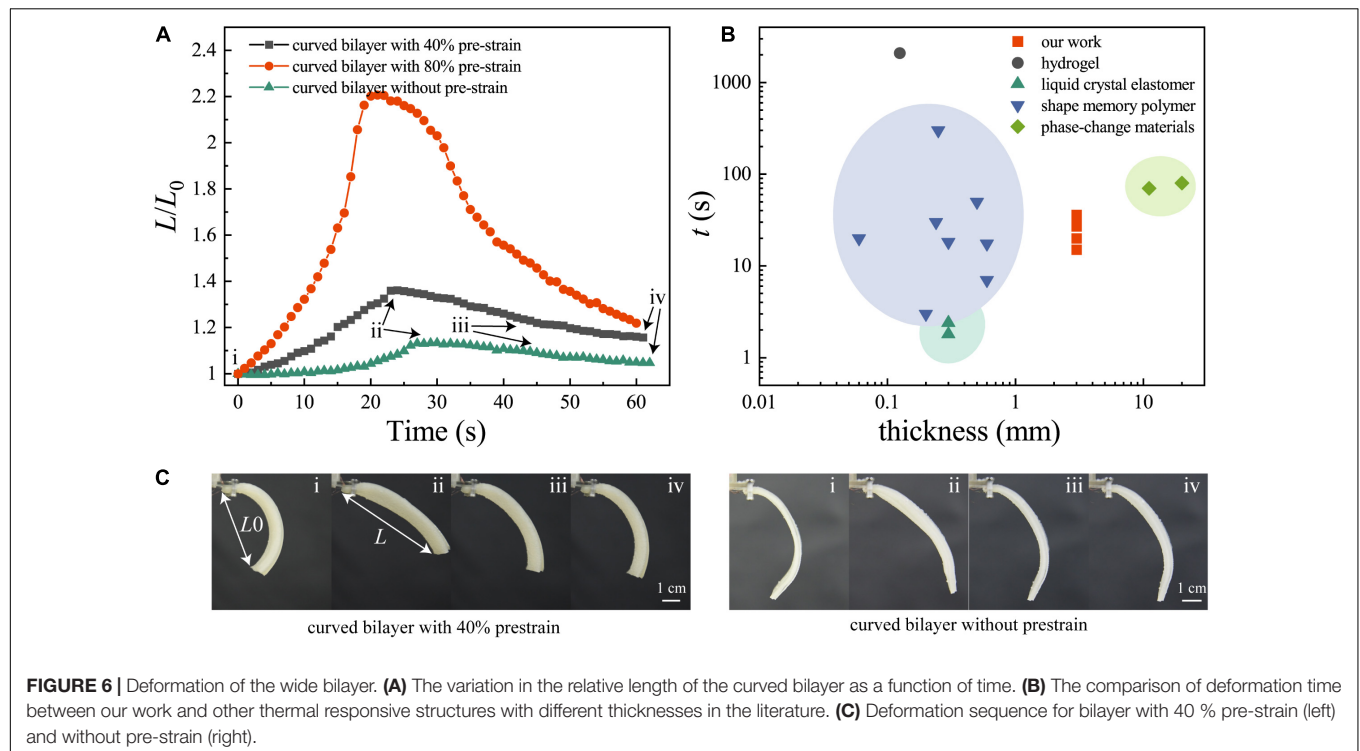
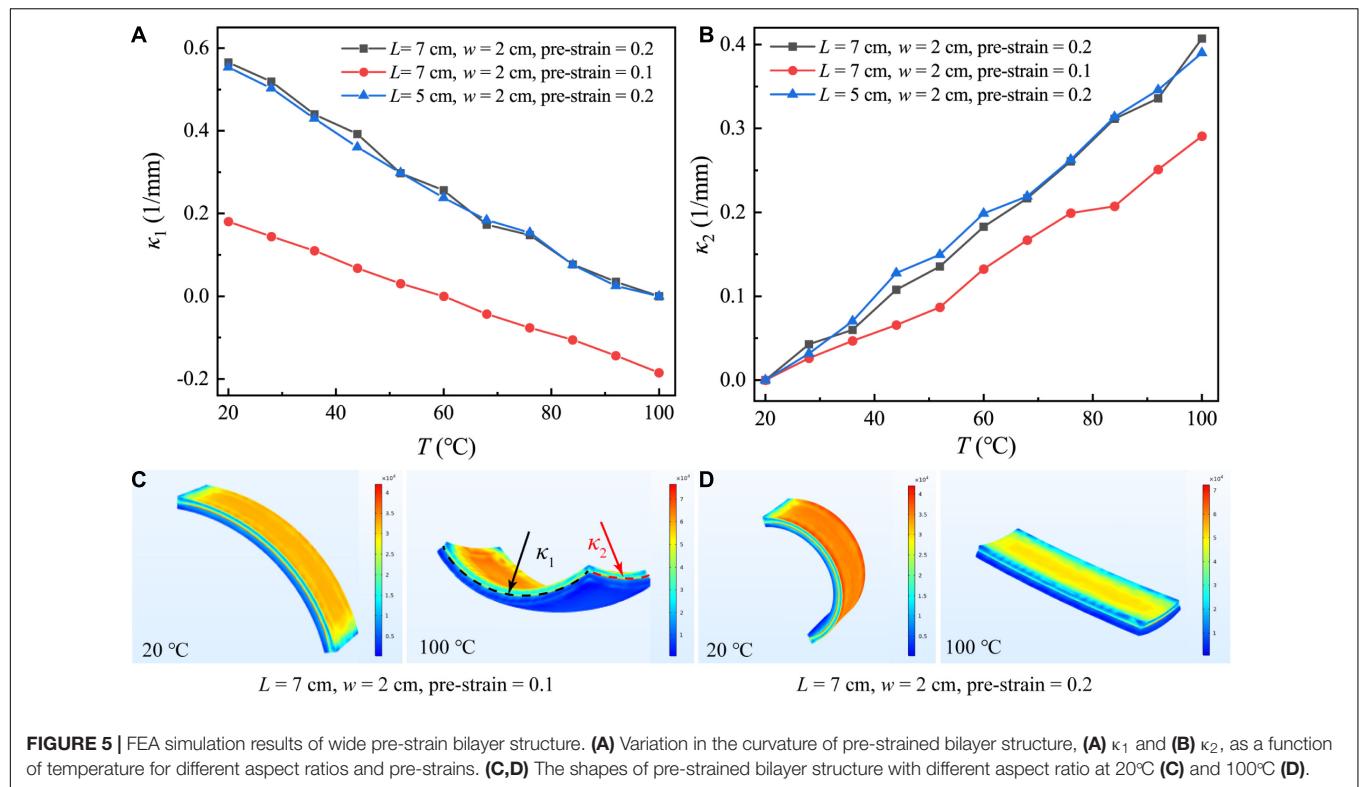
The effect of pre-strain on the deformation speed of wide curved bilayer structure is further explored. For the bilayer with

pre-strain, it bends when it is released at the beginning without heating. While for the bilayer without pre-strain, we curve it as a control group. The relative length (L/L_0) of the curved bilayer is selected as the variable to measure the deformation as shown in **Figure 6A**. The sizes and materials of all the bilayer structures are the same, i.e., the length of 7 cm, the width of 2 cm, top layer (PDMS) thickness of 1 mm, bottom layer (ethanol-silicon composite) thickness of 2 mm. The heating power is 7 W. As shown in **Figure 6A**, as the temperature increases, the relative length of the structure increases and finally reaches to maximum deformation. And then, as the temperature decreases by stopping heating, the relative length decreases. According to the variation rate of L/L_0 during the heating and cooling process, it is demonstrated that the bilayer structure with 80% pre-strain has the fastest deformation speed both upon heating and cooling. Besides, the deformation amplitude of curved bilayer with 80% pre-strain is the largest. In comparison, the bilayer without pre-strain performs smaller deformation and takes longer time. In **Figure 6B**, compared with other thermal responsive structures, the pre-strained bilayer structures present relatively fast deformation speed at centimeter scale (see **Supplementary Table 1**). Thus, the pre-strain can accelerate the actuation of the thermal responsive bilayer structure and provide a larger deformation amplitude.

APPLICATIONS OF PRE-STRAINED 4D PRINTING BILAYER STRUCTURE

In contrast to the slender bilayer structure, the wide bilayer structure has a larger contact area, which is more conducive for grip and crawling. Thus, based on the wide bilayer structure (the length of 7 cm, the width of 2 cm, the PDMS layer thickness of 1 mm, and the ethanol-silicon composite layer thickness of 2 mm), a soft energy-free gripper with high responsive capacity and a soft crawler with a larger locomotion step and high speed are designed and presented in the following.

The wide pre-strained bilayer structure is first used to design a fast and energy-free gripper. In **Figure 7**, four identical wide pre-strained bilayers with 40% pre-strain act as fingers to form a soft gripper. In the absence of thermal stimuli, the wide pre-strained bilayer bends inwards and the soft gripper is in a close “finger” configuration. It is worth noting that the resistance wire is only embedded in the upper half section of the bilayer, namely the heating region as shown in **Figure 7A**. Such a design ensures the end of the “finger” maintain its initial shapes during the heating process so that this soft gripper can capture the object more efficiently. Furthermore, since the heating region is away from the end of the “fingers,” the thermal stimuli has little effect on the object being held. By switching on and off the power supply, we can control the opening and closing of the gripper as shown in **Figure 7C**. Due to the pre-strain, our gripper can open or close the “fingers” quickly. It takes around 10 s to open the “fingers” as shown in **Figure 7A**. Furthermore, the energy-free gripper only needs energy to open the “fingers.” After the gripper capturing the target object, the gripper can hold the object by its pre-strain without extra energy



input. **Figures 7D,E** shows that the gripper can grasp a sphere with a weight of 40 g, and a plastic cup filled with water with a weight of 70 g that is 3.5 times the whole weight of the soft gripper.

We further design and fabricate a soft crawler by utilizing the wide pre-strain bilayer structure. The resistance wire embedded in the structure is connected to the thin copper wire that supplies power for thermal actuation and avoids the effect on

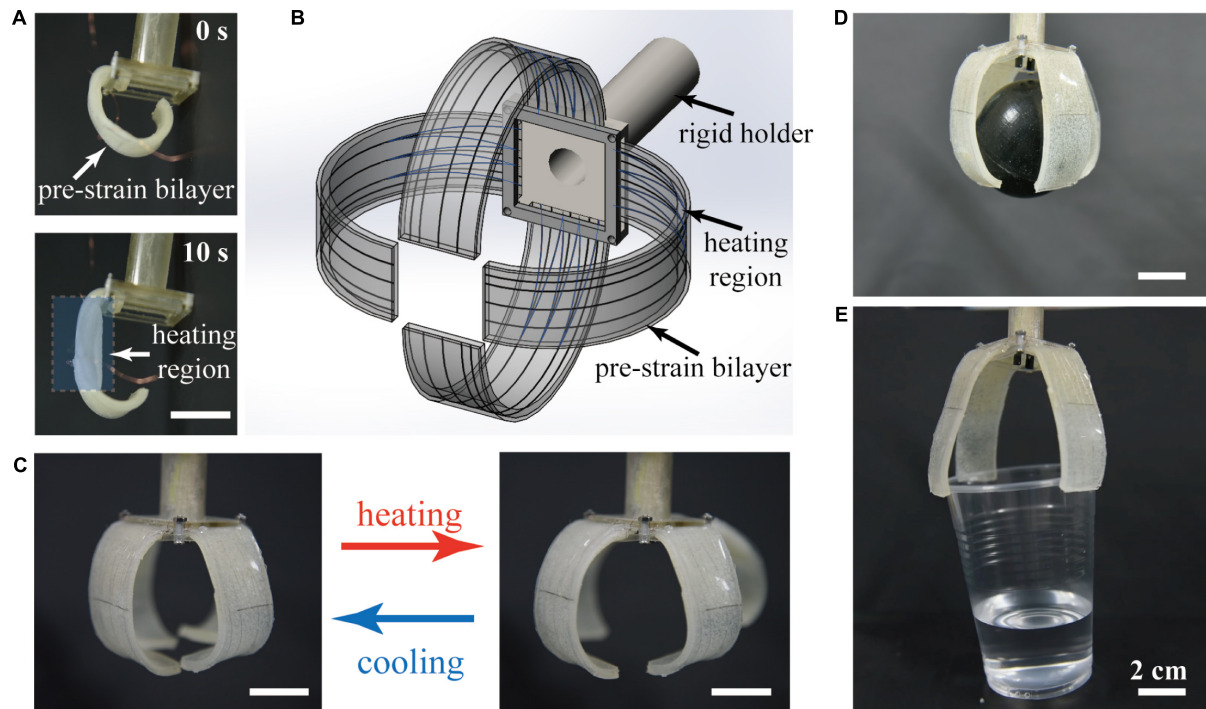


FIGURE 7 | Energy-free gripper based on 4D printing pre-strained bilayer. **(A)** Rapid deformation of pre-strained bilayer upon heating. **(B)** Schematic of pre-strained soft gripper composed of four identical pre-strained bilayers. **(C)** initial closed “fingers” open upon heating and closes upon cooling. **(D,E)** Demonstration of grasping of a sphere with a weight of 40 g, and a plastic cup filled with water with a weight of 70 g. The weight of the soft gripper is 20 g.

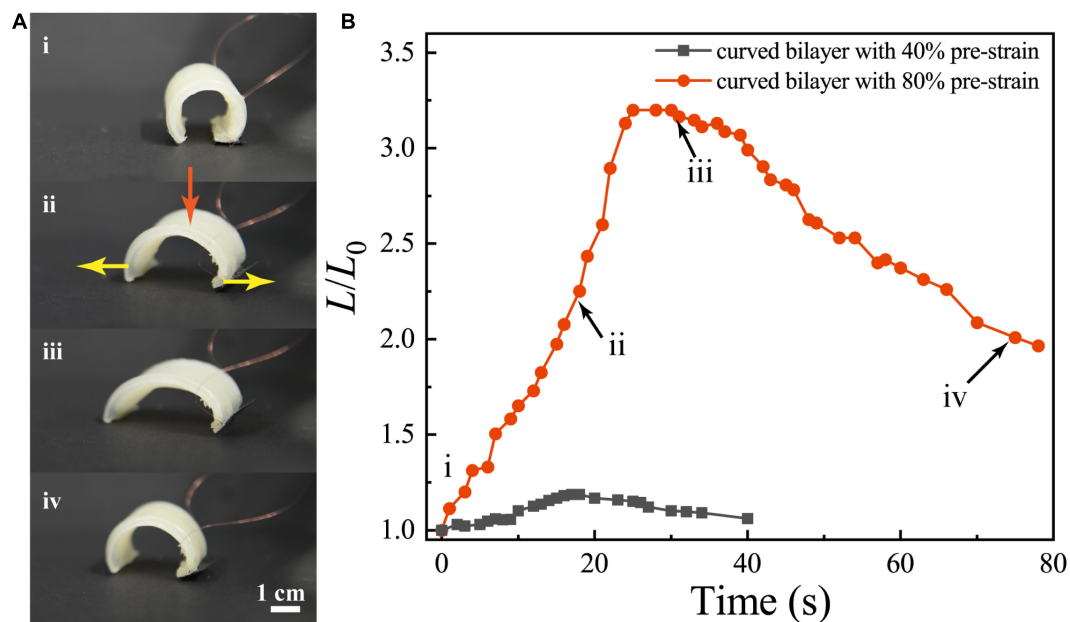


FIGURE 8 | Soft crawler based on 4D printing pre-strained bilayer. **(A)** Snapshot sequences for the crawler with 80 % pre-strain. **(B)** Deformation of the soft crawler as a function of time.

the locomotion of the crawler. To break the symmetry of the crawler and realize effective locomotion, two different flat sheets are attached to the end of the bilayer as shown in reference

(Li et al., 2020). **Figure 8A** shows the locomotion mechanism of the soft crawler. During the heating-cooling cycle, the soft crawler can move forward effectively (**Supplementary Movie 1**)

Figure 8B shows the relative length of the soft crawler with different pre-strain over time. It is experimentally demonstrated that the soft crawler with a larger pre-strain (80%) has a larger motion step and higher speed, i.e., 0.3 mm/s, which is faster than the thermal actuation soft crawler of the previous work (Li et al., 2020).

CONCLUSION

In summary, a pre-strained strategy is proposed to accelerate the actuation of thermal responsive structures. To fabricate the pre-strained bilayer structure, we construct a pre-strained 4D printing platform that can apply strain to the substrate during the printing process. Due to the strain mismatch, the pre-strained layer tensions the non-pre-strained layer, leading to an initial bending of the printed structure. Because of the higher coefficient of thermal expansion of the inner pre-strained layer, the curvature of the pre-strained bilayer structure decrease under the external thermal stimulus. As the temperature increases, the initial bending structure will bend in the opposite direction. We have explored the effects of aspect ratio and pre-strain on the slender pre-strained bilayer structure through experiments and on the wide pre-strained bilayer structure through FEA. The deformation of pre-strained bilayer structure is less sensitive to the aspect ratio while sensitive to the pre-strain. Furthermore, we have studied the deformation speed of wide pre-strained bilayer structure with different pre-strains, and deduce that pre-strain can enhance the deformation speed of bilayer structure. Based on the pre-strained bilayer structure, we have designed a fast and energy-free gripper and a soft crawler with a larger motion step and higher speed. In further research, the pre-strained structure

can be applied to more sophisticated soft robotics for higher responsive capacity.

DATA AVAILABILITY STATEMENT

The original contributions presented in the study are included in the article/**Supplementary Material**, further inquiries can be directed to the corresponding author.

AUTHOR CONTRIBUTIONS

PL and YZ conceived the idea and designed the research. YZ, ZH, and XL co-analyzed the experimental and calculated data. YZ, ZH, XL, and PL contributed to the writing and editing of the manuscript. All authors contributed to the article and approved the submitted version.

FUNDING

Financial support for this work was provided by the National Natural Science Foundation of China under Grant Nos. 91848201, 11988102, 11521202, 11872004, and 11802004.

SUPPLEMENTARY MATERIAL

The Supplementary Material for this article can be found online at: <https://www.frontiersin.org/articles/10.3389/fmats.2021.661999/full#supplementary-material>

REFERENCES

- Ambulo, C. P., Burroughs, J. J., Boothby, J. M., Kim, H., Shankar, M. R., and Ware, T. H. (2017). Four-dimensional printing of liquid crystal elastomers. *ACS Applied Materials & Interfaces* 9, 37332–37339. doi: 10.1021/acsami.7b11851
- Bartlett, M. D., Kazem, N., Powell-Palm, M. J., Huang, X., Sun, W., Malen, J. A., et al. (2017). High thermal conductivity in soft elastomers with elongated liquid metal inclusions. *Proceedings of the National Academy of Sciences of the United States of America* 114, 2143–2148. doi: 10.1073/pnas.1616377114
- Ding, Z., Yuan, C., Peng, X., Wang, T., Qi, H. J., and Dunn, M. L. (2017). Direct 4D printing via active composite materials. *Science Advances* 3, e1602890. doi: 10.1126/sciadv.1602890
- Gao, B., Yang, Q., Zhao, X., Jin, G., Ma, Y., and Xu, F. (2016). 4D bioprinting for biomedical applications. *Trends in Biotechnology* 34, 746–756. doi: 10.1016/j.tibtech.2016.03.004
- Ge, Q., Dunn, C. K., Qi, H. J., and Dunn, M. L. (2014). Active origami by 4D printing. *Smart Materials and Structures* 23, 094007. doi: 10.1088/0964-1726/23/9/094007
- Ge, Q., Qi, H. J., and Dunn, M. L. (2013). Active materials by four-dimension printing. *Applied Physics Letters* 103, 131901. doi: 10.1063/1.4819837
- Gill, E. L., Li, X., Birch, M. A., and Huang, Y. Y. S. (2018). Multi-length scale bioprinting towards simulating microenvironmental cues. *Bio-design and Manufacturing* 1, 77–88. doi: 10.1007/s42242-018-0014-1
- Hardin, J. O., Ober, T. J., Valentine, A. D., and Lewis, J. A. (2015). Microfluidic printheads for multimaterial 3D printing of viscoelastic inks. *Advanced Materials* 27, 3279–3284. doi: 10.1002/adma.201500222
- Kim, Y., Parada, G. A., Liu, S., and Zhao, X. (2019). Ferromagnetic soft continuum robots. *Science Robotics* 4, doi: 10.1126/scirobotics.aax7329 **Q,
- Kim, Y., Yuk, H., Zhao, R., Chester, S. A., and Zhao, X. (2018). Printing ferromagnetic domains for untethered fast-transforming soft materials. *Nature* 558, 274–279. doi: 10.1038/s41586-018-0185-0
- Kotikian, A., Truby, R. L., Boley, J. W., White, T. J., and Lewis, J. A. (2018). 3D printing of liquid crystal elastomeric actuators with spatially programed nematic order. *Advanced Materials* 30, 1706164. doi: 10.1002/adma.201706164
- Kuksenok, O., and Balazs, A. C. (2016). Stimuli-responsive behavior of composites integrating thermo-responsive gels with photo-responsive fibers. *Materials Horizons* 3, 53–62. doi: 10.1039/C5MH00212E
- Le Duigou, A., Chabaud, G., Scarpa, F., and Castro, M. (2019). Bioinspired electro-thermo-hygro reversible shape-changing materials by 4D printing. *Advanced Functional Materials* 29, 1903280. doi: 10.1002/adfm.201903280
- Leist, S. K., and Zhou, J. (2016). Current status of 4D printing technology and the potential of light-reactive smart materials as 4D printable materials. *Virtual and Physical Prototyping* 11, 249–262. doi: 10.1080/17452759.2016.1198630
- Li, X., Duan, H., Lv, P., and Yi, X. (2020). Soft Actuators Based on Liquid-Vapor Phase Change Composites. *Soft Robotics* doi: 10.1089/soro.2020.0018 ***Q,
- Li, Y. C., Zhang, Y. S., Akpek, A., Shin, S. R., and Khademhosseini, A. (2016). 4D bioprinting: the next-generation technology for biofabrication enabled by stimuli-responsive materials. *Biofabrication* 9, 012001. doi: 10.1088/1758-5090/9/1/012001
- Lin, C., Zhang, L., Liu, Y., Liu, L., and Leng, J. (2020). 4D printing of personalized shape memory polymer vascular stents with negative Poisson's ratio structure: A preliminary study. *Science China Technological Sciences* 63, 578–588. doi: 10.1007/s11431-019-1468-2
- Liu, G., Zhao, Y., Wu, G., and Lu, J. (2018). Origami and 4D printing of elastomer-derived ceramic structures. *Science Advances* 4, eaat0641. doi: 10.1126/sciadv.aat0641

- Morrison, R. J., Hollister, S. J., Niedner, M. F., Mahani, M. G., Park, A. H., Mehta, D. K., et al. (2015). Mitigation of tracheobronchomalacia with 3D-printed personalized medical devices in pediatric patients. *Science Translational Medicine* 7, 285ra64. doi: 10.1126/scitranslmed.3010825
- Müller, A., Wapler, M. C., and Wallrabe, U. (2019). A quick and accurate method to determine the Poisson's ratio and the coefficient of thermal expansion of PDMS. *Soft Matter* 15, 779–784. doi: 10.1039/C8SM02105H
- Nadgorny, M., Xiao, Z., Chen, C., and Connal, L. A. (2016). Three-dimensional printing of pH-responsive and functional polymers on an affordable desktop printer. *ACS Applied Materials & Interfaces* 8, 28946–28954. doi: 10.1021/acsami.6b07388
- Naficy, S., Gately, R., Gorkin, R. III, Xin, H., and Spinks, G. M. (2017). 4D printing of reversible shape morphing hydrogel structures. *Macromolecular Materials and Engineering* 302, 1600212. doi: 10.1002/mame.201600212
- Nishiguchi, A., Zhang, H., Schweizerhof, S., Schulte, M. F., Mourran, A., and Möller, M. (2020). 4D printing of a light-driven soft actuator with programmed printing density. *ACS Applied Materials & Interfaces* 12, 12176–12185. doi: 10.1021/acsami.0c02781
- Ober, T. J., Foresti, D., and Lewis, J. A. (2015). Active mixing of complex fluids at the microscale. *Proceedings of the National Academy of Sciences of the United States of America* 112, 12293–12298. doi: 10.1073/pnas.1509224112
- Schneider, F., Draheim, J., Kamberger, R., and Wallrabe, U. (2009). Process and material properties of polydimethylsiloxane (PDMS) for Optical MEMS. *Sensors and Actuators A: Physical* 151, 95–99. doi: 10.1016/j.sna.2009.01.026
- Teoh, J. E. M., An, J., Feng, X., Zhao, Y., Chua, C. K., and Liu, Y. (2018). Design and 4D printing of cross-folded origami structures: A preliminary investigation. *Materials* 11, 376. doi: 10.3390/ma11030376
- Timoshenko, S. (1925). Analysis of bi-metal thermostats. *Josa* 11, 233–255.
- Villar, G., Graham, A. D., and Bayley, H. (2013). A tissue-like printed material. *Science* 340, 48–52. doi: 10.1126/science.1229495
- Wu, Z. L., Moshe, M., Greener, J., Therien-Aubin, H., Nie, Z., Sharon, E., et al. (2013). Three-dimensional shape transformations of hydrogel sheets induced by small-scale modulation of internal stresses. *Nature Communications* 4, 1–7. doi: 10.1038/ncomms2549
- Xin, X., Liu, L., Liu, Y., and Leng, J. (2020). 4D Printing Auxetic Metamaterials with Tunable, Programmable, and Reconfigurable Mechanical Properties. *Advanced Functional Materials* 30, 2004226. doi: 10.1002/adfm.202004226
- Yang, H., Leow, W. R., Wang, T., Wang, J., Yu, J., He, K., et al. (2017). 3D printed photoresponsive devices based on shape memory composites. *Advanced Materials* 29, 1701627. doi: 10.1002/adma.201701627
- Yang, Y., Li, Y., and Chen, Y. (2018). Principles and methods for stiffness modulation in soft robot design and development. *Bio-Design and Manufacturing* 1, 14–25. doi: 10.1007/s42242-018-0001-6
- Zarek, M., Mansour, N., Shapira, S., and Cohn, D. (2017). 4D printing of shape memory-based personalized endoluminal medical devices. *Macromolecular Rapid Communications* 38, 1600628. doi: 10.1002/marc.201600628
- Ze, Q., Kuang, X., Wu, S., Wong, J., Montgomery, S. M., Zhang, R., et al. (2020). Magnetic shape memory polymers with integrated multifunctional shape manipulation. *Advanced Materials* 32, 1906657. doi: 10.1002/adma.201906657
- Zhu, P., Yang, W., Wang, R., Gao, S., Li, B., and Li, Q. (2018). 4D printing of complex structures with a fast response time to magnetic stimulus. *ACS Applied Materials & Interfaces* 10, 36435–36442. doi: 10.1021/acsami.8b12853

Conflict of Interest: The authors declare that the research was conducted in the absence of any commercial or financial relationships that could be construed as a potential conflict of interest.

Copyright © 2021 Zou, Huang, Li and Lv. This is an open-access article distributed under the terms of the Creative Commons Attribution License (CC BY). The use, distribution or reproduction in other forums is permitted, provided the original author(s) and the copyright owner(s) are credited and that the original publication in this journal is cited, in accordance with accepted academic practice. No use, distribution or reproduction is permitted which does not comply with these terms.



Plant-Morphing Strategies and Plant-Inspired Soft Actuators Fabricated by Biomimetic Four-Dimensional Printing: A Review

Luquan Ren¹, Bingqian Li¹, Kunyang Wang¹, Xueli Zhou¹, Zhengyi Song¹, Lei Ren^{2*} and Qingping Liu^{1*}

¹ Key Laboratory of Bionic Engineering, Ministry of Education, Jilin University, Changchun, China, ² School of Mechanical, Aerospace and Civil Engineering, University of Manchester, Manchester, United Kingdom

OPEN ACCESS

Edited by:

Yusheng Shi,
Huazhong University of Science
and Technology, China

Reviewed by:

Yanju Liu,
Harbin Institute of Technology, China
Yunhong Liang,
Jilin University, China
Huaping Wu,
Zhejiang University of Technology,
China

*Correspondence:

Lei Ren
lei.ren@manchester.ac.uk
Qingping Liu
liuqp@jlu.edu.cn

Specialty section:

This article was submitted to
Smart Materials,
a section of the journal
Frontiers in Materials

Received: 10 January 2021

Accepted: 09 March 2021

Published: 04 May 2021

Citation:

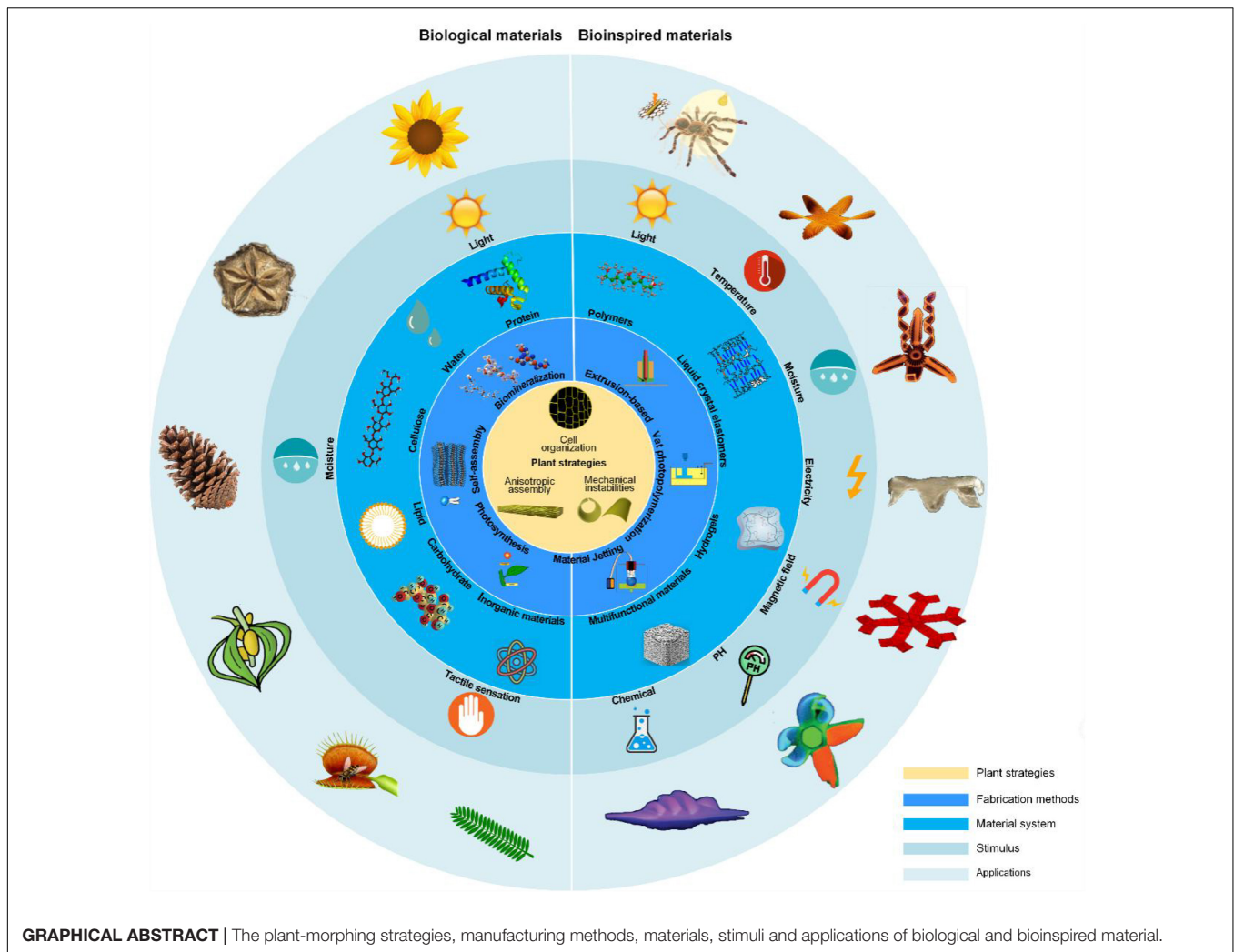
Ren L, Li B, Wang K, Zhou X,
Song Z, Ren L and Liu Q (2021)
Plant-Morphing Strategies
and Plant-Inspired Soft Actuators
Fabricated by Biomimetic
Four-Dimensional Printing: A Review.
Front. Mater. 8:651521.
doi: 10.3389/fmats.2021.651521

For prey, seeding, and protection, plants exhibit ingenious adaptive motions that respond autonomously to environmental stimuli by varying cellular organization, anisotropic orientation of cellulose fibers, mechanical instability design, etc. Notably, plants do not leverage muscle and nerves to produce and regulate their motions. In contrast, they harvest energy from the ambient environment and compute through embodied intelligence. These characteristics make them ideal candidates for application in self-morphing devices. Four-dimensional (4D) printing is a bottom-up additive manufacturing method that builds objects with the ability to change shape/properties in a predetermined manner. A versatile motion design catalog is required to predict the morphing processes and final states of the printed parts. This review summarizes the morphing and actuation mechanisms of plants and concludes with the recent development of 4D-printed smart materials inspired by the locomotion and structures of plant systems. We provide analyses of the challenges and our visions of biomimetic 4D printing, hoping to boost its application in soft robotics, smart medical devices, smart parts in aerospace, etc.

Keywords: soft actuators, biomimetic 4D printing, bioinspired, plant-morphing strategies, plant-inspired soft actuators

INTRODUCTION

Nature endows many organic systems with shape-morphing features, particularly the plant kingdom (Poppinga et al., 2020). Unlike animals, where macroscopic movement is provided by chemical reaction in the molecule level, the locomotion of plants is delivered by microscopic swelling of the cells (Forterre, 2013). After evolution for billions of years, plant organs are gifted with the ability to respond to environmental changes by regulating constituents and structures, forming the “morphological computation” in their growth and reach a final configuration before maturation (Pfeifer and Gomez, 2009; Guo et al., 2015). In reaction to variability within their surroundings, they continuously adjust their morphology and physiology. The dynamic interactions between their morphology and the environment contribute to the adaptability of the plant system, which also generates the principle of “morphological computation” (Zambrano et al., 2014). A representative example of morphological computation is the “passive movements.” For example, pine cones open their scales in dry conditions and close them when hydrated. The organization of plant cell walls accounts for motion, where a soft matrix and stiff embedded

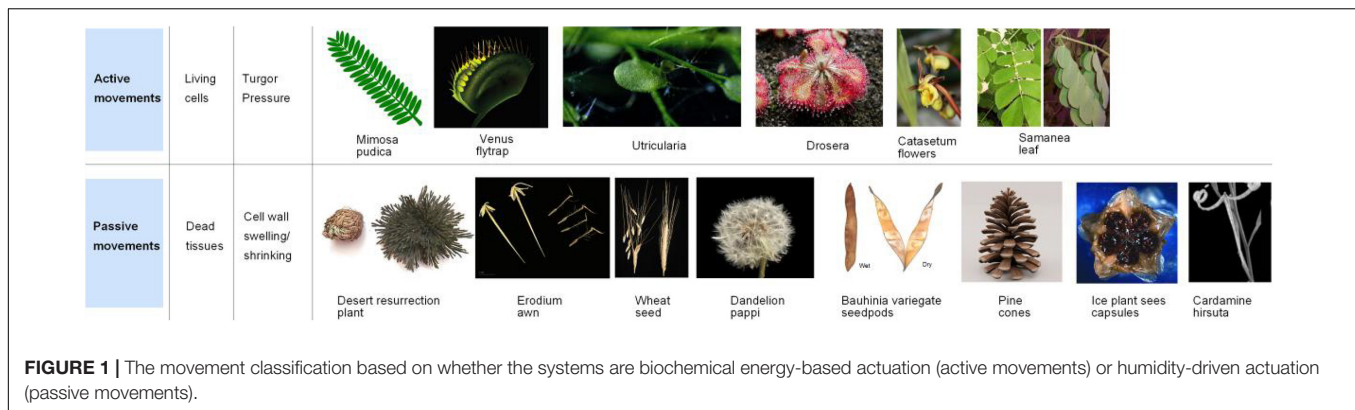


cellulose fibrils drive the movement of the plant organ (Dawson et al., 1997). These systems sense and respond to surrounding changes without additional energy inputs, making them ideal for soft actuations. Similar to the environment of plants, the operating environment of artificial soft actuators is also dynamic (Pfeifer et al., 2012). Structural designs that can self-adapt in both controlled and uncontrolled environments are urgently required.

Biomimetics is a multidisciplinary discipline that examines bio-phenomenology for gaining inspiration in developing artificial systems (Vincent et al., 2006). It is divided into “bottom-up” and “top-down” process (Hashemi Farzaneh et al., 2016), and both of them requires the steps of abstracting, transferring, and applying. The abstracting demands acknowledging the associations of the structural-functional properties of plants. The transferring and applying are not the direct “copy and paste” process but an innovative process, similar to heredity and variation in species evolution process (Gregory, 2009). The bioinspired soft actuators usually consist of delicate and sophisticated heterogeneous structures and are constructed from materials with mechanical properties analogous to living materials (Miriyeve et al., 2017). Thus,

designing and manufacturing bioinspired soft actuators are extremely challenging for traditional technologies, which desires an innovative way rather than artificially assembling elementary blocks like rigid-body actuators (Cho et al., 2009).

Four-dimensional (4D) printing, stemming from the rapid development of 3D printing, smart materials, and systematic programming routes, is an effective way of transferring biological counterparts into artificial structures (Momeni et al., 2017). By incorporating 3D printing technology with smart materials, the concept of 4D printing is proposed to realize components that can regulate their morphologies responding to external stimuli (De Marco et al., 2018). The selection of deformation materials is based on their response to environmental excitation (Shafraneck et al., 2019). The establishment of mathematical models and motion design catalogs is required to predict the fourth dimension (Boley et al., 2019; Kanu et al., 2019). 4D printing is a new manufacturing paradigm that produces tunable intricate 3D structures induced from the 2D counterpart (Yang et al., 2020). In addition, it is a disruptive strategy to construct dynamic structures that can alter their structure, function in a scheduled way (Montero de Espinosa et al., 2017),



which has a variety of applications in MEMS (Sundaram et al., 2017), soft robots (Gul et al., 2018), sensors (Tseng et al., 2018), deployable mechanism (Yang et al., 2019), active arts and costume (Sun et al., 2020), and controlled release medicine (Durga Prasad Reddy and Sharma, 2020).

Biomimetic 4D printing can translate biologically extracted motifs into synthetically dynamic materials *via* the bottom-up accumulation of materials (Sydney Gladman et al., 2016). It needs to undergo the abstracting, transferring process first, and then applying the transferred motifs *via* appropriate 3D printing technologies.

Now, most of the reviews about 4D printing mainly focus on smart materials, printing technologies, and various applications (Mitchell et al., 2018; Kuang et al., 2019a; Zhang et al., 2019). In this review, we concentrate on soft actuation structural designs in plant systems and biomimetic soft actuators with the assistance of 4D printing. We first introduce the movements in the plant system and then conclude with three strategies from various movements: cellular organization, orientation of the cellulose fibers, and mechanical instabilities. Then, we briefly introduce the 4D printing technologies. Next, the bioinspired programming approaches are classified based on whether it is mimicking locomotion or designs of the plant system. These programming methods based on designs from the plant system can be further subdivided into structure-driven 4D printing, parameter-driven 4D printing, and stimulus-driven 4D printing in the light of which is the determinative factor of shape-morphing process. Finally, we propose the challenges and outlook for the biomimetic 4D printing of soft actuators to give some sparks for future researches.

THE MOVEMENTS AND STRUCTURAL STRATEGIES IN THE PLANT SYSTEM

Although plants do not have muscles, they can produce many different movements in a time frame ranging from a few days to a few milliseconds (Forterre, 2013). Their natural formations from micro- to macroscale endow them with capabilities to adapt to the environment without the processing of the nerve system. Plants are capable of responding to a variety of signals and the movements observed are characteristic of the structures, not a

consequence of metabolic processes (Studart and Erb, 2014). Therefore, these principles widely existing in the plant world are more easily extracted and applied to soft actuators.

The Movement Behaviors in the Plant System

The movement of plants is usually categorized into two types: tropistic and nastic movements (Guo et al., 2015). Tropistic movement is the directional actuation in response to stimuli such as gravity, light, and mechanical touches. For example, the growth of tendrils depends on the location and manner in which they contact the supporting object (Scorza and Dornelas, 2011). On the other hand, nastic movements are direction independent in response to stimuli. As a case in point, the closing of the *Dionaea* trap does not rely on the location and orientation of the sensitive hairs being touched (Braam, 2005).

Some studies also discriminated between active and passive systems in plant locomotion based on whether they are biochemical energy-based actuation or humidity-driven actuation (Egan et al., 2015) (Figure 1). The active systems rely on moving ions to alter membrane permeability (Yang and Hinner, 2015), resulting in reversible turgor changes and irreversible growth processes under the stimulation of various types of stimuli (touch, temperature, or light). Plants are allowed to generate motions such as blooming and wilting of flowers, closing of Venus flytraps, and folding of mimosa leaves (Jung et al., 2014). The resulting actuation can be high speed as in *Mimosa pudica* (defense, <1 s) and Venus flytrap (nutrition, ≈100 ms) (Forterre et al., 2016). Notably, the number and properties of cells as well as the exchanging capacity of water limit the performance of the movements (e.g., the amplitude, speed, and frequency). Passive motion refers to the change in configuration of dead tissue in response to environmental changes (Quan et al., 2020). They are already dead tissues that are subject to scheduled changes. The wall of plant cells is a composite that constitutes cellulose microfibrils, polysaccharides, hemicellulose, soluble proteins, etc. (Fagerstedt and Karkonen, 2015). The soft matrix inside the cell wall expands when combined with water molecules. Specifically, the hydrophilic moiety allows water molecules to be stored *via* hydrogen bonding. Many organ movements in plants are triggered by

changes in the water content of cell walls (pine cones, *Selaginella lepidophylla*, *Erodium gruinum*, seed pods, ice plant seeds, dandelion) (Montero de Espinosa et al., 2017). For example, the ancient resurrection plant, *S. lepidophylla*, shows a dramatic curl and uncurl as the plant hydrates. When dehydrated, the stems of *S. lepidophylla* curl, eventually forming a rough sphere (Selaginella et al., 2015). The hygroscopic reactions also induce the opening and closing of pine cones (Reyssat and Mahadevan, 2009), release of seed pods (Armon et al., 2011), and self-burial of the wheat awns and *Erodium* seeds (Evangelista et al., 2011).

Compared with the aforementioned osmotic pressure actuation, hygroscopicity is relatively slow; however, the merit lies in the fact that it does not require any biochemical energy. However, it is not always the case because rapid movements could be achieved by dehydration of dried tissues with the delicate structure designs (mechanical instabilities) (Guo et al., 2015). The passive actuation systems that are not dependent on living cells offer us an excellent source of inspiration.

The Structural Strategies for Movements in the Plant System

The time scale of water diffusion in each tissue determines the speed of motile plant structures. In general, larger plant organs require longer time for water transport, of which some plants have evolved elastic instability to overcome the inherent defect (Skotheim, 2005). The sudden release of energy greatly increases the speed of movement, which is reversible as long as the tissue is not damaged. Elastic instability has been found in many examples of explosive diaspore dispersal. Venus flytrap is one of the representative examples, where the geometric change of its lobes from concave to convex substantially improves the speed of snapping (Forterre et al., 2005).

To enable nonuniform slow/fast sophisticated movements with uniform hygroscopic actuations, plants have evolved various delicate strategies: (1) cellular organization, (2) orientation of the cellulose fibers, and (3) mechanical instabilities (Figure 2). It should be noted that the above briefly summarized plant movements and strategies are only the tip of the iceberg. There are many other reviews providing a broader overview about the plant actuation mechanisms and applications (Poppinga et al., 2016).

Cellular Organization

In the active and passive actuation systems, cellular organization (distribution, density, morphology, etc.) is a frequently used measure to confer various movements to homogeneous materials, for example, the locomotion of pulvinus stems from the volume change and pressure difference between subepidermal and supraepidermal motor cells (Volkov et al., 2010a). Besides, some passive systems, such as *S. lepidophylla* mentioned above, curl their stems to form spheres (Selaginella et al., 2015). They are also caused by the cell density variation within the lower and upper regions of the dry tissue. Another passive actuation example is ice plant seed capsule. To enable seed dispersal, its keel cells have evolved ellipsoid-hexagonal shape, translating a isotropic swelling into a unidirectional deformation and, thus, unfolding of the capsule (Guiducci et al., 2016).

Anisotropic Reinforcement of the Cellulose Fibers

Plant cell wall consists of stiff and orientationally distributed cellulose fibers. The swelling of plant cell walls occurs in a hygroscopic soft matrix, where the direction of moisture absorption and expansion is vertical to the direction of cellulose microfibrils. The underlying principle is the constant length along the fiber alignment and expansion in the perpendicular direction under the stimulation of moistures. Hygroscopic bending and torsional movements in many organs, such as pine cones, wheat awn, and chiral seed pods, have a close association with the variations in fiber orientations (Elbaum and Abraham, 2014). In pine cones, the hinge at the base of the scales consists of two layers of hygroscopic tissue embedded with cellulose fibers (Reyssat and Mahadevan, 2009). These aligned fibers restrict any longitudinal shape changes in the embedded layer. Therefore, reciprocal bending of the pine cone scales can be achieved with the variation of environmental humidity. Besides, the architected orientation of the cellulose fibers enables self-burial of the seed. *Erodium cicutarium* consists of inclined spiral fibers whose seeds show self-buried motion due to the rotation of the awn under changes in humidity (Jung et al., 2014). Specifically, the orientation of the material fibers causes awns to curl in low air humidity and to straighten in high air humidity, thus leading to the burial of the seed. The soft tissues of trees adopt a similar strategy that involves reorienting cellulose fibers in the cell wall to generate stress and thus change the direction of growth (Du and Yamamoto, 2007).

Mechanical Instabilities

The speed of water diffusion limits the response times of both osmotic pressurization and hygroscopic swelling/shrinking merely by ion transportation and the hydrophilic process. In order to move quickly, mobile organs either need to be miniaturized, as in the case of the hydraulically driven *Mimosa pudica* (Volkov et al., 2010b), or rely on mechanical instability and designed failure modes (Dumais and Forterre, 2012). The plant employs structural strategies (bistability, fracture, and water cavitation) to overcome the physical limitation (Figure 3). Indeed, the velocity, accuracy, and efficiency of the fast movements of plants are as essential as the muscle-driven movements in animals. First, the bistable mechanism not only produces fast motion but also reversible motion, which is attractive for artificial designs. The bistable system can be maintained at stable states without the need for consistent pressure supply, achieving rapid and reversible deformation with minimal pressure changes.

One of the most intensively studied plant movement using bistability is the Venus flytrap (Hedrich and Neher, 2018). The trap consists of two connected lobes, and the inner surface of each lobe has many triggering hairs. The closing of Venus flytraps occurs when small hairs are triggered by the movement of insects. Two or more trigger events can cause the trap to close, and thus, avoid closing when there is no prey present. The trap usually shuts in tenths of a second. A carnivorous plant in eastern Australia, *Drosera glanduligera*, also uses snapping tentacles to catapult prey into sticky traps (Poppinga et al., 2012). First, tentacles at the trap periphery quickly flung the prey onto the

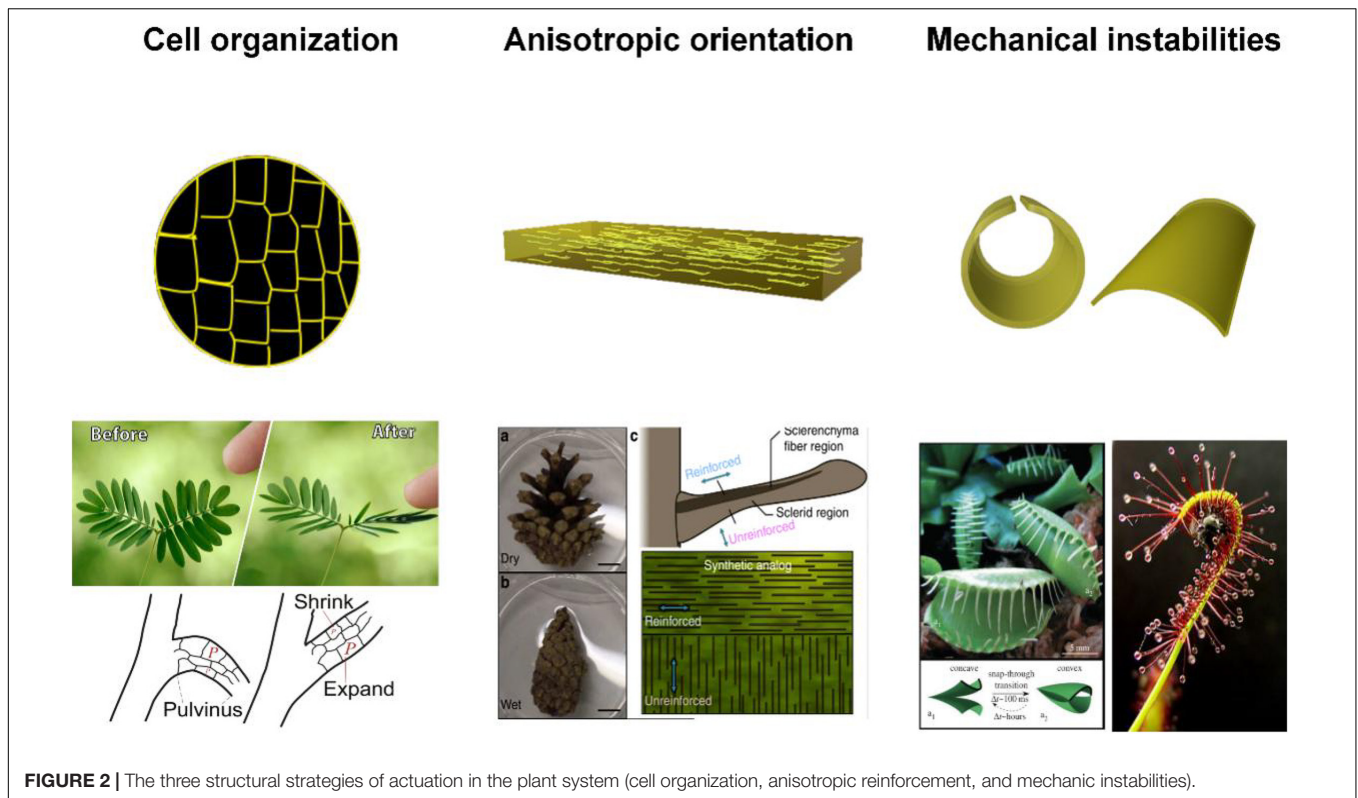


FIGURE 2 | The three structural strategies of actuation in the plant system (cell organization, anisotropic reinforcement, and mechanic instabilities).

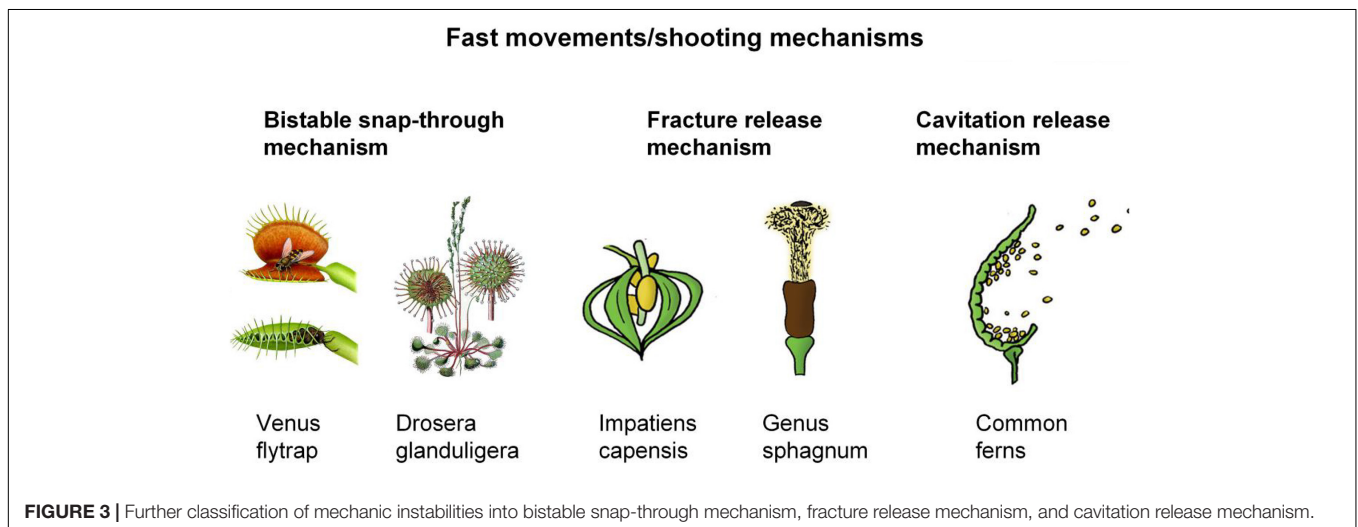


FIGURE 3 | Further classification of mechanic instabilities into bistable snap-through mechanism, fracture release mechanism, and cavitation release mechanism.

adhesive tentacles of the leaf blade in about 0.1 s when stimulated. Then, the glue tentacles move the prey to the concave center of the leaf to digest.

The other elegant and well-studied cases are based on fracture release whose deformations are usually nonreversible. For instance, *Impatiens glandulifera* relies on fracture mechanics to spread its spores. Although the fracturing seems like a result of mechanical instability, it still differs from buckling since it is a one-shot process (Deegan, 2012). It consists of five elongated and curved segments or valves, and each has 5–10 seeds held inside. In the initial state, the valves are straightened by interconnection

of individual valves. When one of the valves is deformed because of drying or changes in external conditions, the chain reaction will begin. The geometry of the remaining valve undergoes a cascade of changes, the seam breaks, and the elastic energy is released instantaneously. The reaction resulted in explosive dehiscence, with the seeds being spread 2 m away from the parent plant and reaching a peak emission velocity of 4.1 m/s. Another fracture example is the spores of *Sphagnum*. It is developed within spherical capsules comprised of two portions containing the upper spore-filled and the bottom air-filled chamber (Sakes et al., 2016). In the water loss state, the matured drying capsules

contract radially and migrate their shape from spherical to cylindrical. Then, the decreasing capsule volume leads to an increase in air pressure until a critical pressure is reached. The explosively released spores are capable of achieving a peak acceleration of 36,697 g and a peak launch velocity of 30 m/s and propelling the spores to 0.20 m above the moss.

Cavitation-based spore discharge is often observed in the family ferns (Poppinga et al., 2015). A stalk and a circular ridge of 12 or 13 cells comprise the spore structure of common ferns. Evaporation of water from the cytoplasm of the cell causes the interior of the lateral wall to collapse, allowing the annulus to open to expose the spores and leading to a sudden release of the stored elastic energy (~ 0.01 ms). This peak launch acceleration, the peak launch velocity, and the launch distance are approximately 100,000 g, 10 m/s, and 0.057 m, respectively.



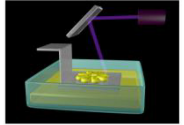
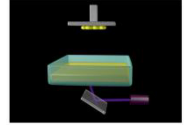
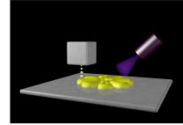
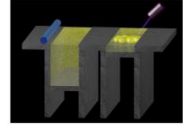
4D PRINTING-RELATED TECHNOLOGIES

The concept of 4D printing combines ongoing 3D printing technology with smart materials to enable printed components that transform their morphology in response to environmental stimuli. The two most vital components in 4D printing are materials and 3D printing technology, and the selection of materials determines the 3D printing technology utilized. The states of the raw materials, physical and chemical properties, curing requirements, special processing needs, etc. all determine the specific 3D printing process that is applicable. There are broad options for 3D printable materials, including shape memory polymers, hydrogels, liquid crystal elastomers, metals and alloys, ceramics, and composites (McCracken et al., 2020). Among these methods, direct ink writing (DIW), fused depositing modeling (FDM), stereolithography (SLA), digital light processing (DLP), material jetting, and selective laser sintering (SLS) are most commonly employed in 4D printing (Deshmukh et al., 2019) (Table 1).

Fused depositing modeling and DIW are both extrusion-based and form a 3D object in a line by line and layer by layer way. The differences stem from their raw materials that FDM melts a solid filament in a heating nozzle and then solidifies materials by cooling. DIW, on the other hand, deposits a viscous liquid ink that can be cured simultaneously or subsequently by UV light, heat, etc. Extrusion-based methods have the advantage of printing a wide range of materials, including various engineered thermoplastic polymers, hydrogels, colloidal materials, and compounds, which can be in solid, liquid, or paste form. The printing resolution of FDM and DIW is mainly limited by the nozzle diameter (100–400 μm). The SLA and DLP are both vat photopolymerization-based methods. A laser beam for photocuring is called SLA; a projector used for photocuring is called DLP. The curing methods of DLP are not confined to photocuring. Vitrification, evaporation, and polymerization can all be applied into the solidification of the materials. The resolution of SLA and DLP is mainly determined by the curing method, and both laser and projector can reach the resolution of 1–50 μm . In the recent researches of 4D printing, the use of switchable vats and tunable light contributes to the advances in multimaterial DLP. Another popular method is material jetting, which utilizes multiple nozzles for spraying different resins to form a layer, and the process is accompanied by subsequent UV curing or lasing. It allows the manufacture of composite materials with various properties at a relatively high resolution with an in-plane resolution of 16 μm for single-material printing. The last method, selective laser sintering (SLS), is a powder bed fusion-based method, which uses a laser (electron beam) to melt thermoplastic powders together. Its resolution can be as fine as 100 μm , depending on the powder granularity and heat source.

In the research of 4D printing of soft actuators, FDM and SLA are the most extensively used printing techniques followed by material jetting and DIW. DLP is also a recently emerged technique with a huge potential for printing 4D active devices. In the next section, we will review the 4D printing of the soft actuators inspired by the plant system using the abovementioned printing technologies.

TABLE 1 | The introduction of 3D printing technologies applied in 4D printing—raw materials, resolutions, and curing methods.

Direct ink writing (DIW)	Fused deposition modeling (FDM)	Stereolithography (SLA)	Digital light processing (DLP)	Material jetting	Selective laser sintering (SLS)
					
Raw materials					
Ink, thermoplastic grain	Thermoplastic filament	Low viscosity ink ($V < 5$ Pa-s)	Low viscosity ink	Low viscosity ink ($V < 0.2$ G Pa-s)	Thermoplastic powder
Approximate resolutions					
1–100 μm	100 μm	1–50 μm	1–50 μm	50 μm	100 μm
Curing methods					
UV light, crosslinking, heating	Cooling	Laser	Vitrification, evaporation, polymerization, UV light	Laser, UV light	Laser

4D PRINTING OF SOFT ACTUATORS INSPIRED BY THE PLANT ACTUATION SYSTEM

4D printing incorporates additive manufacturing processes with dynamic materials, providing an effective tool for next-generation soft actuators. However, these methods lack theoretical models, and the relationship between material distribution, structure, and function needs to be thoroughly studied. There is a growing recognition that the actuation mechanisms of plants can provide inspiration for the development of bioinspired soft actuators. Plants hold a multitude of movement mechanisms, which are increasingly recognized as sources of inspiration for the development of bioinspired actuators. The motile plant structures without localized hinges introduced in the Section “The Movements and Structural Strategies in the Plant System” are ideal candidates as concept generator. In general, soft actuators mimicking plants are subdivided into plant locomotion-inspired actuation and plant design-inspired actuation, both of which have their advantages and disadvantages. Plant locomotion-inspired soft actuators are often only morphologically similar to plants, and there is still a large gap between the comprehensive performance of artificial soft actuators and plant organs. It outperforms plant design-inspired actuators in terms of design freedom when it comes to achieving specific functions. Plant design-inspired soft actuators derive strategies from plant organs. Although they might have more restrictions when selecting material structures, their deforming mechanisms and comprehensive performances resemble biological counterparts in a superior way.

4D Printing of Soft Actuators by Mimicking the Locomotion of the Plant System

In the existing literature, although some actuators might employ distinct actuation mechanisms from those used in nature, they achieve motions and behaviors quite similar to those of plant organs (Menges et al., 2017; Kim et al., 2018; Kuang et al., 2019b; Alapan et al., 2020). For the soft actuators mimicking the locomotion of plants, the strategies they adopted are based on the characteristics of the material itself (or adjusting the composition of the material) and accompanied by some simple geometric designs. In **Figure 4A**, Ge et al. (2016) present the sequential recovery of a multimeral flower by controlling the constituents and compositions of the shape memory polymers in outer and inner petals. Similarly, inspired by the heliotropism of sunflowers (**Figure 4B**), Lui et al. (2019) printed a photoresponsive shape memory sunflower by combining polymers polyurethane (active materials) and photoresponsive carbon black, resembling an actual sunflower going from bud to bloom. In addition to light and heat actuation, Kim et al. (2018) proposed magnetically responsive soft materials that allow for fast transition between complex 3D shapes based on an elastomer composite containing ferromagnetic microparticles (**Figure 4C**). The magnetic field applied to the dispensing nozzle during printing reorients the particles along the applied magnetic field. The capability to

create complex shape changes of the magnetically responsive soft materials can achieve diverse functions although these structures are not to imitate the movement of plants in this research. Besides, pine cone, flytrap, and *M. pudica* are also popular biological concept generators. Correa et al. (2020) employed a bilayer region consisting of a directional TPU-bound layer and a directional moisture-absorbing wood polymer layer to program the multiphase motions (e.g., bending deformation of pine cone scales during desiccation) (**Figure 4D**). Jiang et al. (2019) printed bistable structures with geometries near bifurcation points, and this point is associated with the transfer between bistable and monostable states. As long as the appropriate stimulus is applied, the material will undergo bifurcation, thus triggering large amplitude and fast actuation. They show a similar Venus flytrap-inspired example using two more complex actuation units with more complex control logic (**Figure 4E**) (Jiang et al., 2019). Wang G. et al. (2018) developed an artificial *M. pudica* actuator via the fused deposition modeling 3D printer by combining the conductive polylactide (PLA) on copy paper. When the leaf is triggered, it can achieve a sequence of actuation similar to that of a *M. pudica* (**Figure 4F**) (Wang G. et al., 2018).

4D Printing of Soft Actuators by Mimicking the Designs of the Plant System

Understanding the respective geometry–structure–function relationships of organisms and applying underlying principles to applications would provide a versatile toolbox for generating structures with dynamic responses. We will introduce three programming methods in the subsection, namely using structure design, parameter setting, and imposed stimulus as main motifs to program the shape-morphing behaviors of soft actuators.

The Soft Actuators Mimicked via Structure-Driven 4D Printing

Like cellular organization in nature, soft actuators can achieve various deformations by the material distributions. Wang et al. (2019) designed a line-shaped composite structure enabling a single printed line with eight bending directions by arranging the active line segment, which is composed of actuator [thermoplastic (PLA)] and constraint regions that are different in shrinkage rates (**Figure 5A**). By combining multiple segments with varied bending directions, the soft actuators with more complex geometries and complicated functions (grippers) could be fabricated. Besides, the materials can be distributed in three dimensions. Liu et al. (2019) reported the fabrication of 3D-printed segmented gel tubes consisting of strategic placement of an active swelling gel and a passive nonresponsive gel (**Figure 5B**). In many cases, the distribution of materials is not clearly bounded, and the transitions between materials are in gradient. By printing graded water-responsive elastomeric materials on heat-shrinkable shape memory polymers, Song et al. (2020) demonstrated a bistimulated self-deforming structure that can produce different shape changes with humidity and temperature to mimic the nonuniform distribution of active ingredients in botany (**Figure 5C**).

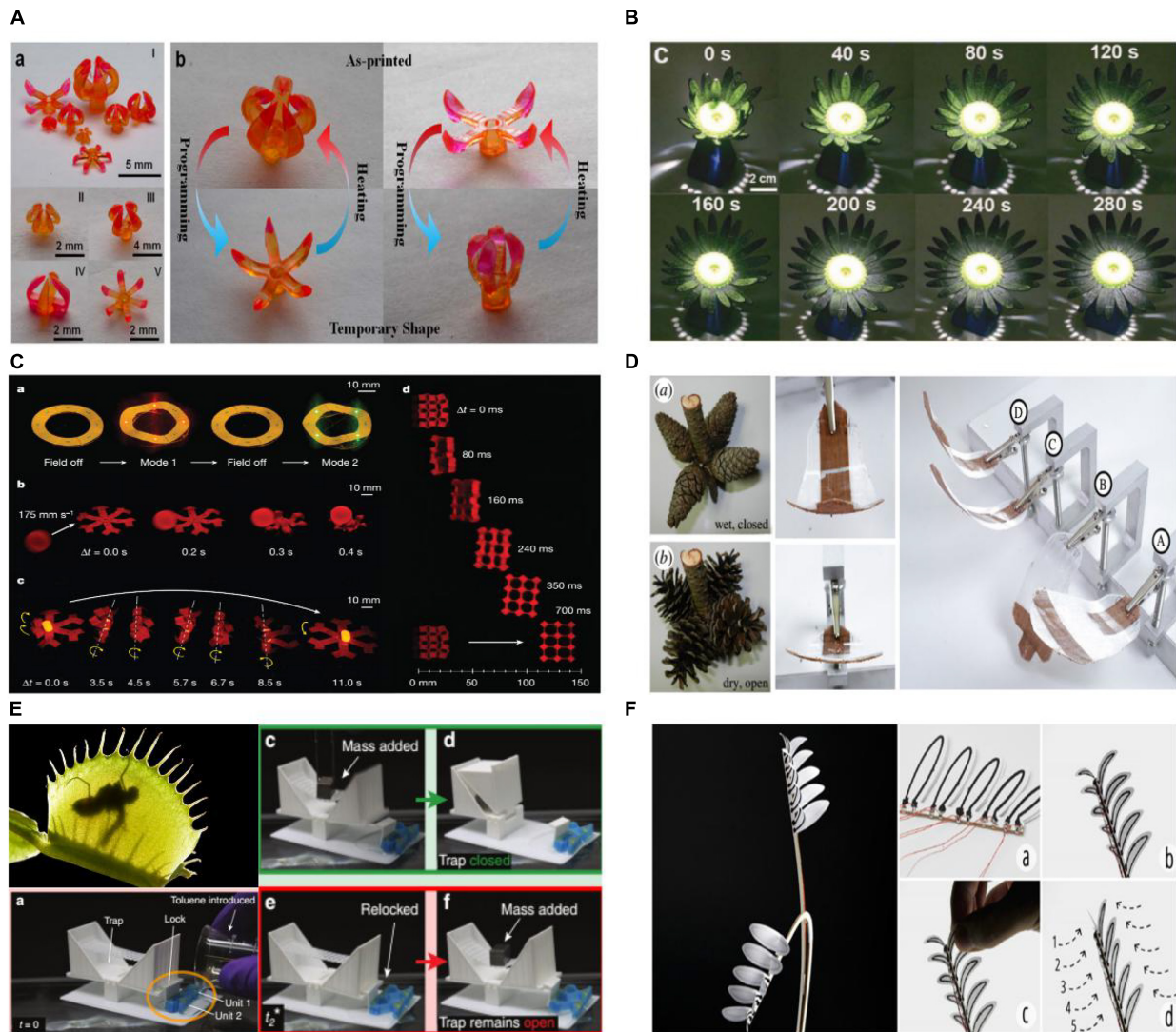
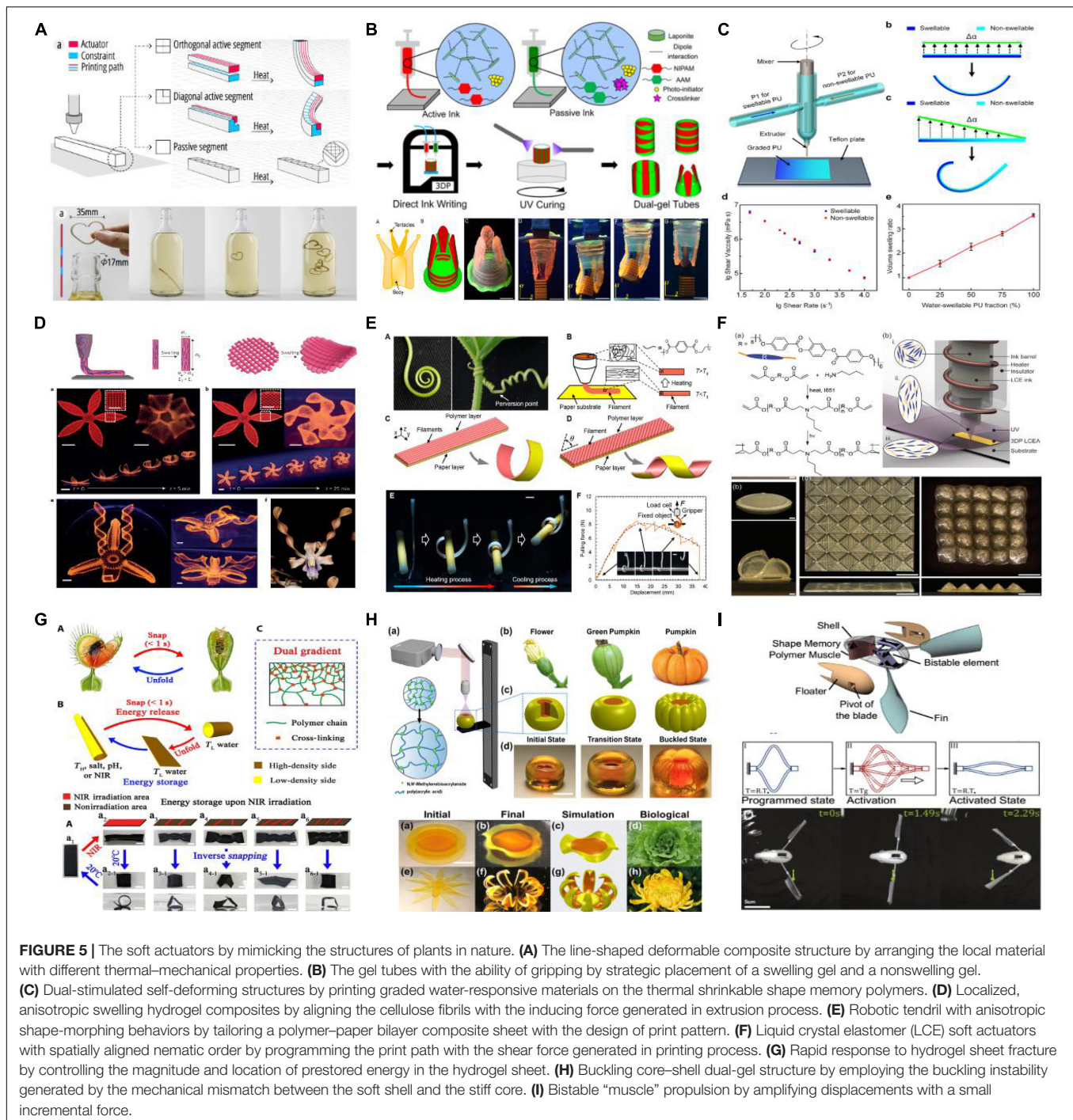


FIGURE 4 | The soft actuators by mimicking the locomotion of plants in nature. **(A)** Sequential recovery of a multimaterial shape memory actuator mimicking the opening and closing of flowers when triggered by heat. **(B)** Blooming of the photoresponsive shape memory composites mimicking the opening of flowers when triggered by light. **(C)** Movements of magnetic responsive soft actuators using programmed magnetic field. **(D)** Bending of the hygroscopic wood polymer composites mimicking the curvature deformation of pine cones. **(E)** Fast closing of two bistable units with embodied logic mimicking the trapping process of the Venus flytrap. **(F)** Sequential actuation of shape memory composites via current-driven Joule heating mimicking the sensing and actuation behaviors of mimosa leaves.

Drawing the principles from the orientation of the cellulose fibers, soft actuators with anisotropic locomotion have been designed and fabricated in the recent research. One of the most representative examples is the hydrogel composite architectures by Lewis and her group (Figure 5D) (Sydney Gladman et al., 2016). They encode local, anisotropic swelling behavior into hydrogel composites *via* aligned cellulose fibers along the prescribed printing path. Using the theoretical framework of the inverse problem and a plant-inspired architecture, complex 3D morphologies are created when immersed in water. Instead of using nanofibers, Wang W. et al. (2018) chose to program anisotropic shape-morphing behaviors by the design of the print pattern (Figure 5E). Due to the internal strains between

bilayers generated in the 3D printing process, the composite sheets with different print patterns transform to diverse shapes. Thus, they developed a robotic tendril imitating the motions of plant tendrils, which is tailored from a polymer–paper bilayer composite sheet. Besides, some active materials can change from isotropic to anisotropic when exposed to certain processing conditions. Kotikian et al. (2018) reported the fabrication of liquid crystal elastomer actuators with aligned nematic order enabled by the shear force generated in the printing process (Figure 5F). The soft actuators possess complex shape-morphing capabilities by designing the print path, including both 2D to 3D and 3D to 3D' transformations as defined in the research.



To fabricate soft actuators with fast response, the above two strategies are insufficient to be used as design principles. Mechanical instability, widely existing in the plant and animal world, is then applied to change this situation and enhance the actuation performance. Fan et al. (2019) reported a nature-inspired responsive hydrogel sheet with the capability of yielding ultrafast snapping-through deformation (Figure 5G). The snapping of the hydrogel sheet is programmed by controlling the magnitude and location of prestored energy within the

hydrogel. Mimicking the circumferential buckling in pumpkins, Yin et al. (2008) reproduced the core-shell double gel structure with bending instability generated by mechanical mismatch between the rigid core-shell and the compliant shell (Figure 5H). It utilizes digital light processing-based technology to design a bending hydrogel, and its buckling behaviors are governed by the radius ratio, swelling ratios, and stiffness mismatch between the core and shell. This design can be widely used for applications like artificial muscle, soft robotics, etc. Chen et al. (2018) created

responsive bistable “muscles” in response to temperature changes using shape memory polymers. Using the bistability instability, a small force can amplify the displacement to the maximum extent (**Figure 5I**).

The Soft Actuators Mimicked *via* Parameter-Driven 4D Printing

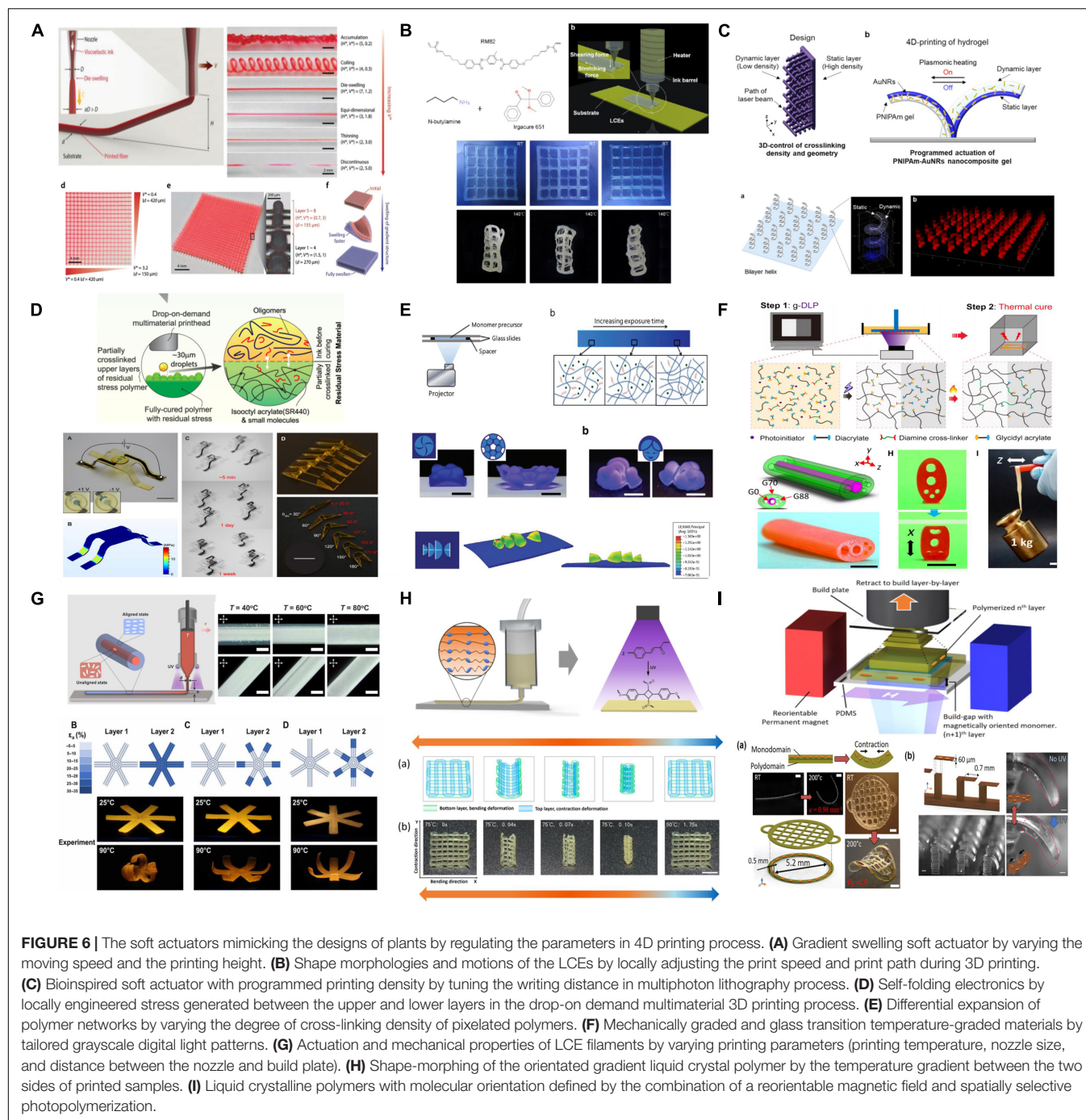
The 4D printing techniques relying on localized structure designs can only be implemented on a pixel-by-pixel basis that inherently limit its speed and resolution. In the process of 3D printing, the properties of printed parts are influenced by the processing parameters. For example, the parameters (e.g., extrusion rate and deposition speed, liquefying and cooling temperature, deposition path, and extrusion head diameter) affect the structures (e.g., degree of molecular order, crystallinity, strength of the line joint, and degree of anisotropy) and properties (e.g., modulus, glass transition temperature, anisotropy, and shape memory property) of the printed components (Bodaghi et al., 2017; Pilz Da Cunha et al., 2019; Zhang et al., 2019). The correlation between the parameters and the material structures (properties) offers us a practical method to regulate the shape-morphing behaviors of the printed components.

Yuk and Zhao (2018) reported a new strategy to print multiple diameters of fibers without changing the nozzle by simply selecting the appropriate printing parameters. Swelling actuator with a gradient 3D mesh has been printed by varying the moving speed and the printing height. As the actuator expands in the solvent, it initially bends to one direction and gradually flattens out (**Figure 6A**). However, they only build the quantitative phase diagrams for the new strategy, and the mechanism underneath is not clarified. In the following research, this concept is applied to smart materials, and the mechanisms have been gradually figured out. Changes in most parameters during the printing process always disturb the microstructures, which is eventually reflected in the deformations of these printed structures. Ren et al. (2020) demonstrated that by local modification of the print speed and print path in the 3D printing process, the orientating degrees of molecules of liquid crystal elastomers are dynamically coded. Hence, the shape-morphing and movement of the LCE strips can be fine sculpted (**Figure 6B**) (Ren et al., 2020). In addition to print speed, print height, and print path, print density has a direct effect on deformation as well. Nishiguchi et al. (2020) reported a biomimetic soft actuator with predetermined 3D geometry and programmed print density at pixel-by-pixel by tuning the writing distance in multiphoton lithography process. The smaller distance between the focal lines leads to a high printing density. The dynamic layer with low printing density is able to actuate in response to external stimuli, so the bilayer structure can exhibit anisotropic shape-morphing (**Figure 6C**). Sundaram et al. (2017) presented a manufacturing method of an electronic composite material that automatically folds at room temperature by locally engineered stress generated in the drop-on demand multimaterial 3D-printing process. The stress is accumulated during the layer-by-layer 3D printing process. A portion of the new ink diffuses into the partially cross-linked layer below before UV light is applied. They automatically fold to form preprogrammed 3D structures

upon release from their restraints (**Figure 6D**). When the liquid resin is cured by light radiation, the light conditions (light dose, light distribution, etc.) are the most important factors influencing the microstructures and the deformation. Huang et al. (2017) created self-deforming polymer networks with different cross-linking densities using different exposure times (light doses). The difference in cross-link density induces differential swelling of the sample in water, which turns the 2D film into a 3D object (**Figure 6E**). Subsequently, Kuang et al. (2019b) present broadly tailored functional gradients (light distribution) using grayscale light patterns to obtain functionally graded materials. The modulus of the customized gradient is up to three orders of magnitude and the glass transition temperature is up to 60°C (**Figure 6F**). Temperature also affects the microstructures of the active materials and, thus, influences the shape-morphing behaviors. Wang et al. (2020) reported a strategy to adjust the kinetic behavior and mechanical properties of printed filaments. Print temperature, nozzle size, and print height are dynamically regulated to investigate their influence on filament morphologies (Wang et al., 2020). As a proof of concept, they designed bilayer structures with six petals and with graded strain in the top layer by controlling the printing temperature, mimicking blooming flowers when heated in hot water (**Figure 6G**). Besides, Zhang et al. (2019) enabled 4D printing with monocomponent liquid crystal polymer inks with an orientation gradient perpendicular to the printing direction through the direct ink writing technology. Due to the temperature gradient between the two sides of the printed sample, an orientation gradient perpendicular to the printing direction is obtained, enabling a strip transforming to a tightly hollow cylinder. The liquid-assisted printing or programmed structure design enables the integration of both bending and shrinking actuation modes on the same printed sample (**Figure 6H**). In addition to the printing parameters of 3D printing itself, external assisting fields (magnetic, electric, etc.) also play an important role in controlling deformation. Tabrizi et al. (2019) exploited the combination of a reorientable magnetic field and spatially selective photopolymerization to independently define molecular orientation of liquid crystalline polymers in light- and/or heat-responsive multimaterial elements. They can adjust digital micromirrors and redirectable magnetic fields to construct complicated geometries like Gaussian curvatures, leading to the multiresponsive robotic manipulators (**Figure 6I**).

The Soft Actuators Mimicked *via* Stimulus-Driven 4D Printing

Most 4D-printed soft actuators tend to focus on the design of the materials and structures of the actuators. These works are often accomplished prior to the 3D printing process. However, there is an alternative approach that allows for local anisotropic actuation as well—the selection and manipulation of multiple stimuli (Lee and Fang, 2012; Deng et al., 2018; Cui et al., 2019, 2020). Kotikian et al. (2019) printed untethered soft robotic matter that allows repeated shaping and self-propulsion in response to external stimuli. The liquid crystal elastomer bilayers are printed with the orthogonal director arrangement and different nematic to anisotropic transition temperatures.



The soft robotic consists of active hinges that interconnect the polymer tiles. When heated above their respective actuation temperatures, the soft robotic exhibits three stable configurations and self-rolling in programmed reactions to thermal stimuli (Figure 7A). Light is also commonly used as sources of energy (light converting to heat) or stimuli (molecule transformation) in the soft actuation. del Pozo et al. (2020) presented light-triggered bending actuators in response to temperature changes *via* liquid crystal oligomeric ink (Figure 7B). When illuminated at room temperature, the LCE actuator produces motion away

from the light source. When lighting at high temperatures ($>45^{\circ}\text{C}$), the same actuator bends toward the direction of the light source. Besides, moisture in the atmosphere can also be manipulated to tune the dynamic performance in the 4D transformation. Correa et al. (2015) present a multimaterial printing method for designing components consisting of synthetic wood and polymers. The wood with moisture-absorbing and swelling properties achieves curling and self-folding behavior through 3D printing technology (Figure 7C). In addition to moisture changes, the chemical stimuli are also



FIGURE 7 | The soft actuators mimicking the designs of plants by manipulating the stimulus in 4D printing process. **(A)** Shape-morphing and self-propelling of liquid crystal elastomer bilayers in programmed responses to thermal stimuli. **(B)** Amphibious light-actuated actuators generating motion toward/away from the light source regulated by temperature. **(C)** The curling and self-folding behaviors of wood in preprogrammed response to moisture. **(D)** Grayscale 4D-printed reversible self-folding structures by immersing in acetone and dried in air. **(E)** Active shape-changing architectures exhibiting magnetically guidable properties by the addition of iron oxide. **(F)** Joule heating stimulated active composites by printing conductive wires into LCE strips. **(G)** Multistimuli-responsive material by the addition of conductive carbon reinforcements into a moisture-sensitive polymer. **(H)** Hydrophobic cross-linked liquid crystal polymer film featuring both activation using moisture gradient and UV light. **(I)** Multiresponsive patternable actuator responding to humidity, temperature, and light via accurate structuring on graphene oxide films by the microstamping of hydrogel.

widely used for deformation. Wu et al. (2018) proposed that 3D grayscale printing could be employed to create reversible self-folding structures when immersed in acetone and dried in air. Removal of the uncured oligomer with acetone results in shrinkage of the polymer volume, inducing reversible self-expansion/shrinkage deformation (Figure 7D). External fields (magnetic fields, electric fields, etc.) as a means of external stimulation often allow for more precise, localized actuation. Wei et al. (2017) integrated 4D shape-changing object by adding iron oxide to exhibit thermal and remotely actuated behavior (Figure 7E). Electricity is a frequently used energy for conventional actuators, and it is also applicable as local manipulation tools of soft actuators. Yuan et al. (2017) printed active composites by electronics and LCEs, where Joule heating

produced by printed conductive wires is utilized to activate LCE strips. The strains generated between the LCE and the substrate cause the deflection of the hinge in the isotropic state (Figure 7F). The integration of several responsive moieties within one material and the combination of several materials with different stimuli response both endow smart materials with complex responsive behaviors. Le Duigou et al. (2019) proposed a multiresponsive composite material based on 4D printing with electrothermal dual actuation. Conductive carbon reinforcements and a moisture-sensitive polymer are used with a specific microstructure mimicking the anisotropic structure of pine cones. Changes in ambient humidity and electrical heating through the Joule effect can both actuate functional materials (Figure 7G). Liu et al. (2017) fabricated hydrophobic cross-linked

liquid crystal polymer films with dual responses of humidity gradients and UV light. The film performs sophisticated motions by being exposed to humidity gradients. In addition, the film with the addition of azobenzene chromophores also responds to UV light. It tilts toward the incidence direction when irradiated by UV light (365 nm, 40 mW cm⁻²), and returns to the initial state when irradiated by light irradiation (530 nm, 60 mW cm⁻²) (Figure 7H). Dong et al. (2019) proposed a multiresponsive actuator in response to humidity, temperature, and light by patterning on a graphene oxide film. They have developed a variety of biomimetic structures. Mimicking a hawk's claw and tendril, they designed intelligent grippers using crossed and spiral structures; mimicking the walk of an inchworm, they designed a soft walking robot that can move forward with the stimulation of infrared light (Figure 7I).

CHALLENGES AND OUTLOOKS

Plants are blueprints for us to understand how the tailored, hinge-free motions and motion sequences are generated *via* simple deformations in a microscale. Plant-inspired 4D printing presents a magnificent initiation into synthetic active materials and structures that can autonomously perceive and respond in a programmed way to the surroundings. How to design the program scheme and embed the programming logic into the materials is fundamental and crucial to 4D printing technology (Joshi et al., 2020). Plants provide the strategy for shape-morphing *via* compositional and structural design motifs. However, the correspondences between specific functions and functioning structures are not fully established. In the steps of biomimicry, it is essential to construct shape-shifting methodologies to have a better understanding of the actuation controllability. The given mechanisms should be able to be scaled, distorted, and reorganized to serve as a variety of structural motifs (Moulia, 2013).

In addition to the theoretical model, there is a need for practical software tools that can model and simulate the shape-shifting procedure. The software should be able to deal with the 4D behavior in a forward and/or inverse way, respectively. Currently, the vast majority of 4D printing researches are based on trial-and-error experiments, which need highly expert abilities and are often time-consuming. To facilitate the development and applications of 4D printing, accessible and straightforward software should be developed (Zolfagharian et al., 2020). In addition, to characterize biological materials with nonhomogeneous and ordered architecture, such as functionally graded materials, a special software is required. On the other

hand, how to replicate the hierarchical and heterogeneous materials plant used *via* 4D printing process is another big challenge that plant-mimetic 4D printing faces. For most 3D printing technologies, they hardly have a control over the constituent and internal structure of the printed materials, which makes it difficult to fabricate such biomimetic materials. A whole workflow for 3D printing of bioinspired materials needs to be developed, involving slicer, firmware, and monitoring (Goh et al., 2020). A new slicer should enable a hybrid model to be processed, deriving not only geometrical but also material and structural information and even the process parameters as well (McPherson et al., 2020). Developments in new printing technologies that merge self-assembly with additive manufacturing to produce microstructural materials and process with the ability to print functionally graded materials are required (Loh et al., 2018).

In general, biomimetic 4D printing provides new design perspectives and fabrication tools for developing the next generation of functional structures that are adaptive in controlled or uncontrolled environmental cues. Its unique bottom-up manufacturing way makes it a promising candidate for the manufacturing of bioinspired hierarchical shape-morphing structures. Rather than just being a new concept, it is a manufacturing model. By the method of 4D printing, new products or applications with unique features that are difficult to manufacture in other ways will be available. Biomimetic 4D printing is still in the early and explosive boosting stage, and there will be a series of applications in a variety of fields in the near future. We envision that it will be extensively applicable to various fields ranging from soft robotics to medical, food, aerospace, and many other domains.

AUTHOR CONTRIBUTIONS

BL and QL wrote the manuscript. LQR and LR helped polish the language and rearranged the structure of the review. All authors contributed to the article and approved the submitted version.

FUNDING

The study was supported by the National Key Research and Development Program of China (Grant No. 2018YFF01012400).

ACKNOWLEDGMENTS

BL acknowledges the financial support of the China Scholarship Council (CSC).

REFERENCES

- Alapan, Y., Karacakol, A. C., Guzelhan, S. N., Isik, I., and Sitti, M. (2020). Reprogrammable shape morphing of magnetic soft machines. *Sci. Adv.* 6:eabc6414. doi: 10.1126/sciadv.abc6414
- Armon, S., Efrati, E., Kupferman, R., and Sharon, E. (2011). Geometry and mechanics in the opening of chiral seed pods. *Science* 333, 1726–1730.
- Bodaghi, M., Damanpack, A. R., and Liao, W. H. (2017). Adaptive metamaterials by functionally graded 4D printing. *Mater. Des.* 135, 26–36. doi: 10.1016/j.matdes.2017.08.069
- Boley, J. W., van Rees, W. M., Lissandrello, C., Horenstein, M. N., Truby, R. L., Kotikian, A., et al. (2019). Shape-shifting structured lattices via multimaterial 4D printing. *Proc. Natl. Acad. Sci. U.S.A.* 116, 20856–20862. doi: 10.1073/pnas.1908806116

- Braam, J. (2005). In touch: plant responses to mechanical stimuli. *New Phytol.* 165, 373–389. doi: 10.1111/j.1469-8137.2004.01263.x
- Chen, T., Bilal, O. R., Shea, K., and Daraio, C. (2018). Harnessing bistability for directional propulsion of soft, untethered robots. *Proc. Natl. Acad. Sci. U.S.A.* 115, 5698–5702. doi: 10.1073/pnas.1800386115
- Cho, K.-J., Koh, J.-S., Kim, S., Chu, W.-S., Hong, Y., and Ahn, S.-H. (2009). Review of manufacturing processes for soft biomimetic robots. *Int. J. Precis. Eng. Manuf.* 10, 171–181. doi: 10.1007/s12541-009-0064-6
- Correa, D., Papadopoulou, A., Guberan, C., Jhaveri, N., Reichert, S., Menges, A., et al. (2015). 3D-printed wood: programming hygroscopic material transformations. *3D Print. Addit. Manuf.* 2, 106–116. doi: 10.1089/3dp.2015.0022
- Correa, D., Poppinga, S., Mylo, M. D., Westermeier, A. S., Bruchmann, B., Menges, A., et al. (2020). 4D pine scale: biomimetic 4D printed autonomous scale and flap structures capable of multi-phase movement. *Philos. Trans. R. Soc. A Math. Phys. Eng. Sci.* 378:20190445. doi: 10.1098/rsta.2019.0445
- Cui, H., Miao, S., Esworthy, T., Lee, S. Jr., Zhou, X., Hann, S. Y., et al. (2019). A novel near-infrared light responsive 4D printed nanoarchitecture with dynamically and remotely controllable transformation. *Nano Res.* 12, 1381–1388. doi: 10.1007/s12274-019-2340-9
- Cui, H., Zhao, Q., Zhang, L., and Du, X. (2020). Intelligent polymer-based bioinspired actuators: from monofunction to multifunction. *Adv. Intell. Syst.* 2:2000138. doi: 10.1002/aisy.202000138
- Dawson, C., Vincent, J. F. V., and Rocca, A.-M. (1997). How pine cones open. *Nature* 390, 668–668. doi: 10.1038/37745
- De Marco, C., Pané, S., and Nelson, B. J. (2018). 4D printing and robotics. *Sci. Robot.* 3, 287–294. doi: 10.1126/scirobotics.aau0449
- Deegan, R. D. (2012). Finessing the fracture energy barrier in ballistic seed dispersal. *Proc. Natl. Acad. Sci. U.S.A.* 109, 5166–5169. doi: 10.1073/pnas.1119737109
- del Pozo, M., Liu, L., Pilz da Cunha, M., Broer, D. J., and Schenning, A. P. H. J. (2020). Direct ink writing of a light-responsive underwater liquid crystal actuator with atypical temperature-dependent shape changes. *Adv. Funct. Mater.* 30:2005560. doi: 10.1002/adfm.202005560
- Deng, H., Zhang, C., Su, J. W., Xie, Y., Zhang, C., and Lin, J. (2018). Bioinspired multi-responsive soft actuators controlled by laser tailored graphene structures. *J. Mater. Chem. B* 6, 5415–5423. doi: 10.1039/c8tb01285g
- Deshmukh, K., Houkan, M. T., AlMaadeed, M. A. A., and Sadasivunidi, K. K. (2019). “Introduction to 3D and 4D printing technology: state of the art and recent trends,” in *3D and 4D Printing of Polymer Nanocomposite Materials: Processes, Applications, and Challenges*, eds K. Sadasivuni, K. Deshmukh, and M. A. AlMaadeed (Amsterdam: Elsevier), doi: 10.1016/B978-0-12-816805-9.00001-6
- Dong, Y., Wang, J., Guo, X., Yang, S., Ozen, M. O., Chen, P., et al. (2019). Multi-stimuli-responsive programmable biomimetic actuator. *Nat. Commun.* 10, 1–10. doi: 10.1038/s41467-019-12044-5
- Du, S., and Yamamoto, F. (2007). An overview of the biology of reaction wood formation. *J. Integr. Plant Biol.* 49, 131–143.
- Dumais, J., and Forterre, Y. (2012). “Vegetable dynamics”: the role of water in plant movements. *Annu. Rev. Fluid Mech.* 44, 453–478. doi: 10.1146/annurev-fluid-120710-101200
- Durga Prasad Reddy, R., and Sharma, V. (2020). Additive manufacturing in drug delivery applications: a review. *Int. J. Pharm.* 589, 119820. doi: 10.1016/j.ijpharm.2020.119820
- Egan, P., Sinko, R., LeDuc, P. R., and Ketten, S. (2015). The role of mechanics in biological and bio-inspired systems. *Nat. Commun.* 6, 1–12. doi: 10.1038/ncomms8418
- Elbaum, R., and Abraham, Y. (2014). Insights into the microstructures of hygroscopic movement in plant seed dispersal. *Plant Sci.* 223, 124–133. doi: 10.1016/j.plantsci.2014.03.014
- Evangelista, D., Hutton, S., and Dumais, J. (2011). The mechanics of explosive dispersal and self-burial in the seeds of the filaree, *Erodium cicutarium* (Geraniaceae). *J. Exp. Biol.* 214, 521–529. doi: 10.1242/jeb.050567
- Fagerstedt, K., and Karkonen, A. (2015). Plant cell wall. *J. Integr. Plant Biol.* 57, 326–445. doi: 10.1111/jipb.12351
- Fan, W., Shan, C., Guo, H., Sang, J., Wang, R., Zheng, R., et al. (2019). Dual-gradient enabled ultrafast biomimetic snapping of hydrogel materials. *Sci. Adv.* 5:eaav7174. doi: 10.1126/sciadv.aav7174
- Forterre, Y. (2013). Slow, fast and furious: understanding the physics of plant movements. *J. Exp. Bot.* 64, 4745–4760. doi: 10.1093/jxb/ert230
- Forterre, Y., Marmottant, P., Quilliet, C., and Noblin, X. (2016). Physics of rapid movements in plants. *Europhys. News* 47, 27–30. doi: 10.1051/epn/2016104
- Forterre, Y., Skotheim, J. M., Dumais, J., and Mahadevan, L. (2005). How the *Venus flytrap* snaps. *Nature* 433, 421–425. doi: 10.1038/nature03185
- Ge, Q., Sakhaei, A. H., Lee, H., Dunn, C. K., Fang, N. X., and Dunn, M. L. (2016). Multimaterial 4D printing with tailorable shape memory polymers. *Sci. Rep.* 6, 1–11. doi: 10.1038/srep31110
- Goh, G. D., Sing, S. L., and Yeong, W. Y. (2020). A review on machine learning in 3D printing: applications, potential, and challenges. *Artif. Intell. Rev.* 54, 63–94. doi: 10.1007/s10462-020-09876-9
- Gregory, T. R. (2009). Understanding natural selection: essential concepts and common misconceptions. *Evol. Educ. Outreach* 2, 156–175. doi: 10.1007/s12052-009-0128-1
- Guiducci, L., Razghandi, K., Bertinetti, L., Turcaud, S., Rüggeberg, M., Weaver, J. C., et al. (2016). Honeycomb actuators inspired by the unfolding of ice plant seed capsules. *PLoS One* 11:e0163506. doi: 10.1371/journal.pone.0163506
- Gul, J. Z., Sajid, M., Rehman, M. M., Siddiqui, G. U., Shah, I., Kim, K. H., et al. (2018). 3D printing for soft robotics—a review. *Sci. Technol. Adv. Mater.* 19, 243–262. doi: 10.1080/14686996.2018.1431862
- Guo, Q., Dai, E., Han, X., Xie, S., Chao, E., and Chen, Z. (2015). Fast nastic motion of plants and bio-inspired structures. *J. R. Soc. Interface* 12:20150598. doi: 10.1098/rsif.2015.0598
- Hashemi Farzaneh, H., Helms, M. K., Muenzberg, C., and Lindemann, U. (2016). “Technology-pull and biology-push approaches in bio-inspired design – comparing results from empirical studies on student teams,” in *Proceedings of International Design Conference*, eds M. Dorian, S. Mario, P. Neven, B. Nenad, and S. Stanko (Glasgow: DESIGN).
- Hedrich, R., and Neher, E. (2018). Venus flytrap: how an excitable, carnivorous plant works. *Trends Plant Sci.* 23, 220–234. doi: 10.1016/j.tplants.2017.12.004
- Huang, L., Jiang, R., Wu, J., Song, J., Bai, H., Li, B., et al. (2017). Ultrafast digital printing toward 4D shape changing materials. *Adv. Mater.* 29:1605390. doi: 10.1002/adma.201605390
- Jiang, Y., Korpas, L. M., and Raney, J. R. (2019). Bifurcation-based embodied logic and autonomous actuation. *Nat. Commun.* 10, 1–10. doi: 10.1038/s41467-018-08055-3
- Joshi, S., Rawat, K., Karunakaran, C., Rajamohan, V., Mathew, A. T., Koziol, K., et al. (2020). 4D printing of materials for the future: opportunities and challenges. *Appl. Mater. Today* 18:100490. doi: 10.1016/j.apmt.2019.100490
- Jung, W., Kim, W., and Kim, H.-Y. (2014). Self-burial mechanics of hygroscopically responsive awns. *Integr. Comp. Biol.* 54, 1034–1042. doi: 10.1093/icb/icu026
- Kanu, N. J., Gupta, E., Vates, U. K., and Singh, G. K. (2019). An insight into biomimetic 4D printing. *RSC Adv.* 9, 38209–38226. doi: 10.1039/c9ra07342f
- Kim, H., Lee, H., Ha, I., Jung, J., Won, P., Cho, H., et al. (2018). Biomimetic color changing anisotropic soft actuators with integrated metal nanowire percolation network transparent heaters for soft robotics. *Adv. Funct. Mater.* 28:1801847. doi: 10.1002/adfm.201801847
- Kim, Y., Yuk, H., Zhao, R., Chester, S. A., and Zhao, X. (2018). Printing ferromagnetic domains for untethered fast-transforming soft materials. *Nature* 558, 274–279. doi: 10.1038/s41586-018-0185-0
- Kotikian, A., McMahan, C., Davidson, E. C., Muhammad, J. M., Weeks, R. D., Daraio, C., et al. (2019). Untethered soft robotic matter with passive control of shape morphing and propulsion. *Sci. Robot.* 4:eaax7044. doi: 10.1126/scirobotics.aax7044
- Kotikian, A., Truby, R. L., Boley, J. W., White, T. J., and Lewis, J. A. (2018). 3D printing of liquid crystal elastomeric actuators with spatially programmed nematic order. *Adv. Mater.* 30:1706164. doi: 10.1002/adma.201706164
- Kuang, X., Roach, D. J., Wu, J., Hamel, C. M., Ding, Z., Wang, T., et al. (2019a). Advances in 4D printing: materials and applications. *Adv. Funct. Mater.* 29:1805290. doi: 10.1002/adfm.201805290
- Kuang, X., Wu, J., Chen, K., Zhao, Z., Ding, Z., Hu, F., et al. (2019b). Grayscale digital light processing 3D printing for highly functionally graded materials. *Sci. Adv.* 5:eaav5790. doi: 10.1126/sciadv.aav5790

- Le Duigou, A., Chabaud, G., Scarpa, F., and Castro, M. (2019). Bioinspired electro-thermo-hygro reversible shape-changing materials by 4D printing. *Adv. Funct. Mater.* 29:1903280. doi: 10.1002/adfm.201903280
- Lee, H., and Fang, N. X. (2012). Micro 3D printing using a digital projector and its application in the study of soft materials mechanics. *J. Vis. Exp.* 69:e4457. doi: 10.3791/4457
- Liu, J., Erol, O., Pantula, A., Liu, W., Jiang, Z., Kobayashi, K., et al. (2019). Dual-Gel 4D printing of bioinspired tubes. *ACS Appl. Mater. Interfaces* 11, 8492–8498. doi: 10.1021/acsami.8b17218
- Liu, Y., Xu, B., Sun, S., Wei, J., Wu, L., and Yu, Y. (2017). Humidity- and photo-induced mechanical actuation of cross-linked liquid crystal polymers. *Adv. Mater.* 29:1604792. doi: 10.1002/adma.201604792
- Loh, G. H., Pei, E., Harrison, D., and Monzón, M. D. (2018). An overview of functionally graded additive manufacturing. *Addit. Manuf.* 23, 34–44. doi: 10.1016/j.addma.2018.06.023
- Lui, Y. S., Sow, W. T., Tan, L. P., Wu, Y., Lai, Y., and Li, H. (2019). 4D printing and stimuli-responsive materials in biomedical aspects. *Acta Biomater.* 92, 19–36. doi: 10.1016/j.actbio.2019.05.005
- McCracken, J. M., Donovan, B. R., and White, T. J. (2020). Materials as machines. *Adv. Mater.* 32:1906564. doi: 10.1002/adma.201906564
- McPherson, J., Bliss, A., Smith, F., Harriss, E., and Zhou, W. (2020). “A slicer and simulator for cooperative 3D printing. in Solid Freeform Fabrication 2017,” in *Proceedings of the 28th Annual International Solid Freeform Fabrication Symposium – An Additive Manufacturing Conference, SFF 2017*, Fayetteville, AR.
- Menges, A., Sheil, B., Glynn, R., Skavara, M., Correa, D., and Menges, A. (2017). “Fused filament fabrication for multi-kinematic-state climate-responsive aperture,” in *Fabricate*, eds A. Menges, B. Sheil, R. Glynn, and M. Skavara (London: UCL Press), 44–47. doi: 10.2307/j.ctt1n7qkg7.30
- Miriye, A., Stack, K., and Lipson, H. (2017). Soft material for soft actuators. *Nat. Commun.* 8, 1–8. doi: 10.1038/s41467-017-00685-3
- Mitchell, A., Lafont, U., Holyńska, M., and Semprinoschnig, C. (2018). Additive manufacturing — A review of 4D printing and future applications. *Addit. Manuf.* 24, 606–626. doi: 10.1016/j.addma.2018.10.038
- Momeni, F., Mehdi Hassani, N. S. M., Liu, X., and Ni, J. (2017). A review of 4D printing. *Mater. Des.* 122, 42–79. doi: 10.1016/j.matdes.2017.02.068
- Montero de Espinosa, L., Meesorn, W., Moatsou, D., and Weder, C. (2017). Bioinspired polymer systems with stimuli-responsive mechanical properties. *Chem. Rev.* 117, 12851–12892. doi: 10.1021/acs.chemrev.7b00168
- Mouli, B. (2013). Plant biomechanics and mechanobiology are convergent paths to flourishing interdisciplinary research. *J. Exp. Bot.* 64, 4617–4633. doi: 10.1093/jxb/ert320
- Nishiguchi, A., Zhang, H., Schweizerhof, S., Schulte, M. F., Mourran, A., and Möller, M. (2020). 4D printing of a light-driven soft actuator with programmed printing density. *ACS Appl. Mater. Interfaces* 12, 12176–12185. doi: 10.1021/acsami.0c02781
- Pfeifer, R., and Gomez, G. (2009). “Morphological computation – connecting brain, body, and environment,” in *Creating Brain-Like Intelligence. Lecture Notes in Computer Science*, Vol. 5436, eds B. Sendhoff, E. Körner, O. Sporns, H. Ritter, and K. Doya (Berlin: Springer), 66–83. doi: 10.1007/978-3-642-00616-6_5
- Pfeifer, R., Lungarella, M., and Iida, F. (2012). The challenges ahead for bio-inspired “soft” robotics. *Commun. ACM* 55, 76–87. doi: 10.1145/2366316.2366335
- Pilz Da Cunha, M., Peeketi, A. R., Mehta, K., Broer, D. J., Annabattula, R. K., Schenning, A. P. H. J., et al. (2019). A self-sustained soft actuator able to rock and roll. *Chem. Commun.* 55, 11029–11032. doi: 10.1039/c9cc05329h
- Poppinga, S., Correa, D., Bruchmann, B., Menges, A., and Speck, T. (2020). Plant movements as concept generators for the development of biomimetic compliant mechanisms. *Integr. Comp. Biol.* 60, 886–895. doi: 10.1093/icb/ica028
- Poppinga, S., Hartmeyer, S. R. H., Seidel, R., Masselter, T., Hartmeyer, I., and Speck, T. (2012). Catapulting tentacles in a sticky carnivorous plant. *PLoS One* 7:e45735. doi: 10.1371/journal.pone.0045735
- Poppinga, S., Haushahn, T., Warnke, M., Masselter, T., and Speck, T. (2015). Sporangium exposure and spore release in the peruvian maidenhair fern (*Adiantum peruvianum*, Pteridaceae). *PLoS One* 10:e0138495. doi: 10.1371/journal.pone.0138495
- Poppinga, S., Weisskopf, C., Westermeier, A. S., Masselter, T., and Speck, T. (2016). Fastest predators in the plant kingdom: functional morphology and biomechanics of suction traps found in the largest genus of carnivorous plants. *AoB Plants* 8:lv140. doi: 10.1093/aobpla/plv140
- Quan, H., Kisailus, D., and Meyers, M. A. (2020). Hydration-induced reversible deformation of biological materials. *Nat. Rev. Mater.* 6, 264–283. doi: 10.1038/s41578-020-00251-2
- Ren, L., Li, B., He, Y., Song, Z., Zhou, X., Liu, Q., et al. (2020). Programming shape-morphing behavior of liquid crystal elastomers via parameter-encoded 4D printing. *ACS Appl. Mater. Interfaces* 12, 15562–15572. doi: 10.1021/acsami.0c00027
- Reyssat, E., and Mahadevan, L. (2009). Hygromorphs: from pine cones to biomimetic bilayers. *J. R. Soc. Interface* 6, 951–957. doi: 10.1098/rsif.2009.0184
- Sakes, A., van der Wiel, M., Henselmans, P. W. J., van Leeuwen, J. L., Dodou, D., and Breedveld, P. (2016). Shooting mechanisms in nature: a systematic review. *PLoS One* 11:e0158277. doi: 10.1371/journal.pone.0158277
- Scorza, L. C. T., and Dornelas, M. C. (2011). Plants on the move: toward common mechanisms governing mechanically-induced plant movements. *Plant Signal. Behav.* 6, 1979–1986. doi: 10.4161/psb.6.12.18192
- Selaginella, R. P., Western, T. L., Pasini, D., and Rafsanjani, A. (2015). Hydro-responsive curling of the resurrection plant *Selaginella lepidophylla*. *Sci. Rep.* 5:8064. doi: 10.1038/srep08064
- Shafraanek, R. T., Millik, S. C., Smith, P. T., Lee, C. U., Boydston, A. J., and Nelson, A. (2019). Stimuli-responsive materials in additive manufacturing. *Prog. Polym. Sci.* 93, 36–67. doi: 10.1016/j.progpolymsci.2019.03.002
- Skothheim, J. M. (2005). Physical limits and design principles for plant and fungal movements. *Science* 308, 1308–1310. doi: 10.1126/science.1107976
- Song, Z., Ren, L., Zhao, C., Liu, H., Yu, Z., Liu, Q., et al. (2020). Biomimetic nonuniform, dual-stimuli self-morphing enabled by gradient four-dimensional printing. *ACS Appl. Mater. Interfaces* 12, 6351–6361. doi: 10.1021/acsami.9b17577
- Stuart, A. R., and Erb, R. M. (2014). Bioinspired materials that self-shape through programmed microstructures. *Soft Matter* 10, 1284–1294. doi: 10.1039/C3SM51883C
- Sun, L., Li, J., Chen, Y., Yang, Y., Tao, Y., Wang, G., et al. (2020). “4DTexture: a shape-changing fabrication method for 3D surfaces with texture,” in *Proceedings of the Conference on Human Factors in Computing Systems*, (New York, NY: Association for Computing Machinery), 1–7. doi: 10.1145/3334480.3383053
- Sundaram, S., Kim, D. S., Baldo, M. A., Hayward, R. C., and Matusik, W. (2017). 3D-printed self-folding electronics. *ACS Appl. Mater. Interfaces* 9, 32290–32298. doi: 10.1021/acsami.7b10443
- Sydney Gladman, A., Matsumoto, E. A., Nuzzo, R. G., Mahadevan, L., and Lewis, J. A. (2016). Biomimetic 4D printing. *Nat. Mater.* 15, 413–418. doi: 10.1038/nmat4544
- Tabrizi, M., Ware, T. H., and Shankar, M. R. (2019). Voxellated molecular patterning in three-dimensional freeforms. *ACS Appl. Mater. Interfaces* 11, 28236–28245. doi: 10.1021/acsami.9b04480
- Tseng, T. L. B., Akundi, A., and Kim, H. (2018). “4-D printing of pressure sensors and energy harvesting devices for engineering education,” in *ASEE Annual Conference and Exposition, Conference Proceedings*, (Washington, DC: ASEE), doi: 10.18260/1-2-29654
- Vincent, J. F. V., Bogatyreva, O. A., Bogatyrev, N. R., Bowyer, A., and Pahl, A.-K. (2006). Biomimetics: its practice and theory. *J. R. Soc. Interface* 3, 471–482. doi: 10.1098/rsif.2006.0127
- Volkov, A. G., Foster, J. C., Ashby, T. A., Walker, R. K., Johnson, J. A., and Markin, V. S. (2010a). *Mimosa pudica*: Electrical and mechanical stimulation of plant movements. *Plant Cell Environ.* 33, 163–173. doi: 10.1111/j.1365-3040.2009.02066.x
- Volkov, A. G., Foster, J. C., Baker, K. D., and Markin, V. S. (2010b). Mechanical and electrical anisotropy in *Mimosa pudica* pulvini. *Plant Signal. Behav.* 5, 1211–1221. doi: 10.4161/psb.5.10.12658
- Wang, G., Do, Y., Cheng, T., Yang, H., Tao, Y., Gu, J., et al. (2018). “Demonstrating printed paper actuator: a low-cost reversible actuation and sensing method for shape changing interfaces,” in *Conference on Human Factors in Computing Systems – Proceedings*, Yokohama, doi: 10.1145/3170427.3186531
- Wang, G., Tao, Y., Capunaman, O. B., Yang, H., and Yao, L. (2019). “A-line: 4D printing morphing linear composite structures,” in *Conference on Human Factors in Computing Systems – Proceedings*, (New York, NY: Association for Computing Machinery), doi: 10.1145/3290605.3300656

- Wang, W., Li, C., Cho, M., and Ahn, S. H. (2018). Soft tendril-inspired grippers: shape morphing of programmable polymer-paper bilayer composites. *ACS Appl. Mater. Interfaces* 10, 10419–10427. doi: 10.1021/acsami.7b18079
- Wang, Z., Wang, Z., Zheng, Y., He, Q., Wang, Y., and Cai, S. (2020). Three-dimensional printing of functionally graded liquid crystal elastomer. *Sci. Adv.* 6:eabc0034. doi: 10.1126/sciadv.abc0034
- Wei, H., Zhang, Q., Yao, Y., Liu, L., Liu, Y., and Leng, J. (2017). Direct-write fabrication of 4D active shape-changing structures based on a shape memory polymer and its nanocomposite. *ACS Appl. Mater. Interfaces* 9, 876–883. doi: 10.1021/acsami.6b12824
- Wu, J., Zhao, Z., Kuang, X., Hamel, C. M., Fang, D., and Qi, H. J. (2018). Reversible shape change structures by grayscale pattern 4D printing. *Multifunct. Mater.* 1:015002.
- Yang, C., Boorugu, M., Dopp, A., Ren, J., Martin, R., Han, D., et al. (2019). 4D printing reconfigurable, deployable and mechanically tunable metamaterials. *Mater. Horizons* 6, 1244–1250. doi: 10.1039/c9mh00302a
- Yang, N. J., and Hinner, M. J. (2015). Getting across the cell membrane: an overview for small molecules, peptides, and proteins. *Methods Mol. Biol.* 1266, 29–53. doi: 10.1007/978-1-4939-2272-7_3
- Yang, R., Zhou, J., Yang, C., Qiu, L., and Cheng, H. (2020). Recent progress in 3D printing of 2D material-based macrostructures. *Adv. Mater. Technol.* 5:1901066. doi: 10.1002/admt.201901066
- Yin, J., Cao, Z., Li, C., Sheinman, I., and Chen, X. (2008). Stress-driven buckling patterns in spheroidal core/shell structures. *Proc. Natl. Acad. Sci. U.S.A.* 105, 19132–19135. doi: 10.1073/pnas.0810443105
- Yuan, C., Roach, D. J., Dunn, C. K., Mu, Q., Kuang, X., Yakacki, C. M., et al. (2017). 3D printed reversible shape changing soft actuators assisted by liquid crystal elastomers. *Soft Matter* 13, 5558–5568. doi: 10.1039/c7sm00759k
- Yuk, H., and Zhao, X. (2018). A new 3D printing strategy by harnessing deformation, instability, and fracture of viscoelastic inks. *Adv. Mater.* 30:1704028. doi: 10.1002/adma.201704028
- Zambrano, D., Cianchetti, M., and Laschi, C. (2014). “The morphological computation principles as a new paradigm for robotic design,” in *Opinions and Outlooks on Morphological Computation*, eds H. Hauser, R. Fuchsli, and R. Pfeifer (Zurich: E-Book), 214–225. doi: 10.13140/2.1.1059.4242
- Zhang, C., Lu, X., Fei, G., Wang, Z., Xia, H., and Zhao, Y. (2019). 4D printing of a liquid crystal elastomer with a controllable orientation gradient. *ACS Appl. Mater. Interfaces* 11, 44774–44782. doi: 10.1021/acsami.9b18037
- Zhang, Y., Huang, L., Song, H., Ni, C., Wu, J., Zhao, Q., et al. (2019). 4D printing of a digital shape memory polymer with tunable high performance. *ACS Appl. Mater. Interfaces* 11, 32408–32413. doi: 10.1021/acsami.9b11062
- Zhang, Z., Demir, K. G., and Gu, G. X. (2019). Developments in 4D-printing: a review on current smart materials, technologies, and applications. *Int. J. Smart Nano Mater.* 10, 205–224. doi: 10.1080/19475411.2019.1591541
- Zolfagharian, A., Kaynak, A., and Kouzani, A. (2020). Closed-loop 4D-printed soft robots. *Mater. Des.* 188:108411. doi: 10.1016/j.matdes.2019.108411

Conflict of Interest: The authors declare that the research was conducted in the absence of any commercial or financial relationships that could be construed as a potential conflict of interest.

The reviewer YL declared a shared affiliation with several of the authors, LQR, BL, KW, XZ, ZS, and QL, to the handling editor at time of review.

Copyright © 2021 Ren, Li, Wang, Zhou, Song, Ren and Liu. This is an open-access article distributed under the terms of the Creative Commons Attribution License (CC BY). The use, distribution or reproduction in other forums is permitted, provided the original author(s) and the copyright owner(s) are credited and that the original publication in this journal is cited, in accordance with accepted academic practice. No use, distribution or reproduction is permitted which does not comply with these terms.



4D Printing Dual Stimuli-Responsive Bilayer Structure Toward Multiple Shape-Shifting

Luquan Ren^{1,2}, Bingqian Li¹, Qingping Liu^{1,2}, Lei Ren^{1,2}, Zhengyi Song^{1,2*}, Xueli Zhou^{1,2} and Peng Gao¹

¹ Key Laboratory of Bionic Engineering (Ministry of Education), Jilin University, Changchun, China, ² Weihai Institute of Bionics, Jilin University, Weihai, China

OPEN ACCESS

Edited by:

Kun Zhou,
Nanyang Technological University,
Singapore

Reviewed by:

Haibao Lu,
Harbin Institute of Technology, China
Xinli Xiao,
Harbin Institute of Technology, China

*Correspondence:

Zhengyi Song
zysong@jlu.edu.cn

Specialty section:

This article was submitted to
Smart Materials,
a section of the journal
Frontiers in Materials

Received: 18 January 2021

Accepted: 12 April 2021

Published: 07 May 2021

Citation:

Ren L, Li B, Liu Q, Ren L, Song Z,
Zhou X and Gao P (2021) 4D Printing
Dual Stimuli-Responsive Bilayer
Structure Toward Multiple
Shape-Shifting.
Front. Mater. 8:655160.
doi: 10.3389/fmats.2021.655160

4D printing has been attracting widespread attention because its shape and performance can change under stimuli. The existing 4D printing technology is mostly limited to responsive to single stimulus, which means that the printing structure can only change under a pre-specified stimulus. Here we propose a 4D printing strategy with dual stimuli-responsive shape-shifting that responds to both temperature and water, by using a direct ink writing 3D printing method to deposit a polyurethane elastomer material with water-swelling characteristics on a heat-shrinkage shape memory polymer material to form a bilayer structure. Based on the systematic study of the adapted printing parameters of the polyurethane elastomer, the effect of programmable variables on the deformation shape was investigated. The diversified printing structure exhibits rich structural changes under one or both of the two stimuli of temperature and water. This research provides a universal multiple stimuli-responsive 4D printing method, which can effectively improve the intelligent responsiveness of 4D printing structures by combining multiple smart materials.

Keywords: 4D printing, multi-stimuli-response, bilayer structures, multiple shape-shifting, transformable soft gripper

INTRODUCTION

4D printing refers to that the shape, property or functionality of 3D printed objects can change over time in response to external stimuli (Kuang et al., 2019; Lui et al., 2019; Rastogi and Kandasubramanian, 2019; Shafraneck et al., 2019), such as water, heat, light, electricity, etc. 4D printing has broad application prospects in many fields such as aerospace (Akbari et al., 2018), drug delivery (Ursan et al., 2013), biomedical equipment (Gao et al., 2016; Yang et al., 2019), and flexible electronic devices (Zarek et al., 2016), and has been attracting widespread attention. To date, most of the research on 4D printing involves the shape-shifting of 3D printed materials or structures. The shape-changing mechanism of 4D printing can be summarized as either using smart materials, such as hydrogels (Champeau et al., 2020; Hu et al., 2020), shape memory polymers (SMP) (González-Henríquez et al., 2019; Zhang et al., 2019c,d; Kong et al., 2020), liquid crystal elastomers (LCE) (Kotikian et al., 2018; Zhang et al., 2019a), etc., or creating mismatch strain within the printed object during the printing process by the combination of different responsive materials (Tibbits, 2014) or the variation of printing process parameters (van Manen et al., 2017), and then the deformation is generated in response to stimuli after printing.

In the research field of 4D printing, multiple stimuli-response is of great significance for broadening the practical application of the printed structure in different environments (Karis et al., 2017; Han et al., 2018). By adding functional fillers to a certain type of smart material, the material has more responsiveness than the original one, which is one of the common strategies for achieving multi-response 4D printing. This draws on the existing multi-response composite method (Hu et al., 2018; Li et al., 2018). In such strategies, thermal is generally used as a basic stimulation. Researchers added carbon nanotubes, ferroferric oxide or other fillers into the SMPs, LCEs or thermally responsive hydrogels to enable the material with the capability to convert electricity to heat (Han et al., 2018; Liu et al., 2019), magnetism to heat (Lin et al., 2019; Zhang et al., 2019b), or light to heat (Cui et al., 2019; del Barrio and Sánchez-Somolinos, 2019), thereby realizing multi-responsive 4D printing. The composites formed from a thermally responsive material and a material responsive to pH (Hu et al., 2020; Lee et al., 2020) or cations (Kirillova et al., 2017; Duigou et al., 2019) also have multiply stimuli responsiveness. In addition, the water-responsive material can also be used as the basis material, and then the response of another material can change the moisture (Duigou et al., 2019), thereby controlling the change of the structure. In essence, these stimuli-responses are ultimately attributed to one stimulation. When multiple stimuli are applied, the resulting responses are consistent. This is not conducive to the use of a single printing structure in multiple environments.

Another pathway to achieve multiple stimuli-response 4D printing is to construct a bilayer structure by combining two materials with different response properties. Compared with the above-mentioned methods, the two layer materials is independent of each other in response to environmental stimuli, and can produce more shapes during the deformation process, thus enriching the deformation mode of the single structure. Regrettably, there are extremely few studies on multiply stimulus-response 4D printing at this stage.

By referring to the bilayer materials each with different responsiveness constructed by other methods (Zhang et al., 2016; Boothby and Ware, 2017; Xiao et al., 2018; Wang et al., 2018), it can be found that the structure has more responsiveness, which greatly enriches the pattern of structural changes. Using the respectively intelligent properties of the two material to stimulate deformation, the structure can deform as pre-defined by programming the type of environmental stimuli. For example, Boothby et al. combined a thermally responsive LCE with a water-responsive polymer to form a dual stimuli-responsive shape-changing bilayer structure (Kirillova et al., 2017). Yang et al. (2019) present a facile method to prepare dual-responsive bilayer hydrogels, consisting of a thermo-responsive layer and a salt-responsive layer through *in situ* sequential radical polymerization (Duigou et al., 2019). However, the structural styles formed by these methods are still relatively simple. 4D printing method can significantly increase the complexity of the structural design, resulting in more shape-changing.

In this article, we propose a 4D printing strategy based on the water-swellaable polyurethane (PU) elastomer and the heat-shrinkage shape memory polymer polyvinyl chloride (SMPVC)

bilayer structure that can produce programmable deformation in response to temperature and water. We investigated the rheological properties of PU, showing good printability. Then the effect of the process parameters of direct inks writing 3D printing on the printing filament width was studied. Further studies on the parameters that may affect the deformation behavior of the PU-SMPVC bilayer structure, including PU thickness, width and angle, were carried out. Based on the research results, we designed and manufactured a variety of shape-shifting structures with diversified morphology changes. Finally, three shapes deformed by the same printing structure under different stimuli were used as three soft gripper to verify the gripping capabilities.

RESULTS

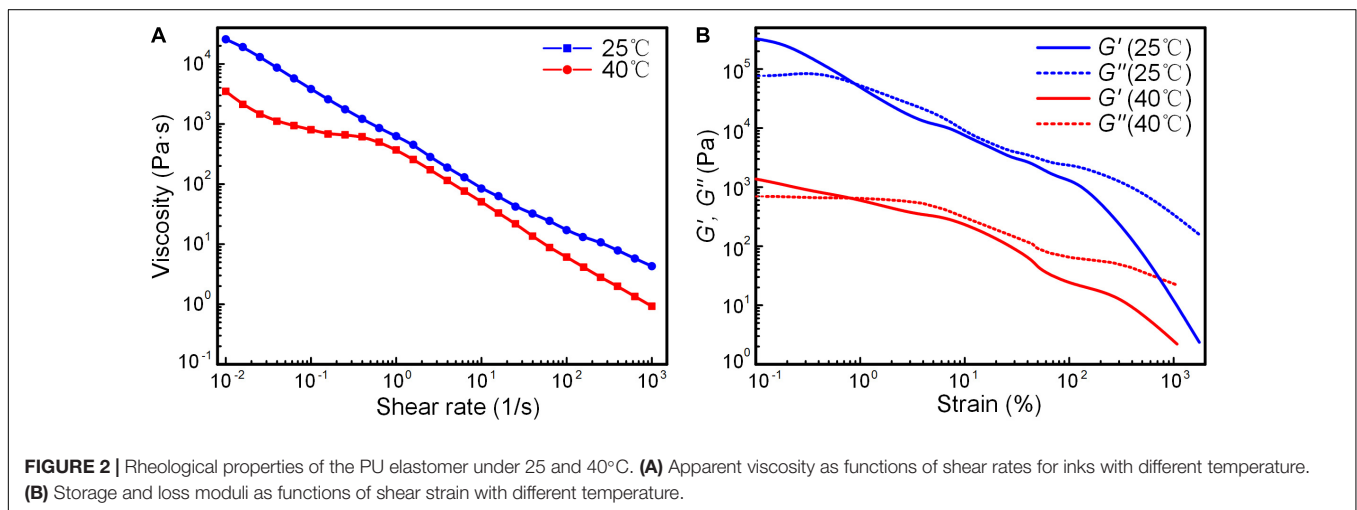
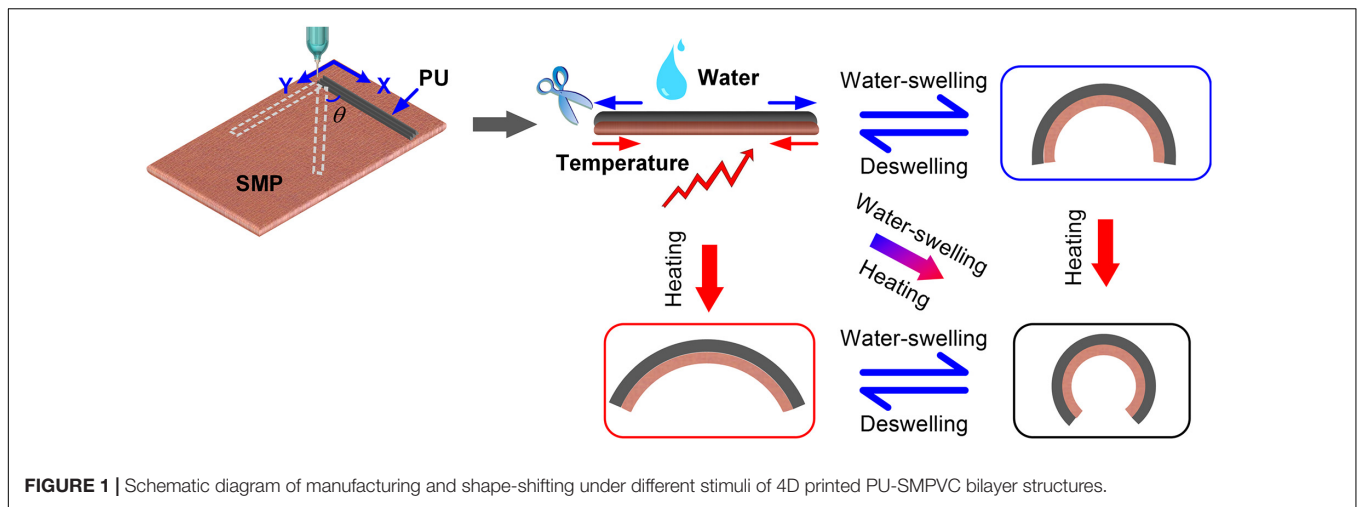
PU-SMPVC Bilayer Structures

This article proposes a 4D printing strategy that can achieve programmable shape changes in response to both temperature and water. As depicted in **Figure 1**, by means of direct ink writing 3D printing method, the water-swellaable PU elastomer is deposited on the thermal-shrinkable shape memory polymer to form a bilayer structure. After the PU is completely cured by absorbing moisture in the air, the PU/SMPVC bilayer structure was obtained by cutting along the outline of the printed sample for subsequent experiments. In response to different stimuli, the mismatch strain caused by water-swelling or thermal-shrinkage drives the printed bilayer structure to produce various shape-shifting. By programming the stimuli, the shape-shifting of the PU-SMPVC bilayer structure can be effectively controlled.

Investigation of Rheological Properties and Printability

In order to realize the printing of PU-SMPVC bilayer structures, the printability of water-swellaable PU has been investigated. First, the rheological properties of PU were measured. As shown in **Figure 2A**, the apparent viscosity of PU gradually decreases with the increase of the shear rate at room temperature of 25°C, showing a shear thinning rheological behavior. Properly elevated temperature (40°C) can decrease the viscosity of PU, which is more conducive to smooth out material from extrusion head. **Figure 2B** shows the changing of the storage modulus (G') and loss modulus (G'') of the PU as function of shear strain at a constant frequency under different temperature conditions. With the gradual increase of the shear strain, G' to G'' gradually decrease. During the process, G' changes from greater than G'' to less than G'' , indicating the transition of the material from solid to viscoelastic under high shear strain conditions, which is suitable for the material extrusion process. In addition, a proper increase in temperature (40°C) will decrease the values of both G' and G'' , but still keep them the similar change trends.

Since this experiment adopts pneumatic-based direct ink writing technology (DIW), the coordination of printing moving speed and air pressure determines the quality of the printed filaments. **Figure 3A** shows whether continuous lines can be extruded under different speeds and different air pressures at 25°C. The line width change of extrudable filaments with



different speeds and air pressures is shown in **Figure 3B**, from which we can conclude that the greater the air pressure and the slower the speed, the greater the width of the extruded filament. Under the condition of air pressure of 0.6 MPa and speed of 5 mm/s, the maximum line width can reach about 0.75 mm, which is basically twice the diameter of the extrusion head (0.41 mm). According to the obtained data, the distribution colormap of filament width and air pressure/speed are drawn out (**Figure 3C**), and on this basis, an appropriate speed and air pressure can be selected to achieve quantitative filament width printing. **Figures 3D–F** depicts whether the filament can be extruded smoothly and the change of the filament width as different speeds and pressures at 40°C. Compared with the condition of 25°C, under the same speed and air pressure, the width of the extruded filament at 40°C is wider. The maximum line width exceeds 1 mm, indicating that the extruded material volume is more. This also reflects the improvement of the rheological properties of the ink, which is consistent with the conclusion obtained from the rheological test. In the case of the same air pressure, in order to achieve the same filament width, the required

printing speed is a bit faster at 40°C than that at 25°C, which can improve the printing efficiency to a certain extent. Therefore, the printing temperature used in this experiment is set as 40°C.

Figures 4A–C shows the examples of 4D printed PU elastomer under a combination of parameters with a printing temperature of 40°C, a speed of 12 mm/s, and an air pressure of 0.4 MPa (**Figure 3F**). These examples are raster structure, ring column and butterfly shape, respectively. All three printed samples can swell by absorbing water with a linear swelling rate of approximately 1.5. From the weight change of the three structures shown in **Table 1** before and after water-swelling, the weight of the ring column and butterfly-shaped structure after water-swelling is 2.9 times the initial weight, while the raster structure is increased to 3.66 times. This may be due to the more water contact area in the structure, which can be capable to absorb water more fully.

The swollen samples can deswell at room temperature or under heating and return to their original shapes. Under the condition of 60°C, it can be seen from the weight changes of different samples (**Figure 4D**) that the sample with raster

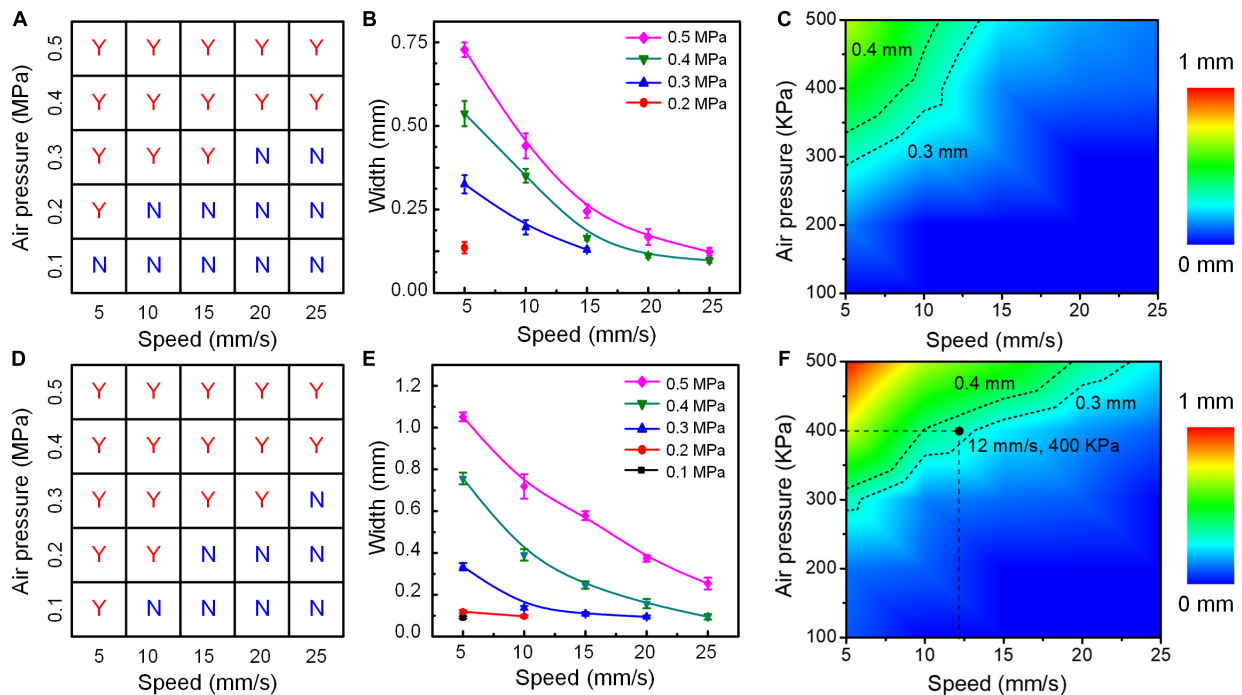


FIGURE 3 | Investigation of the effect of air pressure and moving speed on the printed filaments at 25°C (A–C) and 40°C (D–F).

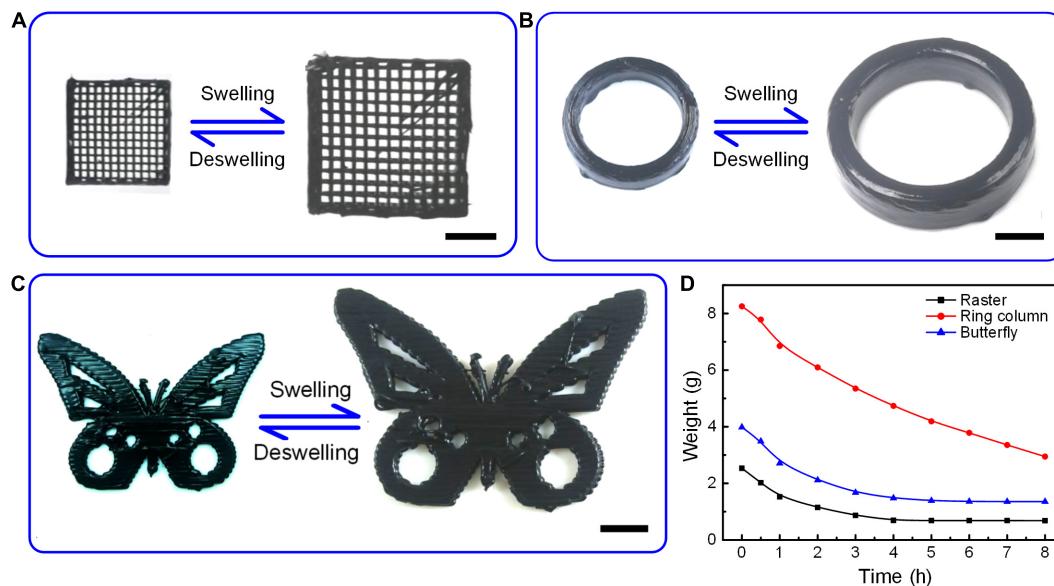


FIGURE 4 | Three printed PU samples with raster structure (A), ring column (B), and butterfly shape (C) and their shapes after water-swelling. (D) Changes in the weight of three printed samples during the deswelling process at room temperature.

structure can recover to the original shape at the fastest speed (4 h), while the butterfly shaped sample can recover the initial shape in about 5 h. However, because there are more areas that are not in direct contact with the air, the rate of water loss of the sample with ring column shape is the slowest, requiring more than 8 h. If the swollen samples are placed at room temperature, it will take longer to fully recover the original shapes.

Relationship Between Printing Parameters and Deformation

The deformability of the printed bilayer structure in response to temperature or/and water was investigated. **Figure 5A** shows the relationship between the deformability of the bilayer structures printed in the radial direction and the thickness of the printed PU layer. With the gradual increase of the printing thickness,

TABLE 1 | Weight change of the printed structures before and after absorbing water.

Shape of the printed samples	Initial weight (g)	Temporary weight (g)	Temporary/Initial
Raster structure	0.708	2.532	3.66
Ring column	2.846	8.251	2.90
Butterfly	1.367	3.984	2.91

the degree of bending deformation caused by the shrinkage of the SMPVC layer gradually decreases (**Figure 5B**), which is caused by the increasing shape-morphing inhibition of the PU layer thickness. Similarly, the bending deformation caused by moisture is also affected by the thickness. The greater the thickness, the larger the bending radius (**Figure 5C**). In the case of integrating two stimuli (**Figure 5D**), both two work together to increase the bending effect. The final bending radius will increase with the increase in thickness. In addition, the relationship between the deformability of the bilayer structures printed in the radial direction and the width of the printed PU layer was also investigated (*cf.* **Supplementary Figure S1**). The results demonstrate that the width of PU elastomer has little effect on the temperature/water response of the bilayer structure.

Then, the relationship between the deformation mode of the bilayer structure printed at an oblique angle of 45° to the radial direction and the thickness of the printed PU layer was investigated. Herein, the bending deformation responding to water is no longer considered because its deformation is consistent with the bending deformation caused by water along the radial direction. **Figure 6A** shows the shapes of the printed samples with different PU layer thickness after thermal stimulus and their shape transition after water-swelling. With the gradual increase of the printing thickness, the degree of spiral formed by thermal shrinkage gradually decreases, which is manifested as the gradual increase in pitch, and the spiral radius also shows a gradually increasing trend (**Figures 6B,C**). When the thermal-induced spiral shape samples are placed in a water environment,

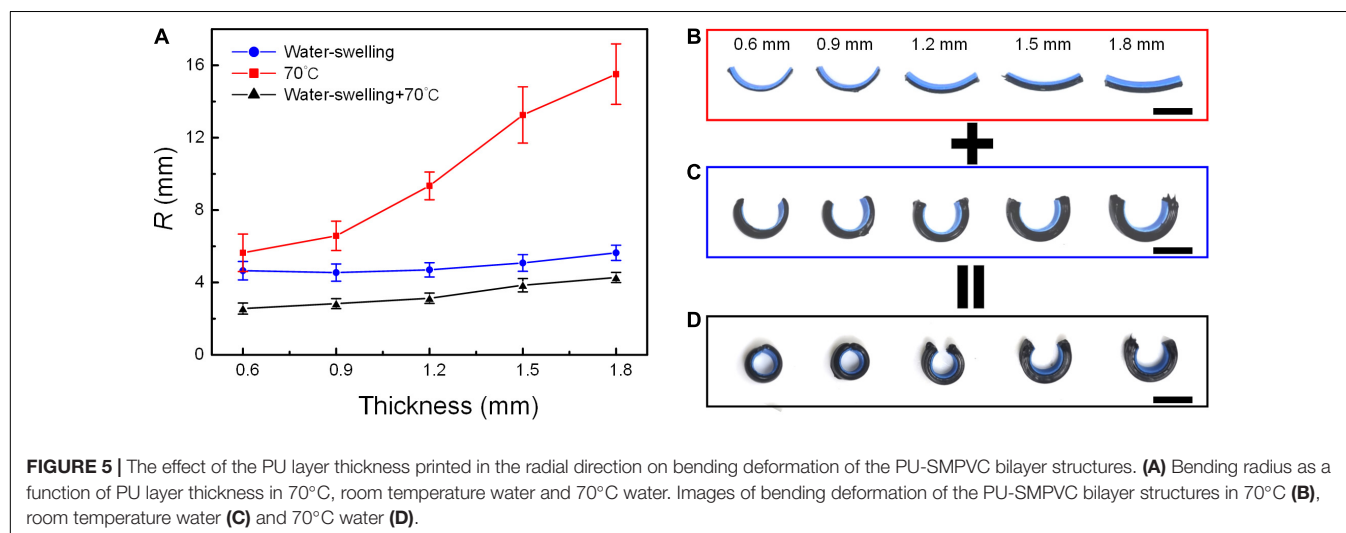
the spiral degree will change to a certain extent. The spiral pitch becomes smaller, but the radius becomes slightly larger. On the whole, the pitch and degree still keep increasing as the thickness increases. Moreover, the width has almost no effect on the spiral deformation of the bilayer structure printed at an oblique angle of 45° , which means that the pitch and radius before and after deformation are independent of the width (*cf.* **Supplementary Figure S2**).

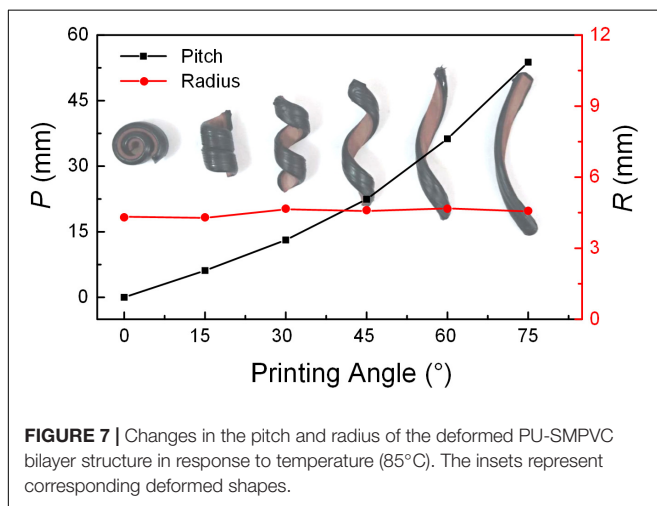
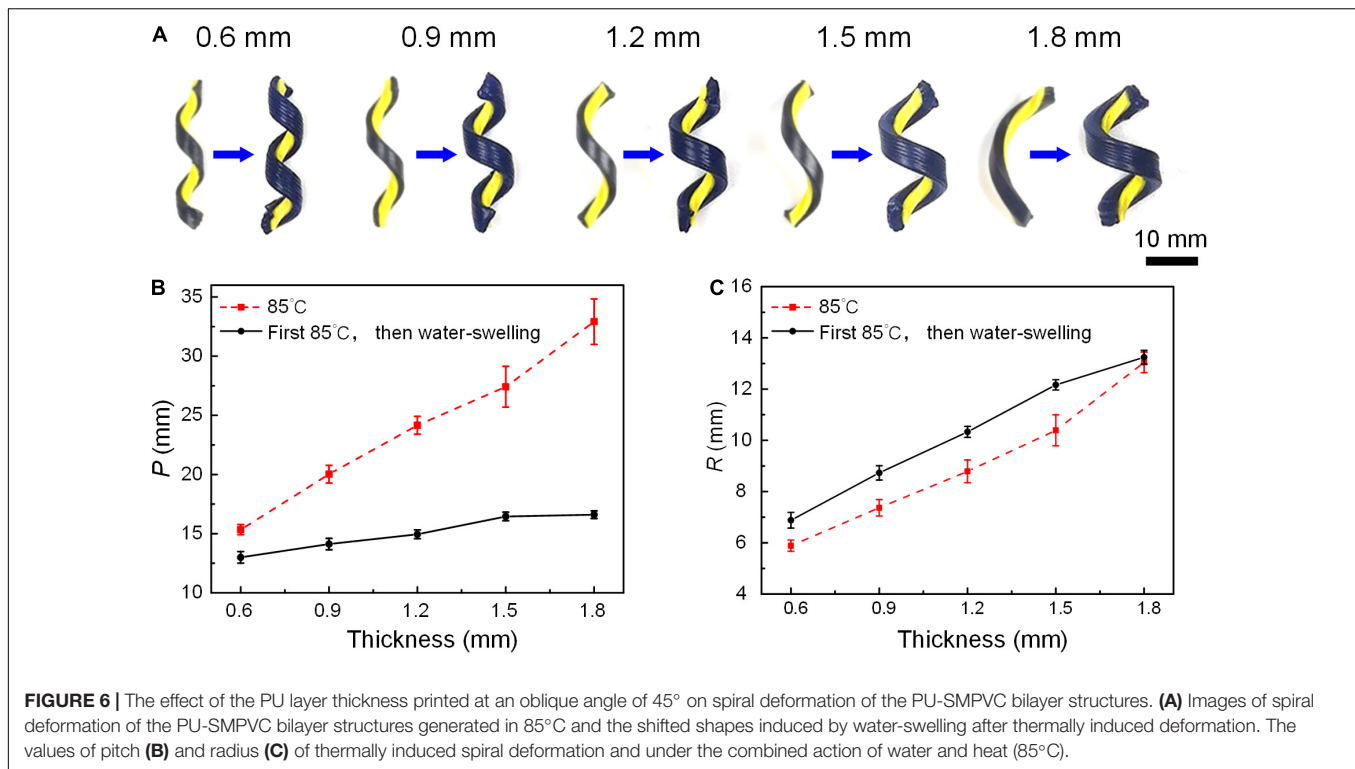
In view of the difference between the radial shrinkage and axial shrinkage of the SMPVC layer, the angle of the printed PU layer will also affect the deformation mode of the PU-SMPVC bilayer structure. As shown in **Figure 7**, when responding to temperature (85°C), as the angle gradually increases, the printed structure produces regular deformation, which is manifested from pure bending deformation to spiral deformation. The pitch increases with the angle, but the radius remains unchanged.

Multi-Morphic Deformation

After learning the influence of printing parameters on structural deformation, a variety of samples with multi-morphic structural deformation were designed and manufactured. Based on the effect of the printing thickness of the PU layer on the shape changing of the bilayer structure, a structure with a gradient in thickness was printed, as shown in **Figure 8**. When the structure respond to water alone or temperature alone, it can evolve into an involute spiral shape.

Considering that the angle can affect the deformation of the bilayer structure under temperature, we printed a bilayer structure with a quadrant shape, which can realize the transformation of the inclination angle from 0° to 90° , as shown in **Figure 9**. This structure can produce different morphological transformation under different stimuli. Utilizing the characteristics of anisotropic shrinkage of SMPVC can achieve the gradient change of pitch from 0 to infinity, showing a gradient spiral shape. Moreover, the level of stimulated temperature can affect the shrinkage degree of the SMPVC, thereby resulting in different deformation modes of the bilayer





structure. As shown in the Figure, the gradient spiral shapes produced at 70 and 90°C are significantly different. The non-uniform spiral at high temperature (90°C) is more obvious, and the spiral shape formed after water-swelling is also more prominent. In addition, by first undergoing water-swelling to deform into a circle, and then receiving thermal stimulus at different temperatures, different non-uniform spiral shapes can also be obtained.

Figure 10 shows the shape morphing of a bilayer structure with a printed semicircular shape under different stimuli, which is symmetrical along the axial direction. Both sides can produce gradient spiral deformation with opposite spiral directions in

response to temperature. After water-swelling, the bending deformation effect enables the two sides to further spirally deform toward respective direction, forming a greater non-uniform spiral shape. Another way to get the final shape is to first achieve uniform bending deformation by water-swelling, and then receive thermal stimulation to obtain a bilaterally symmetrical non-uniform spiral structure.

Another example shown in **Figure 11** is a bilayer structure composed of four branches with a quarter circle shape. When excited by water, the four branches will bend evenly, which finally makes the structure present a sequential overlapping pattern. In response to temperature, the four branches will produce non-uniform spiral deformation. The two opposite branches have the same deformation pattern. Based on this, the four branches can be divided into two groups, one of which is spirally deformed from the inside to the outside, and the other is the opposite. When responding to two stimuli, the synergy of the water-induced bending effect and the thermally induced non-uniform spiral effect creates a new form. More structures with multiple deformations are shown in the **Supplementary Material** (cf. **Supplementary Figures S3, S4**).

Transformable Soft Gripper

Harnessing the multiple shape-shifting of the PU-SMPVC bilayer structure, a transformable soft gripper is designed, as shown in **Figure 12A**. The PU layer is distributed on the SMPVC layer in a crisscross shape with an angle of 45° in the radial direction of the SMPVC layer. In response to water, the four branches bend evenly in the SMPVC direction to form a curved soft gripper. When responding to temperature, the four branches are uniformly

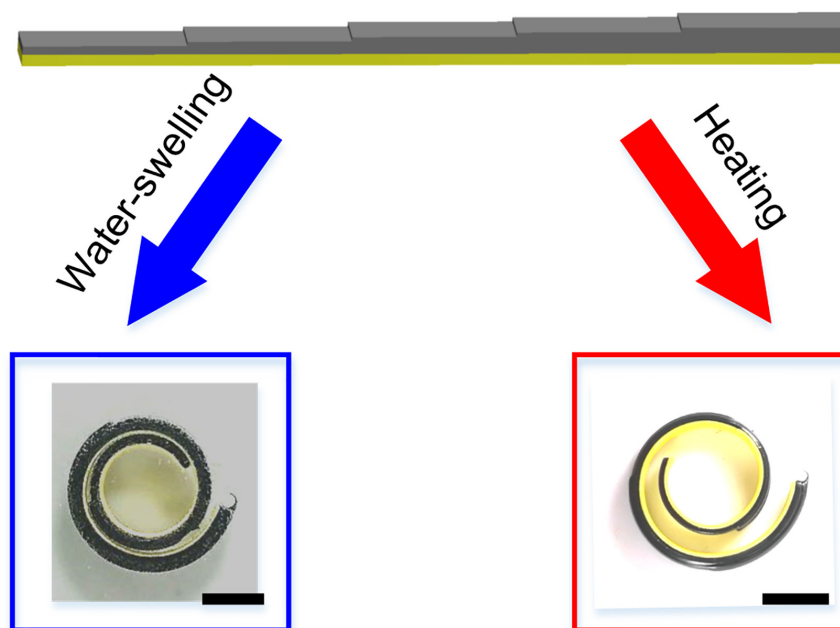


FIGURE 8 | PU-SMPVC bilayer structure with a gradient PU layer thickness, which can produce an involute shape undergoing water-swelling or heating.

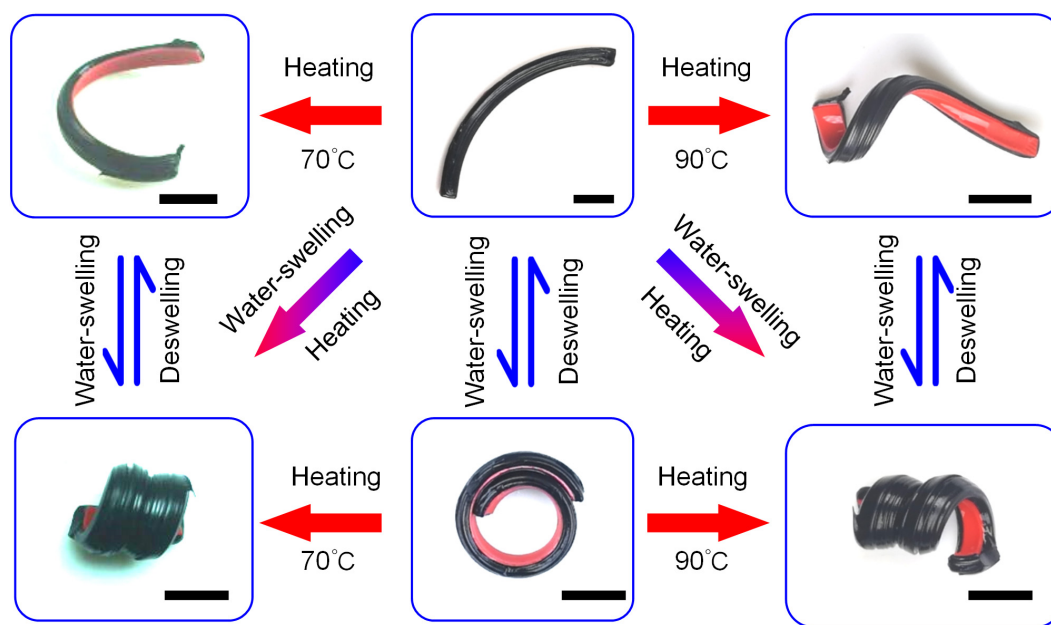


FIGURE 9 | Deformation of a PU-SMPVC bilayer structure with a quadrant shape in response to different stimuli.

spiral in the SMPVC direction. According to the spiral direction, the structure can be divided into two groups with opposite spiral directions. The two adjacent gripping arms intersect at one point, forming a spiral soft gripper. In response to the dual stimuli of temperature and water, the water-induced bending effect and the thermally induced spiral effect cause the structure to produce a greater degree of spiral deformation toward the SMPVC side,

resulting in the third deformation pattern. All the three 3D shapes transformed from the PU-SMPVC bilayer flat structure can be used as a soft gripper. The gripping capabilities of the three soft grippers are compared through the relationship between the output force and displacement during the process of gripping the fixed bolt, as shown in **Figure 12B**. It can be seen that the deformation caused by the dual stimuli produces the largest

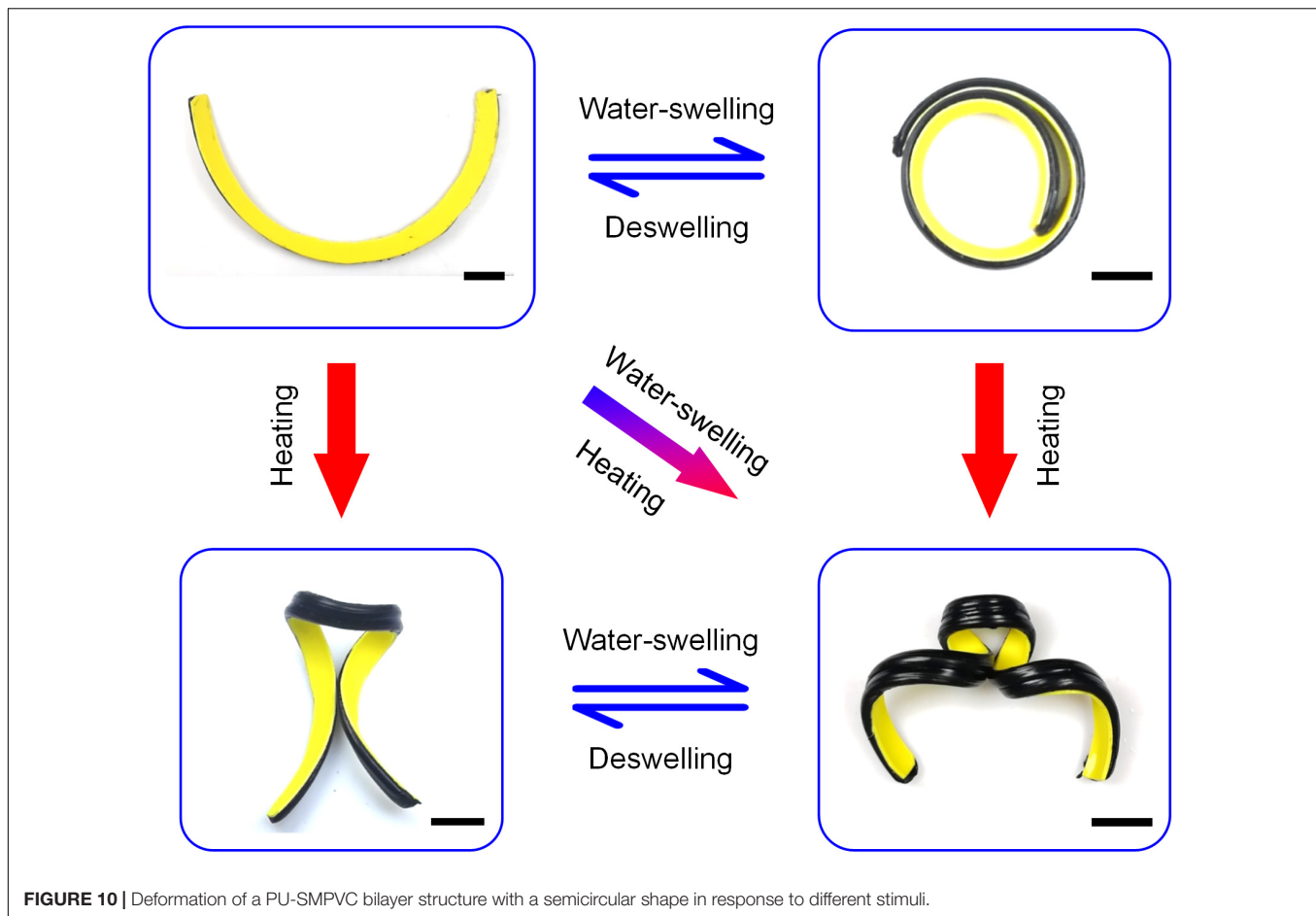


FIGURE 10 | Deformation of a PU-SMPVC bilayer structure with a semicircular shape in response to different stimuli.

force during the desorption process, while the desorption force generated only in response to water is the smallest, and the desorption force generated in response to temperature (90°C) is in the middle. The result proves that the soft gripper under the dual stimuli has better gripping ability.

CONCLUSION

In this article, we demonstrated a facile and feasible 4D printing method that can achieve dual stimuli-responsive shape-shifting in response to temperature or/and water. Harnessing DIW 3D printing method to deposit the water-swelling PU material on the heat-shrinkage SMPVC material, a bilayer structure was construed. Moreover, the printability of PU enables the manufacture of complex deformation structures. In addition, the effects of printing thickness and printing angle on deformation ensures the shape-shifting diversity of the printing structure. Based on previous research, multiple multi-morphic deformation structures have been designed. Finally, the usefulness of dual stimuli-response is verified by a transformable soft gripper. This article presents a facile, universal multi-response 4D printing method, which can facilitate the intelligent responsiveness of 4D printed structures by combining multiple smart materials.

MATERIALS AND METHODS

Materials

The water-swelling PU elastomer material with a linear swelling ratio of 150% (Hengchuang Construction Engineering Material Co., Ltd., China) are used in this article. The material is in the form of a black gel and can be directly loaded into the syringe for subsequent printing. The glass transition temperature of PU is -58.79°C (*cf.* **Supplementary Figure S5A**). The thermal decomposition temperature of PU exceeds 200°C (*cf.* **Supplementary Figure S5B**).

A commercial available heat-shrinkable PVC (Polyvinyl chloride, Volsun Co., Ltd., nominal thickness: 0.6 mm) with a 2:1 nominal shrinking ratio in the radial direction and a negligible axial shrinkage ratio was used. In addition, according to the previous research literature, the degree of this SMPVC shrinkage is related with the temperature (Janbaz et al., 2016). The higher the temperature, the greater the shrinkage.

Characterization

A rotational viscometer (Discovery HR-30, America) equipped with 20 mm diameter parallel was employed for investigating the rheological properties of the PU paste. The apparent viscosity was determined in a flow sweep mode at shear rates of $0.01\text{--}10\text{ s}^{-1}$.

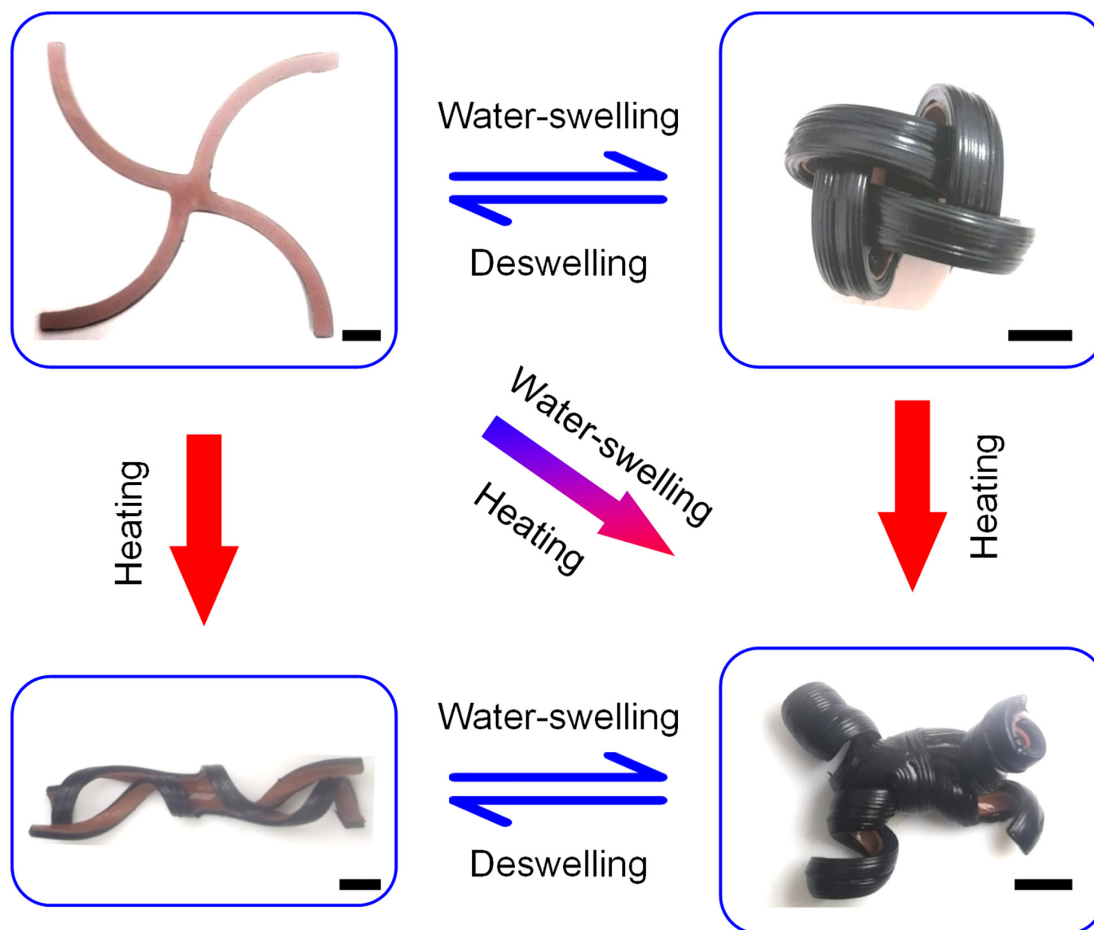


FIGURE 11 | Deformation of a PU-SMPVC bilayer structure composed of four branches with a quarter circle shape in response to different stimuli. Each branch is obtained by rotating the adjacent branch clockwise.

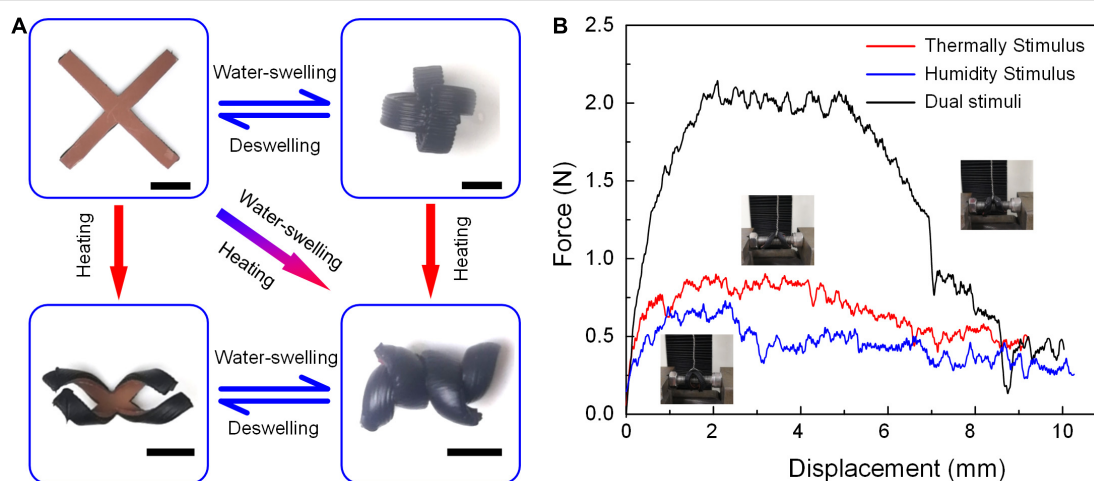


FIGURE 12 | Transformable soft gripper. **(A)** Deformation of a PU-SMPVC bilayer structure in a crisscross shape with an angle of 45° in the radial direction of the SMPVC layer in response to different stimuli. **(B)** The relationship between the desorption force and displacement generated by three soft grippers with different shapes in the process of gripping a fixed bolt.

Gripping tests were carried out using a universal testing machine (ZQ-990A, China). A bolt with a diameter of 6 mm is fixed by a vise clamp. The soft grippers with different shapes formed under different stimuli are attached on the bolt in the form of grasping. The force generated during the upward motion (5 mm/min) was recorded to evaluate gripping ability of different soft grippers.

The values of the filament width, bending radius, helical pitch and helical radius in this article were all measured from the captured image using image analysis software (Digimizer, MedCalc Software, Belgium).

3D Printing and Shape-Shifting

All printed objects were manufactured by using our self-developed pneumatic assisted direct inks writing (DIW) 3D printer. In the printing process, we used stainless steel needles (22G) with a inner diameter of 0.41 mm to print all objects. All prints in this study were conducted at a fixed layer height of 0.3 mm.

During printing of the PU/SMPVC bilayer structure, a flat sheet of SMPVC polished with sandpaper (600-mesh) is fixed on the substrate. The PU elastomer filaments are deposited on the SMPVC layer through the extrusion head. After PU elastomer is thoroughly solidified by absorbing moisture in air (exceed 3 days), the PU/SMPVC bilayer structure was acquired by cutting along the outline of the printed PU filaments.

The morphed shapes in response to temperature, water, and both two stimuli shown in **Figures 4–12** were obtained by submerging the specimens in the hot water bath with different temperature for 25–30 s, in the room temperature water bath for 3 h, and first in the hot water bath with different temperature for 25–30 s, then in room temperature water bath for 3 h, respectively.

REFERENCES

- Akbari, S., Sakhaei, A. H., Kowsari, K., Serjouei, A., Zhang, Y. F., and Ge, Q. (2018). Enhanced multimaterial 4D printing with active hinges. *Smart Mater. Struct.* 27:065027. doi: 10.1088/1361-665X/aabe63
- Boothby, J. M., and Ware, T. H. (2017). Dual-responsive, shape-switching bilayers enabled by liquid crystal elastomers. *Soft Matter*. 13, 4349–4356. doi: 10.1039/c7sm00541e
- Champeau, M., Heinze, D. A., Viana, T. N., de Souza, E. R., Chinellato, A. C., and Titotto, S. (2020). 4D printing of hydrogels: a review. *Adv. Funct. Mater.* 30:1910606. doi: 10.1002/adfm.201910606
- Cui, H., Miao, S., Esworthy, T., Lee, S. J., Zhou, X., Hann, S. Y., et al. (2019). A novel near-infrared light responsive 4D printed nanoarchitecture with dynamically and remotely controllable transformation. *Nano Res.* 12, 1381–1388. doi: 10.1007/s12274-019-2340-9
- del Barrio, J., and Sánchez-Somolinos, C. (2019). Light to shape the future: from photolithography to 4D printing. *Adv. Opt. Mater.* 7:1900598. doi: 10.1002/adom.201900598
- Duigou, A. L., Chabaud, G., Scarpa, F., and Castro, M. (2019). Bioinspired electro-thermo-hygro reversible shape-changing materials by 4D printing. *Adv. Funct. Mater.* 29:1903280. doi: 10.1002/adfm.201903280
- Gao, B., Yang, Q., Zhao, X., Jin, G., Ma, Y., and Xu, F. (2016). 4D bioprinting for biomedical applications. *Trends Biotechnol.* 34, 746–756. doi: 10.1016/j.tibtech.2016.03.004

DATA AVAILABILITY STATEMENT

The original contributions presented in the study are included in the article/**Supplementary Material**, further inquiries can be directed to the corresponding author/s.

AUTHOR CONTRIBUTIONS

LR, QL, ZS, and LR participated in design and procedure planning of the experiment. BL, ZS, XZ, and PG were responsible for different parts of the experiment. All authors have contributed to the article, read, and approved the manuscript.

FUNDING

This work was supported by the Key Scientific and Technological Project of Jilin Province (20170204061GX), the National Key Research and Development Program of China (2018YFB1105100 and 2018YFF01012400), and the Scientific Research Project of Jilin Provincial Department of Education (JJKH20211117KJ).

ACKNOWLEDGMENTS

We would like to acknowledge PE Jiang for technical assistance of rheological testing.

SUPPLEMENTARY MATERIAL

The Supplementary Material for this article can be found online at: <https://www.frontiersin.org/articles/10.3389/fmats.2021.655160/full#supplementary-material>

- González-Henríquez, C. M., Sarabia-Vallejos, M. A., and Rodríguez-Hernández, J. (2019). Polymers for additive manufacturing and 4D-printing: materials, methodologies, and biomedical applications. *Prog. Polym. Sci.* 94, 57–116. doi: 10.1016/j.progpolymsci.2019.03.001
- Han, D., Farino, C., Yang, C., Scott, T., Browe, D., Choi, W., et al. (2018). Soft robotic manipulation and locomotion with a 3D printed electroactive hydrogel. *ACS Appl. Mater. Interfaces* 10, 17512–17518. doi: 10.1021/acsami.8b04250
- Hu, Y., Wang, Z., Jin, D., Zhang, C., Sun, R., Li, Z., et al. (2020). Botanical-inspired 4D printing of hydrogel at the microscale. *Adv. Funct. Mater.* 30:1907377. doi: 10.1002/adfm.201907377
- Hu, Z., Zhang, D., Lu, F., Yuan, W., Xu, X., Zhang, Q., et al. (2018). Multistimuli-responsive intrinsic self-healing epoxy resin constructed by host-guest interactions. *Macromolecules* 51, 5294–5303. doi: 10.1021/acs.macromol.8b01124
- Janbaz, S., Hedayati, R., and Zadpoor, A. A. (2016). Programming the shape-shifting of flat soft matter: from self-rolling/self-twisting materials to self-folding origami. *Mater. Horiz.* 3, 536–547. doi: 10.1039/C6MH00195E
- Karis, D., Ono, R., Zhang, M., Vora, A., Storti, D., Ganter, M. A., et al. (2017). Cross-linkable multi-stimuli responsive hydrogel inks for direct-write 3d printing. *Polym. Chem.* 8, 4199–4206. doi: 10.1039/c7py00831g
- Kirillova, A., Maxson, R., Stoychev, G., Gomillion, C. T., and Ionov, L. (2017). 4D biofabrication using shape-morphing hydrogels. *Adv. Mater.* 29:1703443. doi: 10.1002/adma.201703443

- Kong, D., Li, J., Guo, A., and Xiao, X. (2020). High temperature electromagnetic shielding shape memory polymer composite. *Chem. Eng. J.* 408:127365. doi: 10.1016/j.cej.2020.127365
- Kotikian, A., Truby, R. L., Boley, J. W., White, T. J., and Lewis, J. A. (2018). 3D printing of liquid crystal elastomeric actuators with spatially programmed nematic order. *Adv. Mater.* 30:1706164. doi: 10.1002/adma.201706164
- Kuang, X., Roach, D. J., Wu, J., Hamel, C. M., Ding, Z., Wang, T., et al. (2019). Advances in 4D printing: materials and applications. *Adv. Funct. Mater.* 29:1805290. doi: 10.1002/adfm.201805290
- Lee, Y. W., Ceylan, H., Yasa, I. C., Kilic, U., and Sitti, M. (2020). 3D-printed multi-stimuli-responsive mobile micromachines. *ACS Appl. Mater. Interfaces* 13, 12759–12766. doi: 10.1021/acsami.0c18221
- Li, G., Hong, G., Dong, D., Song, W., and Zhang, X. (2018). Multiresponsive graphene-aerogel-directed phase-change smart fibers. *Adv. Mater.* 30:1801754. doi: 10.1002/adma.201801754
- Lin, C., Lv, J., Li, Y., Zhang, F., Li, J., Liu, Y., et al. (2019). 4D-printed biodegradable and remotely controllable shape memory occlusion devices. *Adv. Funct. Mater.* 29:1906569. doi: 10.1002/adfm.201906569
- Liu, Y., Zhang, F., Leng, J., Fu, K., Lu, X. L., Wang, L., et al. (2019). Remotely and sequentially controlled actuation of electroactivated carbon nanotube/shape memory polymer composites. *Adv. Mater. Technol.* 4:1900600. doi: 10.1002/admt.201900600
- Lui, Y. S., Sow, W. T., Tan, L. P., Wu, Y., Lai, Y., and Li, H. (2019). 4D printing and stimuli-responsive materials in biomedical aspects. *Acta Biomater.* 92, 19–36. doi: 10.1016/j.actbio.2019.05.005
- Rastogi, P., and Kandasubramanian, B. (2019). Breakthrough in the printing tactics for stimuli-responsive materials: 4D printing. *Chem. Eng. J.* 366, 264–304. doi: 10.1016/j.cej.2019.02.085
- Shafraneck, R. T., Millik, S. C., Smith, P. T., Lee, C. U., Boydston, A. J., and Nelson, A. (2019). Stimuli-responsive materials in additive manufacturing. *Prog. Polym. Sci.* 93, 36–67. doi: 10.1016/j.progpolymsci.2019.03.002
- Tibbits, S. (2014). 4D printing: multi-material shape change. *Archit. Des.* 84, 116–121. doi: 10.1002/ad.1710
- Ursan, I. D., Chiu, L., and Pierce, A. (2013). Three-dimensional drug printing: a structured review. *J. Am. Pharm. Assoc.* 53, 136–144. doi: 10.1331/JPhA.2013.12217
- van Manen, T., Janbaz, S., and Zadpoor, A. A. (2017). Programming 2D/3D shape-shifting with hobbyist 3D printers. *Mater. Horiz.* 4, 1064–1069. doi: 10.1039/C7MH00269F
- Wang, L., Jian, Y., Le, X., Lu, W., Ma, C., Zhang, J., et al. (2018). Actuating and memorizing bilayer hydrogels for a self-deformed shape memory function. *Chem. Commun.* 54, 1229–1232. doi: 10.1039/c7cc09456f
- Xiao, S., Zhang, M., He, X., Huang, L., Zhang, Y., Ren, B., et al. (2018). Dual salt- and thermoresponsive programmable bilayer hydrogel actuators with pseudo-interpenetrating double-network structures. *ACS Appl. Mater. Interfaces* 12, 6351–6361. doi: 10.1021/acsami.9b17577
- Yang, G. H., Yeo, M., Koo, Y. W., and Kim, G. H. (2019). 4D bioprinting: technological advances in biofabrication. *Macromol. Biosci.* 19:e1800441. doi: 10.1002/mabi.201800441
- Zarek, M., Layani, M., Cooperstein, I., Sachyani, E., Cohn, D., and Magdassi, S. (2016). 3D printing of shape memory polymers for flexible electronic devices. *Adv. Mater.* 28, 4449–4454. doi: 10.1002/adma.201503132
- Zhang, C., Lu, X., Fei, G., Wang, Z., Xia, H., and Zhao, Y. (2019a). 4D Printing of a liquid crystal elastomer with a controllable orientation gradient. *ACS Appl. Mater. Interfaces* 11, 44774–44782. doi: 10.1021/acsami.9b18037
- Zhang, F., Wang, L., Zheng, Z., Liu, Y., and Leng, J. (2019b). Magnetic programming of 4D printed shape memory composite structures. *Compos. Part A Appl. Sci. Manuf.* 125:105571. doi: 10.1016/j.compositesa.2019.105571
- Zhang, L., Desta, I., and Naumov, P. (2016). Synergistic action of thermoresponsive and hygroresponsive elements elicits rapid and directional response of a bilayer actuator. *Chem. Commun.* 52, 5920–5923. doi: 10.1039/c6cc01193d
- Zhang, Y., Huang, L., Song, H., Ni, C., Wu, J., Zhao, Q., et al. (2019c). 4D printing of a digital shape memory polymer with tunable high performance. *ACS Appl. Mater. Interfaces* 11, 32408–32413.
- Zhang, Y., Le, X., Jian, Y., Lu, W., and Chen, T. (2019d). 3D fluorescent hydrogel origami for multistage data security protection. *Adv. Funct. Mater.* 29:1905514. doi: 10.1002/adfm.201905514

Conflict of Interest: The authors declare that the research was conducted in the absence of any commercial or financial relationships that could be construed as a potential conflict of interest.

Copyright © 2021 Ren, Li, Liu, Ren, Song, Zhou and Gao. This is an open-access article distributed under the terms of the Creative Commons Attribution License (CC BY). The use, distribution or reproduction in other forums is permitted, provided the original author(s) and the copyright owner(s) are credited and that the original publication in this journal is cited, in accordance with accepted academic practice. No use, distribution or reproduction is permitted which does not comply with these terms.



Four-Dimensional Printing of Alternate-Actuated Composite Structures for Reversible Deformation under Continuous Reciprocation Loading

Guanghao Chu^{1,2}, Bin Zhou^{1,2}, Guangbin Shao^{1,2}, Dianjin Zhang^{1,2} and Longqiu Li^{1,2*}

¹State Key Laboratory of Robotics and System, Harbin Institute of Technology, Harbin, China, ²Key Laboratory for Micro-systems and Micro-structure Manufacturing, Ministry of Education, Harbin Institute of Technology, Harbin, China

OPEN ACCESS

Edited by:

Yusheng Shi,
Huazhong University of Science and
Technology, China

Reviewed by:

Yanjie Wang,
Hohai University, China
Bin Su,
Huazhong University of Science and
Technology, China

*Correspondence:

Longqiu Li
longqiuli@hit.edu.cn

Specialty section:

This article was submitted to
Smart Materials,
a section of the journal
Frontiers in Materials

Received: 31 January 2021

Accepted: 03 May 2021

Published: 18 May 2021

Citation:

Chu G, Zhou B, Shao G, Zhang D and
Li L (2021) Four-Dimensional Printing
of Alternate-Actuated Composite
Structures for Reversible Deformation
under Continuous
Reciprocation Loading.
Front. Mater. 8:661593.
doi: 10.3389/fmats.2021.661593

Four-dimensional (4D) printed structures are usually designed with reduced stiffness to enlarge the deformation response and weaken the loading capacity in actuated states. These actuators are suitable for non-persistent loads, such as is involved in grabbing action by a 4D printed claw. However, reduced stiffness cannot support continuous external loads during actuation. To tackle the trade-off between deformation and loading capacity, we propose herein a design using alternate actuation to attain competent loading capacity in different deformed states. In this alternate design, each unit consists of two actuated components featuring the same deformation but reciprocal stiffness, which provides the overall structural stiffness required to attain competent loading capacity during the entire deformation process. The two components are programmed to have the deformation behavior and are stimulated by thermal-expansion mismatch between polylactic acid (PLA) and carbon-fiber-reinforced PLA. An actuator featuring alternate components was designed and 4D printed to contrast its loading capacity with that of the traditional design. Experiments demonstrate a significantly improved loading capacity during actuation. This work thus provides a designing strategy for 4D printed actuators to retain competent loading capacity during the entire deformation process, which may open promising routes for applications with continuous external loads, such as 4D printed robotic arms, walking robots, and deformable wheels.

Keywords: 4D printing, design method, alternate actuation, loading capacity, reversible deformation

INTRODUCTION

Four-dimensional (4D) printing is a creative manufacturing technology that combines three-dimensional (3D) printing technology with smart materials or structures, where the shape, property, or functionality for 4D structures can be programmed and controlled in space and time (Momeni et al., 2017; Kuang et al., 2018). The structures can be manufactured by using 3D printing technology such as fused filament fabrication (Cheng et al., 2020), direct ink writing (Yuan et al., 2017), stereolithography (Ge et al., 2016), or polyjet (Ding et al., 2018), all of which can change their morph or function by optical stimulation (Liu et al., 2017), electrical stimulation (Bar-Cohen et al., 2017; Zhao et al., 2019), variations in humidity (Gladman

et al., 2016; Lee et al., 2020), magnetic stimulation (Kim et al., 2018), thermal variations (Ge et al., 2014; Ding et al., 2017), etc.

The internal properties of materials can change before, during, and after the environmental stimulation. The deformation process of the structure may be destroyed when the external load exceeds the stiffness of the component (Shi et al., 2020). Therefore, one of the most important issues in 4D printing is the loading capacity and deformation force in different actuated states. Most research focuses on characterizing the response of 4D printed structures made of the proposed materials and elucidating the associated principles. These 4D printing studies fall into three categories: The first is to use shape memory polymer materials with desirable mechanical properties. For example, Akbari et al. (2018) enhanced the recovery force by combining active hinges with flexible elastic hinges that store elastic strain energy during programming. A 50 g weight was placed on an actuator to demonstrate the recovered shapes of the deployable structure under load. Xin et al. (2020) showed that the recovery force of the active sandwich structures can exceed 300 mN. The structure in this study is appealing in terms of its high loading capacity during deformation, but only one-way deformation has been achieved under an external load. The second category of 4D printed structures can deform reversibly but cannot guarantee the deformation process under continuous loads. The arched strip presented by Mao et al. (2016) had a loading capacity of 250 mN in the cooling state, which endowed it with single-state stiffness through a multi-material design. Yuan et al. (2021) reported a 500 g loading capacity at various temperatures for a 3D structure constructed by a multi-material, direct 4D printing. In addition, the origami structure printed by Zhang et al. (2020) can withstand 200 g after deformation. The goal of both studies was to investigate the stiffness of 4D printed structures after drying. Yang et al. (2017) measured the thermal deformation of composite materials when the temperature is below the glass-transition temperature and found that the maximal deformation and deformation force for carbon fiber-PLA specimens are 7 mm and 100 mN, respectively, with the structure deformed in a single direction. Finally, the third category of 4D printed structures uses thin-film materials such as liquid crystal elastomer (LCE). Kotikian et al. (2018) and López-Valdeolivas et al. (2018) demonstrated the contraction of LCE with loads of 5 and 20 g, respectively, in the tensile direction. However, the LCE structure is not sufficiently stiff in the other directions.

As mentioned above, existing studies focus on the structural stiffness of a single actuated state or on the deformation force in a one-way process of 4D printing but ignores the loading capacity during the entire deformation process. The key problem in changing shape under continuous loads is the relationship between actuated internal forces and structural stiffness. The internal forces caused by environmental stimulation can change the shape of 4D printed structures by overcoming structural stiffness. However, this internal force is generally small, so that 4D printed structures are not expected to be stiff during deformation. This explains why current 4D printed structures with significant deformation usually have low stiffness during actuation: it is caused by a decrease in the modulus of the smart

material due to an externally induced deformation (Shiblee et al., 2018; Chen et al., 2020) or by a reduced stiffness of the deformation area due to a hinge structure (Zhu et al., 2018). The end result is that the structure is unable to carry loads at certain points in the deformation process. To improve loading capacity during the entire deformation process and maintain deformation behavior, there are two ways to solve this issue. On the one hand, we can propose a method to improve internal forces and, on the other hand, we can propose a design that avoids the conflicts between deformation behavior and structural stiffness.

We propose a design strategy that involves connecting two actuated components in parallel so that the 4D printed structure offers sufficient loading capacity during the reversible deformation process. By alternately heating the parallel components, the endpoint of each component has the same deformation path but the opposite stiffness. The structure can thus carry continuous loads during two-way deformations but with high stiffness in each state. The actuator component is driven by a current joule heating for a 4D printed carbon fiber reinforced composite structure. We investigate this design by using a multilayer composite structure that changes shape in response to thermal stimuli (Momeni et al., 2017). We develop a design method and printing process for this thermal mismatch principle and extend the design method to arbitrary curved structures. Next, we compare the alternate-actuated structure with traditional designs to demonstrate the advantages of the proposed design in terms of deformation capacity under continuous loads. We also design a walking robot to further demonstrate the multi-directional loading capability of the alternate actuation design. This study thus proposes a method to retain the mechanical properties of 4D printed structures subjected to various deformed states and provides a useful strategy for 4D printed structures to function under continuous loads.

MATERIALS AND METHODS

Materials and Principle for Four-Dimensional Printing

We designed a 4D printed composite structure for two layers, one layer composed of thermoplastic resin and the other layer composed of continuous fiber composite material, as shown in **Figure 1A**. During heating, the 4D printed structure bends and then, upon cooling, recovers its initial state. We fabricated a composite structure by using a six-axis parallel manipulator (Zhang et al., 2019a) with coaxial nozzles (Qiao et al., 2019), based on the polylactic acid (PLA, JG Maker Corp. in China) as matrix material and continuous carbon fiber (TORAY Corp. in Japan) as reinforcement. Current-driven joule heating was provided by carbon fiber to actuate the 4D printed structure (Wang et al., 2018a). Thus, we could drive different actuated units in multiple areas of the same structure at different times to produce a variety of deformations.

During printing, the structure was observed in three different states: the printed state, cooling state, and heating state (see

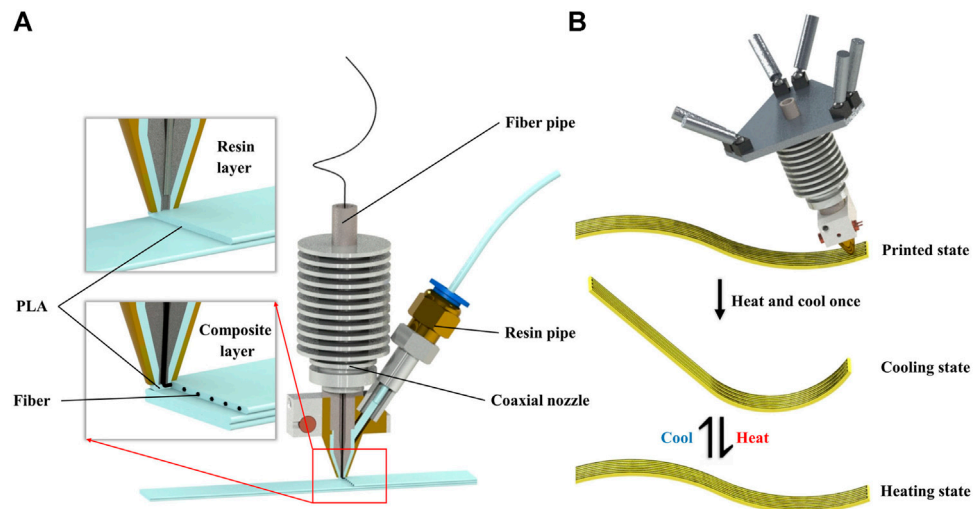


FIGURE 1 | 4D printed structure consisting of a composite layer and a resin layer. **(A)** Two-layer structure model and printing schematic. **(B)** Three different states of 4D printed structure showing their transformations.

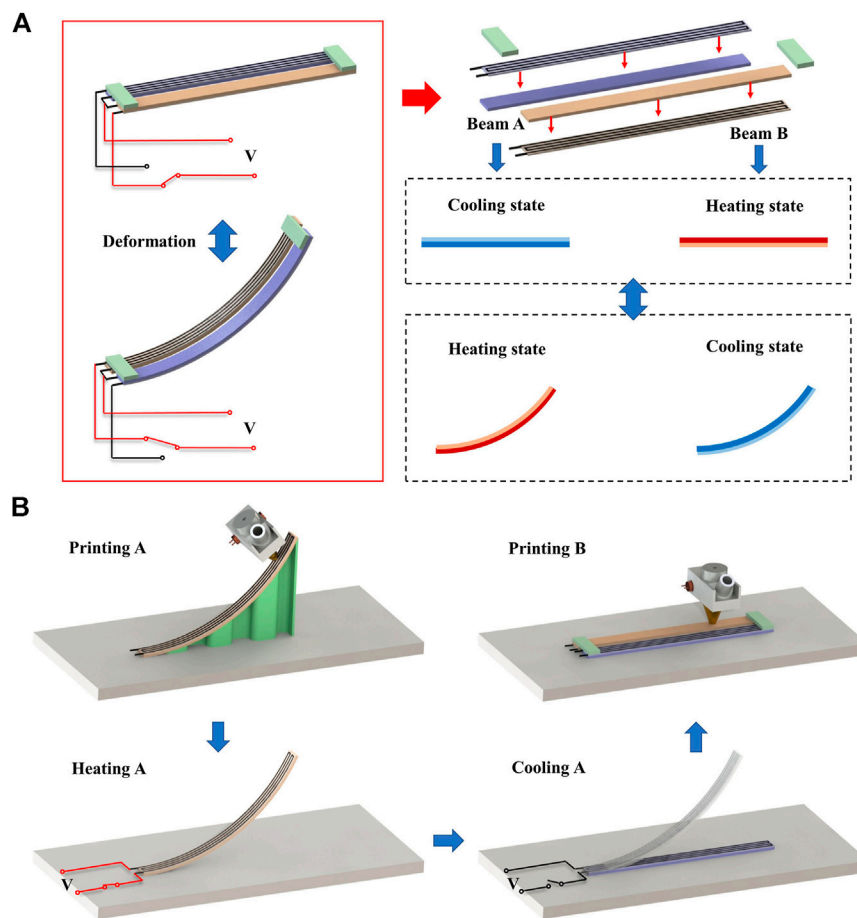


FIGURE 2 | Design of alternate-actuated structure for **(A)** two groups of beam structures and **(B)** printing process.

Figure 1B). The printed state is the state of the structure after being printed. Due to the rapid cooling, the printed structure is undeformed and has no inherent thermal stress. Any thermal stress is attributed to the difference in thermal expansion coefficients between the continuous fiber composite material and the thermoplastic resin. Later, an additional heat cycle is applied to release the residual stress inside the printed structure (Wang et al., 2018b). When heating, the residual stress is released to offset any deformation causing by thermal expansion mismatch. As the material cools, the structure enters the cooling state by bending toward the side of resin layer, which does not affect without the influence for the residual stress. Finally, a potential difference is applied across the carbon fiber in the composite layer to drive a current and transform the cooling state into the heating state. Once the potential difference is removed, the material cools and re-enters the cooling state. The heating state is like the printed state, and the change in bending angle between the cooling state and heating state depends on the design parameters of the structure and on the actuation.

Alternate Actuation Design

The structural stiffness decreases as the temperature increases because of the temperature dependence on the mechanical properties of the matrix materials (Zhang et al., 2019b). At excessively high actuating temperature, 4D printed structures cannot provide a high loading capacity during the actuated state. With low actuating temperature, the structural deformation becomes too small to provide any function as an actuator. Therefore, traditional designs have trouble simultaneously producing the desired mechanical properties and deformation properties of 4D printed structures.

Figure 2A introduces an alternate design for actuation. The structure for deformation is split into at least two groups of parallel beam structures, namely, beams A and B. The two beam groups have the same endpoints in the opposite actuated status. In other words, the endpoints of beam A at low temperature are the same as those of beam B at high temperature, and vice versa. We alternately heated the fiber drive circuit in beams A and B to ensure that the low-temperature beam always provides sufficient stiffness to support the load.

Fabrication Process

We designed the printing paths for beams A and B in the heating state. Next, we predicted the cooling state of beam A and designed the printing paths for the structure that connects the cool state of beam A to the hot state of beam B. Herein, we equate the printed state with the heating state of beam B to simplify the complexity of design and printing.

We used a multi-axis fused filament fabrication printing device to create the designed structure and connected the deformable components by using the fabrication process shown in **Figure 2B**. The main steps are as follows:

- 1) Appropriate support is designed and printed with pure resin, following which we print the heating state of beam A and then remove the support after beam A cools.
- 2) We interrupt the printing process and energize the internal fibers. When heating, any residual stress in beam A is released.
- 3) We disconnect the heating power and wait for beam A to cool to room temperature. As it cools, the deformed beam A enters the cool state.
- 4) We print the heating state of beam B and connect beam B to the cool state of beam A to finish the fabrication of the alternate-actuated structure.

Currently, the two parallel components deform in the same way under opposite actuation conditions. Beams A and B both provide benefits for bending in the same direction to retain the deformation performance while improving the structural loading capacity.

RESULTS AND DISCUSSION

Bending Behavior of Four-Dimensional Printed Composite Structures

The design goal of the alternate-actuated structures is to ensure that the endpoint of beam A in the cool state is the same as that of beam B in the heating state and vice versa. And the end trajectories of the beam A and beam B should be similar when shape changing, to reduce interference as the structure deforms. Therefore, the different states of the 4D printed structure need to be defined in advance.

We control the bending direction by adjusting the fiber orientation and present a mathematical model to predict the deformation amplitude. The bending angle $\Delta\theta$ during beam deformation is given as (Goo et al., 2020; Tian et al., 2020)

$$\theta = \frac{n(\alpha_f - \alpha_r)\Delta TL}{a \frac{\sum_{i=1}^n E_r(T_i)}{nE_f} + b + c \frac{\sum_{i=1}^n nE_f}{\sum_{i=1}^n E_r(T_i)}} \quad (1)$$

where α_r and α_f are the thermal expansion coefficient of resin and fiber, respectively; $n\Delta T = T_1 - T_2$ is the deformation temperature; $E_r(T_i)$ is the resin storage modulus and is a function of temperature; E_f is tensile modulus of the carbon fiber; and L is the beam length. The detailed derivation process is shown in **Section 1** in **Supplementary Presentation S1**.

The three parameters a , b , c depend on the sectional structure, yielding

$$a = \frac{h(\rho^3 - 3\rho^2 - 63\rho + 81)}{36\rho} \quad (2)$$

$$b = \frac{h(-2\rho^2 + 3\rho + 63)}{36} \quad (3)$$

$$c = \frac{h\rho^2}{36} \quad (4)$$

where ρ is the volume fraction of fibers in the composite material and h is the thickness of the printing layer. Here, the cross-sectional model is composed of two layers of resin and one layer of composite material **Supplementary Figure S1**.

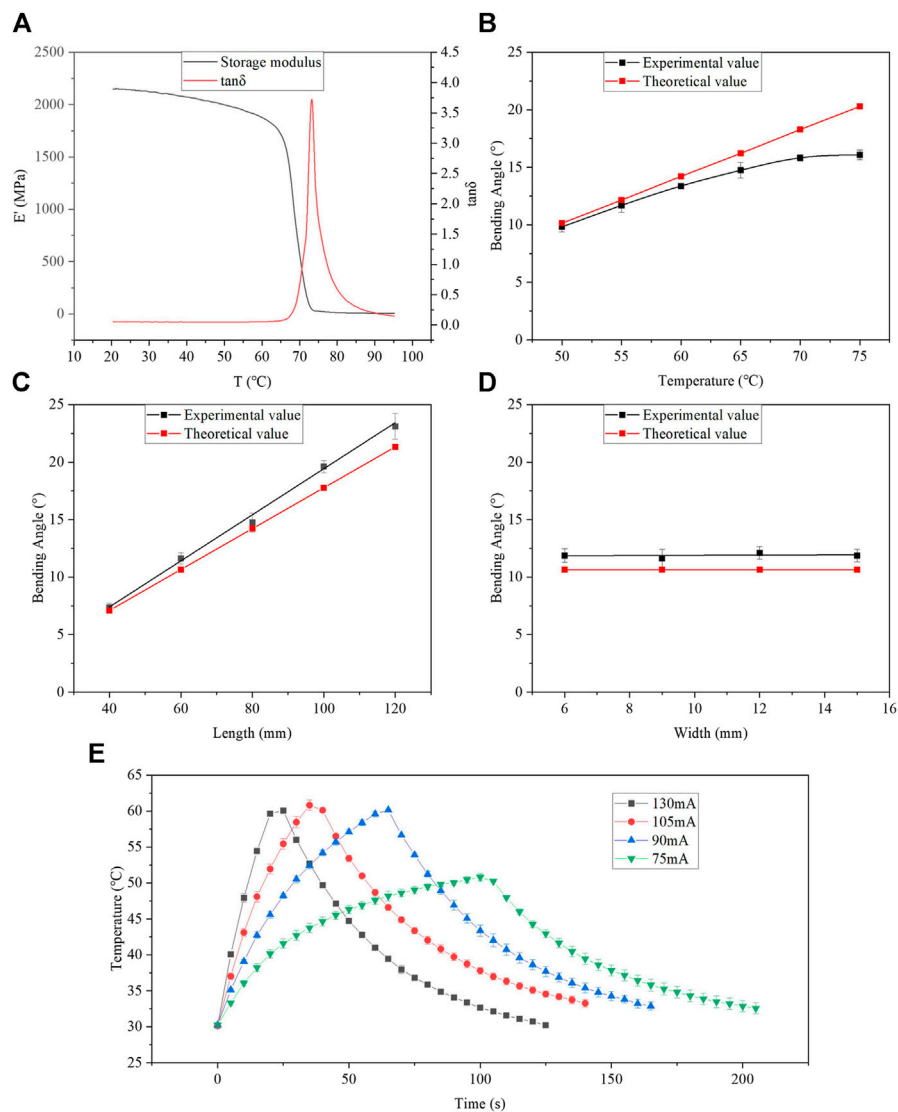


FIGURE 3 | (A) Results of DMA test of matrix material. Characterization of bending angle as a function of **(B)** actuation temperature, **(C)** design length, **(D)** design width. **(E)** Temperature as a function of time for various actuation currents.

It can be obtained from the formula that the material properties, actuation parameters and structural design parameters affect the deformation behavior of a single actuator. The bending performance correlates positively to the actuation temperature and the length of the strip, whereas the bending angle is independent of strip width. The influence from the sectional structure is more complicated. It can be found that the thickness distribution of the fiber layer and the resin layer, the volume fraction of the fiber bundle, and the arrangement density of the fibers all affect the cross-sectional morphology. This part is greatly affected by the printing process, which is not discussed in this article.

To predict the deformation, we apply a dynamic thermomechanical analysis (DMA) to the polymer matrix material to determine the glass-transition temperature and the

storage modulus as a function of temperature. For this, we use the DMA tester model NETZSCH DMA 242 from TA Instruments (New Castle, DE, United States). The temperature of the samples cut to 20 mm × 5 mm × 1 mm was increased from 20 to 95°C at a rate of 5°C per min. **Figure 3A** shows the temperature dependence of the storage modulus and tan δ. The glass-transition temperature of the matrix material is about 70°C.

We demonstrate the accuracy with which the theoretical model predicts the experimental results. The test samples are designed as long strip structures with the same cross section as in the theoretical model. The fibers in the composite layer were arranged lengthwise in the structure. The thickness and the distance between adjacent fibers were fixed at 1.5 mm, and the volume fraction of fibers in the composite material is calculated to be 5%. We move the nozzle at speed of 0.005 m/s to complete the

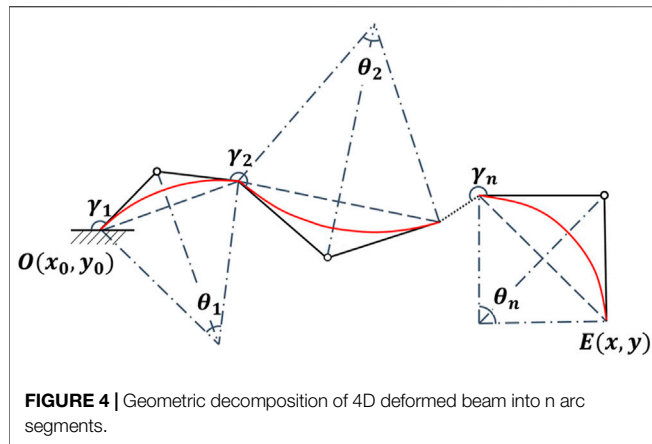


FIGURE 4 | Geometric decomposition of 4D deformed beam into n arc segments.

printing of PLA matrix and fiber-reinforced composite material at 210°C. The single printing path has a line width of 1.5 mm and a layer height of 0.5 mm. The fiber material printed into the resin matrix is 1 K Toray carbon fiber. During printing, we embedded thermal elements to better control the temperature and the accuracy of the 4D printing through a temperature-control feedback circuit. **Figure 3B** shows the bending angle as a function of temperature. The theoretical prediction is obtained from **Eqs 1–4** combined with the DMA test parameters and the actual structure parameters. The experimental results were obtained by using Image J to measure the bending angle of the sample. We used a structure size of 60 mm × 6 mm × 1.5 mm. It is apparent from this result that the bending angle has a significant positive correlation with the actuation temperature. When the temperature is less than 70°C, the margin of error between the experimental and theoretical results remains within 10%. At higher temperatures, the experimental results depart significantly from theory, which is attributed to the fact that gravity affects the experiment when the sample softens above the glass-transition temperature. **Figures 3C,D** show the relationship between bending angle and structural design parameters. The experimental results obtained at 60°C confirm the positive correlation between the bending angle and the length of the strip. Then shown in **Figure 3D**, the bending angle does not change with the width of the strip. All experimental data fall within 10% of the theoretical results.

Figure 3E shows the temperature during actuation by different currents. The sample size is 60 mm × 9 mm × 1.5 mm, and the ambient temperature is 20°C. During heating, the heating rate gradually decreases with increasing temperature so that the sample may reach thermal equilibrium with the help of external heat dissipation. During natural cooling, the cooling rate of the sample gradually reduces as the temperature decreases until the temperature reaches the ambient temperature. The variations in temperature during heating and cooling both go from fast to slow, which is advantageous to maintain consistent deformation for the parallel components of composite structure. A driving current of 80 mA proved best to ensure synchronous deformation. Both the heating and cooling phases were designed as 1 min with temperature variation between 35 and 60°C.

Design of Deformation for Arbitrary Curved Components

To confirm that the design strategy is suitable for complex structural design, arbitrary curved components now replace simple strips or beams in the alternate-actuated structure. The key is to ensure that the deformation endpoints follow consistent paths for both components.

This study used geometric analysis to summarize the general design. The beam structure with a single fiber orientation is divided into n segments of unequal arcs. As presented in **Figure 4**, θ_i is the central angle of arc i , and γ_i is the angle from the tangent at the end of arc $(i - 1)$ to the tangent at the start of arc i in the clockwise direction. Therefore, the chord of the two arcs clockwise from section $(i - 1)$ to section i is α_i :

$$\alpha_i = \gamma_i + \frac{\theta_{i-1} + \theta_i}{2} \quad (5)$$

Let $O(x_0, y_0)$ be the known starting point of the entire beam structure, then the coordinates of the endpoint of the structure can be deduced by a geometric calculation as follows:

$$x = x_0 + \sum_{i=1}^n \frac{2l_i}{|\theta_i|} \sin \frac{|\theta_i|}{2} \cos(2\pi - \alpha_{i-1} - \alpha_i) \quad (6)$$

$$y = y_0 + \sum_{i=1}^n \frac{2l_i}{|\theta_i|} \sin \frac{|\theta_i|}{2} \sin(2\pi - \alpha_{i-1} - \alpha_i) \quad (7)$$

In the same way, the coordinates of the end of the structure after deformation can be expressed using **Eqs 5–7**. The new θ_i is calculated as $\theta_i - \Delta\theta_i$, where $\Delta\theta_i$ is the bending angle for the arc i and can be calculated by using **Eqs 1–4**. The central angle θ_i has a positive and negative difference with respect to the formula above. When the arc is convex (concave), θ_i is positive (negative).

We consider the sample shown in **Figure 5A** to demonstrate the proposed design method. The sample consists of two different parallel components, with diverse shape in opposite actuated state. We split each component into the length of the two curves where $l_{A1} = l_{B1} = 30$ mm, $l_{A2} = l_{B2} = 35$ mm and set the initial positions of the two components at $O_A(0, 0)$ and $O_B(0, 8)$, then add design constraints to maintain the end point at $x = 60$ mm. The deformation along the y axis is set to 5.5 mm. **Eqs 5–7** and the geometric analysis give the final structural design parameters of the sample, which are listed in **Table 1**.

The deformed sample is shown in **Figure 5B**. And the print process, cross-sectional images and deformation video are shown in **Supplementary Figures S2, S3; Supplementary Video S1**. The deformation along the y axis was measured by using ImageJ and is about 5.1 mm, which is 92% compared to the design value. The main reason for the reduced deformation is the uneven thickness caused by insufficient printing accuracy. In addition, the rigid connection at the end of the structure also has negligible effect on the deformation.

Analysis of Deformation Capacity under Continuous Force

To compare the loading capacity of the alternate actuation design with that of traditional designs, we tested reversible variations in

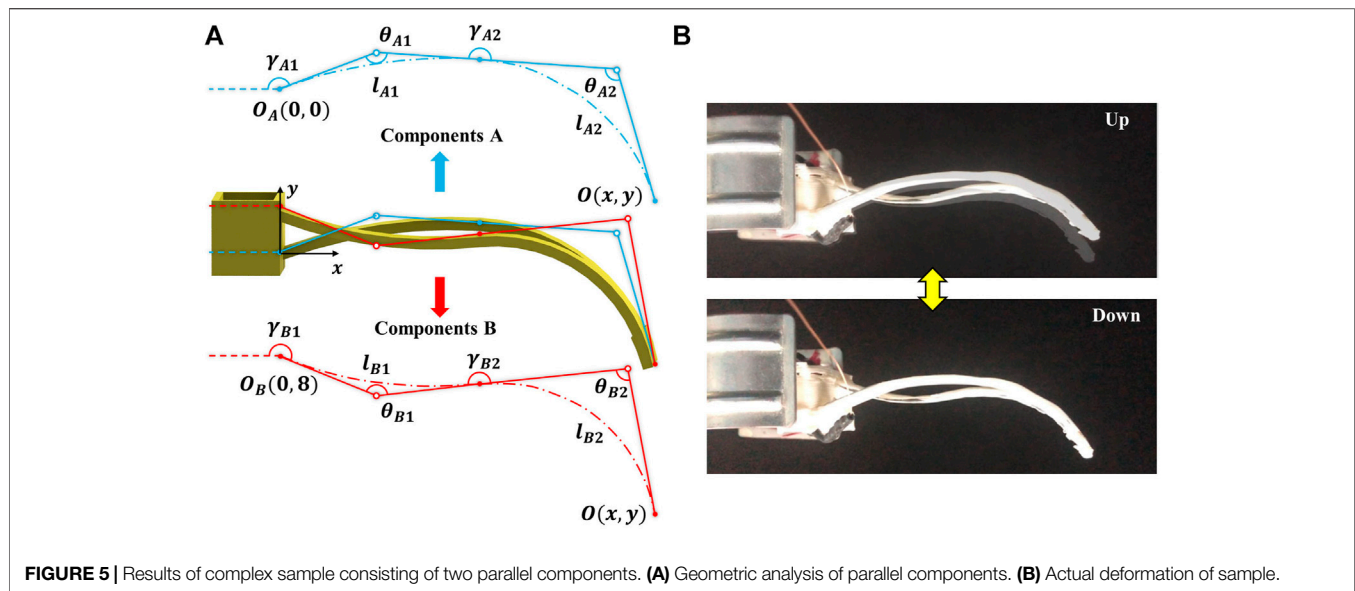


FIGURE 5 | Results of complex sample consisting of two parallel components. **(A)** Geometric analysis of parallel components. **(B)** Actual deformation of sample.

TABLE 1 | Design parameters of each parallel components.

	θ_1	θ_2	γ_1	γ_2
Component A	$\theta_{A1} = 23.9^\circ$	$\theta_{A2} = 69.8^\circ$	$\gamma_{A1} = 159.6^\circ$	$\gamma_{A2} = 180^\circ$
Component B	$\theta_{B1} = -27.8^\circ$	$\theta_{B2} = 85.5^\circ$	$\gamma_{B1} = 201.6^\circ$	$\gamma_{B2} = 180^\circ$

shape under a hanging load. When actuating with a 90 mA current, the structural deformation and recovery both last 60 s. **Figure 6A** shows how the traditional sample swings up under a 10 g load. The sample was designed with parallel beams which the fiber arrangements for two parallel components are on the same side. **Figure 6C** shows the results for the bending angle first heating and then cooling under different loads, both of the heating phase and cooling phase are 60 s. The black, red and blue curves correspond to bending performance under 0, 10, and 100 g loads. The results show that the bending curve early recover at 40 s instead of 60 s. It means that the load capacity of the structure at 40 s is no longer able to carry 10 g load because the stiffness decreases due to rising temperature. The curve under a load of 100 g also shows the destruction of deformation behavior when the structure is heated in 0~60 s. Additionally, the structure has additional reverse deformation when they recover under the 10 and 100 g load. In the heating phase, the structure is irreversibly deformed under the influence of load, so the deformation at the end of heating is much smaller than the no-load deformation. But in the cooling phase, the structure in high temperature state is subjected to a small force in the direction of recover because of the irreversibly deformed. Therefore, recovery of the structure is less affected by the load, the recovery angle is similar as the no-load bending angle. The difference in deformation between heating and cooling caused this additional reverse deformation. In summary, the traditional deformation structure cannot be used under more than 10 g load because of the influence of early recovery during heating and additional reverse deformation during cooling.

Figure 6B shows the alternate-actuated structure swing under a 100 g load. The overall configuration of the alternate-actuated structure is the same as that of the traditional structure, but the fibers are on the opposite surfaces of the two parallel components. **Figure 6D** shows the deformation of the alternate-actuated structure under different loads, where the black, red, and blue curves are deformation under no load, a 10 g load, and a 100 g load, respectively. The alternate-actuated structure still swings up and down under the 100 g load without early recovery during heating and additional reverse deformation during cooling, which demonstrates that the load capacity in reversible deformation process of this structure is an order of magnitude greater than that of the traditional actuated structure. Because the dual parallel beam design allows one beam to be hot while the other is cold during the entire deformation, one beam remains in the cooling state to provide sufficient structural stiffness. The alternate-actuated structure reveals no significant mechanical defects during the two-way deformation process. The bending angle of the alternate-actuated structure is the same under no load and the 10 g load as the traditional actuated structure, and the deformation is reduced by about 50% at 100 g comparing with no-load deformation. To summarize, the alternate-actuated structure presents no significant mechanical performance defects in the two-way deformation process. It deforms reversibly under a load more than tenfold greater than what is possible with the traditional design.

Four-Dimensional Printed Walking Robot

Given the ability to change shape under continuous loads, the alternate-actuated structures have significant potential for use in robotic arms, load-moving devices, and posture adjustments. **Figure 7A** shows a walking robot that we designed to further demonstrate the potential of this technology. Each robot has six deformable legs divided into walking legs and supporting legs. The two legs in the middle are the walking legs, while the others are supporting legs. The walking legs carry the weight of the robot

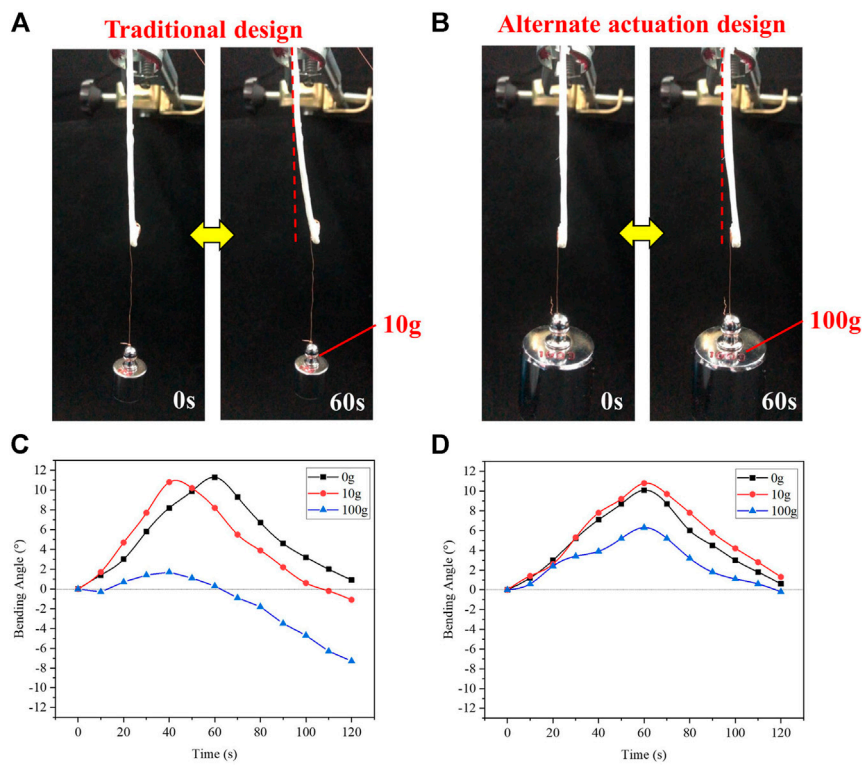


FIGURE 6 | Comparison of deformation under load of traditional design and alternate-actuation design. **(A)** Traditional structure deformed under 10 g load. **(B)** Alternate-actuated structure deformed under 100 g load. **(C)** Bending angle as a function of time for traditional structure under different continuous loads. **(D)** Bending angle as a function of time for alternate-actuated structure under continuous loads.

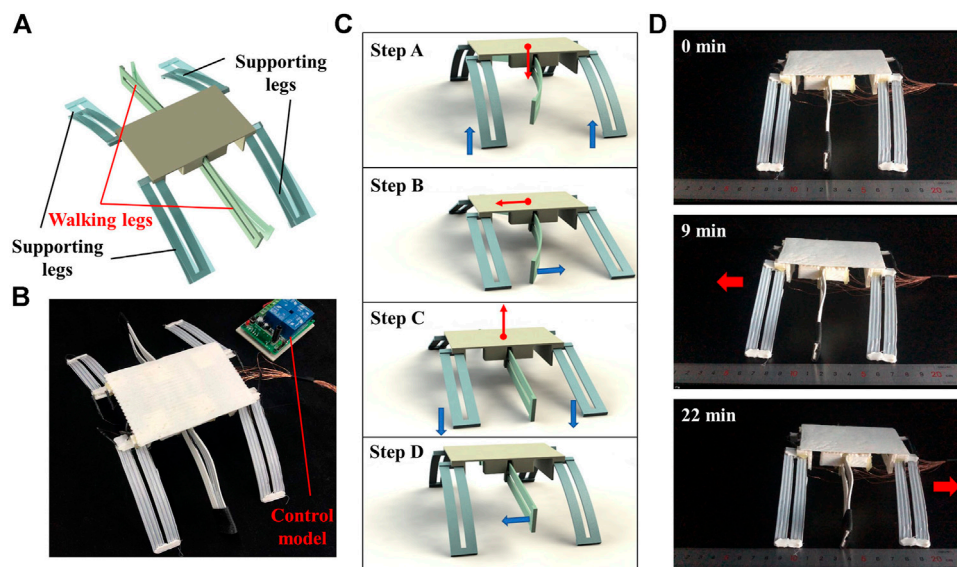


FIGURE 7 | Demonstration of walking robot. **(A)** Design model. **(B)** Photograph of walking robot. **(C)** Four steps in a gait cycle of walking robot. **(D)** Forward and backward motion of walking robot.

body and provide forward and backward propulsion during the swing phase. Therefore, the walking legs must offer sufficient structural stiffness in two-way deformations. Therefore, we designed the walking legs using the alternate-actuated parallel structure to ensure successful swinging under continuous loads in different directions.

Figure 7B shows the fabricated walking robot. Each leg is controlled by a separate circuit to allow independent actuation. **Figure 7C** shows the gait of the robot, where one gait cycle requires four steps: Firstly, the support legs are heated and gradually lose their capacity to support weight. The center of gravity of the walking robot thus shifts down. The two walking legs contact the ground to maintain the structural stability together with the support legs. Secondly, the walking legs swing back. The friction force exerted on the walking legs is greater than that on the support legs, so the walking robot is pushed in the opposite direction. Thirdly, the support legs cool and gradually recover their deformation and structural stiffness, so the center of gravity of the walking robot rises and the walking legs lose contact with the ground. Finally, the walking legs recover their shape when hanging in the air and are prepared for the next stride. The total time for a gait cycle is approximately 180 s, which includes 30 s for step A, 60 s for step B, and 90 s for steps C and D. Step D, when the walking legs lose contact with the ground, starts 30 s after step C and ends at the same time as step C.

Figure 7D shows the forward and backward motion of the walking robot. The robot moves forward by 12 mm over 9 min in three gait cycles and then moves backward by 16 mm over 13 min in four gait cycles. The results show that a single gait cycle translates the robot by about 4 mm, whether the robot moves forward or backward. These results demonstrate that the alternate-actuated structures can undergo two-way deformation under continuous load and that two-way deformation produces a similar driving force. Video of the robot walking is shown in **Supplementary Video S2**.

The main reason of the slow walking speed is that the walking robot takes 1 min for each deformation of the walking legs. The deformation of the walking legs with the alternate-actuated structure includes the heating phase and cooling phase of the two groups of parallel components at the same time, the heating and cooling speed should be matched to ensure the consistency of their end position. It takes 1 min for the components from the actuated temperature to environment temperature, so the deformation time of the walking legs are 1 min. In order to improve the walking speed of the robot, an air-cooling system or a fluidic cooling microchannel can be integrated to reduce cooling phase in the future.

In addition, the usable range of the alternate-actuated structures are not limited to the deformation principle described herein. It can be expanded to other deformations that involve variations in structural stiffness, such as thermally driven deformations of LCE composite structures (Roach et al., 2018), photothermally driven deformation (Hua et al., 2018), and wetting- or drying-driven deformation (Baker et al., 2019).

CONCLUSION

This study proposes an alternate-actuation design to provide reversible, two-way deformation without stiffness attenuation under continuous loads. We use the design to print an actuator based on thermal mismatch to demonstrate that the deformation of two parallel components is the same for opposite actuation conditions. We develop a mathematical model to predict with 90% accuracy the bending angle for the 4D printed structure. We also propose a design strategy for the complex parallel components consisted with arbitrary curve components. The actual deformation of the parallel components is within 8% of the design value. The alternate-actuated structure can carry loads during the entire reversible deformation, and it offers a tenfold increased loading capacity compared with the traditional design. Finally, we design a walking robot to demonstrate the use of the alternate-actuation design for forward and backward translation. We use the alternate-actuation design on the swing legs and demonstrate that the legs swing normally under the multi-directional continuous loads. Thus, the robot legs deform reversibly under continuous loads, which is promising for applications involving soft robots, smart actuators, and artificial muscles.

DATA AVAILABILITY STATEMENT

The original contributions presented in the study are included in the article/**Supplementary Material**, further inquiries can be directed to the corresponding author.

AUTHOR CONTRIBUTIONS

GC, GS, and DZ contributed to the conception of the study; GC led the experiments with assistance from BZ and wrote the manuscript; LL, GS, and DZ. contributed significantly to analysis and manuscript preparation; All authors provided feedback.

FUNDING

Financial support from Key-Area Research and Development Program of Guangdong Province, China (Grant No. 2020B090923003) is gratefully acknowledged.

SUPPLEMENTARY MATERIAL

The Supplementary Material for this article can be found online at: <https://www.frontiersin.org/articles/10.3389/fmats.2021.661593/full#supplementary-material>

REFERENCES

- Akbari, S., Sakhaei, A. H., Kowsari, K., Yang, B., Serjouei, A., Yuanfang, Z., et al. (2018). Enhanced Multimaterial 4D Printing with Active Hinges. *Smart Mater. Struct.* 27 (6), 065027. doi:10.1088/1361-665X/aabe63
- Baker, A. B., Bates, S. R. G., Llewellyn-Jones, T. M., Valori, L. P. B., Dicker, M. P. M., and Trask, R. S. (2019). 4D Printing with Robust Thermoplastic Polyurethane Hydrogel-Elastomer Trilayers. *Mater. Des.* 163, 107544. doi:10.1016/j.matdes.2018.107544
- Bar-Cohen, Y., Carrico, J. D., and Leang, K. K. (2017). Fused Filament 3D Printing of Ionic Polymer-Metal Composites for Soft Robotics. *EAPAD*. 2017, 10163. doi:10.1117/12.2259782
- Chen, D., Liu, Q., Han, Z., Zhang, J., Song, H., Wang, K., et al. (2020). 4D Printing Strain Self-Sensing and Temperature Self-Sensing Integrated Sensor-Actuator with Bioinspired Gradient Gaps. *Adv. Sci.* 7 (13), 2000584. doi:10.1002/adv.202000584
- Cheng, C.-Y., Xie, H., Xu, Z.-y., Li, L., Jiang, M.-N., Tang, L., et al. (2020). 4D Printing of Shape Memory Aliphatic Copolyester via UV-Assisted FDM Strategy for Medical Protective Devices. *Chem. Eng. J.* 396, 125242. doi:10.1016/j.cej.2020.125242
- Ding, Z., Weeger, O., Qi, H. J., and Dunn, M. L. (2018). 4D Rods: 3D Structures via Programmable 1D Composite Rods. *Mater. Des.* 137, 256–265. doi:10.1016/j.matdes.2017.10.004
- Ding, Z., Yuan, C., Peng, X., Wang, T., Qi, H. J., and Dunn, M. L. (2017). Direct 4D Pprinting via Active Ccomposite Mmaterials. *Sci. Adv.* 3 (4), e1602890. doi:10.1126/sciadv.1602890
- Ge, Q., Dunn, C. K., Qi, H. J., and Dunn, M. L. (2014). Active Origami by 4D Printing. *Smart Mater. Struct.* 23 (9), 094007. doi:10.1088/0964-1726/23/9/094007
- Ge, Q., Sakhaei, A. H., Lee, H., Dunn, C. K., Fang, N. X., and Dunn, M. L. (2016). Multimaterial 4D Printing with Tailorable Shape Memory Polymers. *Sci. Rep.* 6, 31110. doi:10.1038/srep31110
- Gladman, A. S., Matsumoto, E. A., Nuzzo, R. G., Mahadevan, L., and Lewis, J. A. (2016). Biomimetic 4D Printing. *Nat. Mater.* 15 (4), 413–418. doi:10.1038/nmat4544
- Goo, B., Hong, C.-H., and Park, K. (2020). 4D Printing Using Anisotropic Thermal Deformation of 3D-Printed Thermoplastic Parts. *Mater. Des.* 188, 108485. doi:10.1016/j.matdes.2020.108485
- Hua, D., Zhang, X., Ji, Z., Yan, C., Yu, B., Li, Y., et al. (2018). 3D Printing of Shape Changing Composites for Constructing Flexible Paper-Based Photothermal Bilayer Actuators. *J. Mater. Chem. C* 6 (8), 2123–2131. doi:10.1039/c7tc05710e
- Kim, Y., Yuk, H., Zhao, R., Chester, S. A., and Zhao, X. (2018). Printing Ferromagnetic Domains for Untethered Fast-Transforming Soft Materials. *Nature*. 558 (7709), 274–279. doi:10.1038/s41586-018-0185-0
- Kotikian, A., Truby, R. L., Boley, J. W., White, T. J., and Lewis, J. A. (2018). 3D Printing of Liquid Crystal Elastomeric Actuators with Spatially Programmed Nematic Order. *Adv. Mater.* 30 (10), 1706164. doi:10.1002/adma.201706164
- Kuang, X., Roach, D. J., Wu, J., Hamel, C. M., Ding, Z., Wang, T., et al. (2018). Advances in 4D Printing: Materials and Applications. *Adv. Funct. Mater.* 29 (2), 1805290. doi:10.1002/afdm.201805290
- Lee, A. Y., Zhou, A., An, J., Chua, C. K., and Zhang, Y. (2020). Contactless Reversible 4D-Printing for 3D-To-3d Shape Morphing. *Virtual Phys. Prototyping* 15 (4), 481–495. doi:10.1080/17452759.2020.1822189
- Liu, Y., Shaw, B., Dickey, M. D., and Genzer, J. (2017). Sequential Self-Folding of Polymer Sheets. *Sci. Adv.* 3 (3), e1602417. doi:10.1126/sciadv.1602417
- López-Valdeolivas, M., Liu, D., Broer, D. J., and Sánchez-Somolinos, C. (2018). 4D Printed Actuators with Soft-Robotic Functions. *Macromol. Rapid Commun.* 39 (5), 1700710. doi:10.1002/marc.201700710
- Mao, Y., Ding, Z., Yuan, C., Ai, S., Isakov, M., Wu, J., et al. (2016). 3D Printed Reversible Shape Changing Components with Stimuli Responsive Materials. *Sci. Rep.* 6, 24761. doi:10.1038/srep24761
- Momeni, F., M.Mehdi Hassani, N. S., Liu, X., and Ni, J. (2017). A Review of 4D Printing. *Mater. Des.* 122, 42–79. doi:10.1016/j.matdes.2017.02.068
- Qiao, J., Li, Y., and Li, L. (2019). Ultrasound-assisted 3D Printing of Continuous Fiber-Reinforced Thermoplastic (FRT) Composites. *Additive Manufacturing*. 30, 100926. doi:10.1016/j.addma.2019.100926
- Roach, D. J., Kuang, X., Yuan, C., Chen, K., and Qi, H. J. (2018). Novel Ink for Ambient Condition Printing of Liquid Crystal Elastomers for 4D Printing. *Smart Mater. Struct.* 27 (12), 125011. doi:10.1088/1361-665X/aac96f
- Shi, Y., Wu, H., Yan, C., Yang, X., Chen, D., Zhang, C., et al. (2020). Four-dimensional Printing – the Additive Manufacturing Technology of Intelligent Components. *Chin. J. Mech. Eng-en.* 56 (15), 1–25. doi:10.3901/jme.2020.15.001
- Shiblee, M. N. I., Ahmed, K., Khosla, A., Kawakami, M., and Furukawa, H. (2018). 3D Printing of Shape Memory Hydrogels with Tunable Mechanical Properties. *Soft Matter*. 14 (38), 7809–7817. doi:10.1039/c8sm01156g
- Tian, X., Wang, Q., and Li, D. (2020). Design of a Continuous Fiber Trajectory for 4D Printing of Thermally Stimulated Composite Structures. *Sci. China Technol. Sci.* 63 (4), 571–577. doi:10.1007/s11431-019-1485-5
- Wang, Q., Tian, X., Huang, L., Li, D., Malakhov, A. V., and Polilov, A. N. (2018a). Programmable Morphing Composites with Embedded Continuous Fibers by 4D Printing. *Mater. Des.* 155, 404–413. doi:10.1016/j.matdes.2018.06.027
- Wang, G., Cheng, T., Do, Y., Yang, H., Tao, Y., Gu, J., et al. (2018b). Printed Paper Actuator. *CHI*. 18 569, 1–12. doi:10.1145/3173574.3174143
- Yang, C., Wang, B., Li, D., and Tian, X. (2017). Modelling and Characterisation for the Responsive Performance of CF/PLA and CF/PEEK Smart Materials Fabricated by 4D Printing. *Virtual Phys. Prototyping* 12 (1), 69–76. doi:10.1080/17452759.2016.1265992
- Yuan, C., Roach, D. J., Dunn, C. K., Mu, Q., Kuang, X., Yakacki, C. M., et al. (2017). 3D Printed Reversible Shape Changing Soft Actuators Assisted by Liquid Crystal Elastomers. *Soft Matter*. 13 (33), 5558–5568. doi:10.1039/c7sm00759k
- Yuan, C., Wang, F., and Ge, Q. (2021). Multimaterial Direct 4D Printing of High Stiffness Structures with Large Bending Curvature. *Extreme Mech. Lett.* 42, 101122. doi:10.1016/j.eml.2020.101122
- Zhang, D., Zhang, G., and Li, L. (2019a). Calibration of a Six-axis Parallel Manipulator Based on BP Neural Network. *Ind. Robot.* 46 (5), 692–698. doi:10.1108/ir-12-2018-0248
- Zhang, Y. F., Zhang, N., Hingorani, H., Ding, N., Wang, D., Yuan, C., et al. (2019b). Fast-Response, Stiffness-Tunable Soft Actuator by Hybrid Multimaterial 3D Printing. *Adv. Funct. Mater.* 29 (15), 1806698. doi:10.1002/adfm.201806698
- Zhang, Q., Kuang, X., Weng, S., Zhao, Z., Chen, H., Fang, D., et al. (2020). Rapid Volatilization Induced Mechanically Robust Shape-Morphing Structures toward 4D Printing. *ACS Appl. Mater. Inter.* 12 (15), 17979–17987. doi:10.1021/acsami.0c02038
- Zhao, S. C., Maas, M., Jansen, K., and van Hecke, M. (2019). 3D Printed Actuators: Reversibility, Relaxation, and Ratcheting. *Adv. Funct. Mater.* 29 (51), 1905545. doi:10.1002/adfm.201905545
- Zhu, P., Yang, W., Wang, R., Gao, S., Li, B., and Li, Q. (2018). 4D Printing of Complex Structures with a Fast Response Time to Magnetic Stimulus. *ACS Appl. Mater. Inter.* 10 (42), 36435–36442. doi:10.1021/acsami.8b12853

Conflict of Interest: The authors declare that the research was conducted in the absence of any commercial or financial relationships that could be construed as a potential conflict of interest.

Copyright © 2021 Chu, Zhou, Shao, Zhang and Li. This is an open-access article distributed under the terms of the Creative Commons Attribution License (CC BY). The use, distribution or reproduction in other forums is permitted, provided the original author(s) and the copyright owner(s) are credited and that the original publication in this journal is cited, in accordance with accepted academic practice. No use, distribution or reproduction is permitted which does not comply with these terms.



4D Printing of Lead Zirconate Titanate Piezoelectric Composites Transducer Based on Direct Ink Writing

Kai Liu^{1,2}, Qingqing Zhang², Chenyang Zhou², Yusheng Shi³, Ce Sun⁴, Huajun Sun^{1,2,4*}, Changxia Yin⁴, Jiaming Hu², Shuyu Zhou², Yuzhen Zhang² and Yu Fu²

¹State Key Laboratory of Silicate Materials for Architectures, Wuhan University of Technology, Wuhan, China, ²School of Materials Science and Engineering, Wuhan University of Technology, Wuhan, China, ³State Key Laboratory of Materials Processing and Die and Mould Technology, Huazhong University of Science and Technology, Wuhan, China, ⁴Advanced Ceramics Institute of Zibo New and High-Tech Industrial Development Zone, Zibo, China

OPEN ACCESS

Edited by:

Marcelo J. Dapino,
The Ohio State University,
United States

Reviewed by:

Venu Gopal Madhav Annamdas,
Continental, Germany
Rouhollah Dermanaki Farahani,
École de technologie supérieure (ÉTS),
Canada

*Correspondence:

Huajun Sun
huajunsun@whut.edu.cn

Specialty section:

This article was submitted to
Smart Materials,
a section of the journal
Frontiers in Materials

Received: 27 January 2021

Accepted: 12 May 2021

Published: 28 May 2021

Citation:

Liu K, Zhang Q, Zhou C, Shi Y, Sun C,
Sun H, Yin C, Hu J, Zhou S, Zhang Y
and Fu Y (2021) 4D Printing of Lead
Zirconate Titanate Piezoelectric
Composites Transducer Based on
Direct Ink Writing.
Front. Mater. 8:659441.
doi: 10.3389/fmats.2021.659441

Lead zirconate titanate (PZT) piezoelectric composites used in transducers were fabricated via direct ink writing (DIW) combined with furnace sintering and resin impregnation. A ceramic slurry with a volume fraction of 52 vol% and suitable viscoelasticity was prepared. After post-process, the PZT ceramic specimens showed a nanoscale grain size with a density of 7.63 g/cm³, accounting for 97.8% of the theoretical density. The effects of different printing rod spacing on the electrical properties of composites were evaluated and lubricated. Finally, an underwater acoustic transducer was assembled by using the PZT piezoelectric composites fabricated by the above method. The electrical signal generated by the underwater acoustic transducer changed autonomously with the acoustic stimulation, which indicated the application mode of 4D printing in functional devices in the future.

Keywords: 4D printing, DIW, piezoelectric composites, performance, underwater acoustic transducer

INTRODUCTION

Underwater acoustic transducer is a kind of functional device that can convert acoustic and electrical signals into each other and its core component is piezoelectric composite material (Tian et al., 2021; Li et al., 2006; Rouffaud et al., 2015). Compared with 0–3, 1–3 and, 2–3 piezoelectric composites, 3–3 ceramic/polymer composites have a bi-continuous architecture comprising an active ferroelectric ceramic phase and a passive flexible polymer phase, which possess high hydrostatic pressure sensitivity and good coupling properties with water, thereby improving the bandwidth and transmitting and receiving sensitivity of the transducer (Newnham et al., 1978; Tressler et al., 1999; Bowen and Topolov, 2003). But traditional fabricating methods, such as the self-assembly method (Liu et al., 1996), the gel-casting method, the cutting-filling method (Viganò et al., 2017) and so on, have certain disadvantages like low material utilization, long production cycles and limited product complexity (Woodward et al., 2015).

Additive manufacturing (AM) technology has the advantage of being easy to prepare complex structural parts, including direct ink writing (DIW), digital light processing (DLP), selective laser sintering (SLS) and other methods. The principle of DIW is to extrude viscoelastic ink from the needle head to form rod-shaped fibers. As the needle head moves, the rod-shaped fibers are deposited into a specific pattern (Revelo and Colorado, 2018; Coppola et al., 2021). DLP technology is to project patterned ultraviolet light onto the photocurable material to cure each single layer, and form a specific shape through the superimposition of layers (Wang et al., 2019; Li et al., 2021). In SLS

technology, a laser is used to melt the binder and bond the ceramic powder to form (Kai et al., 2020). Compared with the DLP and SLS processes, the DIW process has the advantages of simple forming equipment, easy preparation of slurry, and high solid content of the printed green body (An et al., 2020). Recently, AM process combined with smart materials is also called 4D printing and piezoelectric materials are a typical type of smart materials (Kong et al., 2014; Kuang et al., 2019). Therefore, this research belongs to the category of 4D printing ceramics. Some researchers have tried to investigate 4D printing of ceramics in recent years. Liu et al. (2018) took the lead in researching ceramic 4D printing, where DIW was used to print a special precursor for ceramics. Firstly, the main structure was printed on a prestressed elastic substrate. When the prestress of the substrate disappears, the main structure is deformed accordingly and became a preset shape. After heating treatment, the required ceramic body was obtained. In this research, “shape change” of ceramic components is realized by using the elasticity of the composites in 4D printing. Grinberg et al. (2018) combined barium titanate (BTO) material with fused deposition technology, and BTO piezoelectric composites were 4D printed for making sensors, which can be implanted into the human body to achieve the function and effect of real-time detection of the force between prosthesis bones. However, there is a lack of exploration of the performance changes caused by the special structure of piezoelectric composites. Zeng et al. (2020) printed 1–3 BTO piezoelectric composite with honeycomb structure through 4D printing by combining BTO material with DLP technology. The structure can increase the acoustic performance of the piezoelectric ceramic, realize the function of ultrasonic sensing. However, due to the limitation of the piezoelectric composite structure, the voltage efficiency is only 0.1%. Compared with BTO ceramics, lead zirconate titanate (PZT) ceramics also have a higher piezoelectric coefficient and are more suitable to be used as a transducer matrix material (Palmero and Bollero, 2020). Chen et al. (2017) and Yan et al. (2018) prepared PZT piezoelectric ceramics columnar array through DLP technology and assembled PZT-based ultrasonic sensors with good sensing effects. However, due to the high acoustic impedance of piezoelectric ceramics, it is not easy to match the acoustic impedance of water, which limits the underwater application of the ultrasonic transducer. At present, there are few studies on the performance and functional changes of 4D printed PZT piezoelectric composites transducer. Through editing the structure and composition of piezoelectric composites freely, 4D printing of electroactive materials including piezo-composites will present a revolutionary significance of fabricating more excellent and flexible piezoelectric materials.

This research aims to present 4D printing of PZT composites transducer based on the DIW process. PZT slurry with high solid content was designed and prepared and the influence of dispersant on the rheological properties of the slurry was explored. Multiple sets of piezoelectric ceramic skeletons were prepared, and the extruded rod fibers were arranged at different intervals. The electrical properties of the piezoelectric composites with different rod spacing were discussed. Finally, the output

voltage evolution stimulated by the vibration of acoustic waves was presented in an underwater environment.

EXPERIMENT

Process Route

Figure 1 shows the fabricating route of underwater acoustic transducers. The PZT ceramic skeleton was printed by DIW method, and epoxy resin was filled into the skeleton to prepare piezoelectric composites, and then the piezoelectric composites were prepared into an underwater acoustic transducer.

Slurry Preparation

First, the raw PZT powder was ball milled to refine the particle size. Trisodium citrate was added as a dispersant into ethanol to prepare a premixed solution. The surfaces of the particles were quickly wetted by dispersants, which increased the energy barrier between the particles in order to eliminate the agglomeration (Walton et al., 2020). After ball milling, the mixture was filtered and dried. Finally, the PZT powder with a particle size of d₅₀: 523 nm was obtained as shown in **Figure 2**. After powder preparation, a 10 wt% polyvinyl alcohol (PVA) aqueous solution containing PZT powder was prepared. The solution also contains a certain amount of ammonium polyacrylate (PAA-NH₄) or sodium polyacrylate homopolymer (PAAS) as dispersant, and 1.75 wt% glycerin as lubricant. After stirring, the slurry was aged for 2 h before printing.

Printing Process

The model was sliced by the slicing software (Ultimaker Cura 4.1) to generate a Gcode file and the movement of the printer needle head is controlled by the program including layer information. The slurry was extruded from the syringe system and the power was supplied by an air pump with a pressure of 0.2 MPa. **Figure 3** shows the direct ink writing 3D printing device and its sketch map. The height of the syringe is 115 mm, and its moving speed is set to be 8 mm/s.

A suitable extrusion needle head is extremely important in the printing process. The smaller the needle head size is, the greater pressure is needed for extrusion. Inversely, if the size of the needle head is too large, it might result in poor printing accuracy. The height of the layer is also an important parameter of printing. If the layer height is too low, the needle head will walk in the previously extruded slurry and cause accumulation. If the height of each layer is too high, the slurry stacking will be misaligned. The diameter of the needle used in this study was 0.6 mm and the height of the printing layer was 0.3 mm, so that it exists no excess drags or accumulation on each extruded fiber.

The stacking directions of the rods between the layers were perpendicular to each other and the size of the woodpile structure designed by 3D modeling software was set to be 20 × 20 × 5 mm. Due to the viscoelasticity of the slurry, a gap could be formed between the rods in the height direction, and the shape of the model maintained. Since there were few volatile substances in the slurry, the green body shrunk insignificantly after drying.

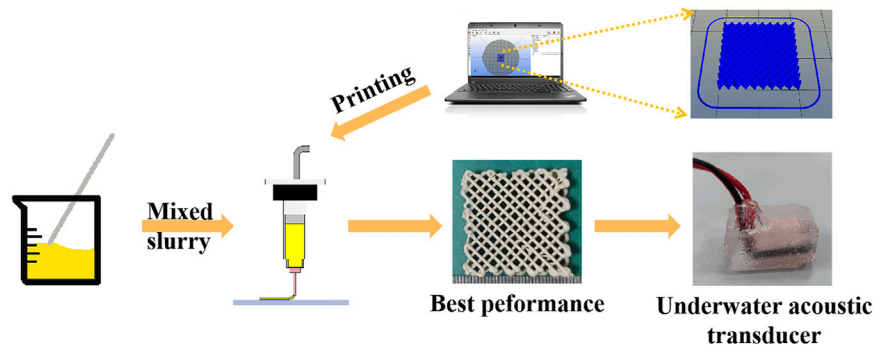


FIGURE 1 | The fabricating route of underwater acoustic transducers.

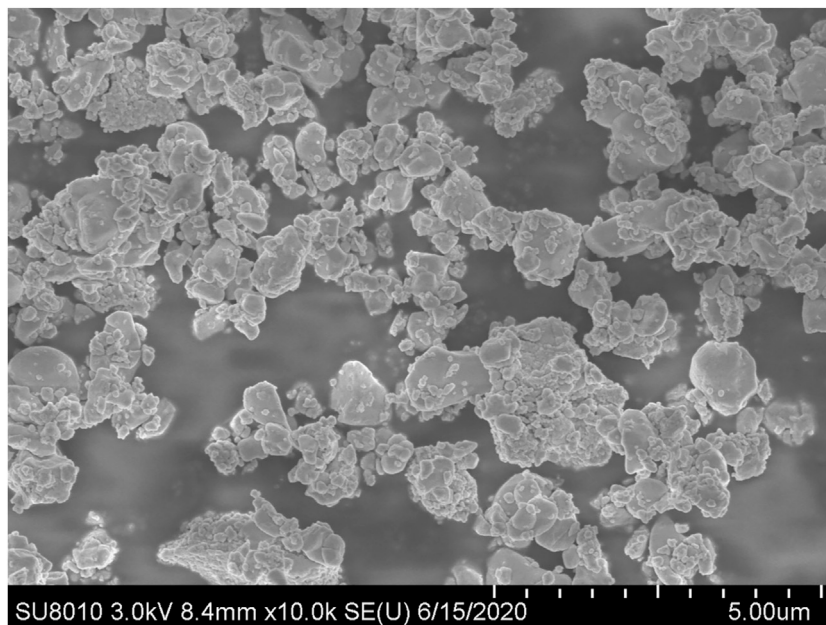


FIGURE 2 | SEM micromorphology of PZT powder.

Post-Treatment Process

The debinding and sintering of the green body were carried out separately to prevent the piezoelectric properties of PZT ceramics from being reduced due to lead volatilization. First, the green body was burned in air to fully discharge the organic phase, and then it underwent a high temperature sintering in a lead-rich environment. The debinding curve was developed by analyzing the TG-DSC curve in **Figure 4**.

As can be seen from the figure, the decomposition of the organic phase in the ceramic is substantially completed when the temperature reached 700°C. The debinding process was designed to heat up to 700°C at a heating rate of 1°C/min, which could avoid the cracks during the debinding process. By holding the temperature at 170, 250, 375, and, 600°C for 1 h separately, the organic phase can fully react with oxygen and be discharged. The whole debinding process is shown in **Figure 5**. The sintering

process was carried out in a sealed crucible, and sufficient PZT powder was used to surround the printed body, thereby providing lead-rich vapor. The sintering temperature increased from room temperature to 1250°C at a rate of 3°C/min, and kept it for 4 h, so that the crystal grains could grow sufficiently. Finally, the sintered body was cooled to room temperature in the furnace.

Filling and Polarization Process

E51 epoxy resin and curing agent were mixed uniformly according to the mass ratio of 4:1, and the polished ceramic skeleton was immersed in the mixture. The epoxy resin can be cured within 1 h at 50°C. The shrinkage during the curing process will produce mechanical stress, which will combine the epoxy resin with the ceramic skeleton. At the same time, due to the porous property of ceramic skeleton, the combination of epoxy resin and ceramic skeleton can be very stable. After the resin was

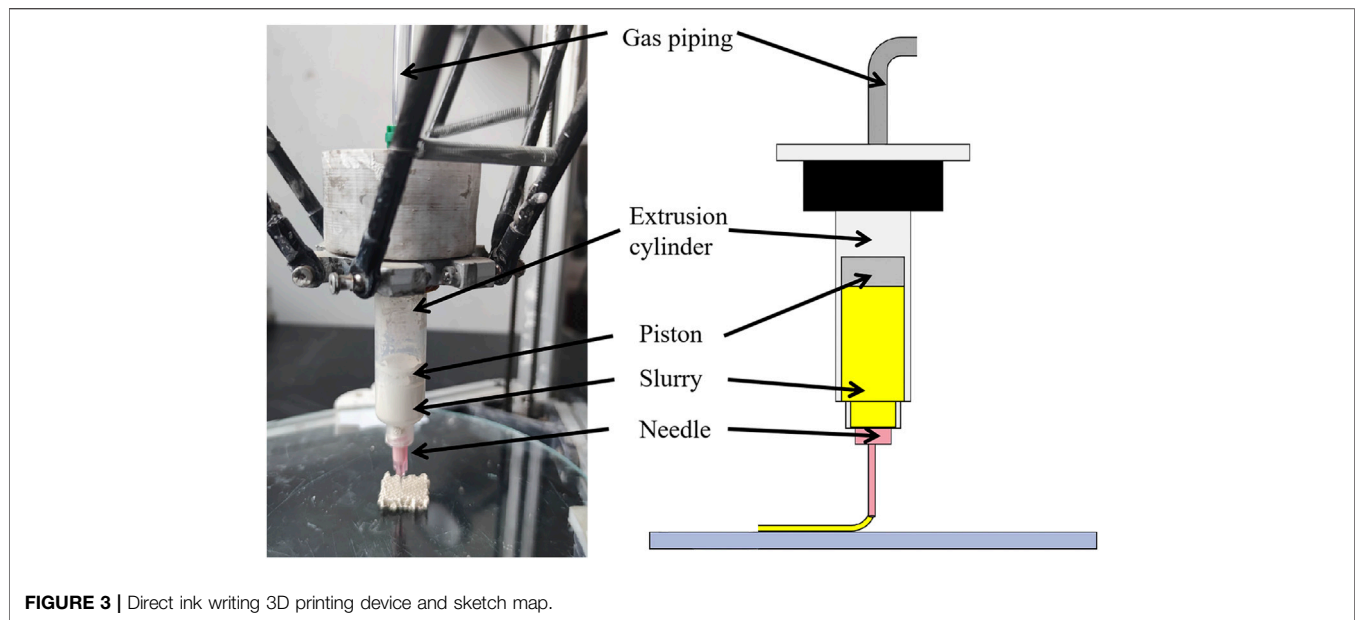


FIGURE 3 | Direct ink writing 3D printing device and sketch map.

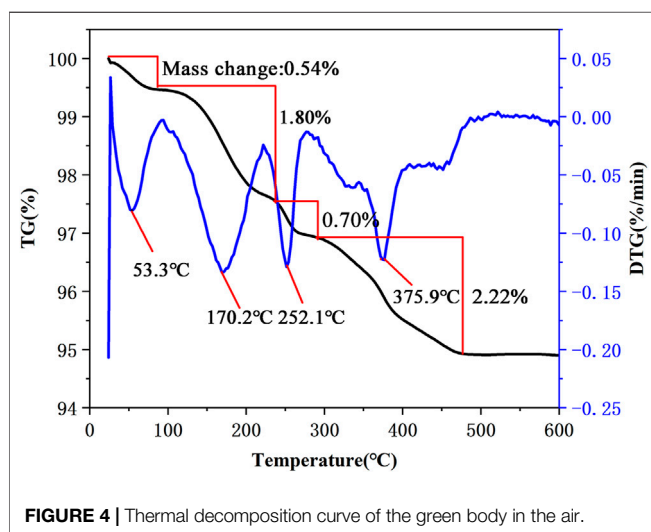


FIGURE 4 | Thermal decomposition curve of the green body in the air.

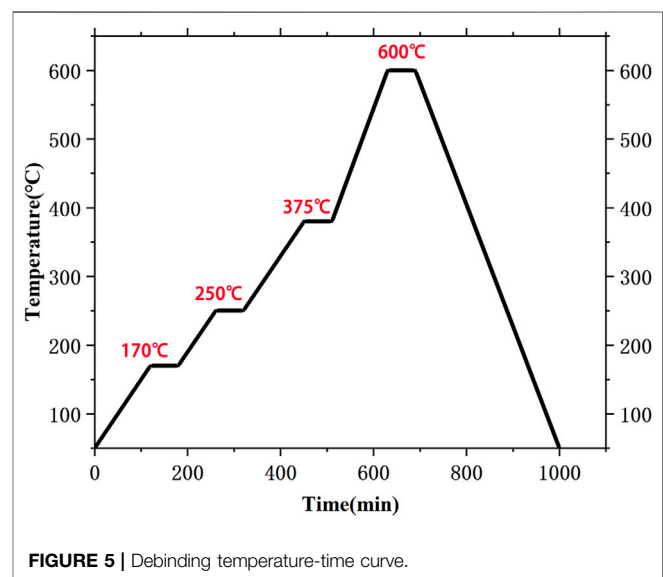


FIGURE 5 | Debinding temperature-time curve.

cured, the top and bottom surfaces of the piezoelectric composite were polished to make them parallel, and the ceramic part of the composites was exposed on the surface.

The top and bottom surfaces of samples were both coated with low-temperature silver slurry and then dried at 110°C for 30 min to form the silver electrode. The sample was connected to a dielectric strength tester and immersed in polymethyl silicone oil which was heated to 80°C. Then the sample was polarized under a 2.5 kV/mm polarization field strength for 30 min. After that, it was deposited at room temperature for 24 h until the discharge was completed before performance testing.

Test

A laser particle size analyzer (Mastersizer 2000) was used to measure the particle size distribution of the ball milled PZT

powder. In addition, the MCR101 dynamic shear rheometer was used to measure the rheological properties of the slurry. The German Netzsch STA449F5 thermogravimetric analyzer was used to heat the sample to 600°C at a heating rate of 10°C/min to measure the weight loss of the printed body. Scanning electron microscope (SEM) was used to observe the cross section of the sintered part. The surface and cross-sectional morphology of the polished piezoelectric composites was observed by an optical microscope. The structural composition was investigated by X-ray diffractometer (Empyrean). The longitudinal piezoelectric strain coefficient (d_{33}), dielectric constant (ϵ_r) and dielectric loss ($\tan\delta$) were investigated by piezometer (ZJ-3 quasi-static d_{33} tester) and Novocontrol test system (Concept 80,

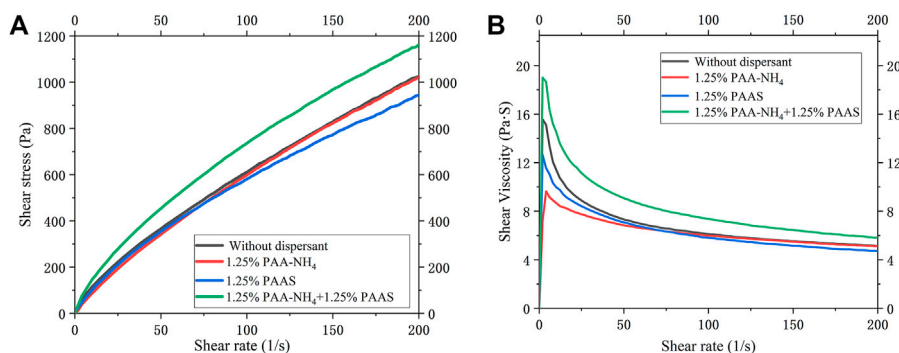


FIGURE 6 | (A) Variation curve of stress versus shear rate of PZT slurry with different dispersants; **(B)** Variation curve of viscosity versus shear rate of PZT slurry with different dispersants.

Germany). Three samples were made for each group of variables, and performance tests were performed on each sample three times. The average of the above test results was used as the final value.

RESULTS AND DISCUSSION

Rheological Behavior of the Slurry

The printability of the slurry is mainly determined by its rheological behavior. In DIW process, a non-Newtonian fluid slurry with viscoelasticity is usually needed. The viscous component allows the slurry to be smoothly extruded through the needle head, while the elastic component gives the extruded filament shape-retention ability and sufficient mechanical strength to support the weight of the subsequent layer (Revelo and Colorado, 2018). Using the synergistic hydrogen bonds between some macromolecules and polymer chains formed by *in-situ* polymerization, high-strength hydrogels with non-Newtonian fluid characteristics can be constructed in the slurry. Using PVA as a macromolecular template, PVA-PAA gel can be obtained by *in-situ* polymerization of acrylic acid (AA). The gel has a three-dimensional grid structure (Lewis, 2010), which can be bound with PZT powder to enhance the elastic strength of the slurry and reduce the viscosity of the slurry (Chen et al., 2017; Rac. et al., 2019; Wu et al., 2020).

PVA and acrylic additives were added to the slurry as binder and dispersant respectively, and the influence of the type and content of the dispersant on the viscosity of the slurry was investigated. First, the influence of two dispersants (PAA-NH₄ and PAAS) on the viscosity of the slurry was explored. Rheological properties of PZT slurry with the same mass fraction were compared under the conditions of no dispersant, 1.25% PAA-NH₄, 1.25% PAAS and the mixture of two dispersants. **Figure 6A** shows the curve of shear stress versus shear rate, which is close to the shape and direction of the shear rate-shear stress curve of classical shear thinning fluid. It shows that the slurries with different types of dispersants all have shear thinning behavior characteristics. Compared to the viscosity levels of each slurry in **Figure 6B**, it can be seen that PAA-NH₄ reduces

the viscosity of the slurry significantly better than other dispersants. When two dispersants are added at the same time, due to the large amount of PVA-PAA gel formed in the slurry, the amount of three-dimensional grid increases, which makes the viscosity of the slurry increase instead.

Furthermore, PAA-NH₄ was used as a dispersant to explore the most suitable addition amount. The rheological properties of the slurry in the range of 0.75~2% of the dispersant added were measured, and the results are shown in **Figure 7A**. It can be seen that the slurries with different add amounts of dispersant all have shear thinning behavior, and the initial viscosity is not much different.

According to the actual situation in the extrusion process, rheological data with practical significance was selected for comparison within the appropriate shear rate range. The shear rate γ of the fluid passing through the conical needle can be calculated by the following formula (M'Barki et al., 2017; Nan et al., 2018).

$$\gamma = \frac{4Q}{\pi R^3} \quad (1)$$

In the formula, Q is the volume flow and R is the radius of the needle. In the printing process, we used a needle with a diameter of 0.60 mm and a printing speed of 8 mm/s. Therefore, according to this formula, the extrusion force during the extrusion process was equivalent to a shear rate of 104.92 s^{-1} applied to the slurry. The rheological data of the shear viscosity flow curve when the shear rate of the gradient dispersant slurry was 105 s^{-1} was collected, as illustrated in **Figure 7B**. At this shear rate, the slurry with 2 wt% PAA-NH₄ has the highest viscosity. This is because a large amount of gel grid has generated in the slurry, and the shear force required to destroy the grid structure is also greater. The slurry added with 1.75 wt% of PAA-NH₄ has a lower viscosity, so the extrusion effect of the slurry is the best under this dispersant content.

Microstructure and Phase Analysis

The phase and microstructure of ceramics at different sintering temperatures were analyzed. The cross-sections SEM images of the samples sintered at different sintering temperatures are shown

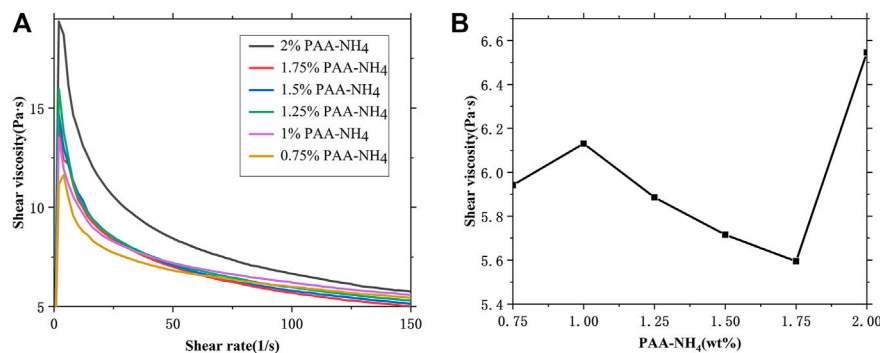


FIGURE 7 | (A) Shear rate-shear viscosity change curve of gradient dispersant content; **(B)** Viscosity change curve of gradient slurry concentration at 105 s^{-1} shear rates.

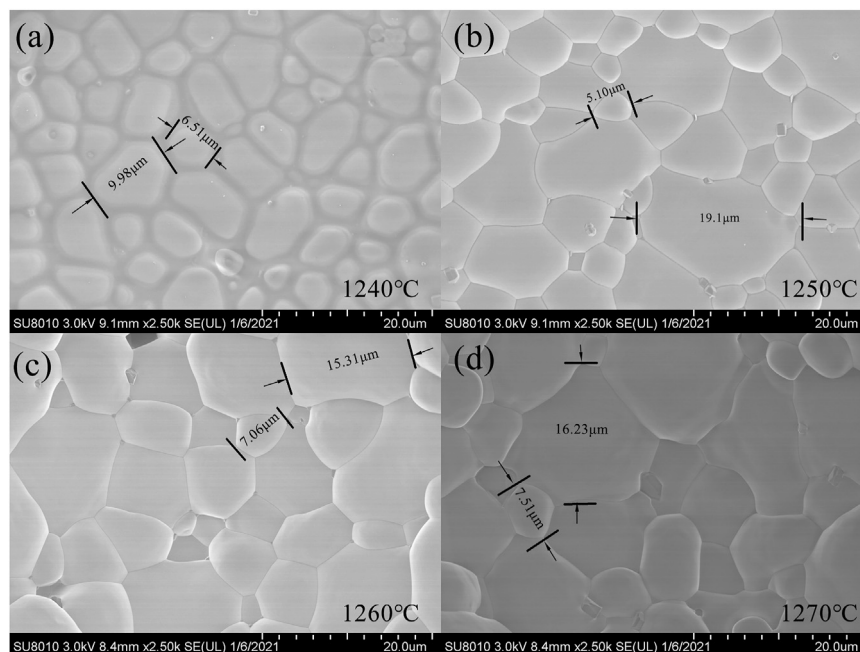


FIGURE 8 | Cross-section morphology and grain size of samples sintered at **(A)** 1240°C, **(B)** 1250°C, **(C)** 1260°C and **(D)** 1270°C.

in **Figure 8**. It can be seen from the figure that when the sintering temperature is 1240°C, the crystal grains are not fully grown. And there is a liquid phase between the grain boundaries, resulting in a small crystal grain size with a maximum size of 9.98 μm. When the temperature is raised to 1250°C, the grain size increases (the maximum size is 19.1 μm), and the grain boundaries are clear. The actual density of the sintered sample is 7.63 g/cm³ and the relative density is 97.8%. As the temperature further increased, the small crystal grains grew further, but when the temperature raised to 1270°C, the grain boundaries were remelted due to the high temperature, resulting in unclear grain boundaries.

It can be seen from **Figure 9** that when the sintering temperature is 1240°C and the heat preservation time is 4 h, the phase structure of ceramics has split peaks in the range of $2\theta = 21\sim 22.5^\circ$ and $43\sim 45^\circ$,

which shows that the ceramic is in the quasi-homotype phase boundary area where the tripartite phase and the tetragonal phase coexist. And the phase diagram has a split peak at $2\theta = 32^\circ$, indicating that the ceramic has a pyrochlore phase structure when the firing temperature is low, and a tripartite perovskite structure can't be formed. However, as the temperature increased to 1250~1270°C, the pyrochlore phase structure in the sintered body is eliminated, and the pure tripartite perovskite structure is formed. From the results of grain growth and phase analysis, 1250~1260°C is the best sintering temperature range.

Performance

The influence of structural parameters on the properties of piezoelectric composites was discussed by changing rod spacing

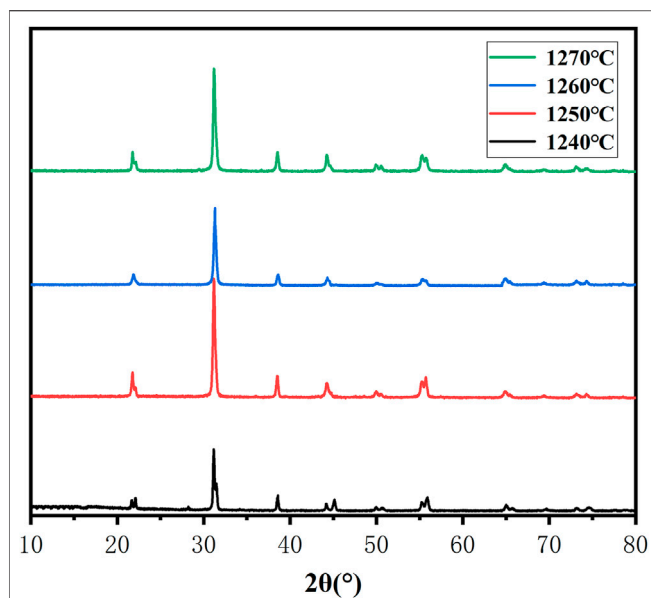


FIGURE 9 | X-ray diffraction pattern of ceramics sintered at 1240, 1250, 1260 and 1270°C.

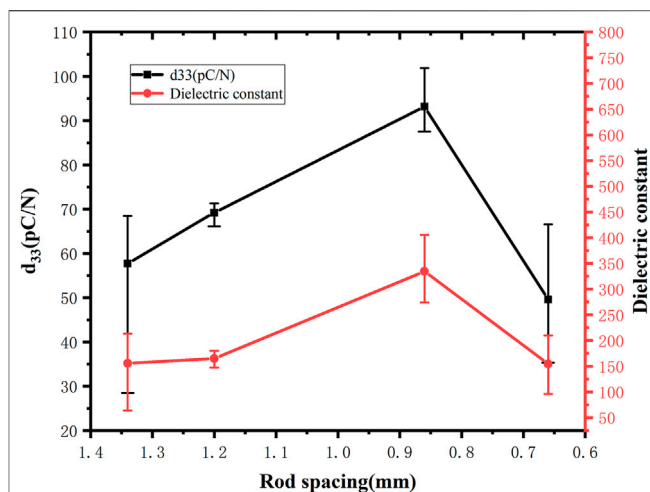


FIGURE 11 | The change curve of d_{33} and relative permittivity of piezoelectric composites with different rod spacings.

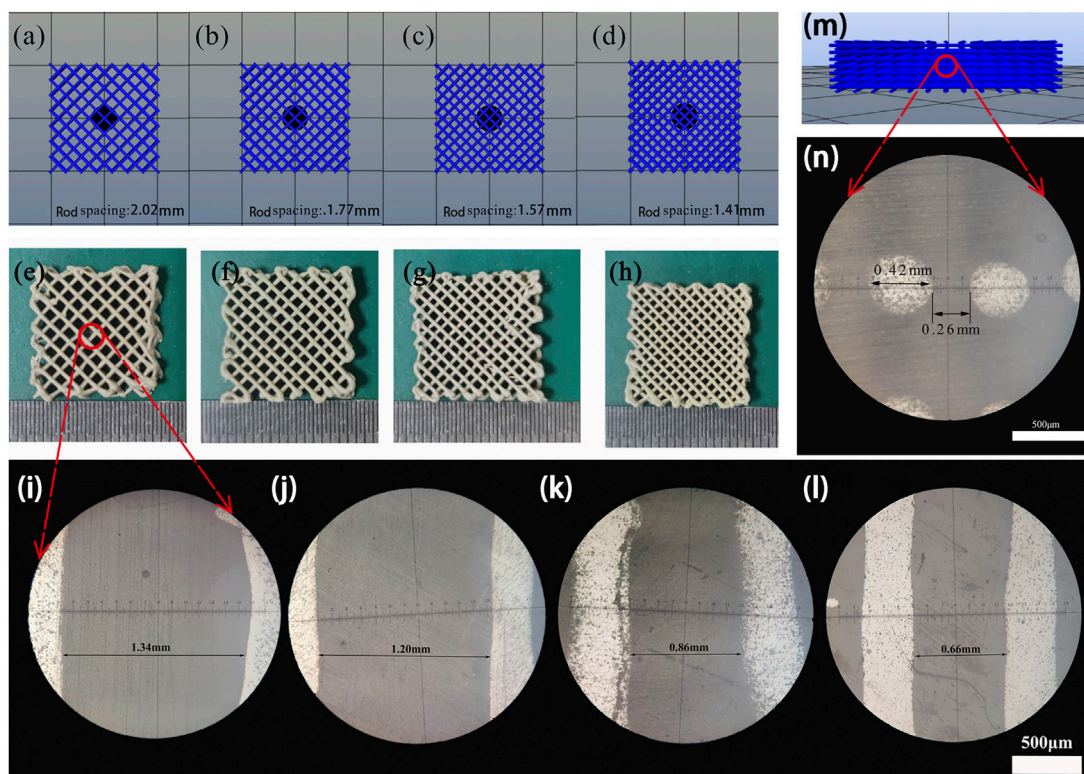


FIGURE 10 | (A, E, I) 20% filling density model, sintered body and size micrograph; (B, F, J) 23% filling density model, sintered body and size micrograph; (C, G, K) 26% filling density model, sintered body and size micrograph; (D, H, L) 29% filling density model, sintered body and size micrograph; (M, N) Model cross section and size micrograph.

of the ceramic skeleton. The filling density was respectively set to 20, 23, 26, and 29%, and the printing effect of the piezoelectric ceramic skeleton is shown in **Figures 10A–H**. After filling the resin, an optical microscope was used to measure the distance between the piezoelectric composite rods, and the corresponding rod spacing was 1.34, 1.20, 0.86, 0.66 mm, as shown in **Figures 10I–L**. Since the overall structure shrinks uniformly after sintering, the size in **Figure 10N** can be used to calculate the rod diameter and layer height shrinkage. Through calculation, the diameter shrinkage rate of the rod is 30%. After the prepared 3–3 piezoelectric composite was polished and polarized, its piezoelectric constant (d_{33}) and relative dielectric constant (ϵ_r) were tested. These performance test data were used to characterize the influence of the distance between the rods on the performance of the piezoelectric composites.

The d_{33} and relative permittivity of the 3–3 piezoelectric composites were tested as a function of the distance between the rods. As shown in **Figure 11**, the error bars in the figure indicate the maximum and minimum values of the piezoelectric coefficient and the relative permittivity of the sample. Within the range of 0.66–1.34 mm rod spacing, both d_{33} and ϵ_r increase first and then decrease. When the rod spacing is 0.86 mm, the electrical performance reaches the maximum, the maximum d_{33} is 103 pC/N, and ϵ_r is 274.34, and the smaller the dielectric constant is, and the smaller the dielectric loss. This is because as the distance between the rods increases, the content of the ceramic phase decreases accordingly. When the composites are under stress, the greater the force acting on the piezoelectric ceramic frame, the more surface induced charges are generated (Runt et al., 1985; Liu et al., 2017; Jin et al., 2020; Wu et al., 2020). However, with the further decrease of the rod spacing, the piezoelectric and dielectric decrease. This is because as the distance between the rod decreases, there is overlap in the vertical direction during the printing process, which converts the precise 3–3 type into piezoelectric composites with other structures (Liu et al., 2017). This leads to the formation of internal closed cells inside the ceramic part after sintering and increases the number of defects. This phenomenon means that the internal pores of the ceramic parts can't be filled and the polarization process is affected, resulting in an increase in $\tan\delta$ (Runt et al., 1985).

Through this investigation, it is found that the reduction of the rod spacing has the law of first increasing and then decreasing in the electrical properties of the 4D printed 3–3 piezoelectric composites. Therefore, with the help of 4D printing technology, we can freely design and change the structural parameters, and explore the influence rules of the parameters, so as to regulate the performance of the structure to meet the controllable changes in performance and functions.

Underwater Acoustic Transducer

The underwater acoustic transducer uses piezoelectric composites with copper foil adhered to the surface as the piezoelectric element. At the same time, Polyurethane (PU) is used as the matching layer of the transducer because of its acoustic impedance close to that of water (Sasikumar et al., 2014; Bian et al., 2020; Yf et al., 2021). In order to characterize the sound-to-electric conversion function of

the manufactured underwater acoustic transducer, a test scene as shown in **Figure 12** was constructed to verify. A signal generator was used to generate electrical signals with different waveforms and frequencies. The signals were then inputted into the speaker to make it emit sound signals of the same waveform and frequency. The distance between the speaker and the sensor is 450 mm, and the sound wave signal generated by the speaker was converted into an electric signal by the underwater acoustic transducer, and the electric signal was displayed on a digital oscilloscope.

Under the input voltage (V_i) of 2–24 V, the loudspeaker can emit 100 kHz and with different amplitudes acoustic signals. After receiving the acoustic signal, the underwater acoustic transducer converts it into a response voltage (V_{pp}), as shown in **Figure 13A** V_{pp} is positively related to V_i . When the input voltage was 24 V, the output voltage was 162 mV, and the voltage conversion efficiency was 0.675%. The demonstration results show that the acoustic electrical conversion of piezoelectric materials in water can be realized by 4D printing. Through changing the structural parameters of piezoelectric composites, the conversion efficiency of the transducer also changes accordingly. Under the optimal printing parameters, the prepared underwater acoustic transducer can generate a maximum voltage of 162 mV. At the same time, through the change of the waveform displayed on the oscilloscope, people can detect the change of the underwater sound source, so as to get a warning.

Above all, this 4D printing method can quickly and autonomously control the printing structure and realize the detection of controllable changes, which is an advantage that traditional manufacturing methods do not have. And in the future, it can be used to prepare optimized piezoelectric structures to further improve the performance of underwater acoustic transducers, which is expected to lead the development direction of 4D printing functional devices.

CONCLUSIONS

This article presents the application of 4D printing in underwater acoustic transducers. The combination of piezoelectric material PZT and direct ink writing is conducive to the development of underwater detection intelligent equipment with high performance and multi-function. The specific conclusions are as follows,

1. The PZT piezoelectric ceramic skeleton was prepared by direct ink writing. The influence of the dispersant on the viscosity of the slurry was explored. It was found that when the addition amount of the dispersant ammonium polyacrylate in the slurry is 1.75 wt%, the slurry has the best printing effect. In addition, the green body has the best sintering effect at 1250–1260°C, which can form a pure trigonal perovskite structure, the relative density after sintering reaches 97.8%.
2. The performance of piezoelectric composites with different rod spacing was tested. As the distance between the rods decreases, the d_{33} and ϵ_r of the piezoelectric composite first increase and then decrease. When the filling density was 26%, the printed structure had the best electrical performance ($d_{33} = 103$ pC/N and $\epsilon_r = 274.34$).

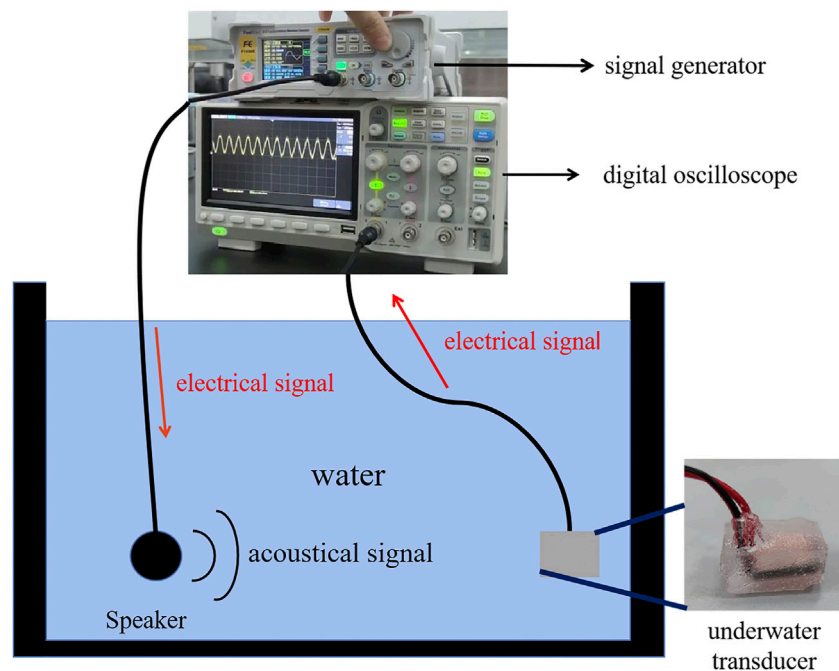


FIGURE 12 | Signal receiving test of underwater acoustic transducer.

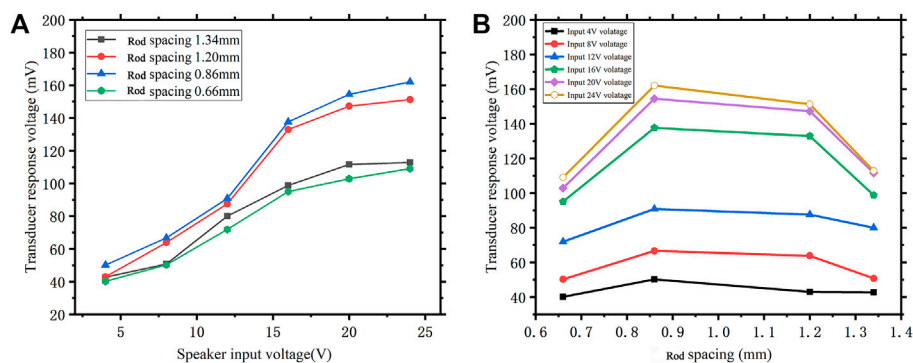


FIGURE 13 | (A) Comparison of signal generator input and digital oscilloscope output; **(B)** The peak-to-peak V_{pp} response of the underwater acoustic transducer at 100 kHz varies with the output voltage of the signal generator.

3. A 4D printed sample was used to prepare an underwater acoustic transducer. Piezoelectric composites with the best electrical performance also have the highest voltage output, and the output voltage maximum was 162 mV. This verifies that this 4D printing method can quickly achieve structural changes, thereby obtaining the best performance.

Therefore, it is necessary to further explore the advantages of using 4D printing technology to realize the free design of piezoelectric structures, and manufacturing of piezoelectric composites. These piezoelectric devices have independently adjustable piezoelectric characteristics and functions, which

have great potential for underwater detection and communication applications.

DATA AVAILABILITY STATEMENT

The original contributions presented in the study are included in the article/Supplementary Material, further inquiries can be directed to the corresponding author.

AUTHOR CONTRIBUTIONS

Experiments were designed by KL. QZ completed the main experimental part. CZ and CS, designed the slurry formula; CY

and JH, performed performance tests on experimental samples; SZ, YZ, and YF designed and assembled a 3D printer. The main paper was written by QZ and KL revised the paper. All authors discussed the results and their implications, participated in the revised manuscripts at various stages, and approved for publication.

FUNDING

This work was supported by the National Innovation and Entrepreneurship Training Program for College Students

REFERENCES

- An, T., Hwang, K. T., Kim, J. H., and Kim, J. (2020). Extrusion-based 3D Direct Ink Writing of NiZn-Ferrite Structures with Viscoelastic Ceramic Suspension[J]. *Ceramics Int.*, 46(5):6469–6476. doi:10.1016/j.ceramint.2019.11.127
- Bian, J., Wang, Y., Liu, Z., Shen, M., Zhao, H., Sun, Y., et al. (2020). Ultra-wideband Underwater Acoustic Transducer with a Gradient Impedance Matching Layer [J]. *Appl. Acoust.* 175. doi:10.1016/j.apacoust.2020.107789
- Bowen, C. R., and Topolov, V. Y. (2003). Piezoelectric Sensitivity of PbTiO₃-Based Ceramic/polymer Composites with 0-3 and 3-3 Connectivity. *Acta Materialia* 51 (17), 4965–4976. doi:10.1016/S1359-6454(03)00283-0
- Chen, K., Liu, J., Yang, X., and Zhang, D. (2017). Preparation, Optimization and Property of PVA-HA/PAA Composite Hydrogel. *Mater. Sci. Eng. C* 78 (sep), 520–529. doi:10.1016/j.msec.2017.04.117
- Coppola, B., Tardivat, C., Richaud, S., Tulliani, J.-M., Montanaro, L., and Palmero, P. (2021). 3D Printing of Dense and Porous Alkali-Activated Refractory Wastes via Direct Ink Writing (DIW). *J. Eur. Ceram. Soc.* 41, 3798–3808. doi:10.1016/j.jeurceramsoc.2021.01.019
- Grinberg, D., Siddique, S., Le, M. Q., Liang, R., Capsal, J. F., and Cottinet, P. J. (2018). 4D Printing Based Piezoelectric Composite for Medical Applications. *J. Polym. Sci. Part. B: Polym. Phys.* 57 (3), 109–115. doi:10.1002/polb.24763
- Jin, C., Hao, N., Xu, Z., Trase, I., Nie, Y., Dong, L., et al. (2020). Flexible Piezoelectric Nanogenerators Using Metal-Doped ZnO-PVDF Films. *Sensors Actuators A: Phys.* 305, 111912. doi:10.1016/j.sna.2020.111912
- Kai, L., Jiang, W., Tian, W., and Huajun, S. (2020). Effects of Carbon Content on Microstructure and Mechanical Properties of SiC Ceramics Fabricated by SLS/RMI Composite Process - ScienceDirect[J]. *Ceramics Int.* 46 (14), 22015–22023. doi:10.1016/j.ceramint.2020.05.18
- Kong, Y. L., Tamargo, I. A., Kim, H., and Kim, J. (2014). 4D Printing: Multi-Material Shape Change[J]. *Architectural Des.* 84 (1), 116–121. doi:10.1002/ad.1710
- Kuang, X., Roach, D. J., Wu, J., Hamel, C. M., Ding, Z., Wang, T., et al. (2019). Advances in 4D Printing: Materials and Applications[J]. *Adv. Funct. Mater.* 29 (2), 1805290.1–1805290.23. doi:10.1002/adfm.201805290
- Lewis, J. A. (2010). Colloidal Processing of Ceramics. *J. Am. Ceram. Soc.* 83 (10), 2341–2359. doi:10.1111/j.1151-2916.2000.tb01560.x
- Li, D., Wu, M., Oyang, P., and Xu, X. (2006). Cymbal Piezoelectric Composite Underwater Acoustic Transducer. *Ultrasonics* 44 (8), e685–e687. doi:10.1016/j.ultras.2006.05.127
- Li, Y., Mao, Q., Yin, J., Wang, Y., Fu, J., and Huang, Y. (2021). Theoretical Prediction and Experimental Validation of the Digital Light Processing (DLP) Working Curve for Photocurable Materials. *Additive Manufacturing* 37, 101716. doi:10.1016/j.addma.2020.101716
- Liu, G., Zhao, Y., Wu, G., and Lu, J. (2018). Origami and 4D Printing of Elastomer-Derived Ceramic Structures[J]. *Sci. Adv.* 4 (8), eaat0641. doi:10.1126/sciadv.aat0641
- Liu, J., Kim, A. Y., Wang, L. Q., Palmer, B. J., Chen, Y. L., Bruinsma, P., et al. (1996). Self-assembly in the Synthesis of Ceramic Materials and Composites. *Adv. Colloid Interf. Sci.*, 69, 131–180. doi:10.1016/S0001-8686(96)00309-0
- Liu, W., Lv, L., Li, Y., Wang, Y., Wang, J., Xue, C., et al. (2017). Effects of Slurry Composition on the Properties of 3-1 Type Porous PZT Ceramics Prepared by (202010497012), self-determined and innovative research funds of WUT (2020-CL-B1-05), the National Natural Science Foundation of China (Grant Nos. U1806221, 51672198), Innovation and Development Project of Zibo City (2017CX01A022), Instruction & Development Project for National Funding Innovation Demonstration Zone of Shandong Province (2017-41-1, 2017-41-3, 2018ZCQZB01, 2019ZCQZB03), Central Guiding Local Science and Technology Development Special Funds (Grant Nos. 2060503), and Key Research & Design Program of Shandong Province (2019GGX102011).
- Ionotropic Gelation - ScienceDirect[J]. *Ceramics Int.* 43 (8), 6542–6547. doi:10.1016/j.ceramint.2017.02.079
- M'Barki, A., Bocquet, L., and Stevenson, A. (2017). Linking Rheology and Printability for Dense and Strong Ceramics by Direct Ink Writing[J]. *Scientific Rep.* 7 (1), 6017. doi:10.1038/s41598-017-06115-0
- Meng, X., Xu, J., Zhu, J., et al. (2020). Porous yttria-stabilized zirconia ceramics with low thermal conductivity via a novel foam-gelcasting method. *J. Mater. Sci.* 55. doi:10.1007/s10853-020-04900-3
- Nan, B., Olhero, S., Pinho, R., Vilarinho, P. M., Button, T. W., and Ferreira, J. M. F. (2018). Direct Ink Writing of Macroporous lead-free Piezoelectric Ba 0.85 Ca 0.15 Zr 0.1 Ti 0.9 O 3. *J. Am. Ceram. Soc.* 102 (7633), 3191–3203. doi:10.1111/jace.16220
- Newnham, R. E., Skinner, D. P., and Cross, L. E. (1978). Connectivity and Piezoelectric-Pyroelectric Composites. *Mater. Res. Bull.* 13 (5), 525–536. doi:10.1016/0025-5408(78)90161-7
- Palmero, E. M., and Bollero, A. (2020). 3D and 4D Printing of Functional and Smart Composite Materials[J]. *Reference Module in Materials Ence and Materials Engineering.* doi:10.1016/b978-0-12-819724-0.00008-2
- Rac, V., Lević, S., Balanć, B., Olalde Graells, B., and Bijelić, G. (2019). PVA Cryogel as Model Hydrogel for Iontophoretic Transdermal Drug Delivery Investigations. Comparison of PAA/PVA and PAA/PVP Interpenetrating Networks. *Colloids Surf. B Biointerfaces* 180, 441–448. doi:10.1016/j.colsurfb.2019.05.017
- Revelo, C. F., and Colorado, H. A. (2018). 3D Printing of Kaolinite clay Ceramics Using the Direct Ink Writing (DIW) Technique. *Ceramics Int.* 44, 5673–5682. doi:10.1016/j.ceramint.2017.12.219
- Rouffaud, R., Granger, C., Hladky-Hennion, A.-C., Thi, M.P., and Levassort, F. (2015). Tonpilz Underwater Acoustic Transducer Integrating Lead-free Piezoelectric Material. *Phys. Proced.* 70, 997–1001. doi:10.1016/j.phpro.2015.08.208
- Runt, J., Safari, A., Galgocsi, E. C., and Newnham, R. E. (1985). The Influence of Interfacial Adhesion on the Piezoelectric Response of Electroceramic/polymer Composites. *Ferroelectrics Lett. Section* 5, 15–20. doi:10.1080/07315178508202461
- Sasikumar, K., Manoj, N. R., Mukundan, T., and Khastgir, D. (2014). Design of XNBR Nanocomposites for Underwater Acoustic Sensor Applications: Effect of MWNT on Dynamic Mechanical Properties and Morphology. *J. Appl. Polym. Sci.*, 131(8):a-n. doi:10.1002/app.40752
- Tian, F., Liu, Y., Ma, R., Li, F., Xu, Z., and Yang, Y. (2021). Properties of PMN-PT Single crystal Piezoelectric Material and its Application in Underwater Acoustic Transducer. *Appl. Acoust.* 175 (4), 107827. doi:10.1016/j.apacoust.2020.107827
- Tressler, J. F., Alkoy, S., Dogan, A., and Newnham, R. E. (1999). Functional Composites for Sensors, Actuators and Transducers. *Composites A: Appl. Sci. Manufacturing* 30 (4), 477–482. doi:10.1016/S1359-835X(98)00137-7
- Vigano, F., Cristiani, C., and Annoni, M. (2017). Ceramic Sponge Abrasive Waterjet (AWJ) Precision Cutting through a Temporary Filling Procedure. *J. Manufacturing Process.* 28 (1), 41–49. doi:10.1016/j.jmapro.2017.05.014
- Walton, R. L., Fanton, M. A., Meyer, R. J., and Messing, G. L. (2020). Dispersion and Rheology for Direct Writing lead-based Piezoelectric Ceramic Pastes with Anisotropic Template Particles. *J. Am. Ceram. Soc.* 103, 6157–6168. doi:10.1111/jace.17350

- Wang, L., Luo, Y., Yang, Z., Dai, W., Liu, X., Yang, J., et al. (2019). Accelerated Refilling Speed in Rapid Stereolithography Based on Nano-Textured Functional Release Film. *Additive Manufacturing* 29, 100791. doi:10.1016/j.addma.2019.100791
- Woodward, D. I., Pursell, C. P., Billson, D. R., Hutchins, D. A., and Leigh, S. J. (2015). Additively-manufactured Piezoelectric Devices. *Phys. Status Solidi A*. 212 (10), 2107–2113. doi:10.1002/pssa.201532272
- Wu, L., Li, L., Fan, L., Tang, P., Yang, S., Pan, L., et al. (2020). Strong and Tough PVA/PAA Hydrogel Fiber with Highly Strain Sensitivity Enabled by Coating MWCNTs - ScienceDirect[J]. *Composites Part A: Appl. Sci. Manufacturing* 138. doi:10.1016/j.compositesa.2020.106050
- Wu, W., Yin, X., Dai, B., Kou, J., Ni, Y., and Lu, C. (2020). Water Flow Driven Piezo-Photocatalytic Flexible Films: Bi-piezoelectric Integration of ZnO Nanorods and PVDF. *Appl. Surf. Sci.* 517, 146119. doi:10.1016/j.apsusc.2020.146119
- Yan, C., Xiulan, B., Chi-Man, W., Cheng, J., Wu, H., Song, H., et al. (2018). PZT Ceramics Fabricated Based on Stereolithography for an Ultrasound Transducer Array Application[J]. *Ceramics Int.* 44, 22725–22730. doi:10.1016/j.ceramint.2018.09.055
- Yf, A., Iik, A., Guan, H., and Peng, Z. (2021). A Review on Polymer-Based Materials for Underwater Sound Absorption[J]. *Polym. Test.* doi:10.1016/j.polymertesting.2021.107115
- Zeng, Y., Jiang, L., Sun, Y., Yang, Y., Quan, Y., Wei, S., et al. (2020). 3D-Printing Piezoelectric Composite with Honeycomb Structure for Ultrasonic Devices. *Micromachines* 11 (8), 713. doi:10.3390/mi11080713

Conflict of Interest: The authors declare that the research was conducted in the absence of any commercial or financial relationships that could be construed as a potential conflict of interest.

Copyright © 2021 Liu, Zhang, Zhou, Shi, Sun, Sun, Yin, Hu, Zhou, Zhang and Fu. This is an open-access article distributed under the terms of the Creative Commons Attribution License (CC BY). The use, distribution or reproduction in other forums is permitted, provided the original author(s) and the copyright owner(s) are credited and that the original publication in this journal is cited, in accordance with accepted academic practice. No use, distribution or reproduction is permitted which does not comply with these terms.



Design of Shape Reconfigurable, Highly Stretchable Honeycomb Lattice With Tunable Poisson's Ratio

Le Dong, Chengru Jiang, Jinqiang Wang and Dong Wang*

Robotics Institute and State Key Laboratory of Mechanical System and Vibration, School of Mechanical Engineering, Shanghai Jiao Tong University, Shanghai, China

OPEN ACCESS

Edited by:

Yusheng Shi,
Huazhong University of Science and
Technology, China

Reviewed by:

Xinli Xiao,
Harbin Institute of Technology, China
Shaoping Qu,
Zhejiang University, China

*Correspondence:

Dong Wang
wang_dong@sjtu.edu.cn

Specialty section:

This article was submitted to
Smart Materials,
a section of the journal
Frontiers in Materials

Received: 29 January 2021

Accepted: 14 May 2021

Published: 31 May 2021

Citation:

Dong L, Jiang C, Wang J and Wang D
(2021) Design of Shape
Reconfigurable, Highly Stretchable
Honeycomb Lattice With Tunable
Poisson's Ratio.
Front. Mater. 8:660325.
doi: 10.3389/fmats.2021.660325

The mechanical behaviors of lattice structures can be tuned by arranging or adjusting their geometric parameters. Once fabricated, the lattice's mechanical behavior is generally fixed and cannot adapt to environmental change. In this paper, we developed a shape reconfigurable, highly stretchable lattice structure with tunable Poisson's ratio. The lattice is built based on a hexagonal honeycomb structure. By replacing the straight beam with curled microstructure, the stretchability of the lattice is significantly improved. The Poisson's ratio is adjusted using a geometric angle. The lattice is 3D printed using a shape memory polymer. Using its shape memory effect, the lattice demonstrates tunable shape reconfigurability as the ambient temperature changes. To capture its high stretchability, tunable Poisson's ratio and shape reconfigurability, a phase evolution model for lattice structure is used. In the theoretical model, the effects of temperature on the material's nonlinearity and geometric nonlinearity due to the lattice structure are assumed to be decoupled. The theoretical shape change agrees well with the Finite element results, while the theoretical model significantly reduces the computational cost. Numerical results show that the geometrical parameters and the ambient temperature can be manipulated to transform the lattice into target shapes with varying Poisson's ratios. This work provides a design method for the 3D printed lattice structures and has potential applications in flexible electronics, soft robotics, and biomedicine.

Keywords: shape reconfigurable, highly stretchable, tunable Poisson's ratio, shape memory behaviors, phase evolution model

INTRODUCTION

Lattice structures can exhibit unusual properties by rationally arranging or adjusting their microstructures (Bertoldi et al., 2017). Among them, tunable Poisson's ratio is of particular interest (Fozdar et al., 2011; Ai and Gao 2017; Chen et al., 2017; Khare et al., 2018; Liu and Zhang, 2018; de Jonge et al., 2019). While most naturally occurring and synthetic materials have a positive Poisson ratio, i.e., they contract transversely while elongating axially and vice versa. Some exceptions exist, including arterial endothelium (Timmins et al., 2010), cat's skin Veronda and Westmann. (1970), cow's teat skin Lees et al. (1991), crystalline α -cristobalite SiO_2 (Williams and Lewis, 1982; Keskar and Chelikowsky, 1992), carbon allotropes (Timmins et al., 2010), microporous polymers and laminates (Caddock and Evans, 1989; Alderson and Evans, 1992; Milton, 1992). For these materials, expansion in lateral direction and elongation in longitudinal direction occur concurrently. Due to this unusual deformation property, lattice structures with negative Poisson

ratios offer superior mechanical performance compared to traditional materials, including high fracture toughness (Li et al., 2016; Saxena et al., 2016; Clayton and Knap, 2018), large energy absorption Li et al. (2018), Chetverikov et al. (2019), Guo et al. (2020), Hu et al. (2020), and strong indentation resistance (Aldeson et al., 2000; Hu et al., 2019; Li et al., 2020). Therefore, lattices with tunable Poisson's ratio have found applications in various areas, such as biomedical devices (Rafsanjani and Pasini, 2016; Yan et al., 2019), soft sensors (Li et al., 2016; Khan et al., 2019), Aerospace Huang and Chen (2016) and automotive engineering (Wang et al., 2016).

Another critical property of lattice structure is high stretchability (Jiang and Wang, 2016; Yiming et al., 2020). Inspired by the non-mineralized soft materials typically constructed from wavy constituents embedded in soft matrices, curved microstructures are commonly used to design lattices (Ma et al., 2016). When the lattices are subjected to external loadings, the microstructures bend, rotate and align to the loading directions and resist excessive loadings by stretching. Therefore, they generally exhibit J-shaped stress-strain curves with low initial modulus and high modulus at a large strain simultaneously, and their stretchability is significantly improved.

The development of 3D printing technologies has enabled the fabrication of complex lattice structures (Yuan et al., 2019). However, once manufactured, the mechanical behavior of the lattice structure is fixed and not reconfigurable. To overcome this problem, several methods have been proposed. One way is to use active materials to fabricate the lattice structure. Active materials have the ability to deform or change their properties under the external stimulus. Therefore, the manufactured lattice can change its shape or properties accordingly. Examples include 4D printed lattice that can deform under thermal stimulus (Yang et al., 2019), 4D printed gripper that deforms under electrical stimulus (Shao et al., 2020), 4D printed structure responding to magnetic field (Ji et al., 2017; Cao et al., 2019; Lantean et al., 2019; Testa et al., 2019; Ze et al., 2020), directly 4D printed structures (Ding et al., 2017; Ding et al., 2018), etc.

Shape memory polymer (SMP) is a class of intelligent polymer material that can maintain a temporary shape and restore its original shape in response to environmental stimuli (Lendlein and Langer, 2002). SMPs have a wide range of modulus varying from ~MPa to ~GPa Lendlein and Kelch (2005) and relatively fast response capability depending on actuation temperatures (Kong et al., 2021a). SMPs with various functions have been developed, such as SMP with high recovery stress reinforced by carbon fibers, self-healing SMPs (Lee et al. (2015), Kong et al. (2019) and SMP with shielding electromagnetic interference (Kong et al., 2021b). The shape-shifting behavior of the SMP has been widely used in 4D printing. Examples include self-driving structures (Bodaghi et al., 2016), reconfigurable metamaterials Ding et al. (2017), and multi-material soft actuators (Ge et al., 2016).

Despite the recent significant progress in lattice structure design, it is still a challenge to realize shape reconfigurable, highly stretchable lattice structures with tunable Poisson's ratio. In this paper, we design a reconfigurable, highly stretchable lattice with tunable Poisson's ratio. A hexagonal

honeycomb structure is used. By replacing the straight beams in the lattice using curled microstructure, the stretchability of the lattice is significantly improved. Under a uniaxial tensile loading, the curled microstructure rotates, bends and aligns to the direction of the applied stress. Therefore, the lattice exhibits a large stretchability, comparing to the traditional hexagonal honeycomb structures. By adjusting a geometric parameter: angle α , the Poisson's ratio can be programmed. Generally speaking, if $\alpha > 90^\circ$, the lattice exhibits a positive Poisson's ratio. The lattice with $\alpha < 90^\circ$ shows a negative Poisson's ratio, while the Poisson's ratio of the lattice is almost zero when $\alpha = 90^\circ$. The lattice is 3D printed using a shape memory polymer. Using its shape memory effect, the lattice shows the capacity to reconfigure its shapes when applying an external stimulus. A phase-evolution model is used to predict the shape reconfigurability of the lattice.

MATERIALS AND METHODS

Geometric Design

The lattice structures are designed by Solidworks (3DS Dassault Systemes, France), as shown in **Figure 1**. The general honeycomb structures are used as the building framework (**Figure 1A**). An angle α is used to control the overall geometry of the lattice. To increase the lattices' stretchability, a curled microstructure is used to replace the straight beams in the honeycomb structure (**Figure 1B**). The curled microstructure consists of two identical curves (**Figure 1D**). The parametric function of the curve is $x(t) = t^{1.5} \cos t$, $y(t) = t^{1.5} \sin t$ ($t = 0$ to π), as shown in **Figure 1C**. The geometrical parameter used are: $L = 10$ mm, $w = 0.2$ mm. The thickness of the lattice is $d = 1$ mm. The curve is scaled to fit the lattice structure.

Comparing to the straight beam, the microstructure exhibits large stretchability. The FE simulated uniaxial tensile stress-strain curves are shown in **Figure 2A**. The Young's modulus of the material is set as 1.2 GPa. The corresponding shapes and the strain maps with strain = 20, 40, and 60% are shown in **Figure 2B**. The stress-strain curve of the microstructure shows a J-shape. Under the uniaxial loading, the microstructure bends and uncurls with a low modulus initially. When the loading force increases further, the microstructure is stretched with a higher modulus, similar as a straight beam. It can be observed that when the total strain is 60%, the maximum local strain is less than 10%. But for a straight beam, the total strain is the same as the local strain. Therefore, the microstructure exhibits a large stretchability compared to the straight beam.

Next, the mechanical behaviors of the lattice structures constructed from the microstructures are investigated. The experimental uniaxial tensile curves of three lattices with $\alpha = 67.5^\circ$, 90° and 112.5° are shown by the solid curves in **Figure 3A**. The lattice structures with 4×4 periodical units are used. The CAD design and the experimental snapshots are shown in **Figure 3B**, **Supplementary Material Video S1–S3**. The lattice structures are fabricated using a commercial 3D printer (Object J750, Stratasys). The shape memory polymer material Vero is used. At room temperature, the elastic modulus of Vero is ~1.2 GPa.

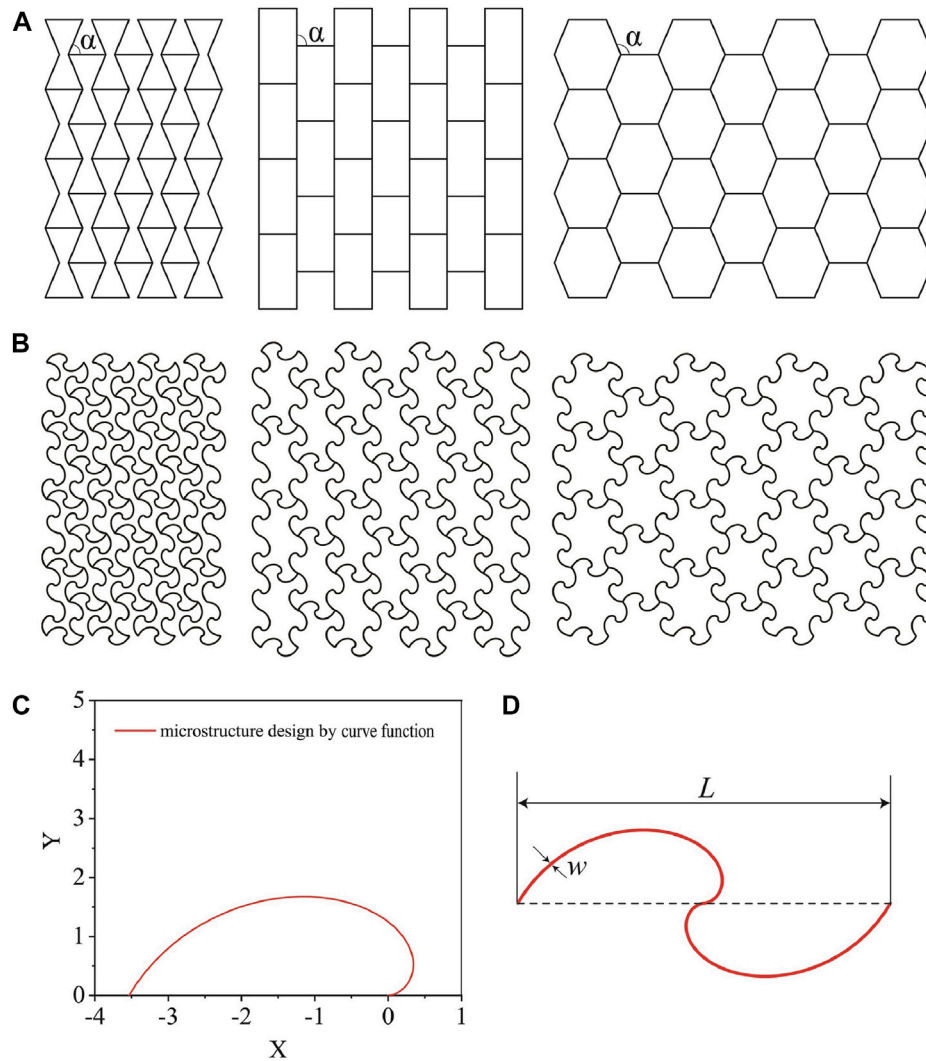


FIGURE 1 | Structural design of the lattice. **(A)** Schematics of three different honeycomb structures. A geometric parameter α is used to control the Poisson's ratios of the honeycomb structures. **(B)** By replacing the straight beam to curled microstructure, the stretchability of the lattice is significantly improved. **(C)** Half of a single microstructure. **(D)** The geometric parameters of a single microstructure.

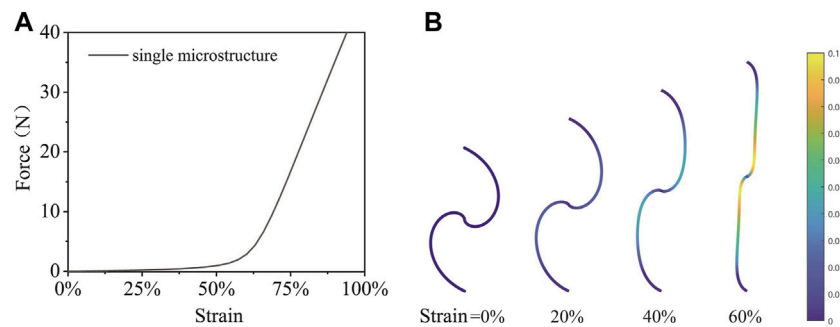


FIGURE 2 | Large stretchability of the microstructure. **(A)** The dependence of the applied force and the axial strain of the microstructure. **(B)** Strain map of a single microstructure at different strains.

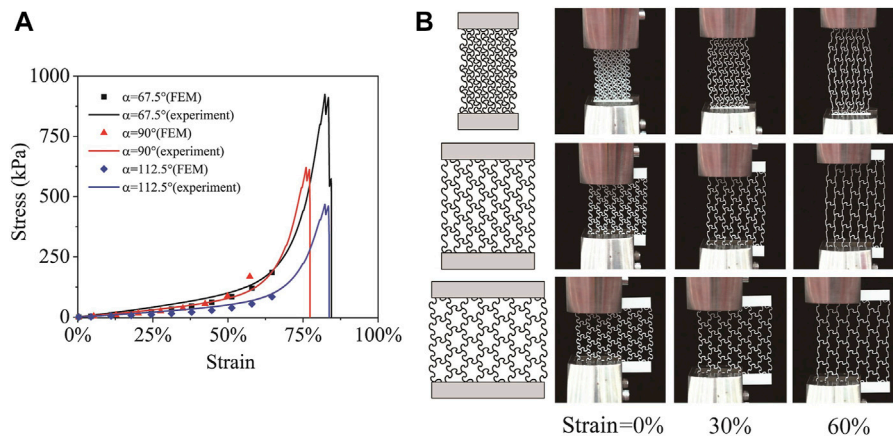


FIGURE 3 | Mechanical behaviors of the lattices under uniaxial tensile loading. **(A)** The experimental and FE simulated curves of three lattices with $\alpha = 67.5^\circ$, 90° , and 112.5° . **(B)** The CAD design and the shapes at various strains are shown.

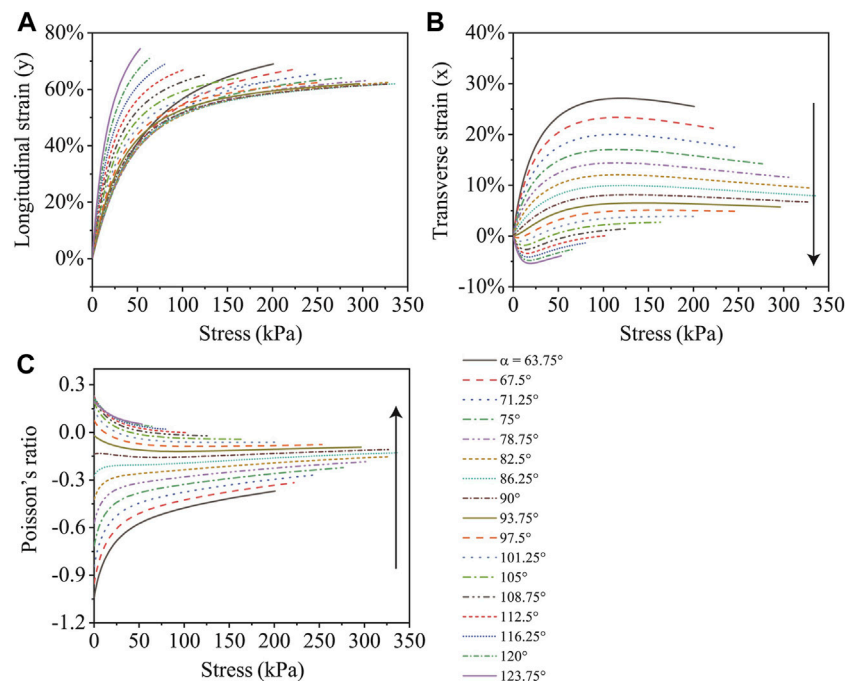


FIGURE 4 | The dependences of the FE simulated **(A)** longitudinal strain, **(B)** transverse strain and **(C)** Poisson's ratio on the applied stress for the highly stretchable lattices with different α .

It can be seen all of the three lattice structures also show a J-shaped stress-strain curve. The failure strain of all three lattices is larger than 70%, while the Vero material's failure strain is generally around 10% (Akbari et al., 2018). By using the microstructure, the stretchability is significantly improved. From the deformed shapes of the lattices, we can observe that: at $\alpha = 67.5^\circ$, the Poisson's ratio is positive, i.e., the lattice expands when stretched. At $\alpha = 90^\circ$, the Poisson's ratio of the lattice is almost zero. The lattice with $\alpha = 112.5^\circ$ exhibits a negative

Poisson's ratio. Therefore, by adjusting the geometric angle α , the Poisson's ratio can be controlled. FE simulations are conducted to simulate the mechanical behaviors of the lattice under uniaxial tensile loading. The FE simulated results are shown by the markers in Figure 3A. The finite element simulation results agree well with the experiments.

We then use the FE simulations to study the lattice's mechanical behaviors with various α . Figure 4 shows the FE simulated uniaxial tensile results for the lattice with α changing

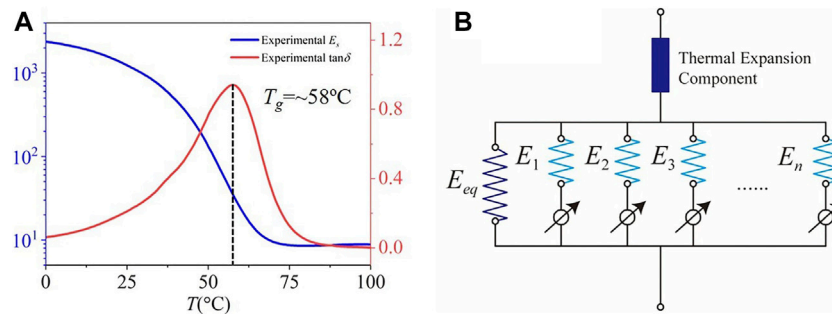


FIGURE 5 | Thermomechanical behaviors of the shape memory polymer Vero. **(A)** The experimental storage modulus and $\tan\delta$ with T . **(B)** The phase evolution model for the lattice.

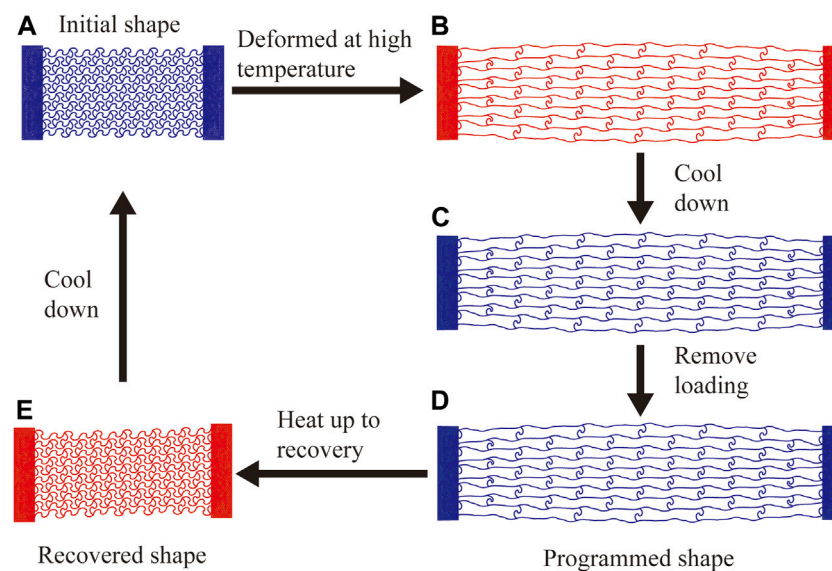


FIGURE 6 | Shape memory cycle of the lattice structures. In Step 1, the lattice deforms from the initial shape **(A)** to **(B)** at high temperature. In Step 2, the lattice is cooled down from **(B)** to **(C)**. In Step 3, the applied loading is removed at low temperature. In Step 4, the programmed shape **(D)** is recovered to shape **(E)** as the temperature increases.

from 63.75° to 123.75° with an interval of 3.75° . The tensile loading is applied in the y -direction. The strain in y (longitudinal strain), x (transverse strain) and the Poisson's ratio are shown in **Figure 4A–C**, respectively. Each lattice structure consists of four units in both the longitudinal and transverse directions.

The modulus of the designed lattice varies with α . All of positive, negative and zero Poisson's ratios can be achieved. As α increases, Poisson's ratio increases from a large negative value to nearly zero and then to a positive value. The Poisson's ratio also changes with the applied stress. Generally, the magnitudes of the Poisson's ratio decreases with the applied stress.

Shape Memory Behaviors of Vero

The material Vero used for the lattice structure is a shape memory polymer. The dependences of storage modulus E_s and $\tan\delta$ on temperature T are experimentally measured using a DMA

machine (TA Instruments, Model Q800), as shown by the solid black curves in **Figure 5A**. As the temperature increases from 0°C – 100°C , the storage modulus of Vero decrease by more than two orders from $\sim 2\text{ GPa}$ ($T = 0^\circ\text{C}$) to $\sim 8\text{ MPa}$ ($T = 100^\circ\text{C}$). Its glassy transition temperature T_g is $\sim 58^\circ\text{C}$.

By fabricating the lattice with the shape memory polymer Vero, the lattice can exhibit large deformation under ambient temperature. Various shapes can then be designed by applying an external stimulus. The shape memory behavior of the lattice is schematically shown in **Figure 6**. Here we take the lattice with $\alpha = 67.5^\circ$ as an example. First, the lattice is stretched at high temperature ($T > T_g$) (**Figure 6B**). Next, the temperature is decreased to a low temperature ($T < T_g$), while the loading or the strain is maintained (**Figure 6C**). The loading is then removed at low temperature (**Figure 6D**). The shape of the lattice in this step is called a programmed shape. By heating the lattice, the lattice will recover to its initial shape (**Figure 6E**).

Phase Evolution Model for Lattice

To model the shape memory behaviors of the honeycomb lattices, a phase evolution model is used (**Figure 5B**) (Wang et al., 2020). The total strain of the lattice is decomposed into two parts: the mechanical strain and the thermal strain. The mechanical strain is modeled by an elastic phase and several glassy phases arranged in parallel. The glassy phases gradually turn on and take effect when T decreases. Depending on the thermomechanical conditions, the glassy phases forming at different times may have different deformation history. As temperature increases, the glassy phases vanish gradually. According to the kinetic description of the heating process, the piece of glassy phase that grows at a later time vanish first. Once a small piece of glassy phase vanishes, the corresponding switch turns off and it does not carry load anymore.

The relation between the applied stress $\sigma(T, \epsilon)$ and the strain ϵ of the honeycomb lattice is assumed to be

$$\sigma(T, \epsilon) = E_s(T)f(\epsilon), \quad (1)$$

in which the effects of temperature and geometric nonlinearity are decoupled. $f(\epsilon)$ represents the geometric nonlinearity due to the lattice structure. For a single solid block, $f(\epsilon) = \epsilon$. The strain comprises of two parts: the mechanical strain $\epsilon^M(T)$ and the thermal strain $\epsilon^T(T)$. The thermal strain can be written as

$$\epsilon^T(T) = (T - T_H)\alpha_r, \quad (2)$$

where α_r is the thermal expansion coefficient. Here we set the thermal strain at a high temperature T_H as the reference state.

In Step 1, the lattice structure deformed at a high temperature $T = T_H$ with an applied stress σ_0 . At $T = T_H$, all of the glassy phases are turned off. Thus only the equilibrium phase works: $E(T) = E_e = 3NkT$ where N is the crosslink density of the shape memory polymer and k is Boltzmann's constant. **Eq. 1** can then be written as:

$$\sigma_0 = 3NkT_H f(\epsilon^M(T_H)), \quad (3)$$

and the mechanical strain can be solved as:

$$\epsilon^M(T_H) = f^{-1}\left(\frac{\sigma_0}{3NkT_H}\right) \quad (4)$$

In Step 2, the applied stress σ_0 is maintained. At the same time, the ambient temperature decreases from T_H to T_L . To ease the derivation, we consider the following two different cases:

- 1) the first glassy phase formed as T decreases.
- 2) the $(a + 1)$ th glassy phase forms.

Case 1) As the ambient temperature T decreases, new glassy phases are generated. We set that the first glassy phase forms when the temperature decreases from T_0 to $T_1 = T_0 - \Delta T_1$. Therefore, the applied stress can be written as the sum of the stress on the equilibrium and the first glassy phases:

$$\sigma_0 = 3NkT_1 f(\epsilon^M(T_1)) + E_1(f(\epsilon^M(T_1)) - f(\epsilon^M(T_0))) \quad (5)$$

Note that the modulus of the equilibrium branch decrease from $3NkT_0$ to $3NkT_1$. $\epsilon^M(T_0)$ can be obtained from **Eq. 4**. $\epsilon^M(T_1)$ is then solved as:

$$\epsilon^M(T_1) = f^{-1}\left(\frac{\sigma_0 + E_1\sigma_0/3NkT_0}{3NkT_1 + E_1}\right) \quad (6)$$

and the strain stored in the first glassy phase $\epsilon_1(T_1)$ at T_1 is then $\epsilon_1(T_1) = \epsilon^M(T_1) - \epsilon^M(T_0)$. We use $\epsilon_1^0 = \epsilon^M(T_0)$ to represent the strain of the lattice structure when the first glassy branch starts to work.

Case 2) At $T = T_a$, the $(a + 1)$ th glassy phase is not formed yet. The applied stress is the sum of the stress on all the currently working branches:

$$\sigma_0 = 3NkT_a f(\epsilon^M(T_a)) + \sum_{i=1}^a E_i(f(\epsilon^M(T_a)) - f(\epsilon_i^0)) \quad (7)$$

where ϵ_i^0 represents the mechanical strain of the lattice structure when i th glassy branch starts to work.

The $(a + 1)$ th glassy phase forms as T decreases from T_a to $T_{a+1} = T_a - \Delta T_{a+1}$. As the new phases forms, the strains in all working branches increases by $\Delta\epsilon_{a+1}$. The stress-strain relation at $T = T_{a+1}$ can be written as:

$$\sigma_0 = 3NkT_{a+1} f(\epsilon^M(T_{a+1})) + \sum_{i=1}^{a+1} E_i(f(\epsilon^M(T_{a+1})) - f(\epsilon_i^0)) \quad (8)$$

By comparing **Eqs 7, 8**, the mechanical strain can then be calculated as:

$$\epsilon^M(T_{a+1}) = f^{-1}\left(\frac{\sigma_0 + \sum_{i=1}^{a+1} E_i f(\epsilon_{i0})}{3NkT_{a+1} + \sum_{i=1}^{a+1} E_i}\right) \quad (9)$$

The strain in each phase now is $\epsilon_i(T_{a+1}) = \epsilon^M(T_{a+1}) - \epsilon_{i0}$, $i = 1$ to $a + 1$.

The applied stress is released at T_L in step 3. Before the applied stress is released, the stress-strain relation is

$$\sigma_0 = 3NkT_L f(\epsilon^M(T_L)) + \sum_{i=1}^n E_i[f(\epsilon^M(T_L)) - f(\epsilon_i^0)] \quad (10)$$

After release, the strain in each phase increase by $\Delta\epsilon$, thus

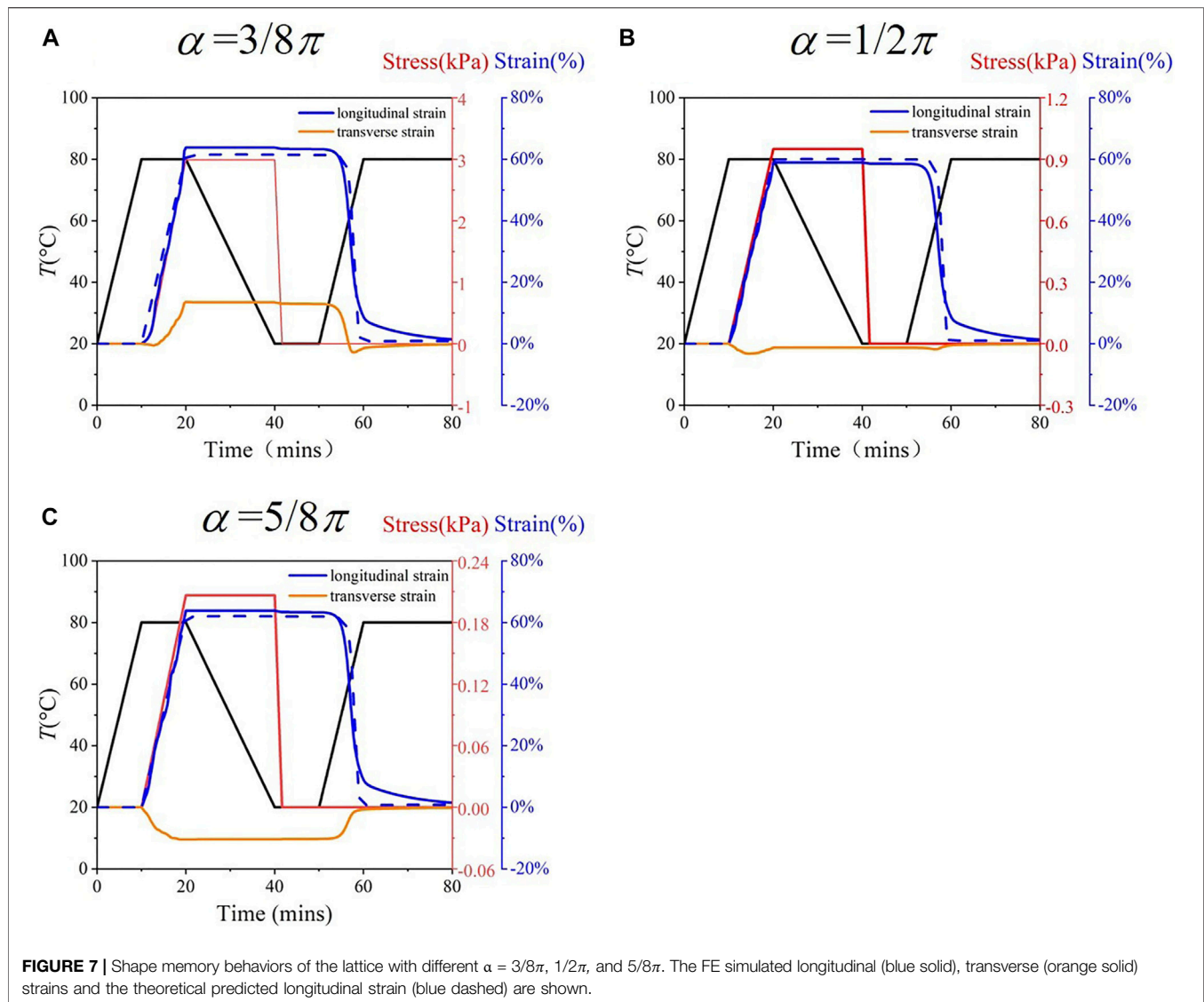
$$0 = 3NkT_L f(\epsilon^M(T_L) + \Delta\epsilon) + \sum_{i=1}^n E_i[f(\epsilon^M(T_L) + \Delta\epsilon) - f(\epsilon_i^0)] \quad (11)$$

$\Delta\epsilon$ can then be calculated from **Eqs 11, 12** as:

$$\Delta\epsilon = f^{-1}\left(f(\epsilon^M(T_L)) - \frac{\sigma_0}{3NkT_L + E_g}\right) - \epsilon^M(T_L) \quad (12)$$

where the term $E_g = \sum_{i=1}^n E_i$ is used.

In Step 4, the programmed shape in Step 3 recover to its initial shape when the temperature increases from T_L to T_H . At this step, the glassy phases switch off one by one, and the stored strain is released. This process is similar to step 2, except the glassy phases are disconnected.



In summary, the thermal strain is given in Eq. 2. The mechanical strain in each step is given in Eqs 4, 6, 9 and 12.

Finite Element Simulations

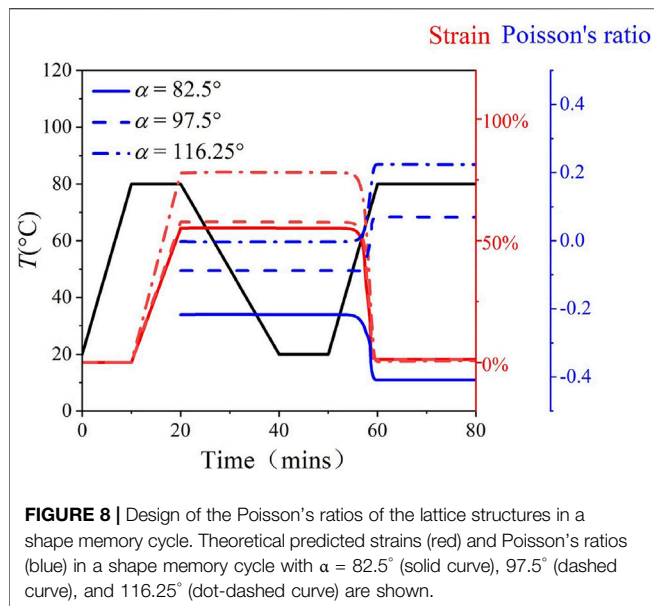
FE simulations are conducted using ABAQUS (3DS Dassault Systemes, France) to analyze the mechanical behaviors and the shape memory effects of the lattice structures. The multi-branch model is used to capture the thermo-mechanical behaviors of the lattices. The 3-node plane strain thermally coupled triangle element CPE3T is used.

RESULTS AND DISCUSSION

Figure 7 presents the FE simulated shape memory cycle (solid curves) of the lattices with $\alpha = 3/8\pi$, $1/2\pi$, and $5/8\pi$. The quantitative dependence of longitudinal (blue) and transverse (orange) strains on time are presented. The theoretical predicted

longitudinal strain is presented by the dashed blue curves. The lattice is under stress control mode. The theoretical prediction and the FE simulated results agree well. All the three lattices demonstrate a significant recovery at $T = \sim 60^\circ\text{C}$. The lattice's transverse strain with $\alpha = 3/8\pi$ is generally larger than 0, indicating a negative Poisson's ratio. The transverse strain also decreases to around 0 when the temperature increases. The Poisson's ratio of the lattice with $\alpha = 1/2\pi$ is almost zero in the whole shape memory cycle. The lattice with $\alpha = 5/8\pi$ always exhibits a negative transverse strain (Positive Poisson's ratio).

It should be noted that there is some discrepancy between the theoretical predicted and FE simulated longitudinal strain, especially in the recovery stage. The FE simulated recovery is slower than the theoretically predicted result. In the theoretical model, the nonlinear phase is only affected by the temperature and independent of time. In the FE simulations, the dependence of the modulus on time is also taken into account. However, compared to the FE simulation's high computational cost, the



theoretical results can be calculated in seconds. Therefore, the theoretical model enables the study of the effects of the geometric parameters.

In **Figure 8**, the dependence of the Poisson's ratios on α is studied by the theoretical model. Three lattices with $\alpha = 82.5^\circ$, 97.5° , and 116.25° are chosen. The FE simulated stress-strain/Poisson's ratio curves shown in **Figure 4** are used as input. $f(\epsilon)$ are obtained from the FE simulated curves. The applied stress in the loading step is 1 kPa. The theoretical predicted strain and Poisson's ratio in a shape memory cycle are shown by the red and blue curves, respectively. It can be seen that: (1) the stiffness of the three lattices are different. The stiffness of the lattice with $\alpha = 116.25^\circ$ is relatively small. All of the strains and Poisson's ratios change significantly around T_g in the heating step. The Poisson's ratio of the lattice with $\alpha = 116.25^\circ$ is always negative. For the lattice with $\alpha = 82.5^\circ$, the Poisson's ratio changes from ~0 to a positive value when T increases. The Poisson's ratio of the lattice with $\alpha = 97.5^\circ$ changes from negative to positive, which indicates that the lattice first expands and then shrinks when T increases. Therefore, by applying an external stimulus, not only the magnitude of the Poisson's ratio but also its directions can be altered.

Reliability and repeatability are important factors of structural safety. The reliability and repeatability of a lattice structure mainly depend on the geometric structure and the material. Specific lattice structures have been designed to improve the reliability with applications in areas such as energy absorption Tancogne-Dejean et al. (2016) and efficient response to impulsive loads (Imbalzano et al., 2017). The lattice structure used in this work by replacing the straight beam with microstructures can significantly reduce the local strain comparing to the traditional honeycomb Queheillalt and Wadley (2005) when the same total strain is applied. As shown in **Figure 2B**, the local strain is generally less than 10% when the microstructure is stretched up to 60%. The small local strain reduces the fatigue of the material

and increases the repeatability of the lattice structure. The use of microstructures can also reduce sensitivity to structural defects (Yan et al., 2020). Furthermore, the material Vero has a tensile strength of around 60 MPa and strong ability to withstand bending (2.2–3.2 GPa) (Ju et al., 2014). Vero's fracture properties have been investigated, and results show that Vero has higher tensile strength and failure strain than natural rock-like materials (Liu et al., 2020). Therefore, by combining structure design and material performance, the structure's reliability and repeatability are improved. We also note that the lattice structure's reliability and repeatability can be improved by optimizing the geometric parameters of the microstructures.

CONCLUSION

In this work, we designed a type of shape reconfigurable, highly stretchable honeycomb lattice structures with tunable Poisson's ratio. Using a geometric angle α , the Poisson's ratio of the lattice structure can be tuned to be positive, negative or zero. To increase the stretchability of the lattice structure, the straight beam in the lattice is replaced by a curled microstructure. When an external loading is applied, the microstructure bends, uncurls and rotates to aligning to the loading direction. Therefore, the stretchability of the lattice structure is significantly improved. Experiments show that the failure strain of the lattice structures is generally larger than 70%, which is seven folds larger than the failure strain of the material.

To enable the lattice's capacity of shape reconfiguration, we use a shape memory polymer Vero to 3D print the lattice. When the ambient temperature increases, the lattice demonstrates a large shape change. To predict the shape change of lattice structure, a phase evolution model is employed. Results show that the theoretically predicted shape changes agree well with the FE simulations. Also, the theoretical model can significantly reduce the computational cost. Theoretical prediction further shows that by increasing the temperature, not only the magnitude of the lattice but also its sign can change. The shape reconfigurable, highly stretchable, Poisson's ratio tunable lattice structures may find a broad range of applications in areas such as shock-absorbing, aerospace morphing structures, soft robotics and minimally invasive biomedical devices.

DATA AVAILABILITY STATEMENT

The original contributions presented in the study are included in the article/**Supplementary Material**, further inquiries can be directed to the corresponding author.

AUTHOR CONTRIBUTIONS

LD, and DW conceived the idea and experimental work; LD CJ led the experiments and simulation with assistance from JW, LD,

and DW contributed to data analysis and interpretation and wrote the paper. All authors provided feedback.

ACKNOWLEDGMENTS

DW acknowledges the support by grants from the National Natural Science Foundation of China (Grant No. 51905336) and the Shanghai Sailing Program from Shanghai Municipal

Committee of Science and Technology (Grant No. 19YF1423000).

SUPPLEMENTARY MATERIAL

The Supplementary Material for this article can be found online at: <https://www.frontiersin.org/articles/10.3389/fmats.2021.660325/full#supplementary-material>

REFERENCES

- Ai, L., and Gao, X.-L. (2017). Micromechanical Modeling of 3D Printable Interpenetrating Phase Composites with Tailorable Effective Elastic Properties Including Negative Poisson's Ratio. *J. Micromech. Mol. Phys.* 02, 1750015. doi:10.1142/s2424913017500151
- Akbari, S., Sakhaei, A. H., Kowsari, K., Yang, B., Ahmad, S., Zhang, Y., et al. (2018). Enhanced Multimaterial 4D Printing with Active Hinges. *Smart Mater. Structures* 27, 065027. doi:10.1088/1361-665x/aabe63
- Alderson, K. L., and Evans, K. E. (1992). The Fabrication of Microporous Polyethylene Having a Negative Poisson's Ratio. *Polymer* 33, 4435–4438. doi:10.1016/0032-3861(92)90294-7
- Alderson, K. L., Fitzgerald, A., and Evans, K. E. (2000). The Strain Dependent Indentation Resilience of Auxetic Microporous Polyethylene. *J. Mater. Sci.* 35, 4039–4047. doi:10.1023/a:1004830103411
- Bertoldi, K., Vitelli, V., Christensen, J., and Van Hecke, M. (2017). Flexible Mechanical Metamaterials. *Nat. Rev. Mater.* 2, 1–11. doi:10.1038/natrevmats.2017.66
- Bodaghi, M., Damanpack, A. R., and Liao, W. H. (2016). Self-expanding/shrinking Structures by 4D Printing. *Smart Mater. Struct.* 25, 105034. doi:10.1088/0964-1726/25/10/105034
- Caddock, B. D., and Evans, K. E. (1989). Microporous Materials with Negative Poisson's Ratios. I. Microstructure and Mechanical Properties. *J. Phys. D: Appl. Phys.* 22, 1877–1882. doi:10.1088/0022-3727/22/12/012
- Cao, C., Gao, X., and Conn, A. T. (2019). A Magnetically Coupled Dielectric Elastomer Pump for Soft Robotics. *Adv. Mater. Technol.* 4, 1900128. doi:10.1002/admt.201900128
- Chen, Y., Li, T., Scarpa, F., and Wang, L. (2017). Lattice Metamaterials with Mechanically Tunable Poisson's Ratio for Vibration Control. *Phys. Rev. Appl.* 7, 024012. doi:10.1103/physrevapplied.7.024012
- Chetverikov, A. P., Dmitriev, S. V., Korznikova, E. A., and Sergeev, K. S. (2019). Dissipative Solitons and Crowdions in Triangular Lattice of Active Particles. *J. Micromech. Mol. Phys.* 04, 1850005. doi:10.1142/s2424913018500054
- Clayton, J. D., and Knap, J. (2018). Geometric Micromechanical Modeling of Structure Changes, Fracture and Grain Boundary Layers in Polycrystals. *J. Micromech. Mol. Phys.* 03, 1840001. doi:10.1142/s2424913018400015
- de Jonge, C., Kolken, H., Zadpoor, A., and Zadpoor, A. A. (2019). Non-Auxetic Mechanical Metamaterials. *Materials* 12, 635. doi:10.3390/ma12040635
- Ding, Z., Yuan, C., Peng, X., Wang, T., Qi, H. J., and Dunn, M. L. (2017). Direct 4D Printing via Active Composite Materials. *Sci. Adv.* 3, e1602890. doi:10.1126/sciadv.1602890
- Ding, Z., Weeger, O., Qi, H. J., and Dunn, M. L. (2018). 4D Rods: 3D Structures via Programmable 1D Composite Rods. *Mater. Des.* 137, 256–265. doi:10.1016/j.matdes.2017.10.004
- Fozdar, D. Y., Soman, P., Lee, J. W., Han, L.-H., and Chen, S. (2011). Three-Dimensional Polymer Constructs Exhibiting a Tunable Negative Poisson's Ratio. *Adv. Funct. Mater.* 21, 2712–2720. doi:10.1002/adfm.201002022
- Ge, Q., Sakhaei, A. H., Lee, H., Dunn, C., and Fang, N. X. (2016). Multimaterial 4D Printing with Tailorable Shape Memory Polymers. *Scientific Rep.* 6, 1–11. doi:10.1038/srep31110
- Guo, Y., Zhang, J., Chen, L., Du, B., Liu, H., Chen, L., et al. (2020). Deformation Behaviors and Energy Absorption of Auxetic Lattice Cylindrical Structures under Axial Crushing Load. *Aerospace Sci. Tech.* 98, 105662. doi:10.1016/j.ast.2019.105662
- Hu, C., Dong, J., Luo, J., Qin, Q.-H., and Sun, G. (2020). 3D Printing of Chiral Carbon Fiber Reinforced Polylactic Acid Composites with Negative Poisson's Ratios. *Composites B: Eng.* 201, 108400. doi:10.1016/j.compositesb.2020.108400
- Hu, L. L., Zhou, M. Z., and Deng, H. (2019). Dynamic Indentation of Auxetic and Non-auxetic Honeycombs under Large Deformation. *Compos. Structures* 207, 323–330. doi:10.1016/j.compstruct.2018.09.066
- Huang, C., and Chen, L. (2016). Negative Poisson's Ratio in Modern Functional Materials. *Adv. Mater.* 28, 8079–8096. doi:10.1002/adma.201601363
- Imbalzano, G., Tran, P., DLee, T., Lee, P. V., and Peter, T. D. (2017). Three-dimensional Modelling of Auxetic sandwich Panels for Localised Impact Resistance. *Jnl Sandwich Structures Mater.* 19, 291–316. doi:10.1177/1099636215618539
- Ji, Z., Yan, C., Yu, B., Wang, X., and Zhou, F. (2017). Multimaterials 3D Printing for Free Assembly Manufacturing of Magnetic Driving Soft Actuator. *Adv. Mater. Inter.* 4, 1700629. doi:10.1002/admi.201700629
- Jiang, Y., and Wang, Q. (2016). Highly-stretchable 3D-Architected Mechanical Metamaterials. *Scientific Rep.* 6, 1–11. doi:10.1038/srep34147
- Ju, Y., Xie, H., Zheng, Z., Lu, J., Mao, L., Gao, F., et al. (2014). Visualization of the Complex Structure and Stress Field inside Rock by Means of 3D Printing Technology. *Chin. Sci. Bull.* 59, 5354–5365. doi:10.1007/s11434-014-0579-9
- Keskar, N. R., and Chelikowsky, J. R. (1992). Negative Poisson Ratios in Crystalline SiO₂ from First-Principles Calculations. *Nature* 358, 222–224. doi:10.1038/358222a0
- Khan, K. A., Al-Mansoor, S., Khan, S. Z., and Khan, M. A. (2019). Piezoelectric Metamaterial with Negative and Zero Poisson's Ratios. *J. Eng. Mech.* 145, 04019101. doi:10.1061/(asce)em.1943-7889.0001674
- Khare, E., Temple, S., Tomov, I., Zhang, F., and Stoyan, K. S. (2018). Low Fatigue Dynamic Auxetic Lattices with 3D Printable, Multistable, and Tuneable Unit Cells. *Front. Mater.* 5, 45. doi:10.3389/fmats.2018.00045
- Kong, D., Li, J., Guo, A., Yu, J., and Xiao, X. (2021a). Smart Polyimide with Recovery Stress at the Level of High Temperature Shape Memory Alloys. *Smart Mater. Structures* 30, 035027. doi:10.1088/1361-665x/abe182
- Kong, D., Li, J., Guo, A., and Xiao, X. (2021b). High Temperature Electromagnetic Shielding Shape Memory Polymer Composite. *Chem. Eng. J.* 408, 127365. doi:10.1016/j.cej.2020.127365
- Kong, D., Li, J., Guo, A., Zhang, X., and Xiao, X. (2019). Self-healing High Temperature Shape Memory Polymer. *Eur. Polym. J.* 120, 109279. doi:10.1016/j.eurpolymj.2019.109279
- Lantean, S., Barrera, G., Pirri, C. F., Tiberto, P., Sangermano, M., Roppolo, I., et al. (2019). 3D Printing of Magneto-responsive Polymeric Materials with Tunable Mechanical and Magnetic Properties by Digital Light Processing. *Adv. Mater. Technol.* 4, 1900505. doi:10.1002/admt.201900505
- Lee, J. H., Hinchet, R., Kim, S. K., Kim, S., and Kim, S.-W. (2015). Shape Memory Polymer-Based Self-Healing Triboelectric Nanogenerator. *Energy Environ. Sci.* 8, 3605–3613. doi:10.1039/c5ee02711j
- Lees, C., Vincent, J. F. V., and Hillerton, J. E. (1991). Poisson's Ratio in Skin. *Bio-medical Mater. Eng.* 1, 19–23. doi:10.3233/bme-1991-1104
- Lendlein, A., and Kelch, S. (2005). Shape-memory Polymers as Stimuli-Sensitive Implant Materials. *Clin. Hemorheol. Microcirc.* 32, 105–116.
- Lendlein, A., and Langer, R. (2002). Biodegradable, Elastic Shape-Memory Polymers for Potential Biomedical Applications. *Science* 296, 1673–1676. doi:10.1126/science.1066102
- Li, S., Hassanin, H., Attallah, M. M., Adkins, N. J. E., and Essa, K. (2016). The Development of TiNi-Based Negative Poisson's Ratio Structure Using Selective Laser Melting. *Acta Materialia* 105, 75–83. doi:10.1016/j.actamat.2015.12.017

- Li, T., Chen, Y., Hu, X., Li, Y., and Wang, L. (2018). Exploiting Negative Poisson's Ratio to Design 3D-Printed Composites with Enhanced Mechanical Properties. *Mater. Des.* 142, 247–258. doi:10.1016/j.matdes.2018.01.034
- Li, T., Liu, F., and Wang, L. (2020). Enhancing Indentation and Impact Resistance in Auxetic Composite Materials. *Composites Part B: Eng.* 198, 108229. doi:10.1016/j.compositesb.2020.108229
- Li, Y., Luo, S., Yang, M.-C., Liang, R., and Zeng, C. (2016). Poisson Ratio and Piezoresistive Sensing: A New Route to High-Performance 3D Flexible and Stretchable Sensors of Multimodal Sensing Capability. *Adv. Funct. Mater.* 26, 2900–2908. doi:10.1002/adfm.201505070
- Liu, J., and Zhang, Y. (2018). Soft Network Materials with Isotropic Negative Poisson's Ratios over Large Strains. *Soft Matter* 14, 693–703. doi:10.1039/c7sm02052j
- Liu, P., Ju, Y., Fu, G., and Ren, Z. (2020). Visualization of Full-Field Stress Evolution during 3D Penetrated Crack Propagation through 3D Printing and Frozen Stress Techniques. *Eng. Fracture Mech.* 236, 107222. doi:10.1016/j.engfracmech.2020.107222
- Ma, Q., Cheng, H., Jang, K.-I., Luan, H., Hwang, K.-C., Hwang, Keh-Chih., et al. (2016). A Nonlinear Mechanics Model of Bio-Inspired Hierarchical Lattice Materials Consisting of Horseshoe Microstructures. *J. Mech. Phys. Sol.* 90, 179–202. doi:10.1016/j.jmps.2016.02.012
- Milton, G. W. (1992). Composite Materials with Poisson's Ratios Close to -1. *J. Mech. Phys. Sol.* 40, 1105–1137. doi:10.1016/0022-5096(92)90063-8
- Queheillalt, D. T., and Wadley, H. N. G. (2005). Cellular Metal Lattices with Hollow Trusses. *Acta Materialia* 53, 303–313. doi:10.1016/j.actamat.2004.09.024
- Rafsanjani, A., and Pasini, D. (2016). Bistable Auxetic Mechanical Metamaterials Inspired by Ancient Geometric Motifs. *Extreme Mech. Lett.* 9, 291–296. doi:10.1016/j.eml.2016.09.001
- Saxena, K. K., Das, R., and Calius, E. P. (2016). Three Decades of Auxetics Research – Materials with Negative Poisson's Ratio: A Review. *Adv. Eng. Mater.* 18, 1847–1870. doi:10.1002/adem.201600053
- Shao, L.-H., Zhao, B., Zhang, Q., Xing, Y., and Zhang, K. (2020). 4D Printing Composite with Electrically Controlled Local Deformation. *Extreme Mech. Lett.* 39, 100793. doi:10.1016/j.eml.2020.100793
- Tancogne-Dejean, T., Spierings, A. B., and Mohr, D. (2016). Additively-manufactured Metallic Micro-lattice Materials for High Specific Energy Absorption under Static and Dynamic Loading. *Acta Materialia* 116, 14–28. doi:10.1016/j.actamat.2016.05.054
- Testa, P., Style, R. W., Cui, J., Donnelly, C., Borisova, E., Derlet, P. M., et al. (2019). Magnetically Addressable Shape-Memory and Stiffening in a Composite Elastomer. *Adv. Mater.* 31, 1900561. doi:10.1002/adma.201900561
- Timmins, L. H., Wu, Q., Yeh, A. T., Moore, J. E., and Greenwald, S. E. (2010). Structural Inhomogeneity and Fiber Orientation in the Inner Arterial media. *Am. J. Physiology-Heart Circulatory Physiol.* 298, H1537–H1545. doi:10.1152/ajpheart.00891.2009
- Veronda, D. R., and Westmann, R. A. (1970). Mechanical Characterization of Skin-Finite Deformations. *J. Biomech.* 3, 111–124. doi:10.1016/0021-9290(70)90055-2
- Wang, D., Xu, H., Wang, J., Jiang, C., Zhu, X., Ge, Q., et al. (2020). Design of 3D Printed Programmable Horseshoe Lattice Structures Based on a Phase-Evolution Model. *ACS Appl. Mater. Inter.* 12, 22146–22156. doi:10.1021/acsami.0c04097
- Wang, Y., Wang, L., Ma, Z.-d., and Wang, T. (2016). A Negative Poisson's Ratio Suspension Jounce Bumper. *Mater. Des.* 103, 90–99. doi:10.1016/j.matdes.2016.04.041
- Williams, J. L., and Lewis, J. L. (1982). *Properties and an Anisotropic Model of Cancellous Bone from the Proximal Tibial Epiphysis*. New York: The American Society of Mechanical Engineers (ASME).
- Yan, D., Chang, J., Zhang, H., Liu, J., Song, H., Xue, Z., et al. (2020). Soft Three-Dimensional Network Materials with Rational Bio-Mimetic Designs. *Nat. Commun.* 11, 1–11. doi:10.1038/s41467-020-14996-5
- Yan, Z. G., Wang, B. L., Wang, K. F., and Zhang, C. (2019). A Novel Cellular Substrate for Flexible Electronics with Negative Poisson Ratios under Large Stretching. *Int. J. Mech. Sci.* 151, 314–321. doi:10.1016/j.ijmecsci.2018.11.026
- Yang, C., Boorugu, M., Dopp, A., Ren, J., Martin, R., Han, D., et al. (2019). 4D Printing Reconfigurable, Deployable and Mechanically Tunable Metamaterials. *Mater. Horiz.* 6, 1244–1250. doi:10.1039/c9mh00302a
- Yiming, B., Wu, L., Zhang, M., Han, Z., Zhao, P., Li, T., et al. (2020). Highly Stretchable Bilayer Lattice Structures that Elongate via In-Plane Deformation. *Adv. Funct. Mater.* 30, 1909473. doi:10.1002/adfm.201909473
- Yuan, C., Kowsari, K., Panjwani, S., Chen, Z., Wang, D., Zhang, B., et al. (2019). Ultrafast Three-Dimensional Printing of Optically Smooth Microlens Arrays by Oscillation-Assisted Digital Light Processing. *ACS Appl. Mater. Inter.* 11, 40662–40668. doi:10.1021/acsami.9b14692
- Ze, Q., Kuang, X., Wu, S., Wong, J., Montgomery, S. M., Zhang, R., et al. (2020). Magnetic Shape Memory Polymers with Integrated Multifunctional Shape Manipulation. *Adv. Mater.* 32, 1906657. doi:10.1002/adma.201906657

Conflict of Interest: The authors declare that the research was conducted in the absence of any commercial or financial relationships that could be construed as a potential conflict of interest.

Copyright © 2021 Dong, Jiang, Wang and Wang. This is an open-access article distributed under the terms of the Creative Commons Attribution License (CC BY). The use, distribution or reproduction in other forums is permitted, provided the original author(s) and the copyright owner(s) are credited and that the original publication in this journal is cited, in accordance with accepted academic practice. No use, distribution or reproduction is permitted which does not comply with these terms.

Advantages of publishing in Frontiers



OPEN ACCESS

Articles are free to read
for greatest visibility
and readership



FAST PUBLICATION

Around 90 days
from submission
to decision



HIGH QUALITY PEER-REVIEW

Rigorous, collaborative,
and constructive
peer-review



TRANSPARENT PEER-REVIEW

Editors and reviewers
acknowledged by name
on published articles

Frontiers

Avenue du Tribunal-Fédéral 34
1005 Lausanne | Switzerland

Visit us: www.frontiersin.org

Contact us: frontiersin.org/about/contact



REPRODUCIBILITY OF RESEARCH

Support open data
and methods to enhance
research reproducibility



DIGITAL PUBLISHING

Articles designed
for optimal readership
across devices



FOLLOW US

@frontiersin



IMPACT METRICS

Advanced article metrics
track visibility across
digital media



EXTENSIVE PROMOTION

Marketing
and promotion
of impactful research



LOOP RESEARCH NETWORK

Our network
increases your
article's readership